



Optimization of Hydrophilic-Lipophilic Balance Solid-Phase Extraction of Phthalates in Pharmaceutical Preparations

Pelin Köseoğlu Yılmaz  

Department of Analytical Chemistry, Faculty of Pharmacy, Istanbul University, Istanbul, Turkey.

Abstract: Phthalates, which are used as plasticizers to soften rough polymers in the industrial processes, possess endocrine system disrupting activities. In this study, a hydrophilic-lipophilic balance solid-phase extraction method was optimized for seven phthalates as dimethyl, dipropyl, benzyl butyl, di-n-butyl, dicyclohexyl, di-(2-ethylhexyl) and di-n-octyl phthalates in terms of the type and the volume of the conditioning and the elution solvents. The phthalates were quantified by a validated HPLC/UV method. The recovery values were higher than 80% for dimethyl, dipropyl, benzylbutyl, di-n-butyl and dicyclohexyl phthalates. Using optimized conditions, three types of liquid pharmaceutical preparations as an intravenous isotonic sodium chloride solution, an intravenous dextrose solution and an osmotic laxative kept in polymeric packages were analyzed with high accuracy, precision and recovery. Only the intravenous isotonic sodium chloride solution was determined to be contaminated with dipropyl phthalate at a concentration of 13.2 ± 0.16 $\mu\text{g/L}$.

Keywords: Hydrophilic-lipophilic balance, high performance liquid chromatography, pharmaceutical, phthalate, solid-phase extraction.

Submitted: February 12, 2019. **Accepted:** May 22, 2019.

Cite this: Köseoğlu Yılmaz P. Optimization of Hydrophilic-Lipophilic Balance Solid-Phase Extraction of Phthalates in Pharmaceutical Preparations. JOTCSA. 2019;6(3):271-80.

DOI: <https://doi.org/10.18596/jotcsa.526124>.

Corresponding author: E-mail: pelink@istanbul.edu.tr. Phone: +902124400000-13504.

INTRODUCTION

Phthalates are a class of dialkyl or alkyl aryl esters of 1,2-benzenedicarboxylic acid. They are suspected endocrine-disrupting compounds widely used to increase the flexibility of plastics or in common household products, cosmetics, detergents, flame retardants, plastics, inks, adhesives, metal food can liners, and medical devices (1). Since phthalates are not chemically bounded to polymer matrices, they can easily migrate to foods, beverages, cosmetics, and pharmaceuticals kept in polymeric packages (2).

Some of the phthalates are thought to disrupt the endocrine system by competing with 17β -estradiol for binding to the estrogen receptors (3). Also, toxicological studies have revealed that the lower molecular weight phthalates were irritating to eyes, nose, throat, and larger molecular weight phthalates were suspected carcinogens (1).

Considering the negative impacts of phthalates on human health, it became more of an issue to develop reliable extraction and analysis methods. Because of the low concentration levels and complex sample matrices, direct use of the analytical methods is usually limited by their sensitivity and/or selectivity. Generally, a pre-concentration/clean-up step is necessary prior to analysis. In this purpose, solid-phase extraction (SPE) is one of the mostly used methods in determination of phthalates (4). Different types of SPE sorbents such as PLRP-S (5), C18 (6), polymeric anion exchanger (7), florisil (8), carbon nanotubes (9), magnetic carbon nanotubes (10), magnetic graphene (11, 12) and molecularly imprinted polymers (13) have been used for the extraction of phthalates from various matrices. In a study, hydrophilic-lipophilic balance (HLB) sorbent, which is a hydrophilic modified polymeric reversed-phase material, was used to investigate the potential migration of plasticizers, plastic components and additives from several plastic water bottles (14). Since HLB is water-wettable, it possesses high retention capability even if the

sorbent runs dry. Also HLB contains both nonpolar and polar functional groups, that provides retention of a wide range of analytes from aqueous samples (4).

One of the reasons of the exposure to phthalates for human is the contaminated pharmaceutical preparations kept in polymeric packages. There are several studies on migration and/or determination of pharmaceutical packaging materials in the literature (15, 16). In the present study, it was aimed to determine the phthalate content of liquid pharmaceutical preparation samples in polymeric packages by an offline SPE-HPLC/UV method. A SPE procedure was optimized for the extraction of seven phthalates as dimethyl (DMP), dipropyl (DPP), benzyl butyl (BBP), di-n-butyl (DBP), dicyclohexyl (DCHP), di-(2-ethylhexyl) (DEHP) and di-n-octyl (DOP) phthalates using HLB cartridges. The analytes were detected by a simultaneous HPLC-UV method. Finally, the developed SPE-HPLC/UV method was applied to 3 different types of liquid pharmaceutical preparations as an intravenous isotonic NaCl solution, an intravenous dextrose solution, and an osmotic laxative preparation kept in polymeric packages.

MATERIALS AND METHODS

Materials and chemicals

The analytical standards of DMP, DPP, DBP, BBP, DCHP, DEHP, DOP and formic acid (FA) were purchased from Sigma (Darmstadt, Germany). The stock solution that contained each of the analyzed phthalates at a concentration of 10 mg/L was prepared with HPLC-grade methanol. The standard solutions in the range of 0.05–2.50 mg/L were prepared by diluting the stock solution to appropriate volumes with the mobile phase. Supel™-Select HLB SPE cartridges (200 mg/6 mL) were purchased from Sigma-Aldrich (Düren, Germany). Methanol (MeOH) (HPLC-grade), acetonitrile (ACN) (HPLC-grade), o-phosphoric acid (OPA) and potassium dihydrogen phosphate (KH_2PO_4) were purchased from Merck (Darmstadt, Germany). The phosphate buffer was prepared with 0.78 g KH_2PO_4 and 340 μL of OPA in 1 L of ultra pure water. All of the glassware used was rinsed with n-hexane and dried at 90°C to avoid any contamination of phthalates. Also a blank analysis was carried out to check the purity of the chemicals and SPE cartridge used.

Pharmaceutical preparation samples

Intravenous isotonic NaCl solution, intravenous dextrose solution, and osmotic laxative preparation in polymeric packages were purchased from a local drugstore in Istanbul (Turkey) in 2017.

Instruments and analytical conditions

The quantitative analysis of the phthalates was accomplished with a Shimadzu (Shimadzu, Kyoto, Japan) LC20A HPLC system with UV detection. Analytes were separated on a GL Sciences (GL

Sciences, Tokyo, Japan) Intersil ODS-3 column (C18, 250×4.6 mm, i.d. 5.0 μm) and quantified by a slightly modified HPLC-UV method, which was developed and validated in a former study (2). A gradient program with a mobile phase system consisting of 0.2 M KH_2PO_4 buffer (pH 2.6) and MeOH/ACN (50:50, v/v) was established for the elution. The flow rate was 1 mL/min and the injection volume was set to 20 μL . The column temperature was adjusted to 40°C. The analyte peaks were detected at 230 nm. All of the analyses were performed in triplicate. The data obtained were analyzed by the LabSolutions software (version 1.25).

Quantification of phthalates

Phthalates were identified by comparing their retention times with those of the ones in the samples and with the increase of the peak areas after spiking. Data obtained using different wavelengths were compared. The quantification was performed by the external standard method. The calibration curves were prepared in the concentration range of 0.05–2.50 mg/L with six replicates. The linear regression model of least-squares was used for the calibration and analysis of the results (LabSolutions, Version 1.25).

Optimization of the SPE method

At first, the SPE optimization studies were performed with a standard solution containing each of the phthalates at a concentration of 0.10 mg/L. The volume and the type of the conditioning and the elution solvents were optimized to obtain the highest recovery values. Several conditioning solvents (A: MeOH, water; B: MeOH; C: MeOH, 1% o-phosphoric acid solution; D: MeOH at pH 3.0 by o-phosphoric acid, water; E: MeOH at pH 3.6 by phosphate buffer) were examined to get the best retention. Three different types of elution solvents (MeOH/ACN, 50:50 v/v; ACN; ACN with 1% FA) were compared in terms of elution efficiency. The volumes of the conditioning and the elution solvents were selected following the trials performed with 3, 6 and 12 mL of each. Later, phthalates were extracted from the original and spiked (at 0.10 mg/L) liquid pharmaceutical preparation samples using the optimized SPE procedure. The standard solutions, original and spiked samples were extracted in triplicate to check the repeatability of the method. The precision of the method was determined as the percent relative standard deviation (RSD%) of the three replicate extractions. The recoveries from the standard solutions were calculated using the HPLC analysis data and the real concentration of the solutions. The recovery from the pharmaceutical preparation samples were determined by the data of the original and the spiked samples.

RESULTS AND DISCUSSION

In the present study, Supel™-Select HLB cartridges, which were composed of hydrophilic

modified styrene polymer, were used for the extraction of phthalates. One of the advantages of HLB sorbents for the extraction of analytes with aromatic rings is their selectivity to these compounds by π - π interactions. In addition, HLB sorbents possess both nonpolar and polar functional groups, providing the extraction of a wide range of polar to nonpolar and acidic to basic compounds from aqueous samples. Considering these advantages, an HLB SPE method was developed and applied for the extraction of DMP,

DPP, BBP, DBP, DCHP, DEHP and DOP (Figure 1) from liquid pharmaceutical preparations kept in polymeric packages. The volume and type of the conditioning and the elution solvents were optimized to obtain the highest recovery values. Phthalates were quantified by a slightly modified HPLC-UV method, which was developed and validated by Yılmaz et al. (2). The analytical performance of the present HPLC-UV method was given in Table 1.

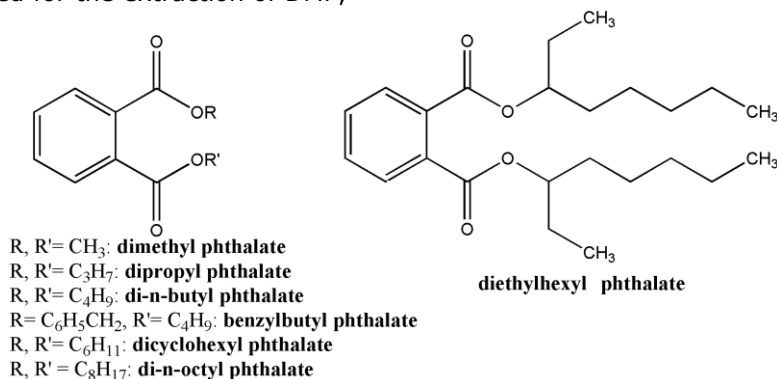


Figure 1. Chemical structures of the analyzed phthalates.

Selection of the conditioning solvent type

The general conditioning procedure for an HLB cartridge includes conditioning with an organic solvent like methanol (MeOH) or acetonitrile (ACN) followed by water or a buffer solution for aqueous samples. In the present study, several conditioning solvent types (A: MeOH, water; B: MeOH; C: MeOH, 1% *o*-phosphoric acid solution; D: MeOH at pH 3.0 by *o*-phosphoric acid, water; E: MeOH at pH 3.6 by phosphate buffer) were examined to get the best retention from a standard solution containing each of the phthalates at a

concentration of 0.10 mg L⁻¹ (Figure 2). Recovery values higher than 80.00% were obtained by using conditioning solvent E. Only DEHP and DOP had lower retention (recoveries 52.88% and 32.62%, respectively) since the polarities of these analytes were significantly lower than the others. After conditioning, 6 mL of the standard solution was loaded. The cartridge was washed with 3 mL of water to avoid the water soluble interferences. Then the analytes were eluted with 6 mL of ACN containing 1% FA.

Table 1. Analytical performance of the HPLC/UV method ($n = 6$).

Analyte	t_R (min)	Calibration range (mg/L)	Linear equation	R^2	LOD (mg/L)	LOQ (mg/L)	Tailing factor	Resolution
DMP	4.285±0.018	0.05-2.50	$y=1016567x+7258.6$	0.9999	0.01	0.02	1.167±0.035	-
DPP	6.589±0.035	0.05-2.50	$y=504397x+4266.2$	0.9999	0.01	0.02	1.145±0.049	12.018±0.162
BBP	7.589±0.095	0.05-2.50	$y=632886x+4272.5$	0.9999	0.01	0.02	1.137±0.085	5.704±0.055
DBP	7.897±0.033	0.05-2.50	$y=290853x+3066.5$	0.9999	0.01	0.03	1.141±0.063	2.057±0.063
DHCP	9.659±0.021	0.05-2.50	$y=250847x+2352.1$	0.9999	0.01	0.02	1.118±0.055	9.481±0.085
DEHP	13.581±0.045	0.05-2.50	$y=2562203x+546.5$	0.9999	0.01	0.02	1.102±0.065	17.764±0.046
DOP	14.415±0.019	0.05-2.50	$y=241992x-2914.6$	0.9977	0.09	0.27	1.110±0.078	2.941±0.084

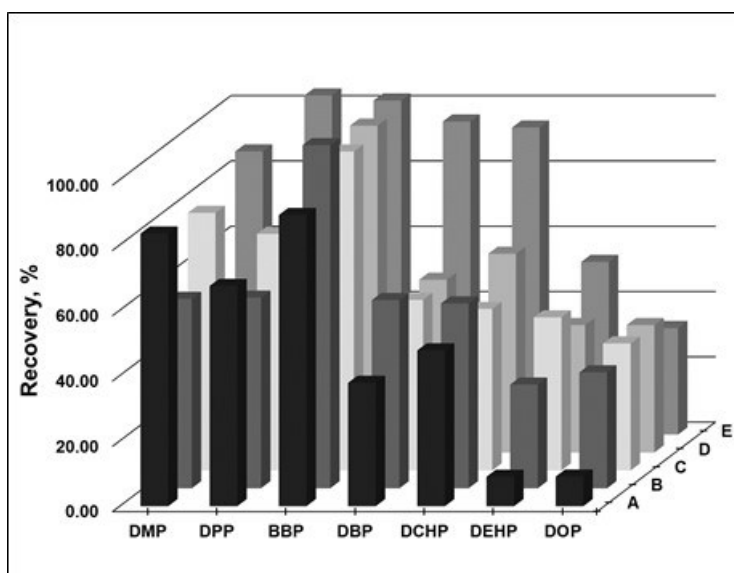


Figure 2. Selection of the conditioning solution. Loading: 6 mL of 0.10 mg/L standard solution, washing: 3 mL H₂O, elution: 6 mL ACN (1% FA). *n* = 3, RSD%: 0.62 – 2.35.

Selection of the elution solvent type

Three different types of elution solvents (MeOH/ACN, 50:50 v/v; ACN; ACN with 1% FA) were examined to optimize the SPE procedure. The highest recovery values were obtained with

ACN containing 1% FA (Figure 3). Non-acidified elution solvents were incapable of breaking the interactions between the phthalates and the HLB sorbent sufficiently.

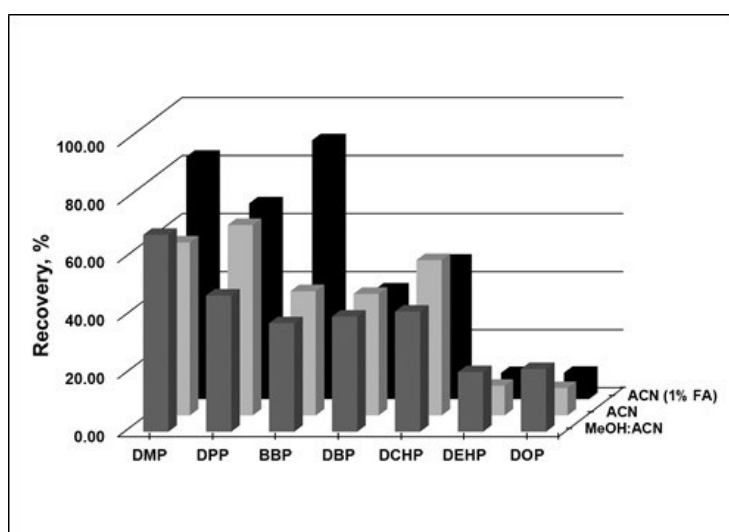


Figure 3. Selection of the elution solvent. Conditioning: 6 mL of MeOH - 6 mL of water, loading: 6 mL of 0.10 mg/L standard solution, washing: 3 mL H₂O. *n* = 3, RSD%: 0.74 – 2.14.

Selection of the conditioning and the elution solvents' volumes

Several studies were performed to optimize the volumes of conditioning and the elution solvents. For this purpose 3, 6, and 12 mL of conditioning and elution solvents were used for the extraction of the phthalates. Considering the recovery values, 6 mL of conditioning solvent (Figure 4) and 6 mL of elution solvent were selected as the optimum volumes (Figure 5). The volume values higher than 6 mL provided similar results of recovery.

Pharmaceutical preparation sample analysis

Using the optimized SPE procedure, phthalates were extracted from three different types of liquid pharmaceutical preparations as an intravenous isotonic NaCl solution, an intravenous dextrose solution, and an osmotic laxative preparation in polymeric packages. Six milliliters of the sample was loaded to HLB cartridge after conditioning with 6 mL of MeOH at pH 3.6 (adjusted by phosphate buffer). The sorbent was washed with 3 mL of water and the analytes were eluted using 6 mL of ACN containing 1% FA. The solvent was evaporated under reduced pressure and the residue was dissolved in 0.6 mL of the mobile phase. Twenty microliters of the filtered solution

(through 0.45 μm) was injected to the HPLC-UV system. The SPE procedure was triplicated for each of the original and the spiked (at 0.10 mg/L) samples. All of the HPLC-UV analyses were performed in triplicate. Precision of the method

was determined in terms of relative standard deviation percent (RSD%), which was lower than 2.85% (Table 2). The recovery values of the phthalates were higher than 80% except DEHP and DOP (Table 2).

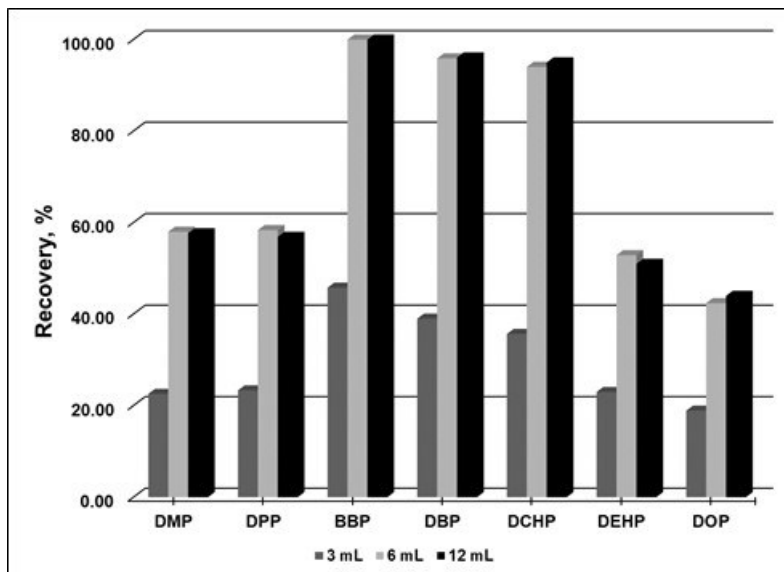


Figure 4. Selection of the conditioning solvent volume. Conditioning: 6 mL MeOH, loading: 6 mL 0.10 mg/L standard solution, washing: 3 mL H₂O, elution: 6 mL of ACN (1% FA). $n = 3$, RSD%: 0.52 – 2.11.

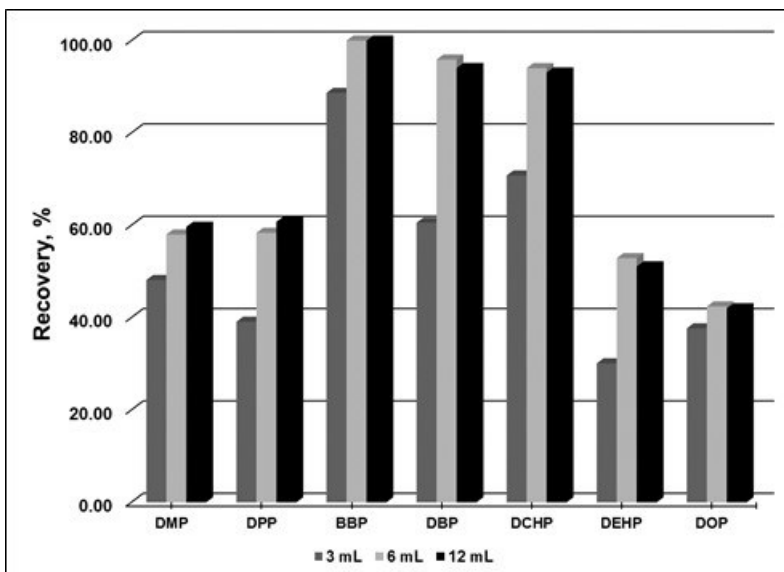


Figure 5. Selection of the elution solvent volume. Conditioning: 6 mL of MeOH, loading: 6 mL 0.10 mg/L std solution, washing: 3 mL of H₂O, elution: 6 mL ACN (1% FA). $n = 3$, RSD%: 0.96 – 2.41.

Table 2. Precision and accuracy of the SPE-HPLC/UV method*.

Analyte	Isotonic NaCl solution		Dextrose solution		Osmotic laxative	
	Recovery%	RSD%	Recovery%	RSD%	Recovery%	RSD%
DMP	92.45	2.36	103.48	1.99	108.96	1.68
DPP	96.33	2.59	100.65	1.86	90.21	2.85
BBP	87.21	1.89	96.55	2.10	90.25	2.01
DBP	86.66	2.45	88.23	1.98	86.63	1.68
DCHP	80.55	1.50	80.55	2.05	81.02	1.56
DEHP	50.88	1.02	54.72	2.01	53.12	2.01
DOP	45.77	2.05	40.52	2.54	41.22	2.11

* Samples were spiked at 0.10 mg/L ($n = 3$).

In other studies, DEHP and DBP were detected in pharmaceutical preparations kept in polyvinyl chloride and polyethylene packages, respectively (16, 17, 18, 19). Unlikely, the analyzed samples did not contain any of the phthalates examined in the present work, except isotonic NaCl solution

which was determined as contaminated with DPP at $13.2 \pm 0.16 \mu\text{g/L}$ (RSD%, 1.24%). HPLC chromatograms belonging to original and spiked isotonic NaCl solution samples were given in Figure 6.

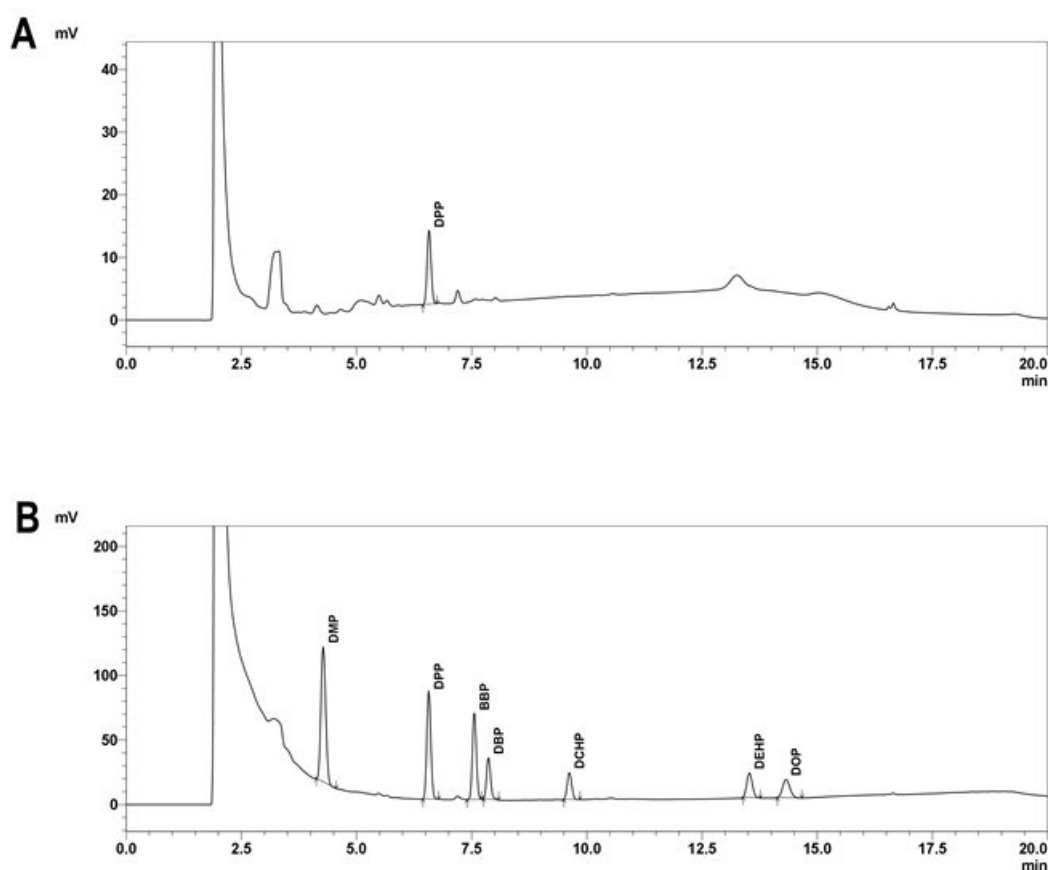


Figure 6. HPLC chromatograms of A) original and B) 0.10 mg/L spiked isotonic NaCl solution sample.

CONCLUSION

In the present study, an SPE method was optimized for the simultaneous extraction of seven phthalates from liquid pharmaceutical preparations by HLB cartridges. The optimized extraction method was capable of extraction of DMP, DPP, DBP, BBP and DCHP with recovery values higher than 80%. The extraction recoveries were below 80% for DEHP and DOP since they have lower polarities. A conditioning solvent with lower polarity might be more

appropriate to improve the retention of DEHP and DOP by HLB sorbent. The optimized SPE method provided determination of low concentrations of phthalates (at level of $\mu\text{g/L}$) with good precision and accuracy using a common HPLC system with UV detection. To the best of our knowledge, the proposed work might be the first report on phthalate content of pharmaceuticals kept in polymeric packages in Turkey.

ACKNOWLEDGEMENTS

A part of this study was presented as an oral presentation in International Eurasian Conference on Biological and Chemical Sciences, 26-27 April, 2018, Ankara, Turkey.

REFERENCES


- Gómez-Hens A, Aguilar-Caballeros M. Social and economic interest in the control of phthalic acid esters. *TrAC Trends in Analytical Chemistry*. 2003 Dec;22(11):847-57.
- Yılmaz PK, Ertaş A, Kolak U. Simultaneous determination of seven phthalic acid esters in beverages using ultrasound and vortex-assisted dispersive liquid-liquid microextraction followed by high-performance liquid chromatography. *Journal of Separation Science*. 2014 Aug;37(16):2111-7.
- Ghisari M, Bonefeld-Jorgensen EC. Effects of plasticizers and their mixtures on estrogen receptor and thyroid hormone functions. *Toxicology Letters*. 2009 Aug;189(1):67-77.
- Russo MV, Avino P, Perugini L, Notardonato I. Extraction and GC-MS analysis of phthalate esters in food matrices: a review. *RSC Advances*. 2015;5(46):37023-43.
- Brossa L, Marcé R., Borrull F, Pocurull E. Application of on-line solid-phase extraction-gas chromatography-mass spectrometry to the determination of endocrine disruptors in water samples. *Journal of Chromatography A*. 2002 Jul;963(1-2):287-94.
- Del Carlo M, Pepe A, Sacchetti G, Compagnone D, Mastrocola D, Cichelli A. Determination of phthalate esters in wine using solid-phase extraction and gas chromatography-mass spectrometry. *Food Chemistry*. 2008 Dec;111(3):771-7.
- Guo Z, Wang S, Wei D, Wang M, Zhang H, Gai P, et al. Development and application of a method for analysis of phthalates in ham sausages by solid-phase extraction and gas chromatography-mass spectrometry. *Meat Science*. 2010 Mar;84(3):484-90.
- Sánchez-Avila J, Fernández-Sanjuan M, Vicente J, Lacorte S. Development of a multi-residue method for the determination of organic micropollutants in water, sediment and mussels using gas chromatography-tandem mass spectrometry. *Journal of Chromatography A*. 2011 Sep;1218(38):6799-811.
- González-Sálamo J, Hernández-Borges J, Afonso M del M, Rodríguez-Delgado MA. Determination of phthalates in beverages using multiwalled carbon nanotubes dispersive solid-phase extraction before HPLC-MS. *Journal of Separation Science*. 2018 Jun;41(12):2613-22.
- Luo Y-B, Yu Q-W, Yuan B-F, Feng Y-Q. Fast microextraction of phthalate acid esters from beverage, environmental water and perfume samples by magnetic multi-walled carbon nanotubes. *Talanta*. 2012 Feb;90:123-31.
- Ye Q, Liu L, Chen Z, Hong I. Analysis of phthalate acid esters in environmental water by magnetic graphene solid phase extraction coupled with gas chromatography-mass spectrometry. *Journal of Chromatography A*. 2014 Feb;1329:24-9.
- Tolmacheva VV, Apyari VV, Kochuk EV, Dmitrienko SG. Magnetic adsorbents based on iron oxide nanoparticles for the extraction and preconcentration of organic compounds. *Journal of Analytical Chemistry*. 2016 Apr;71(4):321-38.
- Chen N, He J, Wu C, Li Y, Suo A, Wei H, et al. Synthesis of molecularly imprinted polymers by atom transfer radical polymerization for the solid-phase extraction of phthalate esters in edible oil. *Journal of Separation Science*. 2017 Mar;40(6):1327-33.
- Guart A, Bono-Blay F, Borrell A, Lacorte S. Migration of plasticizers-phthalates, bisphenol A and alkylphenols from plastic containers and evaluation of risk. *Food Additives & Contaminants: Part A*. 2011 May;28(5):676-85.
- Zdravkovic SA. Solid phase extraction in tandem with GC/MS for the determination of semi-volatile organic substances extracted from pharmaceutical packaging/delivery systems via aqueous solvent systems. *Journal of Pharmaceutical and Biomedical Analysis*. 2015 Aug;112:126-38.
- Petruševski V, Jolevska ST, Ribarska JT, Chachorovska M, Petkovska A, Ugarković S. Development of complementary HPLC-DAD/APCI MS methods for chemical characterization of pharmaceutical packaging materials. *Journal of Pharmaceutical and Biomedical Analysis*. 2016 May;124:228-35.
- Demoré B, Vigneron J, Perrin A, Hoffman MA, Hoffman M. Leaching of diethylhexyl phthalate from polyvinyl chloride bags into intravenous etoposide solution. *Journal of Clinical Pharmacy and Therapeutics*. 2002 Apr;27(2):139-42.
- Mitani K, Izushi F, Kataoka H. Analysis of phthalate contamination in infusion solutions by automated on-line in-tube solid-phase microextraction coupled with high-performance liquid chromatography. *J Anal Toxicol*. 2004 Oct;28(7):575-80.

19. Chaudhary AK, Waske SA, Yadav S, Chandrashekhar TG, Singh V. Validated reverse phase HPLC method for the determination of

DEHP content in reconstituting diluents and in reconstituted solutions of imipenem and cilastatin for injection. E-Journal of Chemistry. 2010;7(2):501-13.



Phytochemical Profiling and Evaluation of *Marrubium sivasense* Aytaç, Akgül & Ekici for Antioxidant Activity and Inhibition Effects on α -Amylase, Lipoyxygenase, Xanthine Oxidase and Tyrosinase Enzymes

Fatih Göger^{1,2,*}  , Gülmira Özek¹,  , Mehmet Tekin⁴,  ,
Süleyman Yur^{1,2},  , Temel Özek^{1,2},  

¹Anadolu University, Faculty of Pharmacy, Department of Pharmacognosy, 26470, Eskişehir, Turkey.

²Anadolu University, Medicinal Plant, Drug and Scientific Research Center (AUBIBAM), 26470, Eskişehir, Turkey.

³Anadolu University, Yunus Emre Vocational School, Department of Pharmacy, Program in Pharmacy Services, 26470, Eskişehir Turkey.

⁴Trakya University, Faculty of Pharmacy, Department of Pharmaceutical Botany, 58140 Edirne, Turkey.

Abstract: In the present study, the extract of an endemic plant ourkey *Marrubium sivasense* Aytaç, Akgül & Ekici was investigated for phytochemical profile, antioxidant properties and inhibition of several enzymes. The chemical composition of the extract was investigated with LC-MS/MS technique. Forsythoside B, verbascoside and leucoseptoside were identified as the main compounds. The free radical scavenging activity of the extract was determined against DPPH• radicals (IC₅₀ 0.34 mg/mL) and ABTS•+ cation radicals (TEAC 2.3 mM). In the xanthine-xanthine oxidase (XO) system and in β -carotene bleaching assay the extract demonstrated moderate activity (Inh% 16.54 and Inh% 43 \pm 1.26, respectively). The extract demonstrated hypoglycemic activity (Inh% 49.67 \pm 1.09) via inhibition of porcine pancreatic α -amylase. The antiinflammatory effect tested via inhibition of 5-LOX was found as Inh% 18.71 \pm 0.74. However, no anti tyrosinase activity was found.

Keywords: *Marrubium sivasense*, extract, LC-MS/MS; antioxidant, xanthine oxidase, α -amylase, tyrosinase.

Submitted: January 23, 2019. Accepted: May 29, 2019.

Cite this: Göger F, Özek G, Tekin M, Yur S, Özek T. Phytochemical Profiling and Evaluation of *Marrubium sivasense* Aytaç, Akgül & Ekici for Antioxidant Activity and Inhibition Effects on α -Amylase, Lipoyxygenase, Xanthine Oxidase and Tyrosinase Enzymes. JOTCSA. 2009;6(3):272–82.

DOI: <https://doi.org/10.18596/jotcsa.516888>.

*Corresponding author. E-mail: fatihgoger@gmail.com, Tel: +90-2223350580 Extn.:3663-3707, Fax: +90-2223306809

INTRODUCTION

The genus *Marrubium* L. (Lamiaceae) consists of 40 species indigenous in Europe, the Mediterranean and Asia. In the Flora of Turkey, the genus is represented by 21 taxa, of which 12 are endemic (1-3). The endemism rate (57%) shows that Turkey is an important center of diversity for the genus (4, 5). Several aspects on chemical and pharmacological potent of the genus *Marrubium* were reported by Meyre-Silva et al (6). A previous phytochemical studies on *Marrubium* species resulted with polyphenols (7), essential oils (8), labdane diterpenoids and sterols (9, 10). Biological activity investigations of *Marrubium* species encompasses antibacterial (11), antioxidant, antiproliferative (12), antinociceptive (13), antidiabetic (14), antihypertensive (15), hepatoprotective (16), antiinflammatory (17), cardioprotective (18) and cytotoxic/cytostatic (19) potentials. Some *Marrubium* species are traditionally used to treat various diseases, including asthma, pulmonary infections, inflammation and hypotension, as cholagogues and sedative agents, and for pain relief. *M. vulgare* (horehound) is cultivated in Lithuania (20) and serves as raw material and source for food flavoring and for medicinal purposes (herbal extracts) and beverage industries (21). The plant has also been used as a substitute for hop in beer-breweries and as an ingredient of pastilles, as a flavoring in stick candy, and candy drops (22, 23). In Turkey, *Marrubium* species are known as "Agor çalbasi" (in Sivas province), "şalba" (in Antalya province) and "kayışkiran otu" (in Kırklareli province) (24).

Marrubium sivasense Aytaç, Akgül & Ekici is the local endemic species in Sivas province of Turkey (1). The local name of this plant is "kukasotu". Taking into consideration the previous literature data on the chemistry and biological activities of *Marrubium* species as well as lacking information about *M. sivasense*, we aimed to investigate chemical composition and biological potential of this species. Therefore, the extract of *M. sivasense* was screened for antioxidant activity using different in vitro methods like 2,2-diphenyl-1-picrylhydrazyl (DPPH[•]) radical scavenging test, Trolox equivalent antioxidant capacity test and β -carotene bleaching test. The antioxidant effect of extract on oxidative damage was also evaluated with enzymatic

method using XO system that generated superoxide anion radical (O₂⁻). The test samples which interact with XO can affect the kinetics of xanthine oxidation to uric acid which causes hyperuricacidemia associated with gout (25). XO has a role in the generation of reactive oxygen species in various pathologies such as viral infection, inflammation, brain tumors or the process of ischemia/reperfusion. Thus, inhibitors of XO are expected to be therapeutically useful for the treatment or prophylaxis of these diseases. Earlier, it has been supposed that the essential oil of *M. peregrinum* L. may contain compounds that would be more effective in the treatment of gout from the widely used allopurinol because of they can inhibit XO as well as neutralize O₂⁻• (26). In literature there is no any information about effect of *Marrubium sivasense* on XO enzyme. Therefore, it was aimed to investigate inhibitory effect of *M. sivasense* extract on XO enzyme.

In the literature there is information about antiinflammatory properties of *M. vulgare* and *M. allyson* (27, 28). The phenylpropanoid glycosides from *M. vulgare* have been reported as the strong inhibitors of enzymes associated with inflammation. Therefore, it was interesting to investigate the extract of *M. sivasense* against 5-lipoxygenase (5-LOX) enzyme, which linked to inflammation process.

Recently, the perspectives of *M. vulgare* as antidiabetic natural product have been discussed in several papers (14, 29, 30). The investigation of *M. sivasense* inhibitory activity against pancreatic α -amylase, which is known as key enzyme in digestion of dietary carbohydrate in organism, may give information on antihyperglycemic potential of the plant. The inhibitors of α -amylase enzyme may be effective in retarding carbohydrate digestion and glucose absorption to suppress postprandial hyperglycemia.

A literature search revealed information about tyrosinase inhibition potent of flavonoids and phenylethanoid glycosides isolated from *M. velutinum* and *M. cylleneum*. (7). In the scope of the present work, we attempted to investigate in vitro potential of *M. sivasense* against tyrosinase enzyme which is the key

enzyme in production of melanin (31). The central role of tyrosinase in dopamine neurotoxicity as well as contribution to the neurodegenerative Parkinson's disease has earlier been well documented (32). The inhibitors of tyrosinase found application in cosmetic products for whitening and depigmentation after sunburn as well as for the treatment of hyperpigmentation. Nowadays, there is increasing demand for naturally derived inhibitors of tyrosinase due to diverse side effects of synthetic products. The tyrosinase inhibitory activity of *M. velutinum* and *M. cylleneum* was reported to be due to flavonoid and phenylethanoid glycosides (7). It was supposed, that flavonoids and cinnamic acid derivatives may contribute to antityrosinase activity of *M. vulgare* extract (33). The above mentioned reports encouraged us to investigate *M. sivasense* for antityrosinase activity. The present research work is the first contribution into the chemistry and biological activities of *M. sivasense*, endemic species from Turkey.

MATERIALS AND METHODS

Chemicals and Enzymes

3,4-Dihydroxyl-L-phenylalanine, β -carotene, linoleic acid, Tween-20, butylated hydroxytoluene (BHT), gallic acid, (\pm)-6-hydroxy-2,5,7,8-tetramethylchromane-2-carboxylic acid (Trolox), 2,2-diphenyl-1-picrylhydrazyl (DPPH[•]), ammonium acetate, kojic acid, acarbose, 3,4-dihydroxy-L-phenylalanine (L-DOPA), nordihydroguaiaretic acid (NDGA), allopurinol, α -amylase from porcine pancreas (Type VI-B, EC 3.2.1.1), tyrosinase from mushroom (EC 1.14.18.1), xanthine oxidase from bovine milk (Grade IV) and lipoxidase from *Glycine max* (Type I-B) were purchased from Sigma-Aldrich (St. Louis, MO, USA). Soluble starch extra pure, iodine and potassium iodide were purchased from Merck (Darmstadt, Germany). Sodium phosphate, disodium phosphate, aluminum chloride, water and methanol were extra pure analytical grade. A C9-C40 n-alkane standard solution was purchased from Fluka (Buchs, Switzerland). All solvents were purchased from Sigma Aldrich (Germany) and were of analytical grade.

Equipment

Shimadzu 20A HPLC system equipped with Applied Biosystem 3200 Q trap MS/MS detector was used for chromatographic analysis of the extract. Microtiter plate assay was performed with Biotek Powerwave XS microplate reader. Ultrapure water was obtained from a Direct-Q Water Purification System (Germany). Spectrophotometric measurements were carried out with a UV-Pharma Spec 1700 (Shimadzu) spectrophotometer.

Plant Material

The aerial parts of *M. sivasense* were collected in Sivas province, vicinity of Mancilik village of Kangal district, on June, 2015 and dried under the shade. Botanical identification was performed by Dr. Mehmet Tekin (Trakya University, Faculty of Pharmacy, Department of Pharmaceutical Botany). The voucher specimen is stored in the Herbarium of Cumhuriyet University, Faculty of Science (CUFH) under herbarium code Tekin 1686.

Preparation of the Extract

Aerial parts of *M. sivasense* (10.0 g) were powdered and subjected to maceration in methanol (200 mL) by shaking (3000 per min) at room temperature for 24 h. The obtained liquid extract was filtered and dried under vacuum. The dried methanol extract was kept at 4°C until phytochemical analysis and biological activity tests.

Liquid-Chromatography - Mass Spectrometry (MS/MS)

LC-MS/MS analysis was carried out using an AbSciex 3200 Q trap MS/MS detector. The experiments were performed with a Shimadzu 20A HPLC system coupled to an Applied Biosystems 3200 Q-Trap LC-MS/MS instrument equipped with an ESI source operating in negative ion mode. For the chromatographic separation, a GL Science Intersil ODS 250 \times 4.6 mm, i.d., 5 μ m particle size, analytical column operating at 40°C was used. The solvent flow rate was maintained at 0.5 mL/min. The detection was carried out with PDA and MS detectors. The elution gradient consisted of mobile phases (A) acetonitrile : water : formic acid (10:89:1,

v/v/v) and (B) acetonitrile : water : formic acid (89:10:1, v/v/v). The composition of B was increased from 10% to 100% in 40 min. LC-ESI-MS/MS data were collected and processed by Analyst 1.6 software.

Identification of Compounds

Identification of phenolic constituents was based on matching of mass-spectral patterns obtained with LC-MS/MS system.

Free Radical Scavenging Activity (DPPH[•] assay)

The hydrogen atoms or electrons donation ability of *M. sivasense* extract was evaluated according to bleaching of purple colored DPPH[•] stable radicals by using of the method of Brand-Williams (34) with slight

$$Inh\% = \left(\frac{Abs_{control} - Abs_{sample}}{Abs_{control}} \right) \times 100 \quad (\text{Eq. 1})$$

where, Abscontrol is the absorbance of the control (containing all reagents except the test compound), Abssample is the absorbance of the sample with added DPPH reagent. The IC50 values were obtained by plotting the DPPH[•] scavenging percentage of each sample against the sample concentration. Data were analyzed using the SigmaPlot software (Version 12.0).

Trolox Equivalent Antioxidant Capacity (TEAC Assay)

The free radical scavenging activity of the extract was tested against 2,2'-azino-bis(3-ethylbenzothiazoline-6-sulfonic acid) (ABTS^{•+}) cation radicals according to the procedure described by Re et al. (35) with slight modifications. 7 mM ABTS and 2.5 mM K2S2O8 dissolved in 10 mL ultrapure water were allowed to stand in the dark for 16 h at room temperature to create ABTS^{•+} cation radicals. Prior to the assay, ABTS^{•+} solution was diluted with absolute ethanol to get an absorbance between 0.7-0.8 at 734 nm. The solutions of the extract (5 mg/mL) and Trolox (standard, 3.0; 2.0; 1.0; 0.5; 0.25; 0.125 mM) were prepared in methanol. In the experiment, the sample solution (10 μ L) was mixed with 990 μ L ABTS^{•+} solution. Ten microliter of methanol instead of the sample mixed with ABTS^{•+} solution was used as the control. Gallic acid solution (0.1 mg/mL) was used as the positive control. Decrease in the

modifications. The solution of DPPH[•] (0.08 mg/mL, in methanol) was freshly prepared daily, kept in the dark at 4 °C between the measurements. The solutions of the extract (10 mg/mL) and gallic acid (0.1 mg/mL) were prepared in methanol. In the experiment, 100 μ L of the sample (extract/ standard) solution and 100 μ L of DPPH solution were pipetted by multichannel automatic pipette (Eppendorf Research[®] plus, Germany) into 96-flat bottom well plate cells and allowed to stand in the dark for 30 min. The control well contained 100 μ L methanol (instead of the sample) mixed with 100 μ L of DPPH. The decrease in the absorbance was recorded at 517 nm. Gallic acid (standard) was used as the positive control. The experiments were performed in triplicate. The free radical scavenging activity of the samples was expressed as percentage of inhibition calculated according to Equation 1:

absorbance after 30 minutes of incubation was recorded at 734 nm to get linear Trolox equation. ABTS^{•+} scavenging activity of the sample was expressed as Trolox equivalent antioxidant capacity and calculated using linear equation obtained for Trolox ($y = 33.644 \times x + 2.6523$, $r^2 = 0.9942$).

β -Carotene/Linoleic Acid Peroxidation Inhibition Assay

β -Carotene/linoleic acid peroxidation inhibition assay used linoleic acid as the model lipid substrate in an emulsified form (with Tween-20) lies in between methods employing only model substrates (e.g. DPPH[•]) and those using real lipids (36). Inhibition of lipid peroxidation by *M. sivasense* extract was measured according to method of Marco (37) with slight modifications. Briefly, β -carotene (5 mg) dissolved in chloroform (5 mL) was added to flask containing linoleic acid (120 mg) and Tween-20 (1200 mg). The content of flask was vigorously shaken and chloroform was evaporated under the vacuum. After evaporation, pure water (300 mL) was added and shaken vigorously. BHT (1 mg/mL) was used as the standard inhibitor. The sample (extract/ standard) solution (10 μ L) and β -carotene emulsion (2 mL) were mixed in the deep well plate. After that, 300 μ L of the mixture was placed by multichannel automatic pipette (Eppendorf, Germany) into a 96-well microplate cells and incubated at 50°C for 2 h.

Control was prepared without sample or standards according to the same procedure. The rate of β -carotene bleaching was monitored by measuring the absorbance at 15 min periods at 470 nm in an ELISA microplate

$$AA\% = \left[1 - \frac{(Abs_{0sample} - Abs_{120sample})}{Abs_{0control} - Abs_{120control}} \right] \times 100$$

where, AA is an antioxidant activity, Abs_{0sample} and Abs_{120sample} are the absorbance values of the sample at 0 min and 120 min, Abs_{0control} and Abs_{120control} are the absorbance values of the control at 0 min and 120 min.

Xanthine Oxidase (XO) Inhibition Assay

The XO inhibition assay was carried out according to procedure reported by Chen (38) with slight modifications. Namely, the stock solution of the extract (5 mg/mL) prepared in methanol was diluted with phosphate buffer (0.1 M, pH 7.5) up to 1 mg/mL. In the experiment, the sample solution (100 μ L), buffer (1.75 mL) and 40 μ L of XO (0.33 U/mL in sodium phosphate buffer) were pipetted in

$$Inh\% = \left[\frac{(Abs_{control} - Abs_{control\ blank}) - (Abs_{sample} - Abs_{sample\ blank})}{Abs_{control} - Abs_{control\ blank}} \right] \times 100$$

where Abs_{control} and Abs_{control blank} are the absorbance values of the control and its blank, Abs_{sample} and Abs_{sample blank} are the absorbance values of the sample and its blank.

Tyrosinase Inhibition Assay

An inhibitory activity of *M. sivasense* extract on tyrosinase was assessed using the modified microplate method reported by Masuda (39). The solution of the extract (1 mg/mL) was prepared in phosphate buffer (pH 6.8) with adding DMSO. The experiment was carried out as follow: eight wells were used, A (three wells, control), B (one well, blank), C (three wells, sample), and D (one well, blank), which contained the following reaction mixtures: A,

$$Inh\% = \frac{(Abs_A - Abs_B) - (Abs_C - Abs_D)}{(Abs_A - Abs_B)} \times 100$$

α -Amylase Inhibition Assay

The inhibitory potential of the extract on activity of α -amylase was measured using Caraway-Somogyi iodine/potassium iodide (I/KI) method (40) with slight modifications.

reader (Biotek Powerwave XS). Analyses were run in triplicate and the results were expressed as average of inhibition percentage values with SEM calculated according to Equation 2:

$$\text{Equation (2)}$$

quartz cuvette and pre-incubated for 10 min at 25 °C. The reaction was initiated by addition of the substrate solution (100 μ L 0.5 mM xanthine in buffer). Then, the mixture was subjected to the second incubation for 12 min at 25 °C. The sample blanks contained all reaction reagents and 40 μ L buffer instead of enzyme. The control cuvette contained all the reagents without the sample (plus equivalent amount of the sample solvent was added). Control incubations, representing 100% enzyme activity were conducted in the same manner replacing the plant extract with the solvent used for the solution of the extract. The standard inhibitor of XO, allopurinol (1 mM in DMSO) was used as the positive control. Absorbance at 295 nm was recorded with a spectrophotometer. The percentage inhibition was calculated according to Equation 3:

$$\text{(Eq. 3)}$$

120 μ L of phosphate buffer (0.1 M, pH 6.8) and 40 μ L of tyrosinase (33.3 U/mL) in the buffer; B, 160 μ L of the buffer; C, 80 μ L of the buffer, 40 μ L of tyrosinase (33.3 U/mL) in the buffer, 40 μ L of the sample-buffer solution containing DMSO; D, 120 μ L of the buffer and 40 μ L of the sample solution containing DMSO. Pipetting was performed with multichannel automatic pipette (Eppendorf Research® plus, Germany). Kojic acid (0.01-0.1 mg/mL in buffer) was used as the positive control. The contents of each well were mixed and then preincubated at 23°C for 10 min, before 40 μ L L-DOPA (2.5 mM) in the buffer was added. After incubation at 23°C for 15 min, the absorbance at 475 nm was measured using an ELISA microplate reader (Biotek Powerwave XS). The percentage inhibition of the tyrosinase activity (Inh %) was calculated according to Equation 4:

$$\text{(Eq. 4)}$$

The substrate solution (0.05 %) was prepared by dissolving soluble potato starch (10 mg) in 20 mL ultrapure water then boiling for 10 min and cooling to room temperature before use. As a positive control experiment, acarbose (0.01-0.1 mg/mL in buffer) was used. The

experiment was carried out as follows: 20 mM sodium phosphate buffer (pH 6.9) was pipetted in the 96-well flat bottom plates with multichannel automatic pipette (Eppendorf, Germany), then 25 μ L sample solution and 50 μ L α -amylase (0.8 U/mL in buffer) were added and incubated for 10 min at 37°C. After incubation, 50 μ L substrate solution was added to the mixture. The mixture was subjected to the second incubation for 10 min at 37°C. The reaction was stopped by addition of 25 μ L HCl (1 M). Finally, 100 μ L of I/KI reagent was added to the wells. The sample blanks contained all reaction reagents and 50 μ L buffer instead of enzyme. The control wells contained all reaction reagents and 25 μ L solvent (instead of the sample solution). The control incubations, representing 100% enzyme activity were conducted in the same manner replacing the plant extract with the solvent used for solution of the extract. The absorbance values were recorded for the sample and blank at 630 nm. The percentage inhibition of the α -amylase activity (Inh %) was calculated according to Equation 3.

Lipoxygenase Inhibition Assay

Inhibition of 5-LOX activity was measured with spectrophotometric method described by Albano et al. (41). The solutions of the extract (1 mg/mL) and NDGA (0.1 mg/mL) were prepared in methanol. The substrate solution (4 mM) was prepared as follows: 50 mg linoleic acid, 50 mg Tween-20, 500 μ L NaOH (1 M) were mixed and the total volume (40 mL) was adjusted with 0.1 M phosphate buffer (pH=8). The enzyme solution was prepared in phosphate buffer (273000 U/mL). In the experiment, 50 μ L of the sample solution (extract/standard), 2.5 mL phosphate buffer and 50 μ L of 5-LOX were mixed in quartz cuvette and incubated for 10 min at 25 °C. Then, the reaction was initiated by adding linoleic acid (25 μ L). Increase in the absorbance at 234 nm was recorded for 6 min.

The percentage inhibition was calculated according to equation 3.

Statistical Analysis of Data

Data obtained from antioxidant and enzyme inhibition experiments were expressed as mean standard error (\pm SEM). IC50 values were estimated using a nonlinear regression algorithm.

RESULTS AND DISCUSSION

In the literature, there are a number of papers promising about phytochemical properties and biological activities of diverse Marrubium species (7,11-19). However, there is no information about phytochemistry and biological potent of endemic species *M. sivasense*. The main objective of the present work was to evaluate chemical composition and confirm the biological potent of non-volatile metabolites of *M. sivasense*. The extract was subjected to evaluations for free radical scavenging, lipid peroxidation inhibition and Trolox equivalent antioxidant capacity. Another goal was to determine inhibitory potential of the extract on enzymes involved in oxidation metabolism (XO), digestion of carbohydrates (α -amylase), process of inflammation (5-LOX), and linked to melanin formation and Parkinson's disease (tyrosinase).

Composition of Extract

In scope of the research, *M. sivasense* methanol extract phenolics were determined with LC-MS/MS technique. Phenylethanoid glycosides: forsythoside B, verbascoside, alyssonoside, martynoside were identified as the main compounds. Chromatographic profile of the extract is presented on Figure 1.

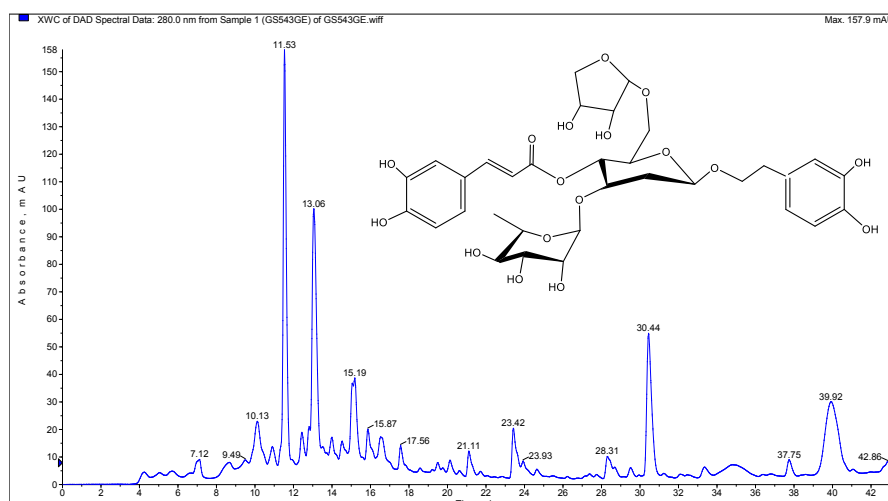


Figure 1: Liquid-chromatographic profile of the methanol extract of *Marrubium sivasense*.

The list of the constituents detected with MS detector is summarized in Table 1. The composition of the extract was constituted by phenylethanoid glucosides as well as cumaroyl glycosides of apigenin. Forsythoside B,

verbascoside and leucoseptoside were found as the main phenolic constituents in *M. sivasense*. Several of these constituents have earlier been reported for *M. alysson*, *M. anisodon* and *M. cylleneum* (42-44).

Table 1: Characterization of chromatographic peaks detected in the methanolic extract of *Marrubium sivasense*.

Rt	[M-H] ⁻ m/z	Fragments	Compound	Reference
11.5	755	593,461, 315, 297, 179,	Forsythoside B	(45)
13.0	623	461, 315, 179	Verbascoside	(43, 46)
13.2	769	593, 575	Alyssonoside	(43, 46)
14.0	463	300, 271	Quercetin glucoside	(7)
15.2	637	461, 315, 297, 175	Leucoseptoside A	(43,45, 46)
15.9	431	311, 269	Apigenin glucoside	(45, 47)
16.3	461	445, 297, 283, 255	Chrysoeriol glucoside	(42)
17.6	651	193, 175, 160	Martynoside	(7)
20.1	377	249, 205	Unknown	
21.1	577	431, 311, 269	Apigenin coumaroylglucoside	(7, 44, 48)
23.4	577	431, 413, 269, 145,	Apigenin coumaroylglucoside	(7, 44, 48)
28.3	723	576, 269	Similar to Apigenin di-coumaroylglucoside	(44,48)
30.5	267	223	Unknown	

Antioxidant Activity

Antioxidant activity assessments of *M. sivasense* extract were performed in vitro by using non-enzymatic and enzymatic systems employing different model substrates: stable free radical DPPH• and cation radical ABTS+• as well as real substrates: linoleic acid peroxides and superoxide anion radicals (O₂•⁻). Such approach allowed obtaining rather

realistic results about the antioxidant potent of the sample. The extract demonstrated antioxidant activity in all antioxidant activity assays. Namely, the extract scavenged DPPH• free radicals with IC₅₀ 0.34 mg/mL. It was more effective than BHT (IC₅₀ 0.50 mg/mL.), but less effective than ascorbic acid (IC₅₀=0.03 mg/mL.) and gallic acid (IC₅₀ 0.003 mg/mL.). The extract prevented bleaching of β-carotene by inhibition of linoleic

acid peroxidation with Inh% 43. In the TEAC assay, the extract demonstrated noteworthy ABTS●+ bleaching activity equivalent to 2.3 mM of Trolox. Such significant activity may be observed due to phenolic compounds detected in the extract as reported in Table 2. In the xanthine/xanthine oxidase system, the extract demonstrated moderate inhibitory effect (16.54 %). As can be seen from the antioxidant activity determination results (Table 2), the extract of *M. sivasense* may be considered as potential source of antioxidant agents in prevention of oxidative damage. LC-MS/MS analysis revealed that extract of *M. sivasense* contained phenylethanoid glucosides: forsythoside, verbascoside and leucoseptoside. It has earlier been reported that these compounds displayed notable antioxidant capacity (49). In the literature, there is increasing evidence that polyphenols have multiple beneficial effects on preventing of oxidative damage. The phenol content is well known to correlate with higher antioxidant activity in plant extracts (50). The mechanism by which polyphenols exert their effects is not fully clarified, but a consensus was reached that polyphenols protect membranes, proteins, and DNA against damage by scavenging free radicals generated through oxidative metabolism.

Enzyme Inhibition Assays

Inhibitory Effect of the Extract on Mushroom Tyrosinase Activity

In scope of the research work, the inhibitory effect of *M. sivasense* extract on mushroom tyrosinase activity was evaluated. The extract was found to be inactive when tested at a concentration of 1 mg/mL (Table 2).

Inhibitory Effect of the Extract on Porcine Pancreatic α -Amylase Activity

M. sivasense extract was evaluated in vitro for hypoglycemic activity via inhibition of the porcine pancreatic α -amylase. As can be seen in Table 2, the extract demonstrated inhibitory activity (Inh% 49.67). It seems to be that *M. sivasense* can be considered as perspective potential source of natural phytochemicals with hypoglycemic effect. Earlier, antidiabetic phytochemicals from different *Marrubium* species have been proved to be effective agents. The hypoglycemic effect of *M. vulgare* extract was clinically documented in patients with type II non-controlled diabetes mellitus (51). It was reported, that *M. radiatum* extract exerted the strongest activity against α -amylase and α -glucosidase (52). The evidenced-based therapeutic usage of many plants is scarce. Nowadays, there is demand for new effective and safe natural products with hypoglycemic property. The efficacy of known synthetic hypoglycemic products is debatable. So, the plants reputed for their antidiabetic effect should be verified either experimentally or clinically.

Inhibitory Effect of the Extract on Lipoxigenase Activity

Antiinflammatory effect of *M. sivasense* was tested with 5-LOX enzyme inhibition system. Actually, 5-LOX catalyzes the oxidation of arachidonic acid, produces 5(S)-hydroxyperoxyeicosatetraenoic acid (5-HETE) which undergoes dehydration, resulting in the formation of leukotriene. Enzymatic hydrolysis of leukotriene, as well as conjugation with other substances, leads to the formation of inflammatory mediators.

In the present study, the extract of *M. sivasense* was found to be as moderate inhibitor of 5-LOX with Inh% 18.71 when tested at 5 mg/mL concentration (Table 2).

Table 2.The biological activity of *M. sivasense* extract*.

	DPPH ^o IC ₅₀ (mg/m L)	β- Carotene ^a , Inh%	TEAC ^a , mM	XOD ^b , Inh%	α-AML ^c , Inh%	LOX ^a , Inh%	TYR ^b , Inh%
Extract	0.34	43.04	2.3	16.54	49.67	18.71	N/A
Gallic acid	0.003	-	-	-	-	-	-
Ascorbic acid	0.03	-	-	-	-	-	-
BHT ^b	0.50	85.0	-	-	-	-	-
Acarbose ^d	-	-	-	-	98.0	-	-
NDGA ^e	-	-	-	-	-	86.38	-
Allopurinol ^f	-	-	-	81.02	-	-	-
Kojic acid ^d	-	-	-	-	-	-	84.0

*Activity values are presented as results of triplicate experiments n=3, p<0.01; BHT: butylated hydroxytoluene; N/A: not active; α-AML: α-amylase; LOX: lipoxygenase; TYR: tyrosinase; NDGA: nordihydroguaiaretic acid; ^sthe deviation from the mean is <0.01 of the mean value; Concentrations of the tested sample: ^a)5 mg/mL; ^b)1 mg/mL; ^c)0.5 mg/mL; ^d)0.3 mg/mL; ^e)0.1 mg/mL; ^f)1.0 mM.

CONCLUSION

The liquid chromatographic analysis of *Marrubium sivasense* methanol extract resulted with identification of phenolic constituents, namely forsythoside B, leucoseptoside A, verbascoside, alyssonoside, martynoside, as well as glucosides of quercetin, apigenin and chrysoeriol, and coumaroylglucoside of apigenin. Evaluation of the extract in different model systems revealed that *M. sivasense* methanol extract is good inhibitor of α-amylase enzyme. However, the extract did not demonstrate noteworthy effect on 5-LOX, XOD and tyrosinase enzymes. The data gathered from the current study support that *M. sivasense* is a good source of flavonoid constituents and other bioactive compounds that might be responsible for the observed antioxidant and some enzyme inhibitory activities. These interesting results encourage further investigation geared towards the isolation of potent phytochemicals of different polarity from *M. sivasense*.

ACKNOWLEDGEMENTS

Authors are grateful to Anadolu University Scientific Research Department for supporting this research project (Grant Number 1705S171).

REFERENCES

1. Aytaç Z, Akgül G, Ekici M. A New Species of *Marrubium* (Lamiaceae) from Central Anatolia, Turkey. *Turk J Bot.* 2012;36:443-9.
2. Akgül G, Ketenoglu O. The new subspecies for the Flora of Turkey: *Marrubium cephalanthum* Boiss. & Noë subsp. *akdağhicum* (Lamiaceae). In: Ürgüp, Turkey: IXth National Conference on Ecology; 7-10 October;; Nevşehir: Nevşehir University Faculty of Science; 2009.
3. Tıylu M, Büyükkartal HN, Akgül G, Kalyoncu H. *Marrubium lutescens* Boiss. ve *M. cephalanthum* Boiss. & Noë subsp. *akdağhicum* (Lamiaceae)'un gövde ve yaprak özelliklerinin anatomik olarak karşılaştırılması. *Süleyman Demirel Univ. J Nat Appl Sci.* 2017;21(1):113-7.
4. Firat M. *Marrubium eriocephalum* (Lamiaceae); a Species New to the Flora of Turkey, with Contributions to its Taxonomy. *PhytoKeys.* 2016(58):9-20.
5. Davis PH, Mill RR, Kit T. *Flora of Turkey and the East Aegean Islands* (Suppl. 1). Edinburgh: Edinburgh University Press; 1988. p. 202-3.

6. Meyre-Silva C, Cechinel-Filho V. A Review Of The Chemical And Pharmacological Aspects of the Genus *Marrubium*. *Curr Pharm Des*. 2010;16(31):3503-18.
7. Karioti A, Protopappa A, Megoulas N, Skaltsa H. Identification of Tyrosinase Inhibitors from *Marrubium velutinum* and *Marrubium cylleneum*. *Bioorg Med Chem*. 2007;15(7):2708-14.
8. Golmakani H, Rabbani Nasab H, Sharifan M, Kamali H, Yadollahi A. The Essential Oil Composition and Antibacterial Activity of *Marrubium duabense* Murata from North Khorassan Province, Iran. *J Essent Oil Bear Plants*. 2016;19(4):963-71.
9. Masoodi M, Ali Z, Liang S, Yin H, Wang W, Khan IA. Labdane Diterpenoids from *Marrubium vulgare*. *Phytochem Lett*. 2015;13:275-9.
10. Piozzi F, Bruno M, Rosselli S, Maggio A. The Diterpenoids of The Genus *Marrubium* (Lamiaceae). *Nat Prod Commun*. 2006;7:585-92.
11. Dehbashi Z, Mazaheri M, Saeedi S, Sabbagh SK. Antibacterial Activity of *Marrubium vulgare* L. Against Antibiotic Resistance *Klebsiella pneumoniae* Strains. *Adv Herb Med*. 2015;1(3):9-14.
12. Hamedeyazdan S, Sharifi S, Nazemiyeh H, Fathiazad F. Evaluating Antiproliferative And Antioxidant Activity of *Marrubium crassidens*. *Adv Pharm Bull*. 2014;4(Supp1):459-64.
13. De Jesus R, Cechinel-Filho V, Oliveira A, Schlemper V. Analysis of the Antinociceptive Properties of *Marrubiin* Isolated From *Marrubium vulgare*. *Phytomed*. 2000;7(2):111-5.
14. Boudjelal A, Henchiri C, Siracusa L, Sari M, Ruberto G. Compositional Analysis And In Vivo Anti-Diabetic Activity Of Wild Algerian *Marrubium vulgare* L. Infusion. *Fitoterapia*. 2012;83(2):286-92.
15. Namjoyan F, Azemi ME, Abdollahi E, Goudarzi N, Nikan K. Angiotensin I Converting Enzyme Inhibitory Activities Of Hydroalcoholic Extract of *Nardostachys jatamansi*, *Prangos ferulacea* and *Marrubium vulgare*. *Jundishapur J Nat Pharm Prod*. 2015;10(2):e17255.
16. Ettaya A, Dhibi S, Samout N, Elfeki A, Hfaiedh N. Hepatoprotective Activity Of White Horehound (*Marrubium Vulgare*) Extract Against Cyclophosphamide Toxicity In Male Rats. *Can J Physiol Pharmacol*. 2015;94(4):441-7.
17. Saad S, Ouafi S, Chabane D. Anti-Inflammatory And Acute Toxicity Evaluation Of Aqueous Infusion Extract Obtained From Aerial Parts of *Marrubium deserti* de Noé growing in Algeria. *Afr J Tradit, Complement Altern Med*. 2016;13(1):71-5.
18. Yousefi K, Soraya H, Fathiazad F, Khorrami A, Hamedeyazdan S, Maleki-Dizaji N, et al. Cardioprotective Effect Of Methanolic Extract Of *Marrubium vulgare* L. on Isoproterenol-Induced Acute Myocardial Infarction In Rats. *Ind J Exp Biol*. 2013;51(8):653-60.
19. Argyropoulou A, Samara P, Tsitsilonis O, Skaltsa H. Polar Constituents Of *Marrubium Thessalum* Boiss. & Heldr.(Lamiaceae) And Their Cytotoxic/Cytostatic Activity. *Phytother Res*. 2012;26(12):1800-6.
20. Pukalskas A, Venskutonis PR, Salido S, de Waard P, van Beek TA. Isolation, Identification And Activity Of Natural Antioxidants From Horehound (*Marrubium Vulgare* L.) Cultivated in Lithuania. *Food Chem*. 2012;130(3):695-701.
21. Letchamo W, Mukhopadhyay S. Variability in Chromosomes, Herb Yield, Essential Oil

Content And Potentials Of Horehound For North American Commercial Production. *J Horticult Sci.* 1997;72(5):741-8.

22. Weel KG, Venskutonis PR, Pukalskas A, Gruzdiene D, Linssen JP. Antioxidant Activity Of Horehound (*Marrubium vulgare* L) Grown in Lithuania. *Eur J Lipid Sci Tech.* 1999;101(10):395-9.

23. Orhan IE, Belhattab R, Şenol F, Gülpinar A, Hoşbaş S, Kartal M. Profiling of cholinesterase inhibitory and antioxidant activities of *Artemisia absinthium*, *A. herba-alba*, *A. fragrans*, *Marrubium vulgare*, *M. astranicum*, *Origanum vulgare* subsp. *glandulosum* and Essential Oil Analysis Of Two *Artemisia* Species. *Ind Crops Prod.* 2010;32(3):566-71.

24. Tuzlaci E. A Dictionary of Turkish Plants. *Melisa Matbaacilik*: ALFA Press; 2006.

25. Song H-P, Zhang H, Fu Y, Mo H-y, Zhang M, Chen J, et al. Screening for Selective Inhibitors Of Xanthine Oxidase From *Flos Chrysanthemum* Using Ultrafiltration LC-MS Combined With Enzyme Channel Blocking. *J Chromatogr B.* 2014;961:56-61.

26. Kaurinovic B, Vlasisavljevic S, Popovic M, Vastag D, Djurendic-Brenesel M. Antioxidant Properties Of *Marrubium Peregrinum* L.(Lamiaceae) Essential Oil. *Molecules.* 2010;15(9):5943-55.

27. Sahpaz S, Garbacki N, Tits M, Bailleul F. Isolation and Pharmacological Activity Of Phenylpropanoid Esters From *Marrubium vulgare*. *J Ethnopharmacol.* 2002;79(3):389-92.

28. Essawy SS, Abo-Elmatty DM, Ghazy NM, Badr JM, Sterner O. Antioxidant and Anti-Inflammatory Effects Of *Marrubium Alysson* Extracts In High Cholesterol-Fed Rabbits. *Saudi Pharm J.* 2014;22(5):472-82.

29. Benkhniq O, Ben Akka F, Salhi S, Fadli M, Douira A, Zidane L. Catalogue Des Plantes Médicinales Utilisées Dans Le Traitement Du Diabète Dans La Région d'Al Haouz-Rhamna (Maroc). *J Anim Plant Sci.* 2014;23(1):3539-68.

30. Orch H, Douira A, Zidane L. Étude Ethnobotanique Des Plantes Médicinales Utilisées Dans Le Traitement Du Diabète, Et Des Maladies Cardiaques Dans La Région d'Ízarène (Nord du Maroc). *J Appl Biosci.* 2015;86(1):7940-56.

31. Tsukamoto K, Jackson IJ, Urabe K, Montague PM, Hearing V. A Second Tyrosinase-Related Protein, TRP-2, Is A Melanogenic Enzyme Termed Dopachrome Tautomerase. *EMBO J.* 1992;11(2):519-26.

32. Xu Y, Stokes AH, Freeman WM, Kumer SC, Vogt BA, Vrana KE. Tyrosine mRNA is Expressed In Human *Substantia Nigra*. *Mol Brain Res.* 1997;45(1):159-62.

33. Namjoyan F, Jahangiri A, Azemi ME, Arkian E, Mousavi H. Inhibitory Effects of *Physalis alkekengi* L., *Alcea rosea* L., *Bunium persicum* B. Fedtsch. and *Marrubium vulgare* L. on Mushroom Tyrosinase. *Jundishapur J Nat Pharm Prod.* 2015;10(1):1-6.

34. Brand-Williams W, Cuvelier M-E, Berset C. Use Of A Free Radical Method To Evaluate Antioxidant Activity. *LWT-Food Sci Technol.* 1995;28(1):25-30.

35. Re R, Pellegrini N, Proteggente A, Pannala A, Yang M, Rice-Evans C. Antioxidant Activity Applying An Improved ABTS Radical Cation Decolorization Assay. *Free Rad Biol Med.* 1999;26(9-10):1231-7.

36. Prior RL, Wu X, Schaich K. Standardized Methods For The Determination Of Antioxidant Capacity And Phenolics In Foods And Dietary Supplements. *J Agric Food Chem.* 2005;53(10):4290-302.

37. Marco GJ. A Rapid Method For Evaluation Of Antioxidants. *J Am Oil Chem Soc.* 1968;45(9):594-8.
38. Chen C-H, Chan H-C, Chu Y-T, Ho H-Y, Chen P-Y, Lee T-H, et al. Antioxidant Activity Of Some Plant Extracts Towards Xanthine Oxidase, Lipooxygenase And Tyrosinase. *Molecules.* 2009;14(8):2947-58.
39. Masuda T, Yamashita D, Takeda Y, Yonemori S. Screening For Tyrosinase Inhibitors Among Extracts Of Seashore Plants And Identification Of Potent Inhibitors From *Garcinia subelliptica*. *Biosci Biotech Biochem.* 2005;69(1):197-201.
40. Yang X-W, Huang M-Z, Jin Y-S, Sun L-N, Song Y, Chen H-S. Phenolics from *Bidens bipinnata* And Their Amylase Inhibitory Properties. *Fitoterapia.* 2012;83(7):1169-75.
41. Albano SM, Lima AS, Pedro MGMLG, Barroso JG, Figueiredo AC. Antioxidant, Anti-5-Lipoxygenase And Antiacetylcholinesterase Activities Of Essential Oils And Decoction Waters Of Some Aromatic Plants. *Rec Nat Prod.* 2012;6(1):35.
42. Michelis F, Tiligada E, Skaltsa H, Lazari D, Skaltsounis A-L, Delitheos A. Effects of the Flavonoid Pilloin Isolated From *Marrubium Cylleneum* On Mitogen-Induced Lymphocyte Transformation. *Pharm Biol.* 2002;40(4):245-8.
43. Çalis I, Hosny M, Khalifa T, Rüedi P. Phenylpropanoid Glycosides From *Marrubium alysson*. *Phytochem.* 1992;31(10):3624-6.
44. Hussain A, Perveen S, Malik A, Afza N, Iqbal L, Tareen RB. Urease Inhibitory Flavone Glucosides from *Marrubium anisodon*. *Pol J Chem.* 2009;83(7):1329-35.
45. Mitreski I, Stanoeva JP, Stefova M, Stefkov G, Kulevanova S. Polyphenols in Representative *Teucrium* Species in the Flora of R. Macedonia: LC/DAD/ESI-MS (n) profile and content. *Nat Prod Commun.* 2014;9(2):175-80.
46. Kırmızıbekmez H, Montoro P, Piacente S, Pizza C, Dönmez A, Çalıř İ. Identification by HPLC-PAD-MS and Quantification by HPLC-PAD of Phenylethanoid Glycosides of Five *Phlomis* Species. *Phytochem Anal.* 2005;16(1):1-6.
47. Ulubelen A, Topcu G, Kolak U. Labiatae flavonoids and their bioactivity. In: Atta ur R, editor. *Studies in Natural Products Chemistry.* Vol. 30: Elsevier; 2005. p. 233-302.
48. Buckingham J, Munasinghe VRN. *Dictionary of Flavonoids with CD-ROM:* CRC Press; 2015.
49. Tsvetkov D, Dmitrenok A, Tsvetkov YE, Menshov V, Yashunsky D, Yashin AY, et al. Phenylethanoid Glycosides From Teak Wood Knots And Their Antioxidant Activity. *J Biol Active Prod Nat.* 2016;6(4):272-81.
50. Zhang H, Tsao R. Dietary Polyphenols, Oxidative Stress And Antioxidant And Anti-Inflammatory Effects. *Curr Opin Food Sci.* 2016;8:33-42.
51. Herrera-Arellano A, Aguilar-Santamaria L, Garcia-Hernandez B, Nicasio-Torres P, Tortoriello J. Clinical trial of *Cecropia obtusifolia* and *Marrubium vulgare* Leaf Extracts On Blood Glucose And Serum Lipids In Type 2 Diabetics. *Phytomed.* 2004;11(7-8):561-6.
52. Loizzo MR, Saab AM, Tundis R, Menichini F, Bonesi M, Piccolo V, et al. In vitro Inhibitory Activities Of Plants Used In Lebanon Traditional Medicine Against Angiotensin Converting Enzyme (ACE) And Digestive Enzymes Related To Diabetes. *J Ethnopharmacol.* 2008;119(1):109-16.



Green Preparation of *Hyphaene thebaica* Fiber Grafted Acrylic Acid for Adsorption of Pb(II) ions from Aqueous Solution

Ahmed Salisu^{1*}  and Muhammad Saleh Salga¹ 

¹Umaru Musa Yar' adua University, Faculty of Natural and Applied Sciences, Department of Pure and Industrial Chemistry, PMB 2218, Katsina, Nigeria.

Abstract: In this study, a green chemistry approach was employed in the preparation of *Hyphaene thebaica* fiber grafted polyacrylic acid via microwave assisted method using potassium persulfate as the chemical initiator. The optimum percentage grafting of 92% was achieved under 5 g concentration of acrylic acid, 0.2 g concentration of potassium persulfate (KPS) and 2 minutes of reaction time. The grafted sample was characterized using the following techniques, FTIR, SEM and XRD. The prepared graft copolymer was examined for adsorption of Pb(II) ions from aqueous solution in batch mode systems. The adsorption parameters such as pH, initial metal ion concentration and contact time were also studied. The Langmuir and Freundlich isotherm models were applied to simulate the equilibrium adsorption experimental data. The Langmuir model fitted well with experimental data with maximum adsorption capacity (q_{max}) of 20.37 mg/g at 45 minutes. Higher regression coefficient obtained confirmed the suitability of the Langmuir isotherm model which assumed monolayer coverage on the adsorbent surface. The adsorption studies revealed the efficacy of the grafted fiber for removal of Pb(II) ions from dilute aqueous solutions.

Keywords: *Hyphaene thebaica*, microwave, radiation, potassium persulfate, green procedures.

Submitted: December 21, 2018. **Accepted:** June 18, 2019.

Cite this: Salisu A, Salga M. Green Preparation of *Hyphaene thebaica* Fiber Grafted Acrylic Acid for Adsorption of Pb(II) ions from Aqueous Solution. JOTCSA. 2019;6(3):293–302.

DOI: <https://doi.org/10.18596/jotcsa.500440>.

***Corresponding author.** E-mail: (ahmed.salisu@umyu.edu.ng).

INTRODUCTION

Cotton is by far the largest source of cellulosic fibers. Other substantial sources include; jute, sisal, flax, kenaf coir, hemp, etc. Agricultural waste biomasses such as sugarcane bagasse, rice husk, corn husk, saw-dust, orange peels, etc. are another potential large sources of ligno-cellulose. Cellulose (Figure 1) is a sustainable, less expensive, non-toxic, and biodegradable biopolymer; that has found a wide range of applications in many areas such as textile industry (1), automobile industry (2), civil engineering (3), pharmaceutical industries (4), and catalysis (5). Agricultural wastes are mostly burned after dried, thus presenting a considerable risk of pollution of the environment. Instead, proper utilization of these materials for other value added products has been the keen interest of many researchers (6). Chemical modifications of cellulose such as esterification (7), acetylation

(8), etherification (9), mercerization (10) and grafting with various monomers were explored to alter the porosity and functionality of cellulose. Among these methods, grafting with various monomers present a great opportunity to tailor the physical and chemical properties of cellulose (11). Microwave irradiation initiating system for free radical polymerization reaction displays the best potential for use and fits the concept of green chemistry, i.e. less solvent consumption, shorter reaction time, energy saving, and less toxic (12). Cellulose and its derivatives have been tested for sorption of heavy metals from aqueous solutions (13, 14, 15). Pollution of surface waters has been a major ecological problem in less developed countries. Contamination of surface waters by toxic heavy metals such as Pb, Cd, As, Ni, Cr, Zn, Cu, etc. endangered humans and aquatic organisms (16). For example, lead can cause several disorders that include; renal damage, hepatic damage, central nervous system damage,

and damage to the reproductive system (17). Currently, the existing conventional heavy metal wastewater treatment technologies include chemical precipitation, oxidation, evaporation, electro-deposition, chelation, ion-exchange, coagulation, membrane filtration and adsorption (18). Each of the methods has positive and negative attributes; however, adsorption has been widely reported as cheap, effective and less technical compared to other techniques (19, 20). The focus of the present study is to modify *Hyphaene thebaica* fiber, a huge lingo-cellulose agricultural waste produced in tons annually in most sub-Saharan African countries, with acrylic acid via microwave free radical graft copolymerization, characterize the graft copolymer prepared and tested for its potential for sorption of lead ions from aqueous solution.

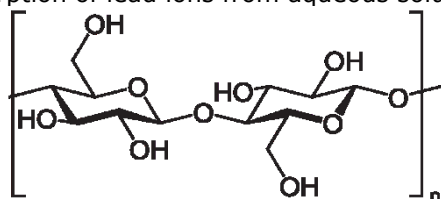


Figure 1: Chemical repeating unit of cellulose.

MATERIALS AND METHODS

Materials

Acrylic acid, acetone, methanol, and potassium persulfate (KPS) were purchased from Sigma-Aldrich (USA). $Pb(NO_3)_2$ was purchased from Loba Chemie (England). A stock solution of Pb(II) ions (1000 mg/L) was prepared by dissolving 1.599 g of $Pb(NO_3)_2$ salt in a beaker (250 mL) with deionized water. The prepared stock solution was transferred to a 1.0 liter volumetric flask, followed by the addition of 100 mL of 0.1M HNO_3 and made to the mark with deionized water. Desired concentrations of the metal solutions were prepared by serial dilution of the stock solution using deionized water. Other chemical reagents were of analytical grade and used as received.

Sample Collection and Pretreatment

A fresh stalk of *Hyphaene thebaica* was collected from the local fields near Kayauki village, along Daura road Katsina State, Nigeria, in clean plastic containers. The stalk (300 g) was cleaned with distilled water, pulverized and soaked in distilled water at room temperature for 24 hrs. Thereafter the fibers were removed and washed thoroughly with distilled water and oven-dried at 50 °C. Subsequently, mercerization of the fiber was carried out with 5% (w/v) aqueous sodium hydroxide (500 mL) for 24 hours in a 1000 mL beaker at room temperature. This treatment removes lignin, wax and oil and also increases hydrophilicity (fiber wetting). The alkali treated fibers were washed thoroughly with distilled water until the pH of wash water becomes neutral. The fibers were oven dried at 50 °C.

Graft Copolymerization of Acrylic Acid onto *Hyphaene Thebaica* Fiber

The graft copolymer was prepared using the procedure described previously (21) with minor modifications. Mercerized *Hyphaene thebaica* fiber (0.5 g) was soaked in 50 mL distilled water in a 250 mL Bomex beaker for 24 hours before graft copolymerization, in order to activate the reaction sites on the fibrous surface. Required amount of acrylic acid and KPS were added and stirred well. The reaction vessel was placed at the center of a rotating ceramic plate in the domestic microwave oven (Model WMO20L-MGSB, Skyrun, Nigeria). The reaction vessel was then exposed to microwave radiation at 900 W power for desired time. Periodically, the microwave irradiation was stopped and the reaction vessel was allowed to cool by placing it in cold water. Reaction parameters such as monomer concentration, initiator concentration and microwave exposure time were varied. Afterwards, polymeric product was precipitated by adding excess acetone and oven-dried at 50 °C. The sample was extracted by Soxhlet extraction with methanol for 6 hours to remove the homopolymer adhered to the fibrous surface. Thereafter, the prepared grafted fiber was oven-dried at 50 °C.

The percentage grafting was measured using equation (1).

$$(\%) \text{ Grafting} = \frac{W_2 - W_1}{W_1} \times 100 \quad (\text{Eq. 1})$$

where W_1 is the initial weight of the fiber sample, W_2 is the weight of the grafted fiber after Soxhlet extraction (22).

Characterization Techniques

Fourier Transform infrared analysis was performed by using a FTIR VERTEX 70/70v spectrometer (Agilent Technologies, USA). A scanning electron microscope (SEM) micrograph of the fiber and its surface morphology was examined using PHENOM PRO X (Netherlands). Powder X-ray diffraction patterns were recorded on ARL X'TRA X-ray Diffractometer (Thermo Scientific, Switzerland) using graphite monochromatic $CuK\alpha_1$ (1.5406 Å) and $K\alpha_2$ operated at 40 kV and 30 mA in the range of 2θ angles of 5-70°.

Batch Equilibrium Adsorption Experiment

Batch experiments were performed by varying different variables such as pH, contact time, metal ions concentration. The experiments were carried out in 250 mL conical flasks by adding 0.1 g of the grafted fiber with 25 mL of various metal ion solution of concentrations, 20, 40, 60, 80, 100, 120, and 140 mg/L and adjusted to desired pH at room temperature using a shaker operating at 300 rpm. At desired times, the adsorption experiments were stopped, all of the 25 mL of metal ion solutions with the grafted fiber was filtered. The metal ion concentration was determined and the separated grafted fiber was

placed again into the same batch and continue to the second adsorption period. All the experiments were conducted in duplicate and averages of duplicate readings were presented. The amount of Pb(II) adsorbed per unit mass of the adsorbent at equilibrium (q_e) (mg/g) was calculated using equation (2)

$$q_e \text{ (mg/g)} = (C_0 - C_e) \frac{V}{M} \quad (\text{Eq. 2})$$

where c_0 is the initial metal ions concentration (mg/L), and c_e is the equilibrium concentration of metal ions in solution (mg/L), V is the volume of metal ions solution used (L) and M is the mass of the grafted fiber used (g). The equilibrium data obtained were tested using the linear forms of Langmuir isotherm model (23) and Freundlich isotherm model (24), using equation (3) and (4), respectively:

$$\frac{C_e}{q_e} = \frac{1}{q_{\max} Q_L} + \frac{C_e}{q_m} \quad (\text{Eq. 3})$$

$$\log q_e = \log K_F + \frac{1}{n} \log C_e \quad (\text{Eq. 4})$$

Adsorption kinetic experimental data were modelled using two kinetic models; pseudo-first-order (25) and pseudo-second-order (26) expressed using equations (5) and (6) respectively.

$$\log(q_e - q_t) = \log q_e - \frac{k_1}{2.303} t \quad (\text{Eq. 5})$$

Where q_e and q_t (mg/g) are the amount of (metal ions) adsorbed at equilibrium and at time t respectively, and k_1 (min^{-1}) is the equilibrium rate constant for pseudo-first-order adsorption process. The plot of $\log(q_e - q_t)$ versus t gives a straight line. From the slope of the straight line, the rate constants k_1 were calculated. Pseudo-second-order kinetic model is expressed by the following equation:

$$\frac{t}{q_t} = \frac{1}{k_2 q_e^2} + \frac{1}{q_e} t \quad (\text{Eq. 6})$$

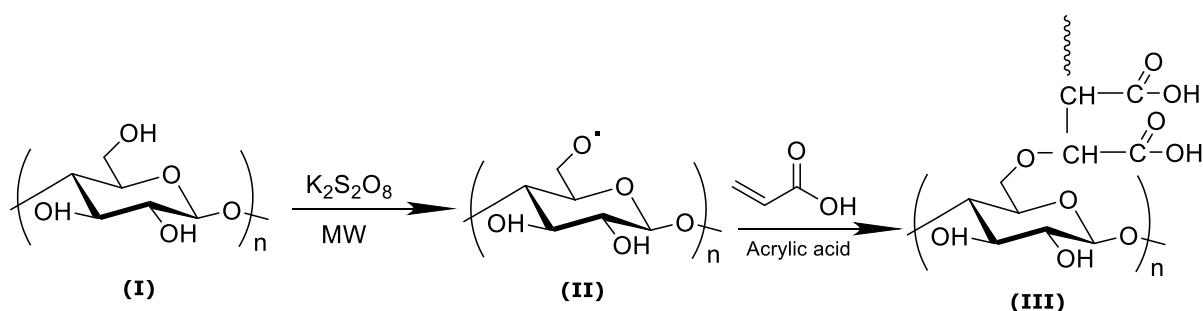
Where q_e and q_t (mg/g) are the amount of the uptake of adsorbate at equilibrium and at time t respectively, and k_2 (g/mg/min) is the equilibrium rate constant for pseudo-second order adsorption process. The slope and intercept of the plot of $\frac{t}{q_t}$ versus t can be used directly to calculate the kinetic parameters, adsorption capacity (q_e) and rate constant (k_2).

RESULTS AND DISCUSSION

The experimental (conditions and results) of graft copolymerization reaction between the fiber and acrylic acid are presented in Table 1.

Table 1: Summary of results and reaction conditions of synthesis Cell-g-PAA.

S/N	wt of fiber (g)	wt of acrylic acid (g)	wt of KPS (g)	Time (S)	% grafting
1	0.5	5	0.1	120	58
2	0.5	5	0.2	120	92
3	0.5	5	0.3	120	73
4	0.5	5	0.4	120	43
5	0.5	2.5	0.2	180	7.2
6	0.5	7.5	0.2	60	27
7	0.5	5	0.5	120	39



Scheme 1: (I) Cellulose, (II) Cellulose-macroradicals, (III) Cell-g-PAA.

A graft copolymer can be defined as a macromolecule that has branches of another polymeric species emanating from different points along its backbone (27). Different grades of graft copolymers were prepared by varying the KPS and acrylic acid concentration (Table 1). The plan of the synthesis involve optimization with regard to KPS, maintaining the acrylic acid concentration constant (i.e. S/N 1, 2, 3 & 4).

Afterwards, optimization with respect to acrylic acid keeping the KPS concentration constant (i.e. S/N 5 & 6). The percentage grafting, $G(\%)$ decreased when the initiator amount was increased above 0.2g. This could be attributed to more free-radical generation that eventually may lead to premature termination (by coupling) of the growing radicals at higher concentration (16). It was observed that the highest percentage

grafting was achieved at acrylic acid concentration of 5 g and KPS concentration of 0.2 g. It was also observed that the reaction reached to the optimum at a very short reaction time of 2 minutes. Microwave assisted synthesis involves synergism between microwave radiation and free radical initiator to form macroradical active sites on the cellulose backbone. Cellulose is having many -OH groups along its length, when exposed by microwave radiation in the presence of persulfate initiator. Persulfate initiator dissociates to produce a pair of persulfate ion radical ($\text{SO}_4^{\cdot-}$). These radicals may abstract H-atom from the easily accessible (-OH) group (28). This would form active sites on the cellulose backbone (macroradicals), this would eventually initiate graft copolymerization on contact with acrylic

acid. The plausible mechanism of the reaction is shown in Scheme 1.

Characterization of The Grafted Fiber

FTIR Analysis

FTIR spectrum of the mercerized fiber is shown in Figure 2. The broad absorption peak at 3335 cm^{-1} was attributed O-H stretching vibrations of cellulose and the absorption peak at 2888 cm^{-1} was assigned to C-H stretching vibration. The peak at 1026 cm^{-1} was attributed to stretching C-O of β -glucosidic linkage of pyranose ring (29). Meanwhile in the spectrum of the grafted fiber (Figure 3), an additional sharp absorption peak at 1707 cm^{-1} indicates the C=O stretching vibration of carboxylic acid functional group, this confirmed that the polyacrylic acid had been successfully grafted onto the surface of the fiber.

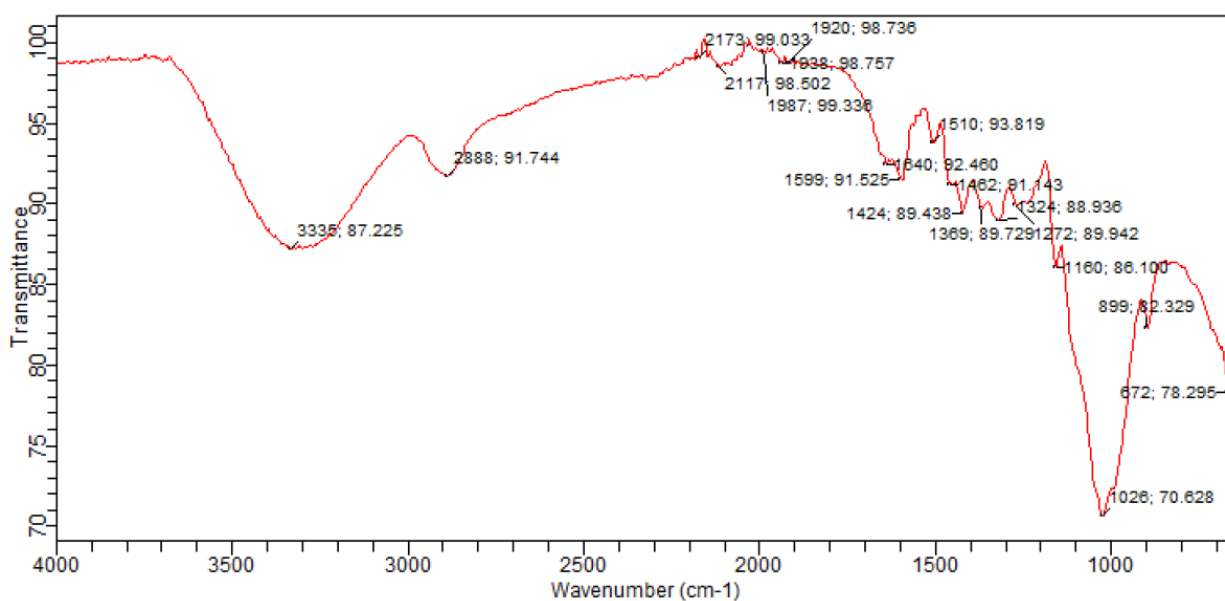


Figure 2: FTIR spectrum of the mercerized fiber.

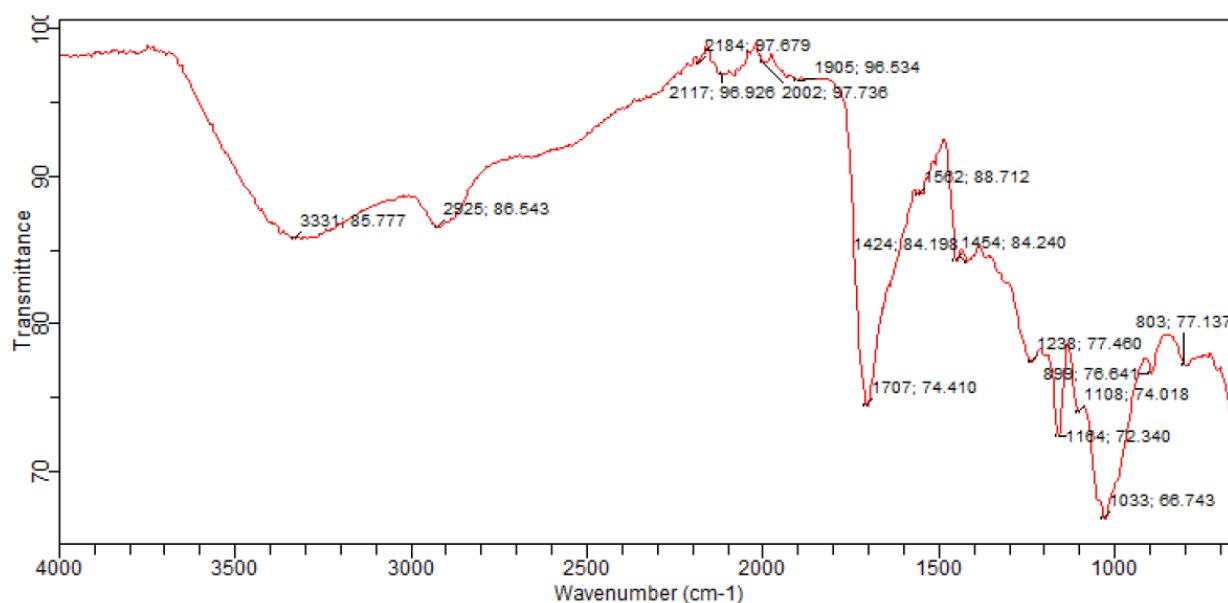


Figure 3: FTIR spectrum of the grafted fiber (Cell-g-PAA).

XRD Analysis

The XRD pattern of mercerized and grafted fiber was presented in Figure 4. The characteristic peaks of mercerized fiber were observed at 22.13° and 14.3° (2θ degree) with relative intensities of 1056 and 606, respectively. The peaks of grafted sample were found at 20.25° and

16.1° (2θ degree) with relative intensities of 806.2 and 509.5, respectively. This showed that grafting has resulted in the decrease in the peak intensity of grafted sample. It was observed that the grafting of polyacrylic acid onto the backbone of the fiber changed most of the crystalline phase to amorphous phase (30).

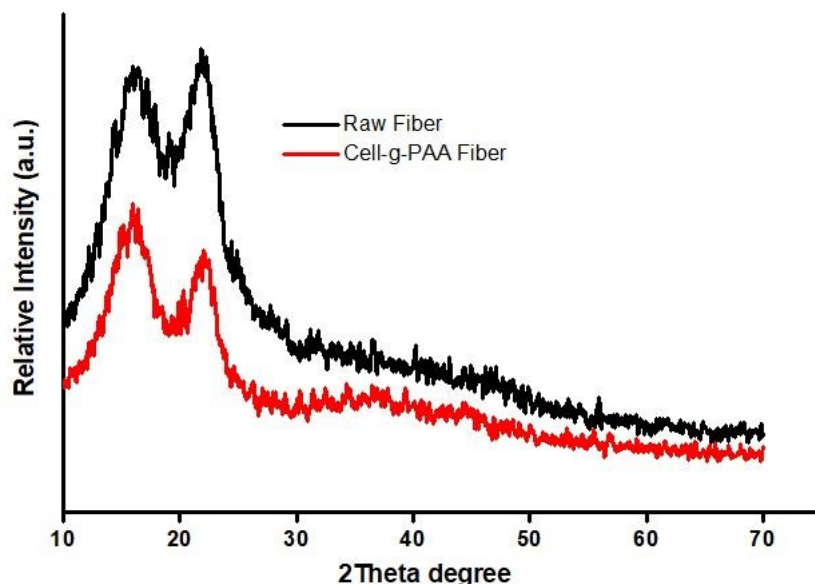


Figure 4: X-ray diffractogram of mercerized fiber and grafted fiber (Cell-g-PAA).

Scanning Electron Microscopy (SEM)

Surface morphology of mercerized fiber and the grafted fiber were examined using a scanning electron microscope. The SEM images of mercerized and grafted fiber were shown in Figure 5a and 5b, respectively. The SEM images were taken at the same magnification for a suitable comparison of morphological changes that occurred. It is clearly seen that the

mercerized fiber was smooth after mercerization which removed lignin lipids and waxes. It can be observed that a substantial amount of polyacrylic acid was left behind on the surface of the grafted fiber after Soxhlet extraction that removed the homopolymer that is unreacted with the fiber. This has confirmed the grafting of polyacrylic acid onto the surface of the fiber.

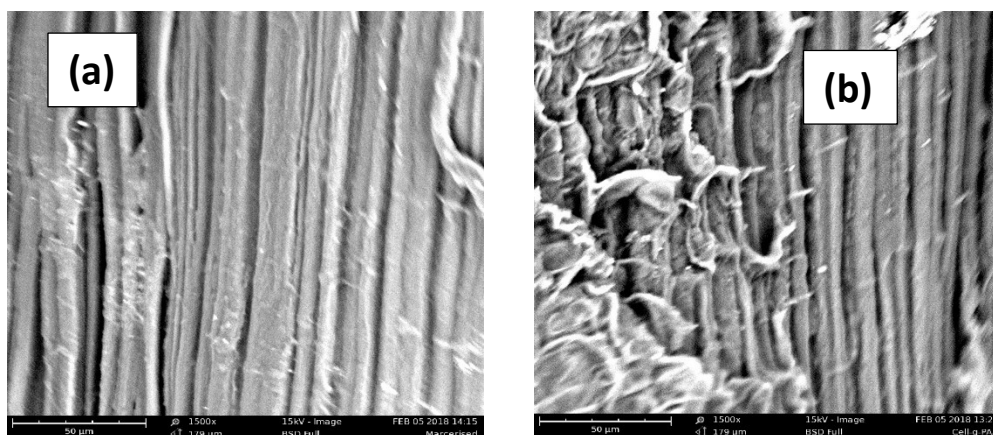


Figure 5: SEM images of (a) mercerized fiber and (b) grafted fiber (Cell-g-PAA).

BATCH ADSORPTION STUDY**Effect of pH of the Solution**

In order to examine the influence of this important parameter on the adsorption of Pb(II), the experiments were conducted in the pH range of pH 2.0-9.0. The adsorption capacity for different values of pH is represented in Figure 6.

The maximum adsorption capacity of Pb(II) takes place at pH 5.0 and decreased afterwards. At low pH values, there is a greater competition between protons and metal ions which may eventually be protonated most of the adsorption sites on the adsorbent surface, resulting in low adsorption capacity because of electrostatic repulsion. With the increase of pH from 6.0-8.0, the carboxyl

groups (-COOH) in polyacrylic acid and hydroxyl groups in cellulose (-OH) become free from protonation due to the diminishing of hydrogen ion concentration, resulting in the decreased in competition of protons with Pb(II) ions for

adsorption sites and subsequently good adsorption capacities were also observed. However the precipitation of Pb(II) may predominates over adsorption at pH values above pH 9.0 that is why they are not considered.

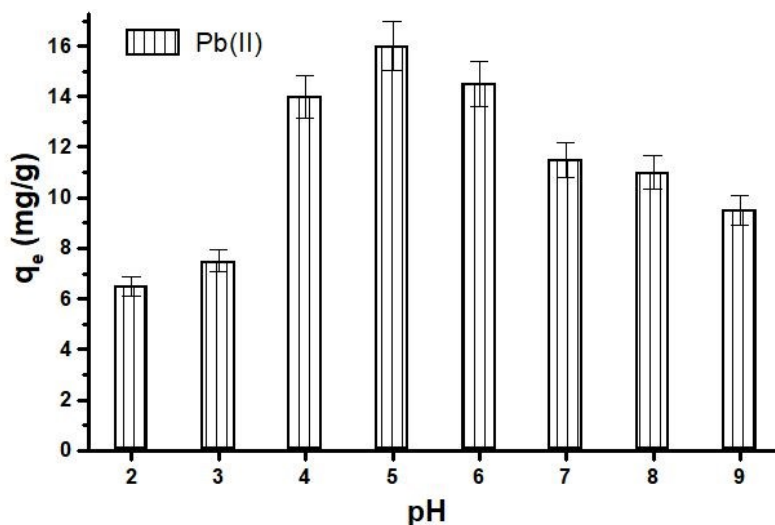


Figure 6: Effect of pH on adsorption of Pb(II) onto Cell-g-PAA (initial Pb²⁺ conc. = 80 mg/L, adsorbent dose = 0.1 g, contact time = 60 min, batch volume = 25 mL).

Effect of Initial Metal Ion Concentration

In order to study the influence of initial metal ion concentration affecting the overall adsorption process, various batch adsorption experiments were carried out for different concentration in the range of 20 to 140 mg/L, keeping other parameters constant. The results are presented in Figure 7. The amount of Pb(II) adsorbed per unit mass of the adsorbent relatively increased with the increased in metal ion concentration

from 20 up to 100 mg/L. However, at concentrations of 100 and 120 mg/L, the amount adsorbed was virtually the same. Having observed this, we concluded that the significant amount of Pb(II) adsorbed at higher concentration could be due to greater driving force at the liquid-solid interface, which consequently affect the mass transfer of the adsorbate from solution to adsorbent surface (31).

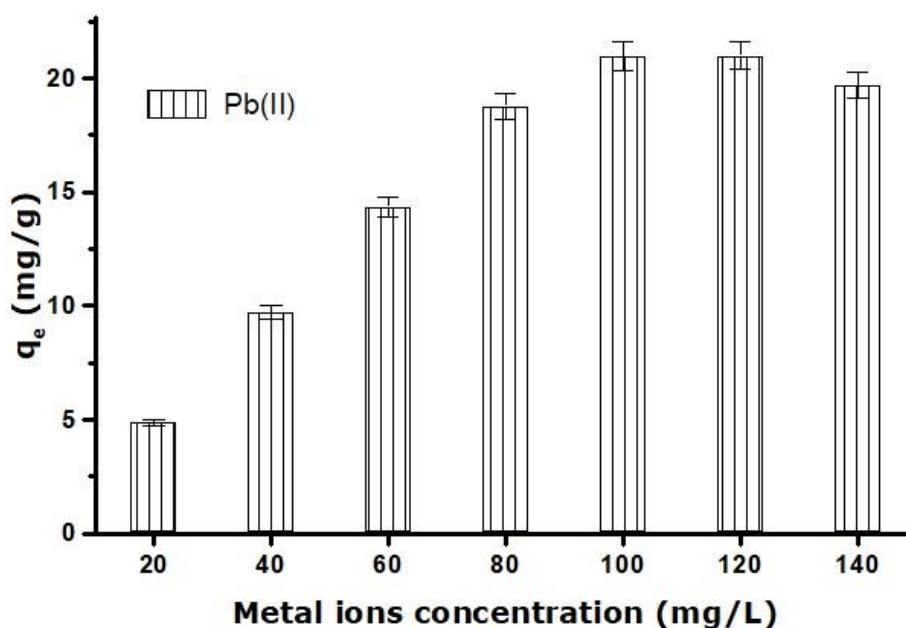


Figure 7: Effect of initial metal ion concentration on adsorption of Pb(II) onto Cell-g-PAA (initial pH = 5.0, adsorbent dose = 0.1 g, batch volume = 25 mL)

Effect of Contact Time

Figure 8 represents the results of equilibrium adsorption time and the adsorption capacity of the adsorbent. It was observed that the adsorption capacities increased steadily with the increased contact time from 5 to 60 minutes, and equilibrium point was attained after 45 mins for 20 mg/L concentration and 50 mins for 40 and 80 mg/L concentration. To ascertain the potential mechanism controlling the rate of adsorption, pseudo-first-order and pseudo-second-order were chosen to fit the experimental data. Table 2

showed the results of the kinetic models after simulations for different initial metal ion concentration. It was clear from the results that the adsorption kinetics followed pseudo-second-order model, with regression coefficients greater than 0.99 in all cases. Furthermore, calculated values of adsorption capacities agreed satisfactorily with the experimental data. Thus, chemisorption was assumed to be the rate-limiting step, indicating strong interactions due to the affinity of the adsorbent for the metal ion.

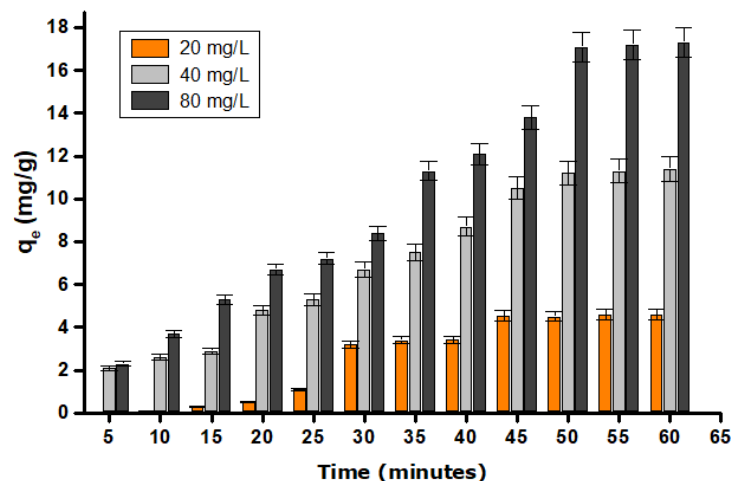


Figure 8: Effect of contact time on adsorption of Pb(II) onto Cell-g-PAA (initial Pb(II) conc. = 100 mg/L, pH = 5.0, adsorbent dose = 0.1 g)

Table 2: Rate constants and regression coefficients for adsorption Pb(II):

Co (mg/L)	Pseudo-first-order model				Pseudo-second-order model		
	q _{max exp} (mg/g)	q _{max cal.} (mg/g)	k ₁ (1/min)	R ²	q _{max cal.} (mg/g)	k ₂ (g/mg/min)	R ²
20	3.81	1.63	0.008	0.711	3.75	0.091	0.996
40	11.30	5.25	0.007	0.882	10.90	0.084	0.999
80	17.62	10.31	0.005	0.912	16.43	0.075	0.998

Analysis of Adsorption Isotherms

Adsorption isotherm models are considered as the most versatile tools to understand adsorption patterns of adsorption systems. In this study, the Langmuir isotherm model was found to fit the experimental data well as illustrated in Figure 9. From the linear plots of the two isotherm models, all the adsorption parameters were determined as presented in Table 3. Based on regression coefficients (R²) of the two models, Langmuir

isotherm model described the adsorption process well with the calculated maximum adsorption capacity of 20.37 mg/g. Furthermore, separation factor (R_L) which is a dimensionless constant calculated was below unity; thus indicating the favorability of the adsorption. Langmuir adsorption model assumed homogenous distribution of adsorbate onto the adsorbent surface (monolayer coverage) (32).

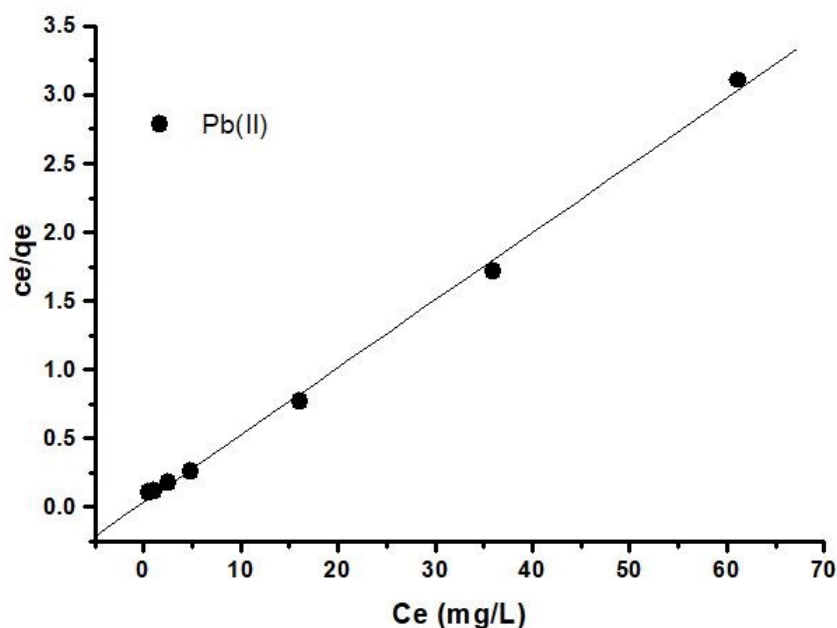


Figure 9: Langmuir isotherm plot for adsorption Pb(II) onto Cell-g-PAA.

Table 3: Isotherm constants and regression coefficients for adsorption of Pb(II)

Langmuir model				Freundlich model		
q_{max} (mg/g)	R_L	Q_L (L/mg)	R^2	K_F (mg/g)	n	R^2
20.37	0.004	0.821	0.998	1.09	20.40	0.739

CONCLUSIONS

Sequestration of Pb(II) ions from aqueous solution was achieved by using a renewable, efficient, modified low-cost agricultural waste biomass. FTIR, SEM and XRD analyses of the grafted sample confirmed the grafting of polyacrylic acid onto cellulosic *Hyphaene thebaica* fiber. It has been observed that Pb(II) ions adsorption increased with an increase of the contact time and metal ion concentration until equilibrium was attained in 45 minutes but decreased at pH values above 6.0. Two popular adsorption isotherms and kinetic models were applied to test the applicability of the adsorption processes. The adsorption isotherm analysis is compatible with a Langmuir isotherm model which assumed monolayer adsorption process where as the kinetic mechanism indicated the prevalence of chemisorption. The study employed a green approach to the synthesis of the graft copolymer. The method is green because it requires less energy, less time, and less organic solvent consumption.

ACKNOWLEDGEMENT

Financial support from the TETFund through the institutional-based research grant is gratefully acknowledged.

REFERENCES

1. Qiu X, Hu S. Smart materials based on cellulose: a review of the preparations, properties and applications. *Materials* (Basel). 2013; 6:738-81.
2. Wei H, Rodriguez K, Rennecker S, Vikesland PJ. Environmental science and engineering applications of nanocellulose-based composites. *Environ. Sci. Nano.* 2014; 1(4):302-16.
3. Siro I, Plackett D. Microfibrillated cellulose and new nanocomposite materials: a review. *Cellulose.* 2014; 17(3): 459-94.
4. Plackett DV, Letchford K, Jackson JK, Burt HM. A review of nanocellulose as a novel vehicle for drug delivery. *Nordic. Pulp Pap. Res. J* 2014; 29(1): 131-41.
5. Gupta VK, Pathania D, Singh P, Rathore BS, Chauhan P. Cellulose acetate-zirconium (IV) phosphate nanocomposite with enhanced photo-catalytic activity. *Carbohydr. Polym.* 2013; 95(1): 434-40.
6. Kumar R, Sharma RK, Singh AP. Cellulose based grafted biosorbents- Journey from lignocellulose biomass to toxic metal ions

- sorption applications- A review. *Journal of Molecular Liquids*. 2017; 232: 62-93.
7. Zhang J, Wu J, Cao Y, Sang S, Zhang J, He J. Synthesis of cellulose benzoates under homogeneous conditions in an ionic liquid. *Cellulose*. 2009; 16(2): 299-308.
 8. Wan Daud WR, Djuned FM. Cellulose acetate from oil palm empty fruit bunch via a one step heterogeneous acetylation. *Carbohydr. Polym.* 2015; 132: 252-60.
 9. Stein A, Klemm D, Syntheses of cellulose derivatives via O-triorganosilyl cellulose I. Effective synthesis of organic cellulose esters by acetylation of trimethyl silyl celluloses. *Die Makromolekulare Chemie Rapid Communications*. 1988; 9(8): 569-73.
 10. Bali G, Meng X, Deneff JI, Sun Q, Arthur JR. The effect of Alkaline pre-treatment methods on cellulose structure and Accessibility. *ChemsusChem Communications*. 2014; 2(3): 1-5.
 11. Roy D, Semsarilar M, Guthriea JT, Perrier S. Cellulose modification by polymer grafting, A review. *Chem. Soc. Rev.* 2006; 38: 2046-64.
 12. Mishra S, Usha GR, Sen G. Microwave initiated synthesis and application of polyacrylic acid grafted carboxymethyl cellulose. *Carbohydr. Polym.* 2011; 87: 2255-62.
 13. Nada AAMA, Alkady MY, Fekry HM. Synthesis and characterization of grafted cellulose for use in water and metal ions sorption. *Bioresources*. 2008; 3:46-59.
 14. Hajeeth T, Sudha PN, Vijayalakshmi TG. Sorption studis on Cr(VI) removal from aqueous solution using cellulose grafted with acrylonitrile monomer. *Int. J. Biol. Macromol.* 2014; 66:295-301.
 15. Okieimen FE, Sogbaike CE, Ebhoaye JE. Removal of cadmium and copper ions from aqueous solution with cellulose graft copolymers. *Sep. Purif. Technol.* 2005; 44: 85-89
 16. Salisu A, Mohd MS, Ahmedy AN, Ibrahim WAW, Khairil JA. Removal of lead ions from aqueous solutions using sodium alginate-graft-poly(methyl methacrylate) beads. *Desal. Water Treat.* 2016; 57(33): 15353- 61.
 17. Naseem R, Tahir SS. Removal of Pb(II) from aqueous solution by using bentonite as an adsorbent. *Water Res.* 2001; 35: 3982-6.
 18. Salisu A, Mohd MS, Ahmedy AN, Ibrahim WAW, Khairil JA. Alginate graft polyacrylonitrile beads for the Removal of lead ions from aqueous solutions *Polym Bull.* 2016; 73: 519-37.
 19. Raji C, Anirudhan TS. Batch Cr(VI) removal by polyacrylamide-grafted sawdust: kinetics and thermodynamics. *Water Res.* 1998; 32: 3772-80.
 20. Sharma S, Pathania D, Singh . Preparation, characterization and Cr(VI) adsorption behavior study of poly(acrylic acid) grafted *Fiscus carica* bast fiber. *Adv. Mater. Lett.* 2013; 4: 271-6.
 21. Rani P, Sen G, Mishra S, Jha U. Microwave assisted synthesis of polyacrylamide grafted gum ghatti and its application as flocculant. *Carbohydr. Polym.* 2012; 89: 275-81.
 22. Isiklan N, Kursun F, Inal M. Graft copolymerization of itaconic acid onto sodium alginate using benzoyl peroxide. *Carbohydr. Polym.* 2010; 101: 665-72.
 23. Langmuir I. The adsorption of gases on plane surfaces of glass, mica and platinum. *J. Chem. Soc.* 1918; 40: 1361-403.
 24. Freundlich HMF. *Über die adsorption in losungen. Zeitschrift für physikalische chemie (Leipzig)*. 1906; 57A, 385-470.
 25. Gurgel LV, Gil LF. Adsorption of Cu(II), Cd(II) and Pb(II) from aqueous single solution by succinylated twice-mercerized sugarcane bagasse functionalized with triethylenetetraamine. *Water Res.* 2009; 43:4479-88.
 26. Ho YS, McKay G. Pseudo-second-order model for sorption processes. *Proc. Biochem.* 1999; 34: 451-465.
 27. David WJ, Hudson SM. Review of vinyl graft copolymerization featuring recent advances toward controlled radical-based reactions and illustrated with chitin/chitosan trunk polymers. *Chem. Rev.* 2001; 101: 3245-73.
 28. Umar A, Mohd MS, Salisu A, Ibrahim WAW, Khairil AJ, Abdul Keyon AS. Preparation and characterization of starch grafted with methacrylamide using ammonium persulphate initiator. *Materials letters*. 2016; 185: 173-6.
 29. Arowona MT, Olatunji GA, Saliu OD, Adeniyi OR, Atolani O, Adisa MJ.

- Thermally stable rice husk microcrystalline cellulose as adsorbent in PTLC plates. JOTCSA. 2018; 5(3): 1177-84.
30. Gupta VK, Agarwal S, Singh P, Pathania D. Acrylic acid grafted cellulosic Luffa cylindrical fiber for the removal of dye and metal ions. Carbohydr. Polym. 2013; 98: 1214-21.
31. Zhou Q, Yan C, Luo W. Preparation of a novel carboxylate-rich wheat straw through surface graft modification for efficient separation of Ce (III) from wastewater. Materials and Design. 2016; 97: 195-203.
32. Dang V, Doan HD, Dang-Vu AL. Equilibrium and kinetics of biosorption of cadmium (II) and copper (II) ions by wheat straw. Bioresource Technol. 2008; 100: 211-19.



Synthesis, Characterization, and Molecular Docking Studies of Fluoro and Chlorophenylhydrazine Schiff Bases

Ayşegül ŞENOCAK  

Tokat Gaziosmanpasa University, College of Science and Arts, Department of Chemistry, 60240, Tokat, Turkey.

Abstract: Six Schiff bases synthesized by condensation reaction of p-fluoro and chlorophenylhydrazines with some carbonyl compounds were reported in this work. Structures of the prepared compounds were elucidated by FT-IR, ¹H- and ¹³C-NMR spectroscopy. FT-IR spectra exhibited characteristic transitions for all compounds. Also, their structures were proved by NMR spectroscopy, especially with the imine peak which is an indicator of the formation of Schiff bases. In addition, molecular docking studies of the Schiff bases were carried out on Alzheimer's disease. The calculated docking scores and inhibition constants pointed out the probability of the usage of 2-chloro-5-nitrobenzaldehyde Schiff bases as a new drug candidate for Alzheimer's disease after structural regulations.

Keywords: Schiff base, Phenylhydrazine, NMR spectroscopy, Alzheimer's disease, Cholinesterases, Molecular docking.

Submitted: March 04, 2019. **Accepted:** July 08, 2019.

Cite this: Şenocak A. Synthesis, Characterization, and Molecular Docking Studies of Fluoro and Chlorophenylhydrazine Schiff Bases. JOTCSA. 2019;6(3):303-10.

DOI: <https://doi.org/10.18596/jotcsa.535441>.

Corresponding author. E-mail: aysegul.senocak@gop.edu.tr, ayseon@gmail.com. Tel: +90 356 252 1616/3051, Fax: +90 356 252 1585.

INTRODUCTION

Schiff bases are regarded as one of the most studied compound group because of their potential using areas ranging from pharmacology and industry to biology and chemistry. Versatility, stability, and ease of synthesis of the Schiff bases induce their broad in scope applications containing catalysts, dyes and pigments, corrosion inhibitors, and bioactive materials (1-8). Among those applications, bioactive materials have come to the forefront especially because of the contribution of the azomethine group to bioactivity by interacting and forming hydrogen bonding with certain sites in the cell structure (9).

For the synthesis of the Schiff bases, various amine compounds have been used. Phenylhydrazine compounds are also used for this purpose especially by converting to pyrazoles and

pyrazolones. In one of the studies about phenylhydrazines, Dayakar et al. synthesized a series of pyrazole and pyrazolone derivatives by refluxing phenylhydrazines with ethyl-4-chloro-3-oxobutanoate (10). Besides, various pyrazole and pyrazolone compounds derived from phenylhydrazine Schiff bases were studied and reported as antimicrobial and anticancer agents by different groups (11-13). In another study, N,O-hydrazone Schiff base ligand and its complexes with nickel and copper were synthesized and catalytic effects of the complexes on oxidation of benzyl alcohol were studied (14). Finally, half-sandwich complexes of phenyl hydrazone Schiff base ligands prepared by Lapasam et al. exhibited good antibacterial activity against *P. aeruginosa* and *B. thuringiensis* (15).

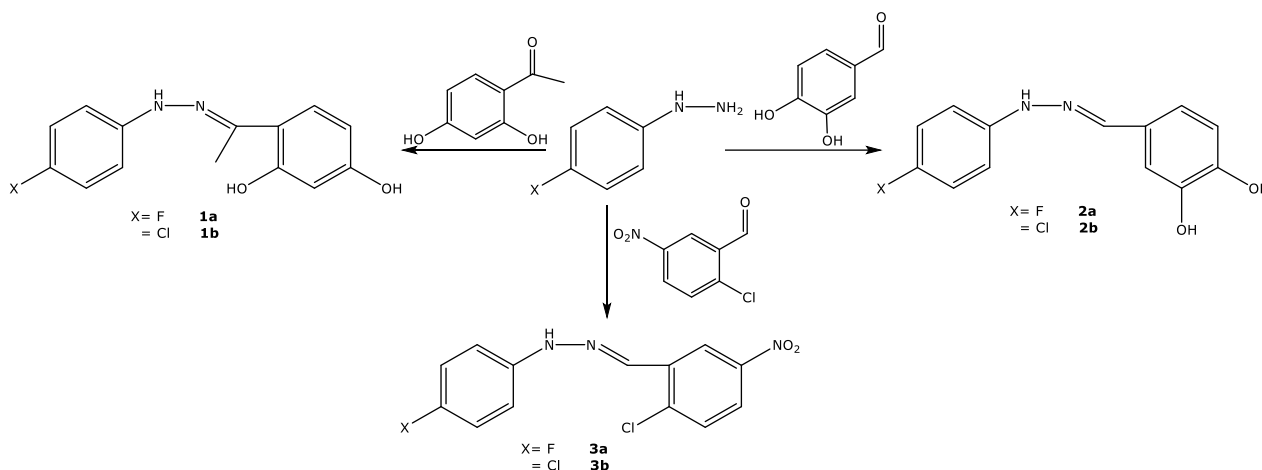
Alzheimer's disease (AD), one of the most common neurodegenerative diseases, most commonly affects people in the 65-90 age range and many studies have been carried out on its treatment. One of the target proteins intensely used in these studies is cholinesterase enzymes. Inhibition of acetylcholinesterase (AChE) and butyrylcholinesterase (BChE) enzymes alleviates the symptoms of AD regulating the level of acetylcholine in certain regions of the brain. Therefore synchronized inhibition of these two enzymes have been promising for the treatment of AD, which may develop for many reasons (16) and there are so many studies on inhibition of AChE and BChE in the literature (16–22).

Andrade-Jorge et al. evaluated new isoindoline and dioxoisoindoline compounds for AChE inhibition. They compared the compounds to observe the effect of carbonyl group on inhibition activity (20). A series of compounds were prepared to evaluate their AChE and BChE inhibitory activities by Arumagum et al. Molecular docking and in vitro studies showed good

inhibitory activities for all compounds(21). In another study, very potent cholinesterase inhibitors based on a weak cholinesterase inhibitor called minaprine were prepared. As a result, two of the compounds exhibiting high activity were revealed for new drug active material candidates (22).

The desire to hinder waste of time and resources of scientists interesting in bioactivity studies have driven forward computer based drug design approaches over the last decades. The usage of these methods before clinic studies has been increased the efficiency drug development process. Especially enzyme inhibition studies about the diseases like tuberculosis, cancer, diabetes, Alzheimer's, and epilepsy have intensely appeared in the literature (23–26).

In this study, six Schiff bases were prepared and defined by FT-IR, ¹H- and ¹³C-NMR spectroscopic methods. Besides, molecular docking studies of the Schiff bases were carried out as AChE and BChE inhibitors against AD.



Scheme 1: The Schiff bases synthesized in this study.

EXPERIMENTAL SECTION

Chemistry

¹H- and ¹³C-NMR spectra of the imine compounds were measured using AC Bruker 400 MHz NMR spectrometer in d-methanol at ambient temperature. FT-IR spectra were recorded on a Jasco FT-IR 4700 spectrometer in the range of 400-4000 cm⁻¹. Elemental analyses were recorded on a Elementar Vario Micro Cube elemental analyzer. Solvents and chemicals were used as received from commercial sources.

Docking Studies

Docking calculations were made by DockingServer (<http://www.dockingserver.com>). In order to energy minimization of ligand molecules, the MMFF94 force field was used by DockingServer (27). Gasteiger partial charges were added to the ligand atoms. Non-polar hydrogen atoms were combined, and rotatable bonds were defined. Docking calculations were

made on AChE (PDB ID: 2ckm) and BChE (PDB ID: 1p0i) proteins. The addition of essential hydrogen atoms, Kollman united atom type charges, and solvation parameters was carried out by AutoDock tools (28). Affinity (grid) maps of 100×100×100 Å grid points and 0.375 Å spacing were created by the aid of the Autogrid program (28). For the calculation of the van der Waals and the electrostatic terms, AutoDock parameter set- and distance- dependent dielectric functions were used. Docking simulations were made through the Lamarckian genetic algorithm (LGA) and the Solis & Wets local search method (29). Initial position, orientation, and torsions of the ligand molecules were set randomly. Every docking experiment included 100 runs that were set to terminate after a maximum of 2500000 energy evaluations. The population size was adjusted to 150. During the search, a translational step of 0.2 Å, and quaternion and torsion steps of 5 were used.

Experimental

Fluoro- or chlorophenylhydrazine (6 mmol) was placed in a round-bottom flask with ethanol (30 mL). After addition of NEt_3 , this solution was mixed until all content was dissolved. Then, the carbonyl compound (6 mmol) was added to the clear solution. The reaction mixture was mixed for a couple of days. During this time the solution has changed to yellow or orange. After reaction's completion, reaction mixture was left to crystallization and the obtained precipitate was washed with ethanol and diethyl ether.

1a: Yield 55%; mp: 161 °C. FT-IR (cm^{-1}): 3320 (N-H), 3268 (O-H), 2999 (C-H), 1596 (azomethine, C=N); $^1\text{H-NMR}$ ($\text{CH}_3\text{OH-d}_4$, δ , ppm): 2.33 (3H, s, CH_3), 6.34 (1H, s, CH), 6.38 (1H, d, CH), 7.01 (4H, dd, CH), 7.35 (1H, d, CH). $^{13}\text{C-NMR}$ ($\text{CH}_3\text{OH-d}_4$, δ , ppm): 11.29, 102.74, 106.43, 112.82, 113.51, 115.05, 115.28, 127.97, 142.22, 149.30, 155.95, 158.30, 158.85, 159.34. Anal. calcd. for $\text{C}_{14}\text{H}_{13}\text{FN}_2\text{O}_2$ (260.27 g/mol): C, 64.61; H, 5.03; N, 10.76. Found: C, 64.47; H, 5.52; N, 11.09%.

1b: Yield 62%; mp: 198 °C (decomp.). FT-IR (cm^{-1}): 3056 (O-H), 2954, 2910 (C-H), 1578 (azomethine, C=N); $^1\text{H-NMR}$ ($\text{CH}_3\text{OH-d}_4$, δ , ppm): 2.81 (3H, s, CH_3), 6.53 (1H, d, CH), 6.60 (1H, dd, CH), 6.99 (2H, dd, CH), 7.35 (2H, dd, CH), 7.78 (1H, d, CH). $^{13}\text{C-NMR}$ ($\text{CH}_3\text{OH-d}_4$, δ , ppm): 15.06, 102.45, 107.86, 109.57, 114.96, 115.98, 126.74, 129.02, 129.15, 133.88, 143.31, 143.72, 161.42, 165.87. Anal. calcd. for $\text{C}_{14}\text{H}_{13}\text{ClN}_2\text{O}_2$ (276.72 g/mol): C, 60.77; H, 4.74; N, 10.12. Found: C, 60.52; H, 5.25; N, 10.89%.

2a: Yield 43%; mp: 197 °C (decomp.). FT-IR (cm^{-1}): 3203 (N-H), 3046 (O-H), 1564 (azomethine, C=N); $^1\text{H-NMR}$ ($\text{CH}_3\text{OH-d}_4$, δ , ppm): 6.76 (1H, s, CH), 6.90 (1H, d, CH), 7.05 (4H, dd, CH), 7.22 (1H, dd, CH), 8.22 (1H, s, CH). $^{13}\text{C-NMR}$ ($\text{CH}_3\text{OH-d}_4$, δ , ppm): 113.61, 115.14, 115.25, 115.40, 115.48, 123.10, 123.42, 141.29, 146.05, 150.70, 159.14, 159.88. Anal. calcd. for $\text{C}_{13}\text{H}_{11}\text{FN}_2\text{O}_2$ (246.24 g/mol): C, 63.41; H, 4.50; N, 11.38. Found: C, 63.79; H, 3.95; N, 11.87%.

2b: Yield 85%; mp: 194 °C (decomp.). FT-IR (cm^{-1}): 3285 (N-H), 3063 (O-H), 1564 (azomethine, C=N); $^1\text{H-NMR}$ ($\text{CH}_3\text{OH-d}_4$, δ , ppm): 6.89 (1H, d, CH), 7.03 (2H, dd, CH), 7.19 (1H, dd, CH), 7.25 (2H, dd, CH), 7.38 (1H, d, CH),

8.17 (1H, s, CH). $^{13}\text{C-NMR}$ ($\text{CH}_3\text{OH-d}_4$, δ , ppm): 113.33, 114.35, 115.33, 116.01, 122.85, 123.88, 124.68, 128.74, 129.02, 144.02, 145.93, 149.02, 150.08. Anal. calcd. for $\text{C}_{13}\text{H}_{11}\text{ClN}_2\text{O}_2$ (262.69 g/mol): C, 59.44; H, 4.22; N, 10.66. Found: C, 59.08; H, 5.02; N, 11.41%.

3a: Yield 61%; mp: 176 °C. FT-IR (cm^{-1}): 3305 (N-H), 3103, 3083 (C-H), 1575 (azomethine, C=N), 1339, 1295 (NO_2); $^1\text{H-NMR}$ ($\text{CH}_3\text{OH-d}_4$, δ , ppm): 7.05 (2H, dd, CH), 7.15 (2H, dd, CH), 7.62 (1H, d, CH), 8.05 (1H, dd, CH), 8.15 (1H, s, CH), 8.82 (1H, s, CH). $^{13}\text{C-NMR}$ ($\text{CH}_3\text{OH-d}_4$, δ , ppm): 113.35, 115.13, 115.36, 119.92, 121.91, 129.52, 130.70, 135.09, 137.14, 141.06, 147.08. Anal. calcd. for $\text{C}_{13}\text{H}_9\text{ClFN}_3\text{O}_2$ (293.68 g/mol): C, 53.17; H, 3.09; N, 14.31. Found: C, 52.83; H, 3.47; N, 14.81%.

3b: Yield 72%; mp: 188 °C. FT-IR (cm^{-1}): 3301 (N-H), 3094, 3074 (C-H), 1575 (azomethine, C=N), 1340, 1289 (NO_2); $^1\text{H-NMR}$ ($\text{CH}_3\text{OH-d}_4$, δ , ppm): 7.13 (2H, dd, CH), 7.25 (2H, dd, CH), 7.62 (1H, d, CH), 8.05 (1H, dd, CH), 8.17 (1H, s, CH), 8.81 (1H, d, CH). $^{13}\text{C-NMR}$ ($\text{CH}_3\text{OH-d}_4$, δ , ppm): 113.59, 120.02, 122.17, 124.54, 128.76, 130.45, 130.75, 135.19, 137.33, 143.37, 147.03. Anal. calcd. for $\text{C}_{13}\text{H}_9\text{Cl}_2\text{N}_3\text{O}_2$ (310.13 g/mol): C, 50.35; H, 2.93; N, 13.55. Found: C, 50.57; H, 3.37; N, 13.98%.

RESULTS AND DISCUSSION

The reaction of carbonyl compounds with fluoro- or chloro-phenylhydrazines in an equimolar ratio completed in a couple of days and target compounds were obtained by crystallization from EtOAc:hexane solvent system (2:1) with moderate to high yields. The compounds were moisture- and air-stable, and soluble in methanol and DMSO. Their structures were proved by FT-IR, ^1H - and $^{13}\text{C-NMR}$ spectroscopic methods.

FT-IR Spectra

The important IR bands were presented in the experimental section. Besides, FT-IR spectra of **1a** was shown in Figure 1. The sharp N-H band of hydrazine compound in **1a** was observed at 3320 cm^{-1} as overlapped with broad O-H stretching vibrations around 3268 cm^{-1} . The band at 1596 cm^{-1} was indicator of the imine bond. Other Schiff bases were observed to exhibit FT-IR spectra with similar frequencies and no important changes.

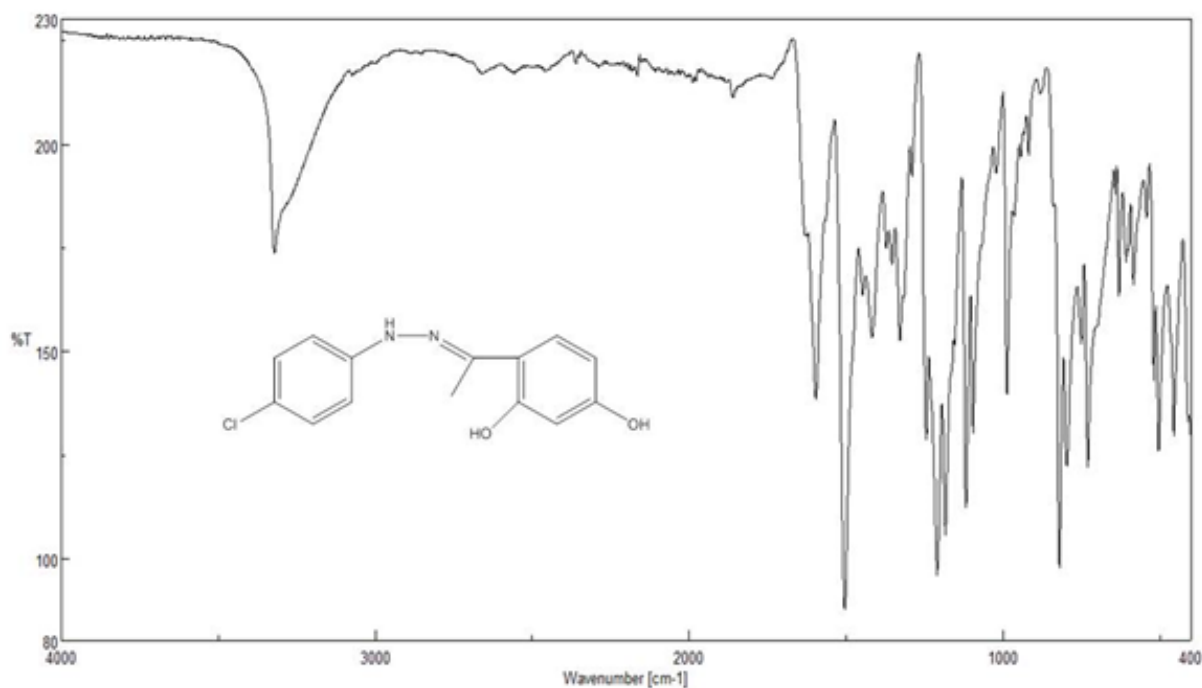


Figure 1: FT-IR spectrum of **1a**.

NMR Spectra

The ^1H - and ^{13}C -NMR spectra of all compounds confirmed the expected Schiff base structures. The ^1H - and ^{13}C -NMR spectra of **1a** were shown in Figure 2. The singlet at about 2.33 ppm was induced by the three protons of the methyl group. The other singlet was attributed to the methine proton placed between two tertiary aromatic carbon of carbonyl compound. While one of the

two doublet peaks belonging to carbonyl compound segment was observed at 6.38 ppm, the other one originating from methine proton adjacent to imine group was at 7.35 ppm. As it comes to phenylhydrazine ring protons, they were observed as overlapped at 7.01 ppm. ^{13}C -NMR peaks were in accordance with that of ^1H -NMR peaks.

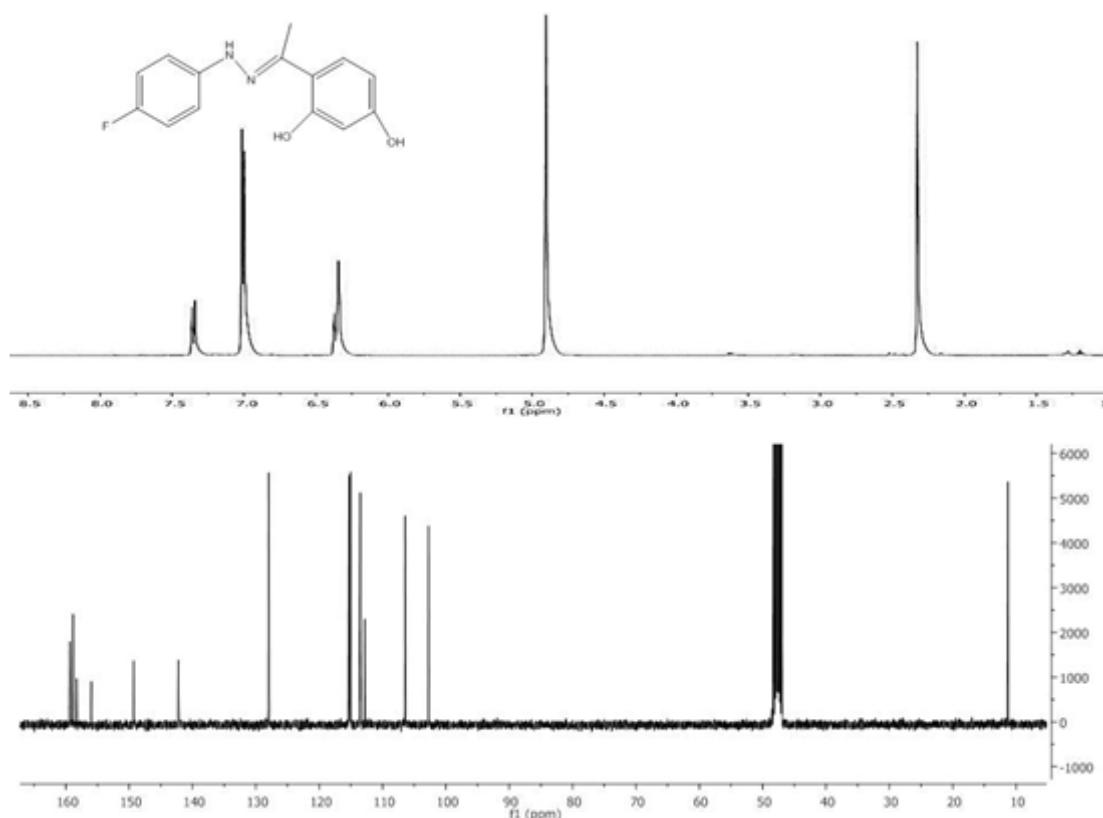


Figure 2: ^1H - and ^{13}C -NMR spectra of **1a**.

Molecular Docking Studies

Schiff bases were docked against AChE (PDB ID: 2CKM) and BChE (PDB ID: 1P0I) downloaded from Protein Data Bank by using Molecular Docking Server (Figure 3). Their binding affinity

and interaction of amino acid residues near their binding sites were also examined. Besides, pymol visual images of interacted proteins and ligands were shown in Table 1.

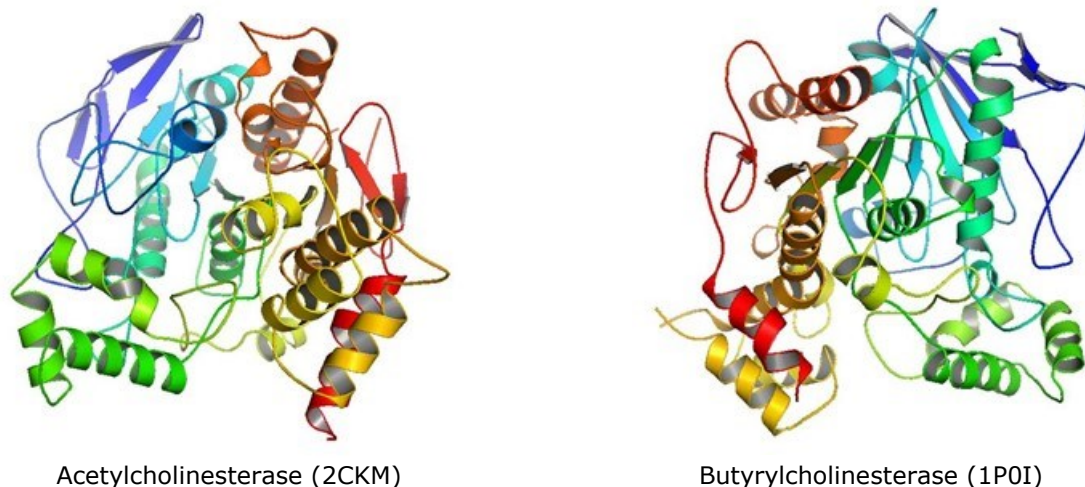


Figure 3: PDB structure of the proteins.

The amino acid fragments predicted to form hydrogen bonds with ligands were GLU 374, GLU 455, TYR 282, TYR 121, ASN 230, SER 87, SER 235, GLN 514, ARG 515, ALA 516, VAL 453. Among six ligands, fluoro derivative had the

higher activity against butyrylcholinesterase while chloro derivative exhibited the higher binding affinity against acetylcholinesterase (Table 2).

Table 1: Pymol visual images of ligand docked proteins.

Ligands	AChE (2CKM)	BChE (1P0I)
1a		
1b		

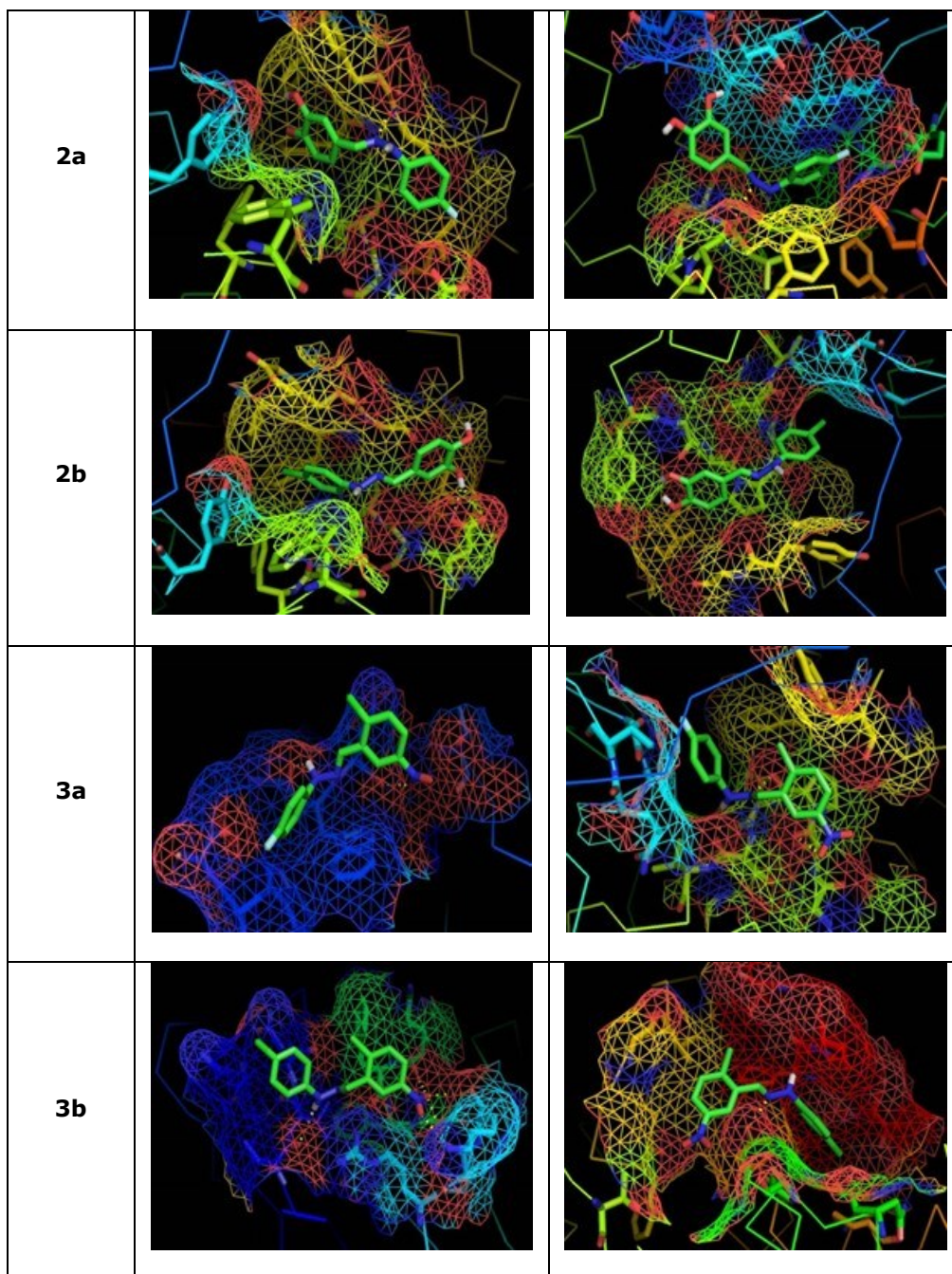


Table 2: Calculated binding affinity values between proteins and ligands.

Ligand	2CKM		1POI	
	Docking Score (kcal/mol)	Estimated Inhibition Constant	Docking Score (kcal/mol)	Estimated Inhibition Constant
1a	-2.62	12 mM	-3.14	5 mM
1b	-2.76	9.42 mM	-3.85	1.52 mM
2a	-3.23	4.31 mM	-3.39	3.25 mM
2b	-3.61	2.26 mM	-3.28	3.96 mM
3a	-3.54	2.53 mM	-4.14	926.18 μ M
3b	-4.31	692.01 μ M	-3.60	2.28 mM

Tacrine (THA) is the first cholinesterase inhibitor, approved by the FDA and then withdrawn from the market because of its adverse effects. Showing lower side effects in comparison with THA, 7-methoxy derivative (7-MEOTA) was observed to exhibit similar activity against cholinesterases. The Schiff base compounds **1a-3b** synthesized in this study exhibited lower docking scores in comparison with THA [-9.9 kcal/mol for AChE (2ckm) and -9.5 kcal/mol for BChE (1p0i)] and 7-MEOTA [-9.8 kcal/mol for AChE (2ckm) and -9.3 kcal/mol for BChE (1p0i)] (30).

CONCLUSIONS

In conclusion, the Schiff bases composed of phenylhydrazine halogen derivatives and carbonyl compounds were synthesized and characterized by spectroscopic methods (FT-IR, ¹H- and ¹³C-NMR). The compounds were prepared by mixing fluoro- or chloro-phenylhydrazine with the carbonyl compounds in equimolar amount in ethanol. The results of spectroscopic methods were used to explain the structures of the compounds and verified the predicted Schiff base structures. Besides, the compounds which were likely to exhibit inhibition activity on Alzheimer's disease were examined by molecular docking methods. The possibility of exhibiting inhibition activity of the Schiff bases on Alzheimer's disease was estimated based on similar chemical groups (phenyl ring and nitrogen atoms) included in their structure with Tacrine. All of the compounds exhibited low to mild binding affinities against acetylcholinesterase and butyrylcholinesterase in comparison with reference compounds (THA and 7-MEOTA). Schiff bases **3a** and **3b** derived from 2-chloro-5-nitrobenzaldehyde showed best results for both cholinesterase proteins. According to the calculated results, especially **3a** and **3b** were decided to be modified so as to use potential therapeutic agents for treating Alzheimer's disease.

REFERENCES

1. Kumar R, Mani G. Exhibition of the Brønsted acid-base character of a Schiff base in palladium(II) complex formation: lithium complexation, fluxional properties and catalysis of Suzuki reactions in water. *Dalt Trans.* 2015;44(15):6896-908.
2. Nejati K, Rezvani Z, Massoumi B. Syntheses and investigation of thermal properties of copper complexes with azo-containing Schiff-base dyes. *Dye Pigment.* 2007;75(3):653-7.
3. Ebenso EE, Isabirye DA, Eddy NO. Adsorption and Quantum Chemical Studies on the Inhibition Potentials of Some Thiosemicarbazides for the Corrosion of Mild Steel in Acidic Medium. *Int J Mol Sci [Internet].* 2010;11(6):2473-98.
4. Cinarli A, Gürbüz D, Tavman A, Birteksöz AS. Synthesis, spectral characterizations and antimicrobial activity of some Schiff bases of 4-chloro-2-aminophenol. *Bull Chem Soc Ethiop.* 2011;25(3):407-17.
5. Alshaheri AA, Tahir MIM, Rahman MBA, Begum T, Saleh TA. Synthesis, characterisation and catalytic activity of dithiocarbamate Schiff base complexes in oxidation of cyclohexane. *J Mol Liq.* 2017;240:486-96.
6. Cuesta-Aluja L, Campos-Carrasco A, Castilla J, Reguero M, Masdeu-Bultó AM, Aghmiz A. Highly active and selective Zn(II)-NN'O Schiff base catalysts for the cycloaddition of CO₂ to epoxides. *J CO₂ Util [Internet].* 2016;14:10-22.
7. Silku P, Özkinali S, Öztürk Z, Asan A, Köse DA. Synthesis of novel Schiff Bases containing acryloyl moiety and the investigation of spectroscopic and electrochemical properties. *J Mol Struct.* 2016;1116:72-83.
8. Karaer H, Gümrükçüoğlu IE. Synthesis and spectral characterisation of novel azo-azomethine dyes. *Turkish J Chem.* 1999;23(1):67-71.
9. Kajal A, Bala S, Kamboj S, Sharma N, Saini V. Schiff Bases: A Versatile Pharmacophore. *J Catal.* 2013;2013:1-14.
10. Dayakar C, Jyothi D, Suman P, Raju BC. Condensation of Ortho-phenylenediamines and Phenylhydrazines with Ethyl 4-Chloro-3-oxobutanoate: A Facile Approach for the Synthesis of Substituted 1 H-Benzimidazoles, Pyrazolones, and Pyrazoles. *Synth Commun [Internet].* 2015;45(14):1642-51.
11. Anush SM, Vishalakshi B, Kalluraya B, Manju N. Synthesis of pyrazole-based Schiff bases of Chitosan: Evaluation of antimicrobial activity. *Int J Biol Macromol [Internet].* 2018;119:446-52.
12. Lv XH, Ren ZL, Li DD, Ruan BF, Li QS, Chu MJ, et al. Discovery of novel double pyrazole Schiff base derivatives as anti-tobacco mosaic virus (TMV) agents. *Chinese Chem Lett [Internet].* 2017;28(2):377-82.
13. Wazalwar SS, Banpurkar AR, Perdih F. Synthesis, Characterization, Molecular Docking Studies and Anticancer Activity of Schiff Bases Derived from 3-(Substituted phenyl)-1-phenyl-1H-pyrazole-4-carbaldehyde and 2-Aminophenol. *J Chem Crystallogr [Internet].* 2018;48(4):185-99.
14. del Mar Conejo M, Cantero J, Pastor A, Álvarez E, Galindo A. Synthesis, structure and properties of nickel and copper complexes containing N,O-hydrazone Schiff base ligand. *Inorganica Chim Acta.* 2018;470:113-8.

15. Lapasam A, Dkhar L, Joshi N, Poluri KM, Kollipara MR. Antimicrobial selectivity of ruthenium, rhodium, and iridium half sandwich complexes containing phenyl hydrazone Schiff base ligands towards *B. thuringiensis* and *P. aeruginosa* bacteria. *Inorganica Chim Acta* [Internet]. 2019;484(August 2018):255–63.
16. Abedinifar F, Farnia SMF, Mahdavi M, Nadri H, Moradi A, Ghasemi JB, et al. Synthesis and cholinesterase inhibitory activity of new 2-benzofuran carboxamide-benzylpyridinium salts. *Bioorg Chem*. 2018;80:180–8.
17. Abbas-Mohammadi M, Moridi Farimani M, Salehi P, Nejad Ebrahimi S, Sonboli A, Kelso C, et al. Acetylcholinesterase-inhibitory activity of Iranian plants: Combined HPLC/bioassay-guided fractionation, molecular networking and docking strategies for the dereplication of active compounds. *J Pharm Biomed Anal*. 2018;158:471–9.
18. Makhaeva GF, Boltneva NP, Lushchekina S V., Rudakova E V., Serebryakova OG, Kulikova LN, et al. Synthesis, molecular docking, and biological activity of 2-vinyl chromones: Toward selective butyrylcholinesterase inhibitors for potential Alzheimer's disease therapeutics. *Bioorganic Med Chem*. 2018;26(16):4716–25.
19. Andrade-Jorge E, Sánchez-Labastida LA, Soriano-Ursúa MA, Guevara-Salazar JA, Trujillo-Ferrara JG. Isoindolines/isoindoline-1,3-diones as AChE inhibitors against Alzheimer's disease, evaluated by an improved ultra-micro assay. *Med Chem Res*. 2018;27(9):2187–98.
20. Larik FA, Shah MS, Saeed A, Shah HS, Channar PA, Bolte M, et al. New cholinesterase inhibitors for Alzheimer's disease: Structure activity relationship, kinetics and molecular docking studies of 1-butanoyl-3-arylthiourea derivatives. *Int J Biol Macromol*. 2018;116:144–50.
21. Arumugam N, Almansour AI, Suresh Kumar R, Altaf M, Padmanaban R, Sureshbabu P, et al. Spiropyrrolidine/spiroindolizino[6,7-b]indole heterocyclic hybrids: Stereoselective synthesis, cholinesterase inhibitory activity and their molecular docking study. *Bioorg Chem*. 2018;79:64–71.
22. Kilic B, Gulcan HO, Aksakal F, Ercetin T, Oruklu N, Umit Bagriacik E, et al. Design and synthesis of some new carboxamide and propanamide derivatives bearing phenylpyridazine as a core ring and the investigation of their inhibitory potential on in-vitro acetylcholinesterase and butyrylcholinesterase. *Bioorg Chem*. 2018;79:235–49.
23. Senthil SL, Chandrasekaran R, Arjun HA, Anantharaman P. In vitro and in silico inhibition properties of fucoidan against α -amylase and α -D-glucosidase with relevance to type 2 diabetes mellitus. *Carbohydr Polym*. 2019;209:350–5.
24. Ghaleb A, Aouidate A, Bouachrine M, Lakhliifi T, Sbai A. Discovery of Novel 1,2,3-Triazole Analogues as Anti-Tuberculosis agents Using 3D QSAR, Molecular Docking, and In Silico ADMET Screening. *Anal Bioanal Chem Res*. 2019;6(1):215–29.
25. Almutairi MS, Leenaraj DR, Ghabbour HA, Joe IH, Attia MI. Spectroscopic identification, structural features, Hirshfeld surface analysis and molecular docking studies on stiripentol: An orphan antiepileptic drug. *J Mol Struct*. 2019;1180:110–8.
26. Chen Y, Liu J, Geng S, Liu Y, Ma H, Zheng J, et al. Lipase-catalyzed synthesis mechanism of tri-acetylated phloridzin and its antiproliferative activity against HepG2 cancer cells. *Food Chem*. 2019;277:186–94.
27. Halgren TA. Merck molecular force field. I. Basis, form, scope, parameterization, and performance of MMFF94. *J Comput Chem*. 1996;17(5–6):490–519.
28. Morris GM, Goodsell DS, Halliday RS, Huey R, Hart WE, Belew RK, et al. Automated docking using a Lamarckian genetic algorithm and an empirical binding free energy function. *J Comput Chem*. 1998;19(14):1639–62.
29. Solis FJ, Wets RJ-B. Minimization by Random Search Techniques. *Math Oper Res*. 1981;6(1):19–30.
30. Spilovska K, Korabecny J, Kral J, Horova A, Musilek K, Soukup O, et al. 7-methoxytacrine-adamantylamine heterodimers as cholinesterase inhibitors in Alzheimer's disease treatment - Synthesis, biological evaluation and molecular modeling studies. *Molecules*. 2013;18(2):2397–418.



Molecular Interaction Between Cationic Polymer Polyethyleneimine and Rose Bengal Dye: A Spectroscopic Study

Tuğba BAYRAKTUTAN^{1*}  

¹Department of Biochemistry, Faculty of Arts and Science, Iğdır University, Iğdır, Turkey

Abstract: The binding mechanism and polymer–fluorescence probe interactions between polyethyleneimine (PEI) and Rose Bengal (RB) were investigated by using UV–Vis absorption, steady-state and time-resolved fluorescence spectroscopy techniques. The spectroscopic data indicated that unusual interactions and binding constant was calculated at $3.75 \times 10^2 \text{ M}^{-1}$ with high linearity for the PEI-RB system. The photophysical parameters of the dye, such as band shifts, fluorescence quantum yields, and fluorescence lifetimes, were determined. Non-radiative (k_{nr}) and radiative (k_r) rate constants were calculated and then compared.

Keywords: Polyethyleneimine, Rose Bengal, Absorption and Fluorescence Spectroscopy, Dye-Polymer Interaction

Submitted: December 28, 2018. **Accepted:** July 10, 2019.

Cite this: Bayraktutan T. Molecular Interaction Between Cationic Polymer Polyethyleneimine and Rose Bengal Dye: A Spectroscopic Study. JOTCSA. 2019;6(3):311–8.

DOI: <https://doi.org/10.18596/jotcsa.504528>.

***Corresponding author: E-mail:** tugba.bayraktutan@igdir.edu.tr.

INTRODUCTION

Among the studies on macromolecule-small molecule interactions, comprehensive studies are available on dye compounds and binding through water-soluble synthetic or natural polymers. Many dyes were found to exhibit very different binding properties to unmodified PEI. Previous studies in this area have shown that the binding affinity of polyethyleneimine (PEI) is suitable (1, 2). Among the cationic polymers, polyethyleneimine (PEI) is an applicable transfection reactant derived from the polyamine group (3). It is a polymer with linear or branched forms. PEI acts as a good polymer chelating agent due to its water solubility and suitable molecular weights. It is a polymer where chelating properties are examined by using potentiometric and spectrophotometric methods (4, 5). In this study, a branched PEI containing primary, secondary, and tertiary amino groups at approximately 1/4, 1/2 and 1/4 rates respectively, were used (6). In this study, PEI provides a change in the spectral properties for Rose Bengal (RB) dye through π - π stacking and electrostatic interaction.

Rose Bengal (RB) is an anionic dye derived from xanthene. It is a water-soluble, xanthene - derived, an anionic dye, which has a high absorbance coefficient in the UV-visible region and high sensitivity to light. The tendency to transfer long life radicals from the triplet excited state and intersystem crossing efficiency is high (7, 8). Since it is a dye that is highly sensitive to a micro-environment, it is much preferred in photophysical studies.

This study aims to examine the polymer-dye interactions between Polyethylenimine (PEI) and Rose Bengal (RB) by using UV-Vis absorption and fluorescence spectroscopy techniques. In this context, PEI is a good candidate because polyamine polymers have a high concentration of amine groups, which provides an effective macromolecular environment in the aqueous solution. In this study, we will provide RB-PEI interaction, and the photophysical parameters will be discussed and an attempt presented for the polymer-dye interaction mechanism. The formation of complex and aggregation in the dye-polymer interactions is one of the most common

situations in the literature. The dye-polymer studies are a powerful tool for determining the binding region, the driving forces in the binding, conformational changes of the polymer and which polymer has an affinity to the dye. In this respect, this study is significant in terms of adding a dye-polymer relationship to the literature.

EXPERIMENTAL

Chemicals

Rose Bengal and Polyethyleneimine (the molecular structures are shown in the Figure 1a and 1b, respectively) were purchased from Sigma. Methanol was purchased from Fluka. RB and PEI were stored in the dark as concentrated stock solutions of 1.0 mM in methanol. The chemicals were used without further purification. All experiments were done in distilled water.

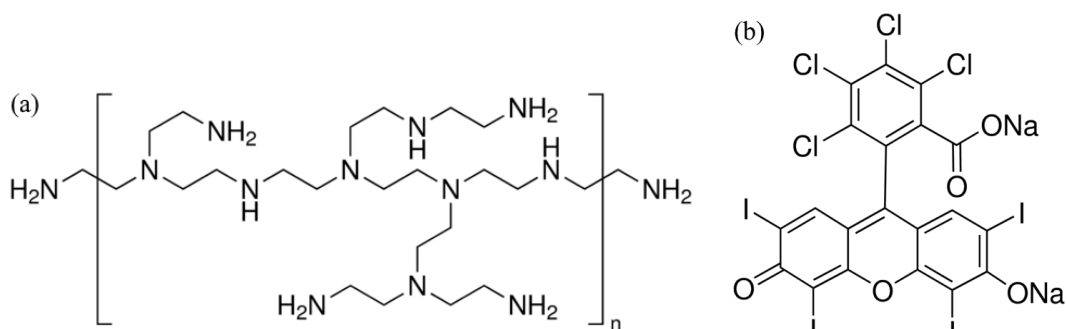


Figure 1. Molecular structures of (a) Polyethyleneimine and (b) Rose Bengal (Rose Bengal b sodium salt).

Equipments

Absorption and fluorescence spectra of samples were taken with Lambda 35 UV / Vis Spectrophotometer and Shimadzu RF-5301PC, respectively. Time-resolved fluorescence measurements were recorded in the Photon Technology Instrument (PTI) Time Master TM3. The excitation and emission slits were adjusted at 1.0 nm. The absorption spectra were recorded in the region of 455 nm to 620 nm at room temperature. For the fluorescence spectra, the system was excited at 520 nm and the fluorescence spectrum was recorded between 525 nm and 620 nm. A more detailed description of the method time depending fluorescence measurements is given other where (9).

Fluorescence Quantum Yield Measurements

Fluorescence quantum yields (Φ_f) were calculated using a reference solution and using equation 1.

$$\phi_S = \phi_r \left(\frac{D_S}{D_r} \right) \left(\frac{n_S}{n_r} \right)^2 \left(\frac{1-10^{OD_r}}{1-10^{OD_S}} \right) \quad (\text{Eq.1})$$

In equation 1, D_S and D_r refer to the integrated area under the corrected fluorescence spectra for

sample and reference, n_S and n_r are refractive indexes of sample and reference solutions, respectively. The ODs are the sample and the ODR is the reference optical density read at the excitation wavelength (10, 11). The fluorescence quantum yield of 1uM Rh101 is 1.00 in methanol (12).

RESULT AND DISCUSSION

Effects of PEI on the absorption spectra of RB

PEI does not show any absorbance in the visible region. The UV-Vis absorption spectra of the RB (2.0 uM) at various PEI concentrations changing from 0.02 to 0.90 mg/mL are shown in Figure 2. Figures 2a and 2b show the absorption spectra and normalized absorption spectra of the dye at room temperature and in a distilled water medium, respectively. RB shows maximum fluorescence absorption at 549 nm. When the various concentration polymer solutions are titrated to the dye solution, spectral shifts occur as a function of the PEI concentration. The biggest shift of about 15 nm was observed at the highest PEI concentration.

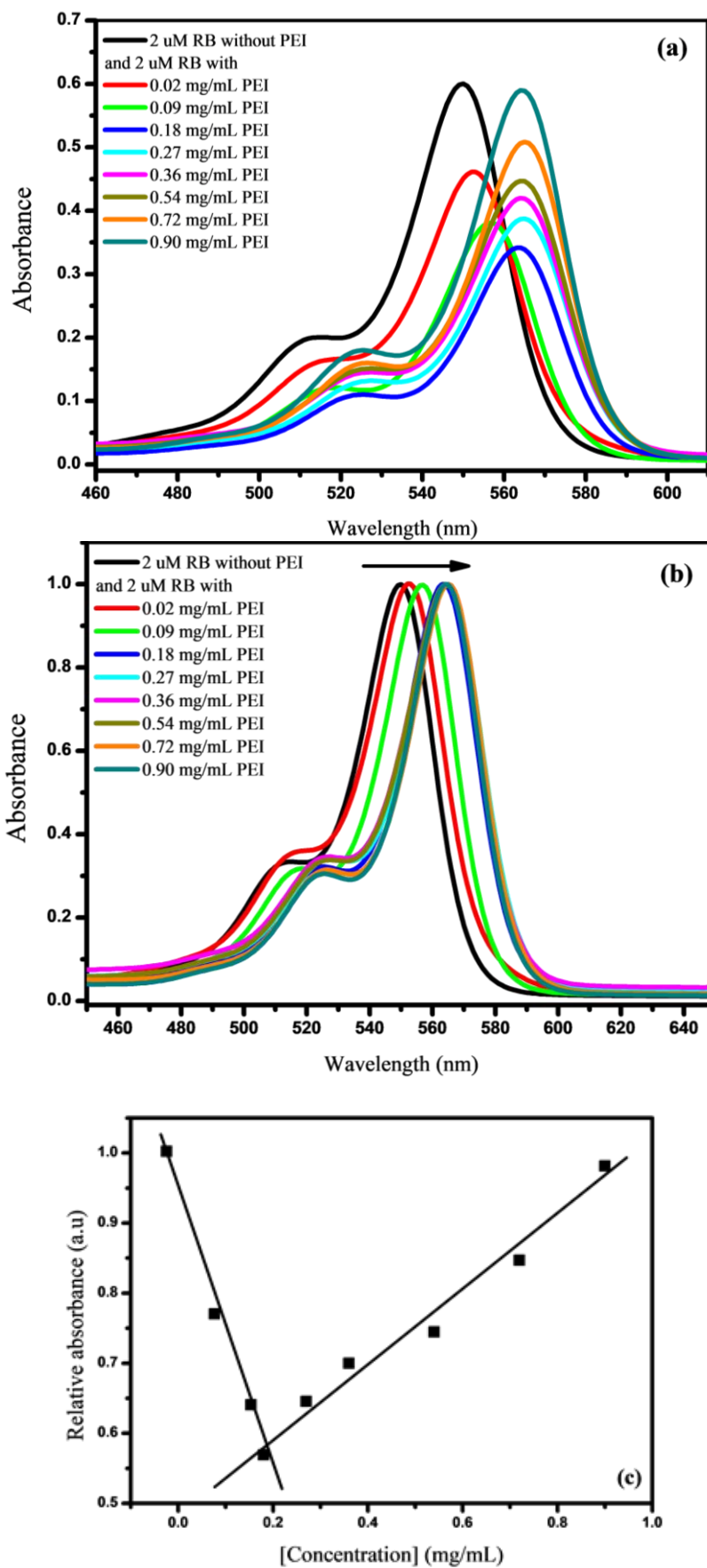


Figure 2. (a) Observed and (b) normalized UV-Vis absorption spectra of RB with various concentrations of PEI in distilled water. (c) Relation between the relative absorbance and the ratio of as a function of concentration of PEI.

According to the theory of molecular exciton, the transition moments are final for the electric dipole changeover from the ground state to the excited state or from the ground state to the higher energized excited state. It is known that a linear transition dipole will cause dimer, aggregation, or higher complexity. Such interactions always result in strong red shifts for the dimer, aggregate, and complex transition (13, 14). The absorption band of RB-PEI expands about 5 nm, and a strong red shift is observed in the comparative absorption bands of the RB alone. These spectral changes confirm the RB attaches to the polymer chain of PEI (15). These interactions lead to a decrease in absorbance at lower PEI concentrations and an increase in absorbance in higher PEI concentrations. This is clearly illustrated in the graph in Figure 1c showing the relative absorbance values based on the PEI concentrations. The change of the interaction of the resulting complex is clearly shown.

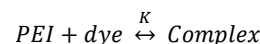
Determination of binding constant and evaluation of the quantities of binding.

Absorbance measurements were made for pure dye and PEI-dye mixture. For dye, A_{dye} refers to absorbance of RB dye alone; A refers to absorbance for the PEI- RB and the difference occurred in absorbance is calculated with the following formula:

$$A - A_{dye} = \Delta A = C_B (\epsilon_{complex} - \epsilon_{dye}) = C_B \Delta \epsilon \text{ (Eq.2)}$$

where C_B is the concentration of bound dye and $\Delta \epsilon$ is the change of the molar absorption coefficient of the bound dye or complex and the

free dye. The balance of complex formation between polymer and dye is shown as follows



where K is the binding constant. If the complex is considered to be composed of 1: 1

$$K = \frac{[complex]}{C_F [PEI]_{free}} = \frac{C_B}{C_F [PEI]_{free}} \text{ (Eq.3)}$$

where C_F refer to the free dye concentration. When the FEI is overdone, $[PEI]_{free} \sim [PEI]_{total}$ and represents $[PEI]_{total}$ as $[PEI]$ be simplified;

$$K = \frac{C_B}{C_F [PEI]} \text{ or } \frac{C_B}{C_F} = K [PEI] \text{ (Eq.4)}$$

The total dye concentration C_T is shown by

$$C_T = C_B + C_F \text{ (Eq.5)}$$

By dividing Eq.5 by Eq.2, we get the following:

$$\frac{C_T}{\Delta A} = \frac{C_B + C_F}{C_B \Delta \epsilon} \text{ (Eq.6)}$$

By simplifying Eq.6 with the replacement of the value of C_B / C_F from Eq.4 we have

$$\frac{C_T}{\Delta A} = \frac{1}{\Delta \epsilon} \left(1 + \frac{1}{K [PEI]} \right) \text{ (Eq.7)}$$

Eq. 7 is the linking of experimentally known or quantifiable amounts of ΔA to K and $\Delta \epsilon$ to the binding study (16). Figure 3 shown the plot of Eq.7 ($C_T/\Delta A$ vs $1 + 1/ K [PEI]$) for system. The experimental data were given in Table 1.

Table 1. Binding Constant and Extinction Coefficients for the PEI-Rose Bengal System

SYSTEM	$\epsilon_{dye} \times 10^5$ ($M^{-1} cm^{-1}$)	$\Delta \epsilon \times 10^5$ ($M^{-1} cm^{-1}$)	$\epsilon_{complex} \times 10^5$ ($M^{-1} cm^{-1}$)	$K \times 10^2$ (M^{-1})
PEI-RB	3.00	1.81	1.19	3.75

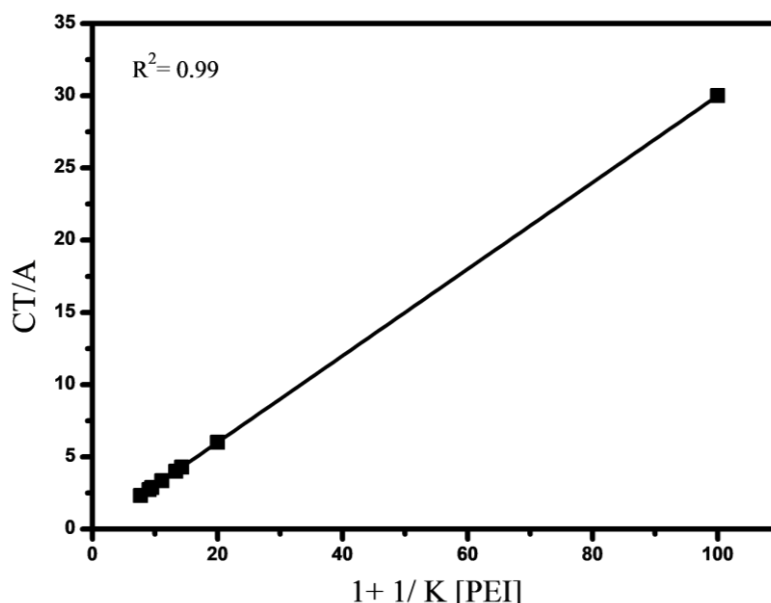
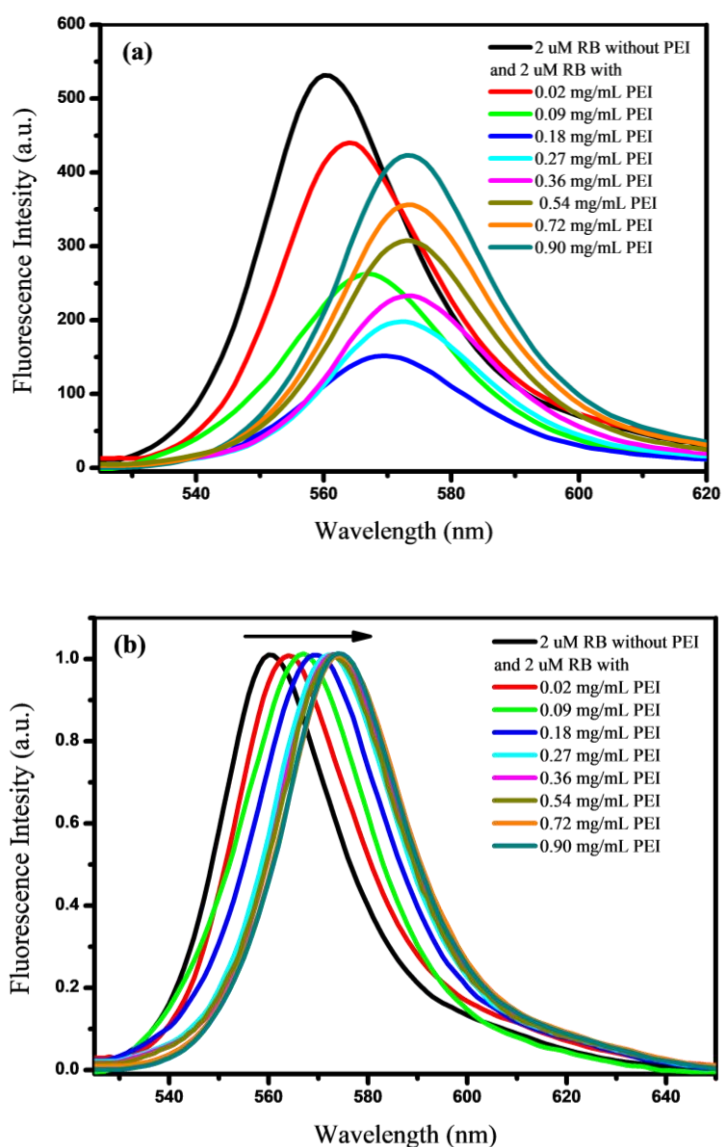


Figure 3. Plot of Eq. (6) for RB-PEI system.

Effects of PEI on the fluorescence spectra of RB

The fluorescence spectra of the RB (2.0 μM) in different PEI concentrations ranging from 0.02 to 0.90 mg/mL are shown in Figure 4. Figures 4a and b show the fluorescence spectra and normalized fluorescence spectra of the dye in a distilled water medium and at room temperature, respectively. PEI does not release any emissions during the absorbance. The fluorescence band of the RB in distilled water was monitored at 560 nm. This band was initially quenched by forming its complex structures depending on the PEI concentration. As the concentration of the PEI continued to increase, fluorescence began to increase. This is clearly shown in Figure 4c in the

graph of relative fluorescence values to the PEI concentration. The increased fluorescence of complex is an indication that the existing interaction converts the RB molecules to aggregates (17, 18). It is known that the formation of aggregate blocks non-radiative decay and increases the fluorescence of dye by intramolecular rotation in the phenyl rings (19, 20). In view of the emission spectra of the RB, the enhanced fluorescence resulting from the increase in the presence of PEI was proven to interact with the tendency of dye. The bands at longer wavelengths arise from the excimer emission of the interplayed aromatic units and aggregate (21, 22).



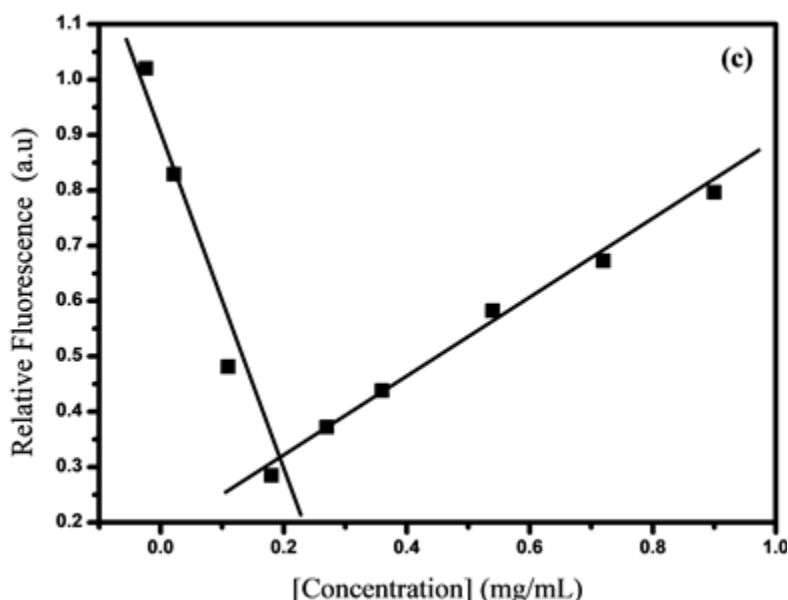


Figure 4. (a) Observed and (b) normalized fluorescence spectra of the RB with various concentrations of PEI in distilled water. (c) Relation between the relative fluorescence and the ratio of as a function of concentration of PEI.

Determination of photophysical parameters for PEI-RB system

The dye-polymer interaction resulted in the band shifting absorption. Similarly, the fluorescence spectra altered the fluorescence intensity of the RB and changed the fluorescence quantum yields (Φ_f) of the dye (Table 2). The data from Table 2 indicates that the quantum yield of RB decreases or increases depending on the fluorescence. Meanwhile, the fluorescence quantum efficiency varies greatly by the nature of the adhesion (23). The fluorescence lifetimes of the dye increased with the concentration of the polymer. The dye

molecules are more stable when they interact with the polymer and this increases the life time values due to the molecule spending more time on excited energy levels (24). The emission band maximum of the dye, which shifted from 560 to 574 nm, proves the formation of the π -stacked binding complex (25). The fluorescence lifetime of the dye is calculated and shown in Table 2. Fluorescence lifetime and fluorescence quantum yield are associated with the non-radiative (k_{nr}) and radiative (k_r) rate constants given in Equations 8 and 9 (26, 27).

Table 2. Photophysical parameters of RB in distilled water and PEI aqueous solutions.

[PEI] (mg/mL)	λ_{Abs} (nm)	λ_F (nm)	Φ_f ($\times 10^{-3}$)	τ_f (ns)	χ^2	k_r (s^{-1}) $\times 10^9$	k_{nr} (s^{-1}) $\times 10^9$	k_{nr} / k_r
Distilled water	550	560	18.0	0.095	1.2	18.95	10.34	54.5
0.02	552	563	19.0	0.123	1.1	15.45	7.975	51.6
0.09	557	566	17.0	0.185	1.0	9.19	5.313	57.8
0.18	563	569	12.0	0.222	1.0	5.40	4.450	82.3
0.27	564	571	16.0	0.246	1.0	6.50	4.000	61.5
0.36	564	573	18.0	0.338	1.1	5.32	2.905	54.6
0.54	565	573	20.0	0.371	1.2	5.39	2.641	49.0
0.72	565	573	22.0	0.413	1.2	5.33	2.368	44.4
0.90	566	574	23.0	0.455	1.1	5.05	2.147	42.5

$$K_r = \Phi_f / \tau_f \quad (\text{Eq.8})$$

$$K_{nr} = 1/\tau_f - k_r \quad (\text{Eq.9})$$

Using these equations, k_{nr}/k_r values were calculated for dye in the PEI solutions and distilled water. Table 2 shows that the k_{nr}/k_r values for dye were higher at PEI concentrations of 0.18 mg/mL. On the other hand, k_{nr}/k_r values are often above the average in similar systems. In addition, high k_{nr}/k_r values of RB show that the

main excited-state deactivation pathway is internal conversion (28).

CONCLUSION

In the present study, the effects of PEI on the photophysical properties of RB dye were examined using spectroscopic techniques. The interactions of the RB dye and PEI in distilled water caused differences in the photophysical and spectroscopic properties of the dyes. RB (2 μM) in

the presence of PEI displays strong red shifts and changes of absorption and emission band intensities when compared to that in distilled water, which are assigned to the dye-polymer interaction. The values of k_{nr}/k_r for the dye are calculated in the PEI media. The changing photophysical parameter values of the RB are due to the local micro viscosity and polarity variations as well as the probe surrounding interactions in this medium and dye interactions. Changing and limiting the photophysical properties of the dye with the concentration of the polymer will be beneficial tools used in optical studies.

ACKNOWLEDGEMENT

The general support by Atatürk University is gratefully acknowledged.

REFERENCES

1. Bayraktutan T, Onganer Y, Meral K. Polyelectrolyte-induced H-aggregation of Merocyanine 540 and its application in metal ions detection as a colorimetric sensor. *Sens. Actuators, B*. 2016;226:52-61.
2. Takagishi T, Yoshikawa K, Hamano H, Kuroki N, Kozuka H. Specific Interaction Between Polyethylenimine And Azo Dyes Carrying Hydroxyl-Groups. *J. Polym. Sci., Part A: Polym. Chem.*. 1985;23(1):37-47.
3. Kunath K, von Harpe A, Fischer D, Peterson H, Bickel U, Voigt K, et al. Low-molecular-weight polyethylenimine as a non-viral vector for DNA delivery: comparison of physicochemical properties, transfection efficiency and in vivo distribution with high-molecular-weight polyethylenimine. *J. Controlled Release*. 2003;89(1):113-25.
4. Bisset W, Jacobs H, Koshti N, Stark P, Gopalan A. Synthesis and metal ion complexation properties of a novel polyethyleneimine N-methylhydroxamic acid water soluble polymer. *React. Funct. Polym.* 2003;55(2):109-19.
5. Kobayashi S, Hiroishi K, Tokunoh M, Saegusa T. Chelating Properties Of Linear And Branched Poly(Ethylenimines). *Macromol.* 1987;20(7):1496-500.
6. Amara M, Kerdjoudj H. Modification of the cation exchange resin properties by impregnation in polyethyleneimine solutions - Application to the separation of metallic ions. *Talanta*. 2003;60(5):991-1001.
7. Neckers DC. Rose-Bengal. *J. Photochem. Photobiol., A* 1989;47(1):1-29.
8. Chang CC, Yang YT, Yang JC, Wu HD, Tsai T. Absorption and emission spectral shifts of rose bengal associated with DMPC liposomes. *Dyes Pigm.* 2008;79(2):170-
9. Bayraktutan T, Onganer Y. Biophysical influence of coumarin 35 on bovine serum albumin: Spectroscopic study. *Spectrochim. Acta, Part A*. 2017;171:90-6.
10. Toprak M, Arik M. An investigation of energy transfer between coumarin 35 and xanthene derivatives in liquid medium. *Turk. J. Chem.* 2010;34(2):285-93.
11. Atahan A, Orhan E. Photophysics, pH Sensing and Hydrolysis Study of a Novel 1,8-Naphthalimide Derivative. *J. Turk. Chem. Soc., Sect. A: Chem.* 2018;5(2):775-784.
12. Kubin RF, Fletcher AN. Fluorescence Quantum Yields Of Some Rhodamine Dyes. *J. Lumin.* 1982;27(4):455-62.
13. Vaitekonis S, Trinkunas G, Valkunas L. Red chlorophylls in the exciton model of photosystem I. *Photosynth. Res.* 2005;86(1-2):185-201.
14. Gungor O, Durmus M, Ahsen V. Investigation of photochemical and photophysical properties of novel silicon(IV) phthalocyanines and their mu-oxo dimers. *Turk. J. Chem.* 2017;41(6):803-8.
15. Moczek L, Nowakowska M. Novel water-soluble photosensitizers from chitosan. *Biomacromol.* 2007;8(2):433-8.
16. Maruthamuthu M, Reddy JV. Binding Of Fluoride Onto Poly(N-Vinyl-2-Pyrrolidone). *J. Polym. Sci., Part C: Polym. Lett.* 1984;22(10):569-73.
17. Hong YN, Lam JWY, Tang BZ. Aggregation-induced emission. *Chem. Soc. Rev.* 2011;40(11):5361-88.
18. Güzel E. Preparation and investigation of aggregation, fluorescence and singlet oxygen generation properties of gallium and metal-free phthalocyanines. *J. Turk. Chem. Soc., Sect. A: Chem.* 2019;5(3):1051-60.
19. Wu WC, Chen CY, Tian YQ, Jang SH, Hong YN, Liu Y, et al. Enhancement of Aggregation-Induced Emission in Dye-Encapsulating Polymeric Micelles for Bioimaging. *Adv. Funct. Mater.* 2010;20(9):1413-23.
20. Chen JW, Law CCW, Lam JWY, Dong YP, Lo SMF, Williams ID, et al. Synthesis, light emission, nanoaggregation, and restricted intramolecular rotation of 1,1-substituted 2,3,4,5-tetraphenylsiloles. *Chem. Mater.* 2003;15(7):1535-46.
21. Block MAB, Hecht S. Poly(propylene oxide)-poly(phenylene ethynylene) block and graft copolymers. *Macromol.* 2008;41(9):3219-27.

22. Wehry EL. Principles Of Fluorescence Spectroscopy - Lakowicz, JR. Am. Sci. 1984;72(4):395-6.
23. Lepecq JB. Citation Classic - A Fluorescent Complex Between Ethidium-Bromide And Nucleic-Acids - Physical-Chemical Characterization. Current Contents/Life Sci. 1984(35):16-20.
24. Datta A, Mandal D, Pal SK, Bhattacharyya K. Intramolecular charge transfer processes in confined systems. Nile red in reverse micelles. J. Phys. Chem. B. 1997;101(49):10221-5.
25. Ozcelik S, Atay NZ. Optical transition rates of a meso-substituted thiocarbocyanine in methanol-in-oil reverse micelles (vol 113, pg 1, 2005). J. Lumin. 2005;114(3-4):314-8.
26. Thomas SW, Joly GD, Swager TM. Chemical sensors based on amplifying fluorescent conjugated polymers. Chem. Rev. 2007;107(4):1339-86.
27. Gur B, Meral K. The effect of poly(vinyl alcohol) on the photophysical properties of pyronin dyes in aqueous solution: A spectroscopic study. Spectrochim. Acta, Part A. 2013;101:306-13.
28. Bayraktutan T, Meral K, Onganer Y. Photophysical properties of pyronin dyes in reverse micelles of AOT. J. Lumin. 2014;145:925-9.



Synthesis and photophysical properties of a non-symmetrically substituted phthalocyanine-pyrene conjugate

Hande Pekbelgin Karaoğlu*, Ayfer Kalkan Burat

Istanbul Technical University, Department of Chemistry, TR34469, İstanbul, Turkey.

Abstract: An unsymmetrical zinc phthalocyanine (ZnPc) (**5**) bearing one pyrene (Py) and six *tert*-butylphenoxy units was synthesized in 3 steps. The unsymmetrical zinc phthalocyanine carrying the protecting group was synthesized in the first step. In the second stage, the protecting group was removed and in the final stage pyrene structure was introduced with the Sonagashira coupling reaction. The new compound was characterized by using spectroscopic techniques. The photophysical measurements of the conjugated structure were performed to determine the effect of the pyrene group on the fluorescence of Pc. It was determined that the absorption of the pyrene structure around 350 nm was overlapping with the B-band of phthalocyanine after conjugation. Fluorescence quantum yield (Φ_F) and lifetime (τ_F) were calculated. The fluorescence quenching examinations were performed by adding the different concentration of 1,4-benzoquinone (BQ) in *N,N*-dimethylformamide (DMF) and the Stern-Volmer constant (K_{sv}) and quenching constant (k_q) values of unsymmetrical zinc phthalocyanine (**5**) were determined.

Keywords: Zinc, pyrene, phthalocyanine, fluorescence, characterization.

Submitted: May 30, 2019. **Accepted:** July 16, 2019.

Cite this: Pekbelgin Karaoğlu H, Kalkan Burat A. Synthesis and photophysical properties of a non-symmetrically substituted phthalocyanine-pyrene conjugate. JOTCSA. 2019;6(3):319–28.

DOI: <https://doi.org/10.18596/jotcsa.572013>.

***Corresponding author.** E-mail: pekbelgin@itu.edu.tr.

INTRODUCTION

Phthalocyanines (Pcs) have 18 π -electron system and they are disc-like aromatic macrocycles. Due to the π -electron delocalization over the molecule, they have unique photophysical, photochemical, redox, and coordination properties, and high chemical and thermal stability (1). The properties of Pcs depend on both the electronic properties of the central metal cations and the nature of substituents. It is advantageous to substitute the functional groups at the peripheral or non-peripheral positions of the Pcs, since they provide solubility and it also tunes the color of the material. Substitution of functional groups also changes the electron density of the phthalocyanines and allows the use in various fields such as solar cells, sensors, liquid crystals, and nonlinear optics (2-6).

Although Pcs display good chemical and photochemical properties, their fluorescence properties are poor (7). Large central metals reduce the fluorescence by enhancement of the

intersystem crossing to the triple state, hence restricting the applications of phthalocyanines in imaging (8). The fluorescence properties of the aromatic structure may alter by the interaction of a Pc core with a fluorescent probe like pyrene group. The chemical or physical binding of the fluorescent probe to the Pc causes a shift in the spectrum or a change in intensity (9).

It is well known that pyrene (Py) has a high quantum yield of fluorescence and a relatively long lifetime of singlet excited state (10). Pyrene is one of the most popular fluorescent chromophores used for photochemical applications. Pyrene derivatives with high quantum yields and lifetime, and are also valuable molecular probes for fluorescence spectroscopy (0.65 and 410 ns, respectively, in ethanol at 293 K) (11). In addition, pyrene and its derivatives have often been used as anchor groups to facilitate electron transfer into the acceptor domains (12).

Phthalocyanine-pyrene (Pc-Py) conjugates appear to be promising candidates for solar cells, sensors, nonlinear optical and photovoltaic applications because of their photophysical and photochemical properties (13-16). According to the literature, the presence of pyrene groups in the structure of phthalocyanine improves the π - π interaction between the Pc-Py and single-wall carbon nanotubes (SWCNT). Non-covalent functionalization of single-wall carbon nanotubes (SWNTs) with Pc-Py molecules were accomplished by Torres *et al.* to form stable hybrids (17). Durmus and coworkers synthesized hybrids of SWNT with phthalocyanines bearing one pyrene unit and studied their sensory response to ammonia vapor (18). They reported that the pyrene units and its derivatives display a strong affinity towards sp^2 -nanocarbon networks (19, 20). In another study, tri- and tetra-pyrene substituted indium phthalocyanines (InPcs) with strong triplet absorption and high triplet yields were investigated for the third- and second-order nonlinearities by Nykong *et al.* (15).

From the point of view, the aim of this study is to synthesize pyrenyl substituted unsymmetrical zinc phthalocyanine for the preparation of light-harvesting antennae. Although there are symmetrically or unsymmetrically substituted phthalocyanine-pyrene conjugated structures in the literature (21-24), unsymmetrically substituted zinc phthalocyanine in which the pyrenyl group was bound to the phthalocyanine ring, was synthesized for the first time. The photophysical properties of this new compound was investigated by fluorescence measurements.

EXPERIMENTAL SECTION

Materials and methods

All reported ^1H -NMR spectra were recorded on an Agilent VNMRS 500 MHz spectrometer. Fluorescence and UV-Vis spectra were obtained using Perkin-Elmer LS55 fluorescence and Scinco LabProPlus UV/Vis spectrophotometers. FTIR spectra of the compounds were recorded on a Perkin-Elmer Spectrum One FTIR spectrometer. Mass spectra were measured on a Bruker Microflex LT MALDI-TOF MS spectrometer. The isotopic patterns for all assigned signals are in agreement with the calculated natural abundance. 4,5-Bis-(4-tert-butylphenoxy)phthalonitrile (**1**), 4-(3-hydroxy-3-methyl-1-butynyl)phthalonitrile (**2**), 2,3,9,10,16,17-hexakis(tert-butylphenoxy)-23-(3-hydroxy-3-methyl-1-butynyl)phthalocyaninato zinc(II) (**3**) and 2,3,9,10,16,17-hexakis(tert-butylphenoxy)-23-(ethynyl)phthalocyaninato zinc(II) (**4**) were prepared according to reported procedures (25-27).

Preparation

Synthesis of 2,3,9,10,16,17-Hexakis(tert-butylphenoxy)-23-(pyrenyl)phthalocyaninato

zinc(II) (5): 100 mg of compound **4** (0.07 mmol) was dissolved in 10 mL of dry tetrahydrofuran (THF)/trimethylamine (1:1) mixture and then 40 mg of 1-bromopyrene (0.13 mmol), 3 mg of bis(triphenylphosphine)palladium(II) chloride (0.004 mmol), and a catalytic amount of copper(I) iodide (1 mmol, 0.1 mg) were added to this solution. The reaction mixture was heated to 60 °C for 24 h under nitrogen (N_2) atmosphere. Once the ethynyl derivative is consumed, monitored by TLC, the mixture was filtered over celite and the solvent was removed under vacuum. The green product was purified by column chromatography on silica gel using first hexane/dioxane (3:1) and then dichloromethane (DCM)/methanol (MeOH) (50:1) as eluents. Solubility: Soluble in THF, CH_2Cl_2 , DMF, and DMSO. Yield: 0.026 g, (24 %). FT-IR ($\nu_{\text{max}}/\text{cm}^{-1}$): 3039 (Ar-C-H), 2957-2869 (Aliph. -C-H), 2206 ($\text{C}\equiv\text{C}$), 1506 (Ar-C=C), 1173 (Ar-O-Ar), 1087 (Ar-O-Ar). UV-Vis λ_{max} (nm) THF: 269, 356, 683; DMF: 267, 365, 684. ^1H -NMR (500 MHz, CDCl_3): δ , ppm 7.65-7.33 (42 H, m, Ar-H) 1.30 (54 H, s, CH_3). Anal. Calc. for $\text{C}_{110}\text{H}_{96}\text{N}_8\text{O}_6\text{Zn}$ (1689.68 g/mol) %: C, 78.11; H, 5.72; N, 6.63 Found: C, 78.12; H, 5.69; N, 6.56. MS (MALDI-TOF): m/z 1689.66 $[\text{M}]^+$.

Photophysical parameters

Fluorescence quantum yields and lifetimes:

The comparative method was used to determine the fluorescence quantum yields (Φ_F) according to the Eq. (1) below (28, 29), utilizing non-substituted ZnPc in DMF as the standard ($\Phi_F = 0.17$) (28, 29):

$$\Phi_F = \Phi_F(\text{Std}) \frac{F_{\text{AStd}} \eta^2}{F_{\text{Std}} A \eta_{\text{Std}}^2} \quad (\text{Eq. 1})$$

where F and F_{Std} are the areas under the fluorescence emission curves of the phthalocyanine (**5**) and the standard, respectively. A_{Std} and A are the respective absorbances at the excitation of standard and **5**, η_{Std} and η are the refractive index of solvent ($\eta_{\text{DMF}} = 1.496$) used for the standard and sample.

The fluorescence lifetime (τ_F), which is the average time of the molecule at the excited state before fluorescing, was found using the PhotochemCAD program and the Strickler-Berg equation. The fluorescence quantum yield (Φ_F) and the fluorescence lifetime (τ_F) value are directly proportional. The natural radiative lifetime (τ_0) was calculated with Eq. (2) (28, 29):

$$\Phi_F = \tau_F / \tau_0 \quad (\text{Eq. 2})$$

Fluorescence quenching by 1,4-benzoquinone:

Fluorescence quenching experiments were carried out in DMF with the addition of BQ solutions ranging from 0 to 0.040 M into the ZnPc solution. With the addition of BQ, an energy

transfer takes place between the excited ZnPc (fluorophore) and the BQ (quencher). The fluorescence spectra of ZnPc were recorded each time after the addition of different concentration of BQ. Changes in fluorescence intensity due to BQ concentration were consistent with the kinetic mechanism of the Stern-Volmer (SV) equation (Eq 3) (30):

$$\frac{I_0}{I} = 1 + K_{SV}[BQ] \quad (\text{Eq. 3})$$

where I_0 and I are the fluorescence intensities of fluorophore in the absence and presence of quencher, respectively. $[BQ]$ is the concentration of the quencher and K_{SV} is the Stern-Volmer constant. K_{SV} is the product of the bimolecular quenching constant (k_q) and the τ_F , and is shown in Eq. (4) (31):

$$K_{SV} = k_q \times \tau_F \quad (\text{Eq. 4})$$

The ratios of I_0/I were calculated and plotted against $[BQ]$ according to Eq. (4), and K_{SV} is determined from the slope.

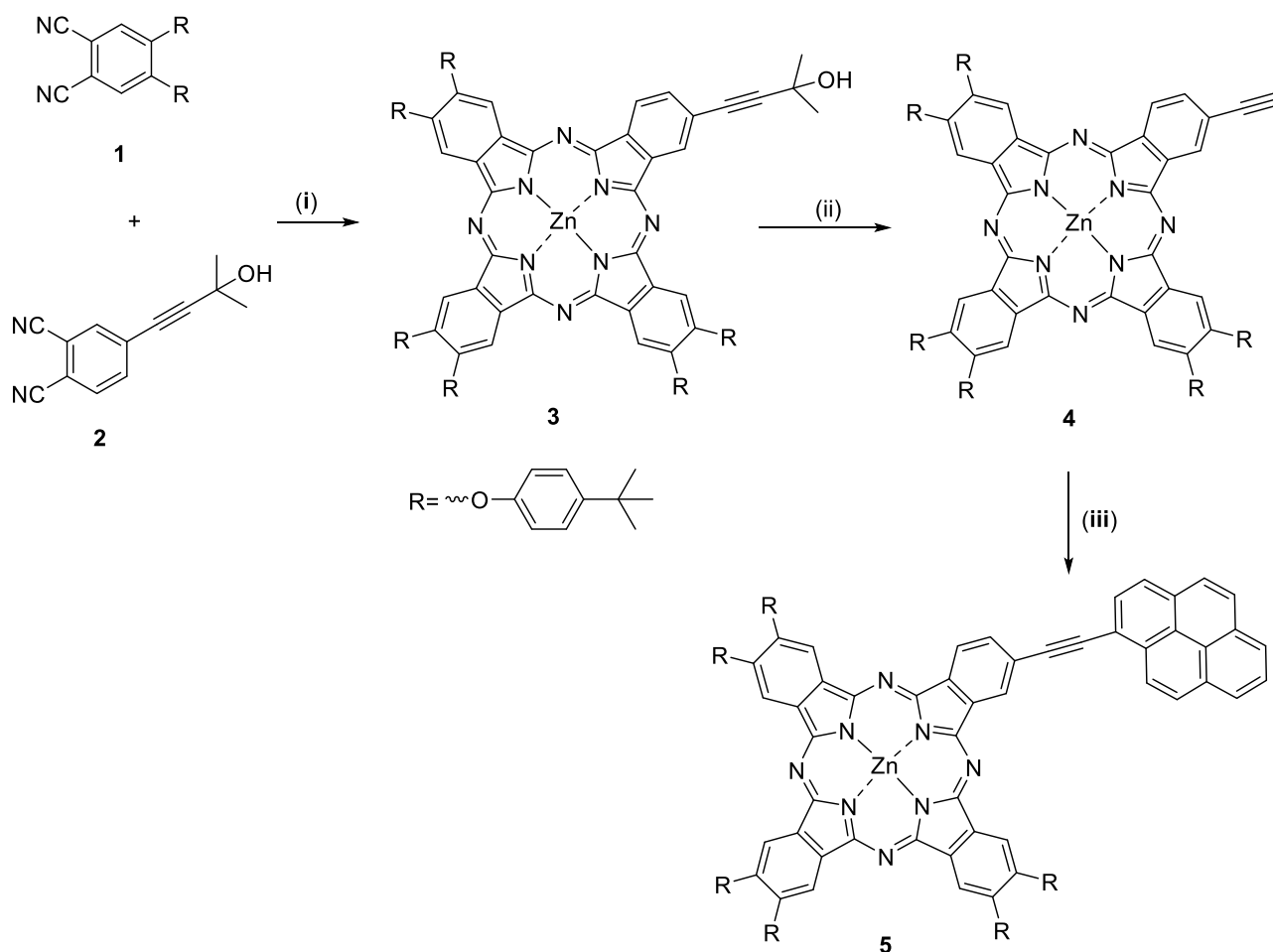
RESULTS AND DISCUSSION

Synthesis and spectroscopic characterization

There are three methods for the preparation of unsymmetrically substituted Pcs. These include a statistical condensation of two different phthalonitriles (32-34), a polymeric support method (35, 36) and a ring-expansion of sub-phthalocyanine (SubPc) (37, 38). Sub-Pcs undergo ring expansion when reacted with diaminoisindoline or its analogues, resulting in the A_3B type phthalocyanines. Although ring expansion reaction is highly selective and the A_3B phthalocyanine is the major product, this only applies to limited phthalonitriles. It is because the ring expansion reaction is dependent on the experimental conditions and the electronic properties of the reactants (39-42). Despite the variety of commercially available polymeric supports, phthalonitriles having a functional

group that can bind to the polymer and then be separated under acidic or alkaline conditions is limited. Therefore, the synthesis of A_3B type phthalocyanines by the polymeric support route is restricted (43, 44). Since the starting materials used in this study do not have a functional group that can bind to the polymer, the statistical condensation method is preferred. If the reactivities of the two phthalonitrile involved in the condensation are similar, the symmetrical A_4 type Pc (33%), the asymmetrical A_3B type Pc (44%) and the remaining Pcs (23%) can be obtained using a 3 : 1 (A:B) ratio. In this method, the use of phthalonitriles with different solubility properties will facilitate purification of the targeted asymmetric phthalocyanine.

Phthalonitrile **1** and phthalonitrile **2** were used as starting materials. Compound **1** was synthesized from the reaction of 4-tert-butylphenol with 4,5-dichlorophthalonitrile in dimethyl sulfoxide (DMSO). The reaction was completed at 90 °C for 4 hours and potassium carbonate (K_2CO_3) was used as the base (25). Nitrile **2** was prepared by the reaction of 2-methylbut-3-yn-2-ol with 4-iodophthalonitrile under typical Sonogashira reaction conditions (26, 45). The mixed condensation of phthalonitrile precursors **1** and **2** with zinc chloride ($ZnCl_2$) in 2-dimethylaminoethanol (DMAE) at 145 °C afforded the corresponding zinc phthalocyanine (**3**) (Scheme 1). The desired phthalocyanine (**3**) was purified by column chromatography. The dioxane:hexane (1:3) mixture was used as the eluent on silica gel and the compound was obtained in moderate yield (14%) (27). The protecting group was then removed by treatment with sodium hydroxide in toluene to give the ethynyl derivative (**4**) (27). The resulting crude product was purified by column chromatography on silica gel by using dioxane:hexane (1:5) as eluent. Phthalocyanine **4** was obtained as green solid in a 69% yield. The Sonogashira coupling reaction between compound **4** and 1-bromopyrene in THF/trimethylamine with bis(triphenylphosphine)palladium(II)chloride and copper(I)iodide as catalyst at 60 °C under N_2 atmosphere led to the formation of **5** in 24% yield.



Scheme 1. Synthetic route to unsymmetrical ZnPc (**5**) (i) ZnCl_2 , DMAE, 24 h, reflux. (ii) NaOH, toluene, reflux, 6h. (iii) 1-Bromopyrene, $\text{Pd}(\text{PPh}_3)_2\text{Cl}_2$, CuI, THF, Triethylamine, 60 °C, 24h.

The spectroscopic characterization of the newly synthesized compound (**5**) included ^1H NMR, IR, mass and UV-Vis. In the FT-IR spectrum of compound **5**, aromatic CH, aliphatic CH, $\text{C}\equiv\text{C}$ and $\text{C}-\text{O}-\text{C}$ vibrations were observed at 3039, 2957–2869, 2206 and 1266–1212 cm^{-1} , respectively. In the ^1H NMR spectrum of **5**, the aromatic protons were observed between 7.65–7.33 ppm as multiplet in CDCl_3 . The aliphatic CH_3 protons were resonated at 1.30 ppm as singlet. In the mass spectrum of compound **5**, the presence of the characteristic molecular ion peak at $m/z = 1689.66$ $[\text{M}]^+$ confirmed the proposed structure.

In the UV spectra of compounds ZnPc (**4**) and ZnPc-Py (**5**) in DMF, the B bands and Q bands

were detected at 354 (**4**), 356 (**5**) and 678 (**4**), 683 (**5**) nm, respectively (**Figure 1**). Two absorption peaks were observed at 267 and 346 nm in the spectrum of pyrene in DMF (**Figure 1**). The Q band of ZnPc (**5**) slightly red shifted (5 nm) after coordination with Py. The reason for this shift is the extended π conjugation of phthalocyanine structure (23). After the conjugation, the B band of ZnPc-Py (**5**) was almost as intense as its Q band because of the pyrene absorption in the B band region (21, 22). As seen in the literature, the Soret band of phthalocyanine (**5**) overlaps with the absorption of pyrene unit at around 346 nm (21-23).

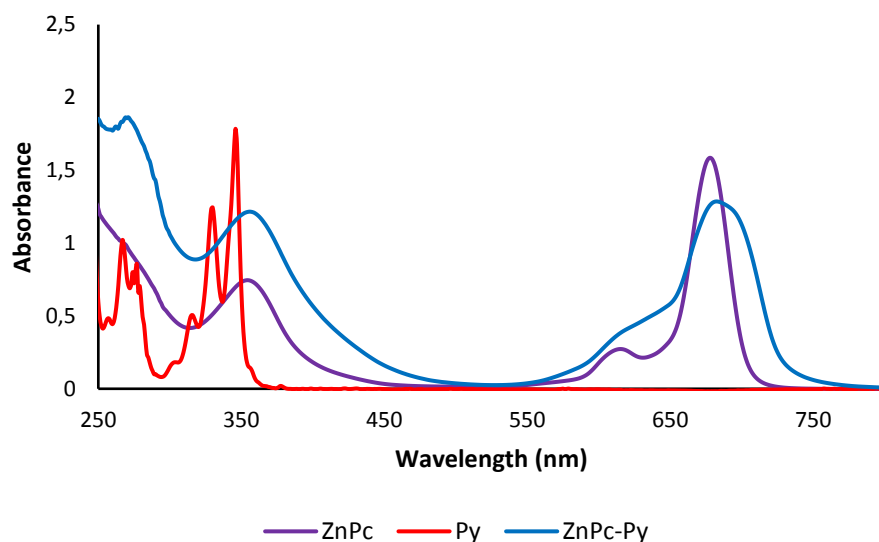


Figure 1. UV/Vis spectra of ZnPc (**4**), ZnPc-Py (**5**) and pyrene (Py) in DMF (6×10^{-5} M)

The fluorescence measurements and fluorescence quenching studies of **5** were performed in DMF upon excitation at 615 nm. The fluorescence emission, excitation, and absorption spectra of **5** were shown in Figure 2. Fluorescence emission peak of **5** was detected at 705 nm and Stokes' shifts was evaluated as 27 nm. The observed Stokes' shift was within the region ~ 20 -30 nm as

typical for Pc complexes (46). The excitation spectrum was similar to absorption spectrum and both were mirror images of the fluorescent spectra for **5** in DMF. This shows that the nuclear configurations of the ground and excited states are similar and not affected by excitation (28, 29).

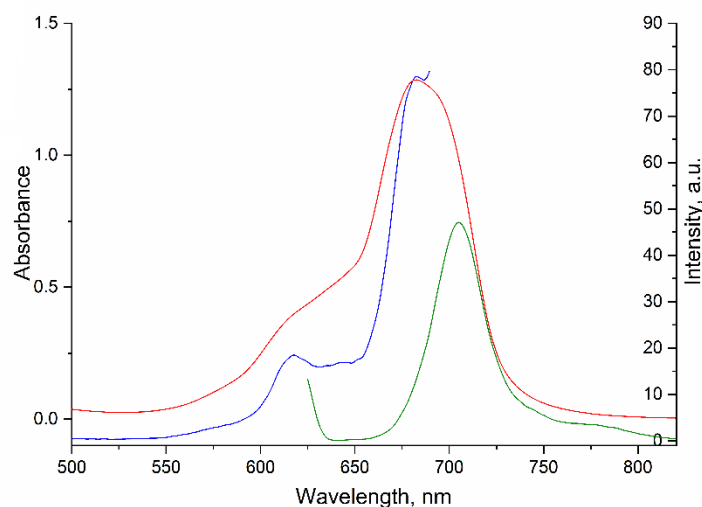


Figure 2. Absorption (red), excitation (blue) and emission (green) spectra of **5** in DMF (4×10^{-6} M)

The fluorescence quantum yield (Φ_F) of compound **5** was calculated as 0.173 which is very close to the Φ_F value of the ZnPc used as reference. According to the literature, the insertion of a diamagnetic central metal is known to increase the fluorescence quantum yield (Φ_F) (47). For standard ZnPc the Φ_F value is known to be 0.17 in DMF (28, 29).

According to the literature, Özçeşmeci and coworkers synthesized phthalocyanines bearing four pyrene units and studied their photophysical properties (21). In another study performed by Sürgün et al., pyrenyl substituted phthalocyanine synthesis and photophysical measurements were

performed (22). In these studies where the pyrene groups were not conjugated to the phthalocyanine ring, the fluorescence quantum yields measured for ZnPc's were close to the value of the standard ZnPc. ZnPc-Py conjugate structure was accomplished by Ogobodu and coworkers (23). They reported that the fluorescence quantum yield of the pyrene substituted unsymmetrical ZnPc was close to the reference yield. In this study, we extend the conjugation of the Pc by adding a pyrenyl group and the fluorescence quantum yield of **5**, was found to be very close to the value in the literature.

The natural radiative lifetime (τ_0) value was calculated as 13.07 ns and the fluorescence lifetime (k_F) value was 2.26 ns. For the unsubstituted ZnPc, the τ_0 and k_F values are 6.05

ns and 1.03 ns, respectively. It was observed that the natural radiative lifetime and the fluorescence lifetime values for **5** were higher than non-substituted ZnPc in DMF.

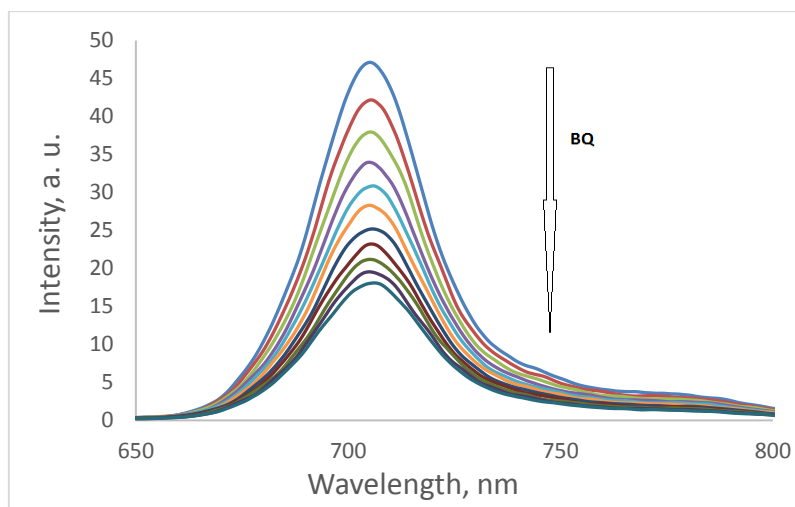


Figure 3. Fluorescent emission spectral changes of **5** (4×10^{-6} M) in DMF in which different concentrations of hydroquinone in DMF were added as quencher. [BQ] = 0.000, 0.008, 0.016, 0.024, 0.032, 0.040 M

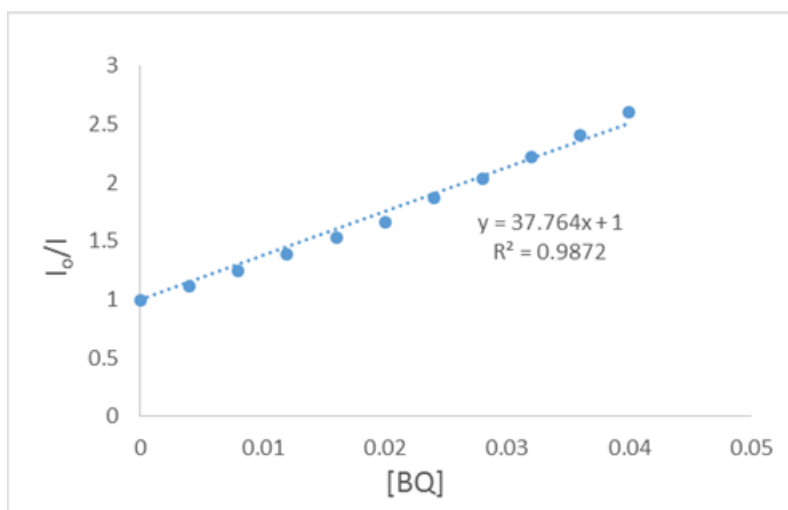


Figure 4. Stern-Volmer plot of **5** for BQ ([BQ] = 0.000, 0.008, 0.016, 0.024, 0.032, 0.040 M)

The fluorescence quenching of the compound **5** by benzoquinone (BQ) in DMF was found to obey Stern-Volmer kinetics, which is consistent with diffusion-controlled bimolecular reactions. The emission spectrum of **5** with the addition of varying concentrations of BQ is shown in **Figure 3**. As the concentration of BQ increases, the intensity of **5** decreases in parallel to the increasing concentration of BQ. The slope of the graph studied for equation 3 is linear, indicating that the diffusion controlled quenching mechanisms. The K_{SV} value from the slope of the graph was found to be 37.76 M^{-1} (**Figure 4**) (28, 29). k_q is the bimolecular quenching constant of **5** in DMF for BQ quenching and the value for **5** is $1.67 \times 10^{10} \text{ s}^{-1}$. The K_{SV} and k_q values of compound **5** are smaller than unsubstituted ZnPc ($K_{SV} = 57.60 \text{ M}^{-1}$, $k_q = 5.59 \times 10^{10} \text{ s}^{-1}$).

CONCLUSION

In the present work, pyrene and *tert*-butylphenoxy substituted unsymmetrical zinc phthalocyanine was synthesized and characterized by various spectroscopic methods and confirmed the proposed structure. The overlap of the Soret band of Py caused an increase in the intensity of B band of compound **5** after conjugation. The slight red shifting of Q band of Pc was also determined after Pc-Py conjugation. The photophysical properties of Pc-Py (**5**) conjugate was investigated and compared with an unsubstituted ZnPc. The fluorescence quantum yield of compound **5** is close to unsubstituted ZnPc, while its lifetime is higher than that of

unsubstituted ZnPc. In addition, the fluorescence quantum yield of compound **5** was compared with the fluorescence quantum yield of other tetrasubstituted ZnPc substituted with pyrene groups in the literature (21-23). The fluorescence quantum yield of **5** is in agreement with the literature values. Furthermore, the fluorescence quenching studies were performed by benzoquinone typically. The Stern-Volmer kinetics were also investigated in DMF. In comparison with unsubstituted zinc phthalocyanine, compound **5** showed lower K_{SV} and k_q values.

ACKNOWLEDGEMENTS

This work was supported by the Research Fund of the Istanbul Technical University.

REFERENCES

- Schmid G, Sommerauer M, Geyer M, Hanack M, Leznoff CC. A.B.P. Lever (Eds.), Phthalocyanines: Properties and Applications, vol. 4, VCH Publishers, New York, 1996, pp. 1-18.
- Basova TV., Parkhomenko RG, Polyakov M, Gürek AG, Atilla D, Yuksel F, et al. Effect of dispersion of gold nanoparticles on the properties and alignment of liquid crystalline copper phthalocyanine films. *Dye Pigment*. 2016; 125: 266-73.
- Çimen Y, Ermiş E, Dumludağ F, Özkaya AR, Salih B, Bekaroğlu Ö. Synthesis, characterization, electrochemistry and VOC sensing properties of novel ball-type dinuclear metallophthalocyanines. *Sensors Actuators, B Chem*. 2014; 202: 1137-47.
- Nagel S, Lener M, Keil C, Gerdes R, Lapok L, Gorun SM, Schlettwein D. Electrochromic Switching of Evaporated Thin Films of Bulky, Electronic Deficient Metallo-Phthalocyanines. *J Phys Chem C*. 2011; 115: 8759-8767.
- Maya EM, Garcia-Frutos EM, Vazquez P, Torres T, Martin G, Rojo G, Agullo-Lopez F, Gonzalez-Jonte RH, Ferro VR, Vega JMG, Ledoux I, Zyss J. Novel Push-Pull Phthalocyanines as Targets for Second-Order Nonlinear Applications. *J Phys Chem A*. 2003; 107: 2110-2117.
- Walter MG, Rudine AB, Wamser CC. Porphyrins and phthalocyanines in solar photovoltaic cells. *J Porphyrins Phthalocyanines*. 2010; 14: 759-792.
- Liu MO, Tai CH, Teh Hu A. The fluorescent and photoelectric conversion properties of phthalocyanineeperylene tetracarboxylic complexes. *J Photochem Photobiol A*. 2004; 165: 193-200.
- Nyokong T, Antunes E. in *The Handbook of Porphyrin Science*, ed. Kadish KM, Smith KM and Guillard R. World Scientific. Singapore, 2010, ch. 34, vol 7.
- Frahn MS, Abellon RD, Jager WF, Luthjens LH, Warman JM. Synthesis and characterization of a new fluorogenic probe molecule N-(1-pyrene)methacrylamide for monitoring radiation-induced polymerization. *Nucl Instrum Methods Phys Res. Sect B*. 2001; 185: 241-47.
- Lerner MG, Reszczenski JM, Amin A, Johnson RR, Goldsmith JI, Johnson ATC. Toward quantifying the electrostatic transduction mechanism in carbon nanotube molecular sensors. *J Am Chem Soc*. 2012; 134: 14318.
- Valeur B. *Molecular fluorescence principles and applications*. Germany, Weinheim: Wiley-VCH; 2002.
- Karabacak M, Cinar M, Kurt M, Sundaraganesan N. Experimental and theoretical FTIR and FT-Raman spectroscopic analysis of 1-pyrenecarboxylic acid. *Spectrochim Acta Part A: Mol Biomol Spectrosc*. 2013; 114: 509-519.
- Roth A, Ragoussi ME, Wibmer L, Katsukis G, Torre G, Torres T, Guldi DM. Electron-accepting phthalocyanine-pyrene conjugates: towards liquid phase exfoliation of graphite and photoactive nanohybrid formation with graphene. *Chem Sci*. 2014; 5: 3432-3438.
- Kaya EN, Tuncel S, Basova TV, Banimuslem H, Hassan A, Gürek AG, Ahsen V, Durmuş M. Effect of pyrene substitution on the formation and sensor properties of phthalocyanine-single walled carbon nanotube hybrids. *Sensors and Actuators B*. 2014; 199: 277-283.
- Sanusi K, Nyokong T. Effects of pyrene on the photophysical and two-photon absorption-based nonlinear optical properties of indium(III) phthalocyanines. *Journal of Coordination Chemistry*. 2014; 67: 2911-2924.
- Kumar RS, Son YA. Synthesis, photophysical and aggregation properties of novel phenanthrene and pyrene substituted phthalocyanines. *Korean Chem Eng Res*. 2018; 56(6): 792-797.
- Bartelmess J, Ballesteros B, Torre G, Kiessling D, Campidelli S, Prato M, Torres T, Guldi DM. Phthalocyanine-pyrene conjugates: A powerful approach toward carbon nanotube solar cells. *J Am Chem Soc*. 2010; 132: 16202-16211.
- Kaya EN, Basova TV, Polyakov M, Durmuş M, Kadem B, Hassan A. Hybrid materials of pyrene substituted phthalocyanines with single-walled carbon nanotubes: structure and sensing properties. *RSC Adv*. 2015; 5: 91855-91862.

19. Su Q, Pang S, Alijani V, Li C, Feng X, Müllen K. Composites of graphene with large aromatic molecules. *Adv Mater.* 2009; 21: 3191-3195.
20. Mann JA, Rodriguez-Lopez J, Abruna HD, Dichtel WR. Multivalent binding motifs for the noncovalent functionalization of graphene. *J Am Chem Soc.* 2011; 133: 17614-17617.
21. Özçeşmeci İ, Gelir A, Gül A. Synthesis and photophysical properties phthalocyaninepyrene dyads. *Dye Pigment.* 2012; 92: 954-960.
22. Sürgün S, Arslanoğlu Y, Hamuryudan E. Synthesis of non-peripherally and peripherally substituted zinc (II) phthalocyanines bearing pyrene groups via different routes and their photophysical properties. *Dye Pigment.* 2014; 100: 32-40.
23. Ogbodu RO, Antunes E, Nyokong T. Physicochemical properties of a zinc phthalocyanine – pyrene conjugate adsorbed onto single walled carbon nanotubes. *Dalton Trans.* 2013; 42: 10769-10777.
24. Ke L, Min J, Adam M, Gasparini N, Hou Y, Perea JD, Chen W, Zhang H, Fladischer S, Sale , Erdmann Spiecker AC, Tykwinski RR, Brabec CJ, Ameri T. A series of pyrene-substituted silicon phthalocyanines as near-ir sensitizers in organic ternary solar cells. *Adv Energy Mater.* 2016; 6 (1502355): 1-13.
25. Maree SE, Nyokong T. Syntheses and photochemical properties of octasubstituted phthalocyaninato zinc complexes. *J Porphyrins Phthalocyanines.* 2001; 5: 782-792.
26. Maya EM, Vazquez P, Torres T. Homo- and hetero-dimetallic ethynyl- and butadiynyl-bridged bisphthalocyaninato complexes. *Chem Commun.* 1997; 1175-76.
27. Garcia-Iglesias M, Torres T, Gonzalez-Rodriguez D. Well-defined, persistent, chiral phthalocyanine nanoclusters via G-quadruplex assembly. *Chem Commun.* 2016; 52: 9446-9449.
28. Karaoğlu HRP, Yenilmez HY, Koçak MB. Phthalocyanines formed from several precursors: synthesis, characterization, and comparative fluorescence and quinone quenching. *Journal of Coordination Chemistry.* 2018; 71(15): 2340-2357.
29. Zorlu Y, Dumoulin F, Durmuş M, Ahsen V. Comparative studies of photophysical and photochemical properties of solketal substituted platinum (II) and zinc (II) phthalocyanine sets. *Tetrahedron.* 2010; 66 (17): 3248-3258.
30. Du H, Fuh RCA, Li J, Corkan LA, Lindsey JS. PhotochemCAD: A Computer-Aided Design and Research Tool in Photochemistry. *Photochem. Photobiol.* 1998; 68: 141-142.
31. Rose J. *Advanced Physico-chemical Experiments*, first ed., Sir Isaac Pitman & Sons Ltd., London, 1964, 257.
32. Kalkan A, Koca A, Bayır ZA. Unsymmetrical phthalocyanines with alkynyl substituents. *Polyhedron.* 2004; 23: 3155-3162.
33. Haas M, Liu SX, Kahnt A, Leiggener C, Guldi DM, Hauser A, Decurtins S. Photoinduced energy transfer processes within dyads of metallophthalocyanines compactly fused to a ruthenium(II) polypyridine chromophore. *J Org Chem.* 2007; 72: 7533-7543.
34. Kimura T, Kanota N, Matsui K, Tanaka I, Tsuboi T, Takaguchi Y, Yomogita A, Wakahara T, Kuwahara S, Nagatsugi F, Akasaka T. Preparation and electrochemical and optical properties of unsymmetrically substituted phthalocyanines with one or two trithiole rings and related symmetric derivatives. *Inorg Chem.* 2008; 47: 3577-3583.
35. Leznoff CC, Hall TW. The synthesis of a soluble, unsymmetrical phthalocyanine on a polymer support. *Tetrahedron Lett.* 1982; 23: 3023-3026.
36. Erdem SS, Nesterova IV, Soper SA, Hammer RP. Solid-phase synthesis of asymmetrically substituted "AB3-type" phthalocyanines. *J Org Chem.* 2008; 73: 5003-5007.
37. Kobayashi N, Kondo R, Nakajima S, Osa T. New route to unsymmetrical phthalocyanine analogs by the use of structurally distorted subphthalocyanines. *J Am Chem Soc.* 1990; 112: 9640-9641.
38. Kobayashi N, Ishizaki T, Ishii K, Konami H. Synthesis, spectroscopy, and molecular orbital calculations of subazaporphyrins, subphthalocyanines, subnaphthalocyanines, and compounds derived therefrom by ring expansion. *J Am Chem Soc.* 1999: 121; 9096-9110.
39. Kobayashi N, Nonomura T. First observation of the circular dichroism spectra of chiral subphthalocyanines with C₃ symmetry. *Tetrahedron Lett.* 2002; 43: 4253-4255.
40. Meller A, Ossko A. Phthalocyaninartige Bor-Komplexe. *Monatsh Chem.* 1972; 103: 150-155.
41. Dabak S, Gül A, Bekaroğlu Ö. Hexakis(alkylthio)-substituted unsymmetrical phthalocyanines. *Chem Ber.* 1994; 127: 2009-2012.
42. Bhatt MV, Kulkarni SU. Cleavage of ethers. *Synthesis.* 1983; 249-282.

43. Hirth A, Sobbi AK, Wöhrle D. Synthesis of a monofunctional phthalocyanine on silica. *J. Porphyrins Phthalocyanines*. 1997; 1: 275-279.

44. De la Torre G, Claessens CG, Torres T. Phthalocyanines: The need for selective synthetic approaches. *Eur J Org Chem*. 2000; 16: 2821-2830.

45. K. Sonagashira, in: F. Diederich, P.J. Stang (Eds.), *Metal-catalyzed cross-coupling reactions*. Wiley-V

CH, Weinheim, 1998, pp. 203-229.

46. Özçeşmeci M, Nar I, Hamuryudan E. Synthesis and electrochemical and spectroelectrochemical characterization of chloromanganese(III) phthalocyanines. *Turk. J. Chem*. 2014; 38: 1064-1072.

47. McKeown NB, Li H, Helliwell M, J. Porphyr. Phthalocyanines. A non-planar, hexadeca-substituted, metal-free phthalocyanine. 2005; 9(12): 841-845.



VALIDATION OF MOHR'S TITRATION METHOD TO DETERMINE SALT IN OLIVE AND OLIVE BRINE

Mürüvvet SEZEY  and Perihan ADUN* 

Department of Food Engineering, Faculty of Engineering, Near East University, 99138 Nicosia-Mersin 10 TRNC, TURKEY.

Abstract: The aim of this study was to test Mohr method's performance characteristics and to check acceptability of test results during the routine salt analysis in the production phase of Çakıstes table olives. The method was validated using three fortified samples, i.e. salt solutions in water, cracked olive's brine and olive at three different levels of 3, 5 and 7% salt concentration at three different times. Overall recovery of the method was 107% for all three commodities over the validation range with a relative standard deviation of 5% (n=162). The regression coefficient (R^2) was found to be 0.998 in olive matrix. Typical limit of detection was 0.1% with the method.

Keywords: Method validation, salt analysis, Mohr method, olive, brine.

Submitted: December 13, 2018. **Accepted:** July 17, 2019.

Cite this: Sezey M, Adun P. VALIDATION OF MOHR'S TITRATION METHOD TO DETERMINE SALT IN OLIVE AND OLIVE BRINE. JOTCSA. 2019;6(3):329-34.

DOI: <https://doi.org/10.18596/jotcsa.496563>.

***Corresponding author. E-mail:** perihan.adun@neu.edu.tr.

INTRODUCTION

Method validation is the series of procedures used to demonstrate that the analytical method utilized for a specific test is suitable for its intended purpose. Results from method validation can be used to evaluate the reliability and precision of that method and it is an integral part of good laboratory practices (1).

Method validation should be applied according to ISO 17025 (2), when a method is developed in-house or obtained from the literature/third parties. Whenever a laboratory undertakes method modification or there is a change in the performance of the method over time, the effects of analytical variables should be established.

Different method performance parameters will be important in different situations. Trueness has at most importance for calculating absolute values of properties or analytes. It should be noted that the

term 'accuracy' is often used in documents/standards referring to method validation. Under current ISO definitions, accuracy could be defined as the agreement between a measurand and a true value, actually it includes the effect of both precision and trueness, since a measurand is an average of individual test results and dispersion of test results effects trueness and bias. Precision, which is closeness of test results to each other, is another important method performance criterion for all measurements but particularly in comparative studies. Method must be tested to assess sensitivity, linearity, working range and limit of detection (LOD). Sensitivity is defined as the slope of the calibration curve. Detection limit is the lowest detectable level of analyte distinguishable from zero. The higher the analytical sensitivity is, the lower the detection limit will be (3).

A test laboratory shall have a procedure for the determination of measurement uncertainty and

shall apply to this procedure. Uncertainty does not assure trueness; however in an analytical point of view, uncertainty defines the range of the values that could reasonably be attributed to an analytical result. Uncertainty arises not only from random errors in the analysis such as short-term deviations in temperature, relative humidity and power source variations, but also from systematic errors such as wrong solvent use, changes in instrumental calibrations. When laboratories report uncertainty together with an analytical result, it gives a quantitative indication of the quality of the analytical result and allows the user to make decision. The confidence can be placed on a result when it is compared with certain limits defined in a specification or regulation. The validation of the result and to compare analytical results from different laboratories can be possible by using uncertainty value (4). Different approaches can be used to estimate measurement uncertainty such as Gum Approach, method validation and use of method performance data, inter-laboratory studies, internal quality control studies and external quality assessment data (5).

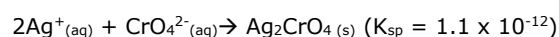
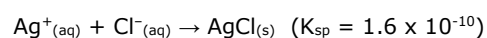
Çakistes is one of the most typical table olive products of Northern Cyprus prepared by cracking pink or green domestic olives. Domat, Memecik and Yamalak varieties are used to prepare Çakistes. After the olives are transported to the plant, they are graded and scratched on 2 or 3 sides and put into fresh water to remove bitter taste. The water should be changed every day to obtain the desired taste. Then, olives are transferred into brine which is composed of 7% NaCl, 1% citric acid and 1% CaCl₂, in fermentation tanks. The brine salt ratio is increased progressively keeping salt ratio constant at 7-8%. When salt ratio in olives reaches to 5-6%, Çakistes olives are now ready for consumption and packaging. This process takes almost one month (6).

Sodium chloride (NaCl) concentration is a crucial parameter which strongly influences the storage and quality of table olives. Its level is very effective to achieve stability of the products, as salt prevents growth of pathogens and hence its spoilage. In recent years, consumers have developed a tendency to low sodium intake, since a diet rich in sodium leads to higher blood pressure. Therefore, scientists have focused on the viability, application and consequences of replacement of sodium with calcium or potassium in table olive fermentation (7).

Selection of a method to determine sodium chloride content of any food is an important criterion designing a quality assurance plan. There are various methods available for determining salt content of food; every single method has their own advantages and limitations. Based on method

performance criteria, analysts prefer standard methods to determine salt content such as refractometry, ion-selective electrodes, and titration (8). Mohr's titration method was applied and validated in this study, since this method is widely used for salt analysis in olive, olive brine and many other food samples.

The Mohr's method, named after Karl Friedrich Mohr, determines the chloride ion concentration of a solution by titration with silver nitrate. As the silver nitrate solution is slowly added, a precipitate of silver chloride forms. The end point of the titration occurs when all the chloride ions are precipitated. Then additional silver ions react with the chromate ions of the indicator, potassium chromate, to form a red-brown precipitate of silver chromate (9):



The aim of this study is to validate Mohr's method to determine the amount of salt in olive and olive brine and to evaluate accuracy and precision of the method and to estimate measurement uncertainty. Acceptability of test results was also checked during the Çakistes production season by an internal quality control technique based on comparisons of duplicated test results.

EXPERIMENTAL

Water, olive brine and olive samples fortified with NaCl at three different levels i.e. 3, 5 and 7% were used as material for validation experiments.

Preparation of fortified water samples

Distilled water enough for the experiments was fortified with pure sodium chloride (NaCl) at 3 different levels i.e. 3, 5 and 7%, for 6 replicates at each level and at three different occasions.

Preparation of fortified olive brine

Olives were manually picked from trees. They were at green color maturity period. Samples were taken in plastic boxes and transferred to factory. Firstly, olives were washed in washing machine and separated according to size in sorting machine. Then they were cracked with crushing machine and put into pure water as same as in practice. Olives were kept in water for 3 days to include olive matrix components into brine water representing the conditions in practice. Olives were then separated from water and this water was fortified with pure sodium chloride (NaCl) at 3 different levels i.e., 3, 5 and 7%, enough for 6 replicates at each level and for three different occasions.

Preparation of fortified olive matrix

2 kg of olive were picked from trees. They were transferred to the laboratory. Olives were washed and fruit flesh were chopped, then comminuted and homogenized. Homogenized olive samples were fortified with pure sodium chloride (NaCl) at 3 different levels, i.e, 3, 5 and 7%, for 6 replicates at each level and for three different occasions. Fortified samples were kept for one day at room temperature, so that NaCl can incorporate with olive matrix. Next day, salty olive samples were filtered through filter cloth.

Preparation of internal quality control test samples

Picked olives were washed in washing machine and sorted. Then, they were cracked with crushing machine and put in polyester boxes. When the box was full with olives, brine, which contained 7% salt and 1% citric acid was added. During fermentation period of olives, brine samples were taken from selected boxes in duplicates and analyzed in different days. Total 18 analyses were performed and the following formula was used to calculate laboratory uncertainty from differences of duplicate measurements of test samples.

$$s = \frac{1}{\sqrt{2}} \sqrt{\frac{\sum d^2}{n}} = \sqrt{\frac{\sum d^2}{2n}}$$

Where s: standard deviation of analysis from duplicate laboratory determinations
d: the difference of duplicates in one laboratory
n: the number of data pairs

Preparation of calibration curve

Calibration curve was constructed to assess limit of detection, although calibration curve is not used for quantitation of NaCl amount in routine analysis. Olives were picked from trees and then transferred to the laboratory. They were washed and fruit flesh were chopped, then comminuted and homogenized. Homogenized olive samples were fortified with pure sodium chloride (NaCl) at 7 different levels, i.e, 1, 2, 3, 4, 5, 6 and 7%. Fortified samples were kept for one day, so that NaCl can

incorporate with olive matrix. Next day, salty olive samples were filtered through filter cloth and then used for the construction of calibration curve with replicate titrations.

Salt analysis by using Mohr's titration method

All fortified samples and olive brine samples taken during the olive fermentation period for internal quality control purpose were analyzed for the salt content by Mohr titration method by 6 replicates at the level of 3, 5 and 7% salt and at three different occasions.

Procedure is described below:

- An aliquot of 1 mL was taken from brine and put into an Erlenmeyer flask.
- 0.5 mL of 5% potassium chromate (indicator) was added.
- The burette was filled with 0.1 N of AgNO₃ until the zero point.
- The sample was titrated with standardized AgNO₃ solution until the first perceptible pale red-brown color.
- The color should remain constant for 30 seconds.
- Titration volume was recorded.
- The following formula was used to calculate the amount of salt.

$$\text{NaCl content (\%)} = \frac{V \times N \times F \times 0.0585 \times 100}{m}$$

V: Consumption of 0,1 N AgNO₃ in titration (mL)
N: Normality of AgNO₃
F: Factor of 0,1 N AgNO₃
m: mass of sample (g)

RESULTS and DISCUSSION**Validation results of fortified matrices**

Table 1 shows the recoveries and repeatability values for all fortified matrices at each occasion of analysis. Salt recoveries from fortified pure water changed between 101% and 121%, from brine 94% to 117% and from olive solutions 100% to 119%. Repeatability values changed from 3% to 6% RSD among the replicates of three different fortification levels at the same day.

Table 1. Method validation characteristics for different matrices (n=162).

Matrix	Days of Analysis	Average Recovery (%)	Precision as Repeatability of Recoveries (RSD%, n=18)
Water	1	109	4
	2	110	4
	3	113	5
Olive brine	1	103	3
	2	105	3
	3	107	5
Olive	1	107	6
	2	106	4
	3	105	3

Accuracy and reproducibility of the Mohr's Method

Table 2 summarizes the recoveries for all fortified matrices at each fortification level. Mean recoveries for olive brine and olives were found as 105% and 106% respectively, whereas 111% for direct aqueous solutions with the relative standard deviations of 4, 4 and 5% respectively (see Figure 1). Our findings are in accordance with the similar

titrimetric method validation criteria, although not any validation data on Mohr's method could be found.

Finally, overall recovery, in other words, accuracy of the Mohr's titration method was 107% with RSD of 5% (n=162) for three matrices, three levels and three different occasions.

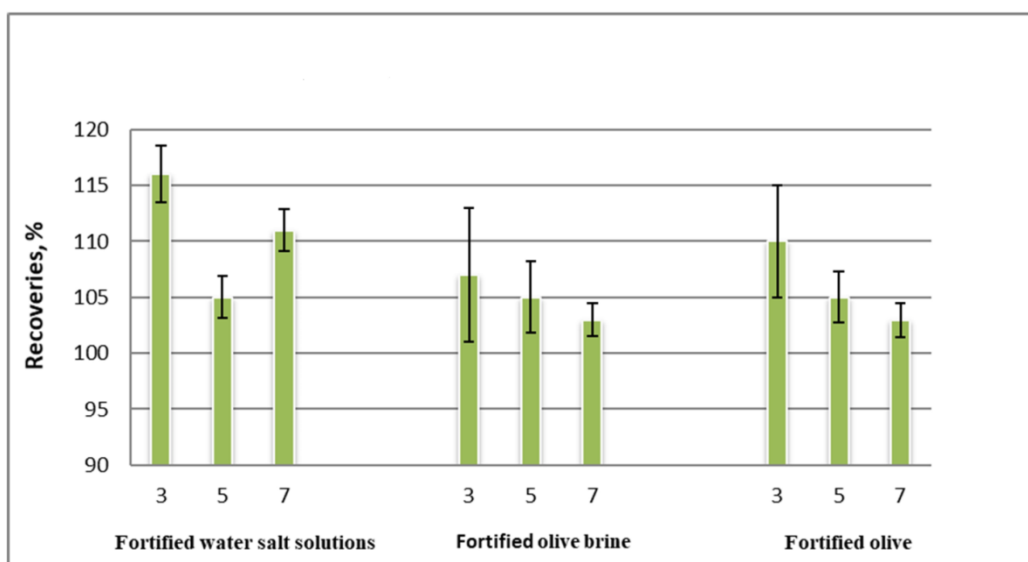


Figure 1. Mean recoveries and RSD values of fortified water solutions, fortified olive brine and fortified olive at three different salt level (%).

Table 2. Method validation characteristics of the method at different levels independent of the matrix. Analysis uncertainty is expressed as CV_A (n=162).

Fortification Level	Accuracy (Average Recovery, %)	Precision as Reproducibility of Recoveries (RSD%, n=18)
3%	111	6
5%	105	2
7%	106	4
Overall recovery	107	5*

*coefficient of variation (CV_A) for the analysis.

Internal Quality Check Results Obtained from Duplicate Analysis of Olive Brine

Olive brine samples were taken during the fermentation period for the estimation of laboratory

uncertainty, three sampling parties were selected during one-month period. Three samples were taken from each barrel with weekly intervals. Sample 1 was analyzed on the day of sampling, the 2nd sample was analyzed the next day and sample

3 was stored as a control sample. Total 18 samples were analyzed in the same manner and laboratory uncertainty was calculated as 3% (Table 3), which was better and in accordance with analysis uncertainty (5%).

Table 3. Results of two groups of measurements under repeatability conditions for the estimation of laboratory uncertainty

Sample	Replicate1	Replicate2	Relative difference between duplicates	Square of relative differences	Sum of squares	CV _{lab}
1	4.50	4.79	-0.062	0.00390	0.01214	0.02597
2	5.82	5.55	0.047	0.00226		
3	6.40	6.40	0	0.00000		
4	4.38	4.38	0	0.00000		
5	6.05	6.14	-0.014	0.00022		
6	6.61	6.55	0.009	0.00008		
7	5.50	5.90	-0.070	0.00492		
8	6.31	6.14	0.027	0.00075		
9	6.23	6.25	-0.003	0.00001		

Linearity and Limit of Detection (LOD)

Linearity and limit of detection are important method performance criteria to be determined in method validation experiments. One simple way to estimate linearity and LOD is the use of calibration curves in matrix (10). The standard deviations of relative residuals (Srr), which is a decisive

parameter in internal quality control of linearity, should be ≤ 0.1 (11-12). This was the case in the study that correlation coefficient R^2 was 0.998 and Srr was 0.03 (Figure 2). Typical LOD value for salt calculated from the calibration curve was found to be 0.1%.

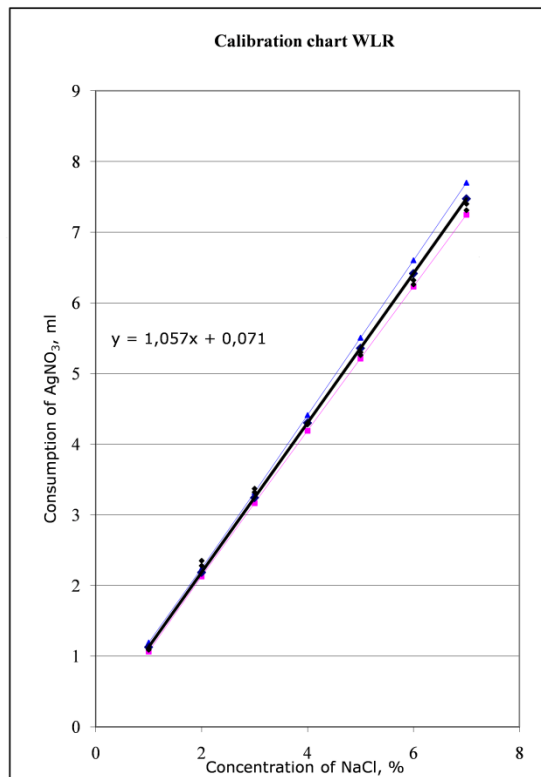


Figure 2. Calibration graph of salt analysis by using Mohr method.

CONCLUSION

Mohr's titration method for the determination of salt amount in olive and/or olive brine was successfully validated, since the accuracy and precision of the method were within the acceptable ranges (accuracy 70-120% and RSD 5%). Laboratory uncertainty value was in accordance with method's reproducibility value (CV_A) from validation study. Mohr's method can be used for routine analysis of salt determination by implementing quality control measures during its use.

This study was presented as an oral presentation at the Thirtieth National Chemistry Congress, 5-8 November 2018, Famagusta, Cyprus.

REFERENCES

1. Huber, L. Validation of Analytical Methods and Procedures. Validation and qualification in Analytical Laboratories. 2007; 125.
2. Karaman, D., Akalın, A.S. Süt teknolojisinde metot validasyonu ve uygulamaları. Türkiye 10. Gıda Kongresi. 2008; 749-51.
3. Method Validation Course 1125 © 2015 LGC Limited
4. EURACHEM/CITAC Guide. Quantifying Uncertainty in Analytical Measurement. Second Edition. 2000.
5. Türk Akreditasyon Kurumu (TURKAK). R20.02, Deney/Analiz Sonuçlarındaki ölçüm belirsizliği tahmini için TURKAK Prensipleri. 09.07.2015.
6. "Present and Future of the Mediterranean Olive Sector". Zaragoza (Spain). 26-28 November 2012.
7. Romeo, F.V. Microbiological aspects of table olives. The microbiological hazards in table olives. 2012.
8. Masulli, D. Determining salt in food. 2015; Retrieved from: www.foodqualityandsafety.com/.../determining-salt-in-food
9. Yoder, L. "Adaptation of the Mohr Volumetric Method to General Determinations of Chlorine". Industrial & Engineering Chemistry. 1919; 11 (8): 755.
10. Aysal, P., Ambrus, A., Lehotay, S.J., Cannavan, A. Validation of an efficient method for the determination of pesticide residues in fruits and vegetables using ethyl acetate for extraction. Journal of Environmental Science and Health Part B. 2007; 42 (5): 481 – 90.
11. Gozek, K.; Yucel, U.; Ilim, M.; Cayci-Aysal, P. & Tuncbilek, A.S. C14-dimethoate residues in olive oil during oil processing. Isotope Aided Studies of Pesticide Residues during Food Processing. 1995; 33-40.
12. Miller, J.N., Ambrus, A. Statistics in calibration analysis. Manual on Basic Statistics. FAO/ IAEA Training and Reference Centre for Food and Environmental Protection Section. 2000; 1-18.



Methanolysis of Gmelina Seed Oil to Biodiesel with KNO_3 Activated MgO-ZnO Composite Catalyst

Hamza R. Sani  and Umar I. Gaya* 

Department of Pure and Industrial Chemistry, Bayero University,
700241 Kano, Kano State, Nigeria

Abstract: The present study juxtaposes for the first time the heterogeneous methanolysis of gmelina oil over KNO_3 activated MgO-ZnO with a NaOH base methanolysis for biodiesel production. The conditions for biodiesel production such as temperature, reaction time, NaOH (or KNO_3 dose) and methanol-gmelina oil ratio were optimised. The 4%w/w KNO_3 activated MgO-ZnO afforded high biodiesel yield (71.5%) at 65 °C, predominantly consisting of C13-C25 cuts of linear fatty acid methyl esters (FAME). This heterogeneous catalyst was characterised using X-ray diffraction (XRD), energy dispersive X-ray (EDX) analyser, scanning electron microscopy (SEM) and Fourier transform infrared spectroscopy (FTIR). Gas-chromatography-mass spectrometry (GC-MS) revealed the selectivity to petroselinic acid methyl ester. The fuel properties of the biodiesel and its blends were consistent with standards. Relatively, the NaOH process yielded higher biodiesel (96.8%) at 60°C, 90 min, 1.2% NaOH and 9:1 methanol-oil ratio.

Keywords: Transesterification, methyl esters, composite, gmelina.

Submitted: December 03, 2018. **Accepted:** July 30, 2019

Cite this: Sani H, Gaya U. Methanolysis of Gmelina Seed Oil to Biodiesel with KNO_3 Activated MgO-ZnO Composite Catalyst. JOTCSA. 2019;6(3):335-48.

DOI: <https://doi.org/10.18596/jotcsa.491458>.

*Corresponding author. E-mail: uiqaya.chm@buk.edu.ng. Tel: +2348039169418. Fax: +234-64-665-904.

INTRODUCTION

Concerns on the hike, non-renewability, unfriendliness, and non-biodegradable nature of crude oil products have jointly necessitated an intensive search for alternative fuels (1-3). By far, numerous approaches and technologies such as supercritical method (4), pyrolysis (5), emulsification (6) and transesterification (7) have been engaged in sustainable biodiesel production from fat- or oil-based triglycerides. Among these technologies, transesterification is at the forefront due to its greenness, cost-effectiveness, and convenient properties of triglyceride feed. Basically, transesterification involves the reaction of lipids with short-chain alcohols such as methanol (in a process called methanolysis) or ethanol (by ethanolysis), to yield long-chain fatty acid methyl esters (known popularly as biodiesel), and glycerol as co-product (8). Even though alkaline methanolysis is known to achieve high biodiesel yield in shorter process time,

drawbacks such as catalyst recovery and severe corrosion necessitate the need to search for alternative materials such as heterogeneous catalysts and biocatalysts (9-12).

There has been considerable motivation to invest in heterogeneous biodiesel synthesis with emphasis on cost-effectiveness, biodiesel yield, process efficiency, the viability of the fatty acid feedstock and quality of the biodiesel produced (13-16). The high activity of co-precipitation-derived CaO-ZnO mixed oxides with or without doses of K_2CO_3 have proved effective for the methanolysis of sunflower oil (15,16). In the present study, we investigate the efficiency of KNO_3 activated, co-precipitation derived MgO-ZnO for the synthesis of biodiesel from gmelina oil. Because the industrial process of biodiesel synthesis exploits homogeneous alkaline catalysts, NaOH methanolysis was also studied. Nowadays, edible oils are considered unviable feedstocks and are marginally utilised in biodiesel

synthesis as opposed to vegetable and animal oils. The choice of gmelina oil for this study is therefore governed by the fact that it is non-edible and the source plant *Gmelina arborea* Linn. Roxb., is widely available in the wild of tropical countries (17).

MATERIALS AND METHODS

Seed samples and chemicals

The seeds of *Gmelina arborea* were collected from Bayero University Old Campus, Kano, in March, 2015. Methanol (99.8%, Sigma-Aldrich), $Zn(NO_3)_2 \cdot 4H_2O$ (98%, BDH), $Mg(NO_3)_2 \cdot 4H_2O$ (99%, BDH), KNO_3 (99%, BDH), NH_4OH (Sigma Aldrich, 36%), n-hexane (98%, Sigma Aldrich) were used as received from the manufacturers. Petrodiesel standard was obtained from Kaduna Refinery and Petrochemical Company (KRPC), a subsidiary of Nigeria National Petroleum Corporation (NNPC). De-ionised water was used in all preparations.

Oil extraction and pre-treatment

Gmelina oil was extracted from the *Gmelina arborea* seeds in the same manner described by Kansedo and Lee (18). Seeds were cleaned and dried in an oven at 100 °C overnight. The dry seeds were ground to fine particles using a mortar and pestle and then re-dried to remove moisture. The oil was extracted with n-hexane using soxhlet apparatus, operated at 70 °C for 4 h. Pre-treatment steps followed to remove free fatty acids from the oil were those of Šánek *et al.* (19). Exactly 40.7 g of the extracted oil was mixed thoroughly with 43.7 mL of methanol and 8.4 mL of 25% methanolic solution of tetramethylammonium hydroxide. The resultant mixture was shaken for 10 min and allowed to separate overnight in separating funnel and the phases so obtained were subsequently withdrawn and analysed.

Preparation of heterogeneous catalyst

The solid catalysts used in this work were prepared by co-precipitation followed by impregnation. The method of Istadi *et al.* (13) was applied, but substituting calcium for magnesium precursor. A solution of $Zn(NO_3)_2 \cdot 4H_2O$ (2 mol/L) was co-precipitated with solution of $Mg(NO_3)_2 \cdot 4H_2O$ (2 mol/L) in presence of NH_4OH . The gel formed was collected, washed with deionised water, and then dried in the oven overnight at 110 °C. The dry solid was calcined at 600 °C for 3 h in a muffle furnace to obtain $MgO-ZnO$ composite. This material was then impregnated with appropriate amounts of KNO_3 and dried in an oven at 110 °C overnight to produce 1 to 6%w/w. The resulting solid catalysts were calcined in the furnace at 600 °C for 3 h.

Heterogeneous methanolysis

The production of biodiesel by using the KNO_3 activated $MgO-ZnO$ catalysts was performed in a two-necked 500 mL glass reactor, and fitted with

a condenser and thermometer. The catalyst amount was fixed at 0.8 g, but the impregnation solution was varied from 1 to 6%w/w. Prior to methanolysis, the catalyst was first activated in methanol at 40 °C with constant stirring for 40 min. After activation of the catalyst, 40 g of oil (heated at 100 °C for 30 min prior to the reaction) was added to the batch reactor. The system was agitated using a magnetic stirrer. In order to separate the catalyst, the resulting mixture was filtered through a Whatman filter paper (125 mm diameter, 2.5 µm pore size). The filtrate was allowed to stand for 24 h in separating funnel. Subsequently, the glycerol resident at the bottom was separated from the biodiesel. The percentage of biodiesel yield was calculated using the following equation:

$$\text{Biodiesel yield (\%)} = \frac{\text{weight of biodiesel produced}}{\text{weight of oil used}} \times 100 \quad (1)$$

Homogeneous methanolysis

In order to compare the rate of the heterogeneous methanolysis with the conventional NaOH base methanolysis, biodiesel was produced using a previously described method (20). Exactly 40 g of oil was measured and poured into 500 mL round bottom flask. The catalyst was weighed and 20 mL methanol was added to it in a conical flask and stirred until the pellet dissolves, to form sodium methoxide solution. The solution was poured into the oil; the resultant mixture was refluxed at 50 to 70 °C for 90 min, in the presence of desired methanol to oil molar ratio and a known amount of NaOH. Agitation speed was 600 rpm. After completion of the reaction, the mixture was transferred into a separating funnel and allowed to stand overnight to allow for proper settling of the glycerol.

In order to remove residual by-products such as soap, residual methanol and glycerol, the biodiesel produced was purified by several washing cycles, using de-ionized water. The biodiesel was diluted (30%), stirred for 2 min and transferred to a clean separating funnel and allowed to stand for 5 h. The top layer was pure biodiesel. The impure bottom layer was re-extracted repeatedly until no appearance of by-products. The resulting biodiesel was then allowed to form pure biodiesel (B100) by standing for 24 h. Biodiesel blends, B20 and B50, were prepared by mixing petroleum diesel and pure biodiesel in a ratio of 80:20 and 50:50.

Gmelina oil and biodiesel characterisation

Free fatty acids (FFA) content and a saponification value of the gmelina oil were determined using the titrimetric methods described by the American Oil Chemists Society (AOAC) (21, 22). Fuel properties of the gmelina oil, biodiesel and petrodiesel such as kinematic viscosity, flash point, cloud point and specific gravity were determined using the methods of American Society for Testing and Materials (ASTM) (23). The composition analysis of the biodiesel was

performed with the aid of gas chromatography-mass spectroscopy (GC-MS) using a Shimadzu QP2010 Plus GCMS. The injector of the GC was kept at 200 °C. Injection mode was split by a ratio of 20. The column was VF-5, held at 60 °C for 2 min and ramped at the rate of 10 °C/min to 280 °C for 7 min.

Effect of reaction variables

The operation parameters (methanol to oil molar ratio, KNO₃ loading levels, reaction time and temperature) for the heterogeneous system were varied from 3:1 to 18:1, 1 to 6%w/w, 2 to 7 h, 45 to 65 °C by the classical one factor at a time method at fixed agitation velocity (600 rpm), catalyst amount (0.8 g) and initial gmelina oil mass (40 g). All parameters were optimised. The potential of reuse of the solid catalyst was investigated at the optimised conditions using the recovery method. On the other hand, the homogeneous process was investigated using 3.1 to 9:1 methanol to oil molar ratios, 0.4 to 2.0% NaOH for 30 to 90 min reaction times at 45 to 70 °C.

Characterization of the solid catalyst

The solid catalyst with an outstanding performance was characterised. X-ray diffraction (XRD) analysis was performed on a Philips X'Pert Pro diffractometer, using Cu-K α source ($\lambda=1.56877$ Å). The diffractometer was run at 30 kV and 30 mA, over a 2θ range of 10° to 120°. Scanning electron microscopy was carried out on Leica Stereoscan-440 SEM hyphenated with Phoenix energy dispersive X-ray analyser. Crystallite size was estimated using the Debye-Scherer formula:

$$D = \frac{k\lambda}{\beta \cos\theta} \quad (2)$$

where D is the crystalline diameter; k is the crystallographic constant (0.9, for spherical crystals), λ is the wavelength of CuK α radiation, 0.156877 nm; β is the full width of half maximum (FWHM) while θ is the diffraction angle. As crystallite sizes depend mainly on diffraction angles, the average crystallite size of the catalyst was calculated using equation (3).

$$\text{Average crystallite size} = \frac{\sum(\text{crystallite size})}{\text{Number of peaks}} \quad (3)$$

Elemental measurements were carried out on Leica Stereoscan-440 scanning electron microscope instrument interfaced with Phoenix Energy-dispersive X-ray spectrometer. The instrument was operated using Pd X-ray tube at 25 kV and 1.2 mA. Fourier transform infrared spectroscopy was performed on an Agilent Cary 630 diamond attenuated total reflectance Fourier transform infrared spectrometer (ATR-FTIR), within a spectral range of 1000-650 cm⁻¹.

RESULTS AND DISCUSSION

Catalyst characterization

The crystalline structure of 4% w/w KNO₃ activated MgO-ZnO, the best performing composite, was characterised using XRD plot (Figure 1). From the figure, the XRD peaks of ZnO are clearly seen at 2θ angle of 31.8°, 34.48°, 36.3°, 47.6°, 56.6°, 62.9°, 66.47°, 69.1°, 71.8°, 76.8°, 80.7° (JCPDS card 36-1451). The diffractogram also clearly reveals peaks of MgO at 2θ angle of 42.9°, 53.76°, 62.2°, 73.7°, 78.6°, 83.7°, 86.1° (JCPDS file 01-072-0447). It also shows reflection peaks consistent with that of K—O (JCPDS file 77-2176) with 2θ angles of 23.08°, 26.7°, 28.96°, 40.7°, 82.78°, 90.1°, 91.3°, 109.76°. The average crystallite size of the catalyst was calculated using Debye-Scherer equation to be 66.45 nm.

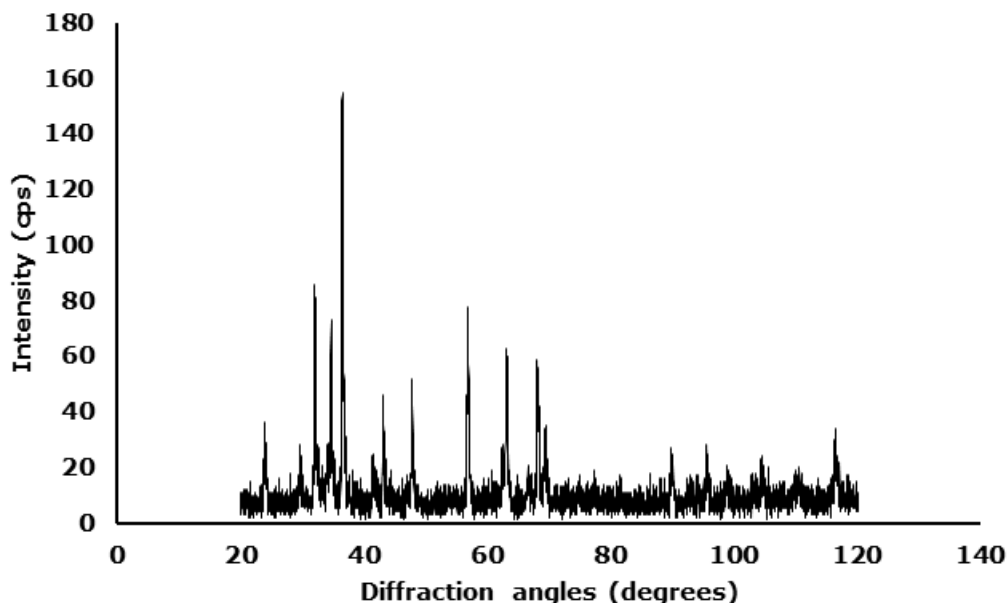


Figure 1. The X-ray diffractogram of 4%w/w KNO_3 activated MgO-ZnO. shows lumps of organised grains. Section analysis informs of the dimension of the grains to be in the order of hundreds to a thousand plus nanometer.

The external morphology of the synthesised catalyst is displayed in Figure 2. The SEM image

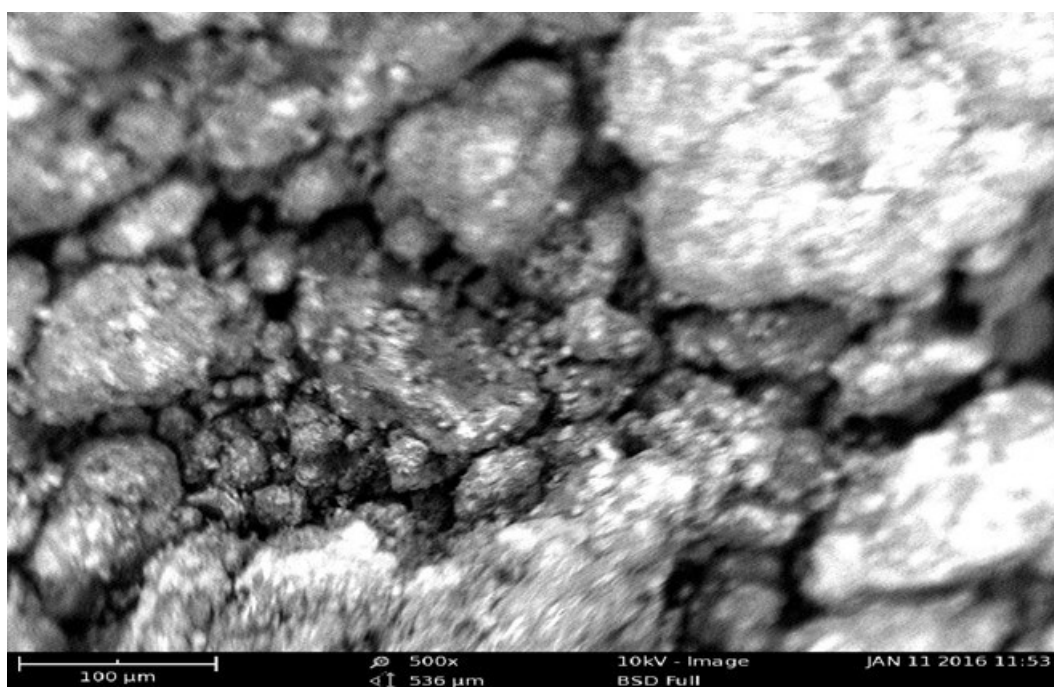


Figure 2. Scanning electron micrograph of the heterogeneous catalyst.

The elemental composition of the 4% w/w KNO_3 activated MgO-ZnO catalyst is presented in Table 1. The ratios of the EDX peak concentrations in the table revealed atomic ratios which confirm the formula of 4% w/w KNO_3 activated MgO-ZnO catalyst to be the non-stoichiometric oxide $\text{K}_{4.08}\text{N}_{0.73}\text{Mg}_{0.54}\text{-ZnO}_{2.38}$. The ATR-FTIR spectrum

of the prepared catalyst revealed the sharp peak between at 527 cm^{-1} characteristics of stretching mode of Zn-O bond (24). The incorporation of Mg^{2+} into the ZnO crystal structure is corroborated by the intense Mg-O peak at 474 cm^{-1} (25). The formation of K-O bond was confirmed by the peak at 491 cm^{-1} .

Table 1. Energy dispersive X-ray data of the composite.

Element	Weight percentage (%)	Relative ratios
K	48.1	4.08
O	25.1	2.38
Zn	11.8	1.00
Mg	6.4	0.54
N	8.6	0.73

Optimisation of reaction conditions

Primarily, the methanolysis of oil to biodiesel is a stoichiometric reaction involving 1 mole of triglyceride with 3 moles of methanol to yield methyl esters and glycerol. However, because the methanolysis of triglycerides is a reversible reaction excess methyl alcohol is required to favour the rate of reaction that forms the biodiesel. The yield-methanol profiles for both the heterogeneous catalyst and the NaOH mediated counterpart are shown in Figure 3. The figure shows a general increase in the yield of the methyl ester with increasing methanol-oil ratio from 3:1 up to 12:1 for the solid catalyst (and 9:1 for the NaOH catalysed process). This may be

attributed to the equilibrium shift in the direction of methyl ester. Excess amounts of methyl alcohol do not improve the biodiesel yield as indicated by the levelling off of both curves in Figure 3. The decline in yield may be as a result of the dissolution of glycerol in the excess methyl alcohol which hinders the interaction of the reactants with the catalyst. From the figure, the methanol to oil molar ratio of 12:1, with a yield of 72.85%, is considered optimum for the heterogeneous process while 9:1 is optimum for the homogeneous process. Feyzi and Shahbazi (3) achieved a higher yield (96.1%) with 6 wt% Al-Sr/ZSM-5 catalyst at a methanol-oil molar ratio of 12:1.

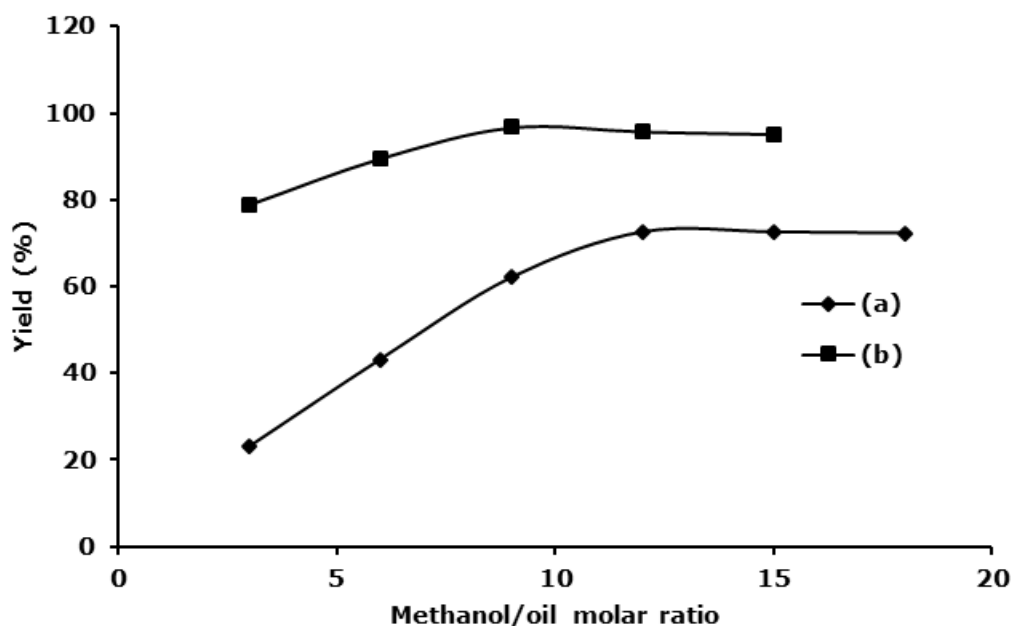


Figure 3. Effect of methanol to oil molar ratio on biodiesel yield in presence of (a) 1% NaOH catalyst. Temperature = 65 °C, agitation velocity = 600 rpm, initial mass of oil = 40 g, reaction time = 90 min. (b) 4% w/w KNO₃ activated MgO-ZnO catalyst. Mass of gmelina oil = 40 g, reaction temperature = 60 °C, reaction time 4h, catalyst loading = 0.8 g, stirring speed = 600 rpm.

The influence of KNO₃ promoter (1 to 6% w/w) in the MgO-ZnO catalysts was investigated at the predetermined optimum methanol-oil ratio. The methyl ester yield increased proportionally with the addition of 1 to 4% w/w KNO₃, with the highest yield (72.85%) corresponding to the

limiting catalyst dose (4% w/w) (Figure 4). Therefore, KNO₃ loading of 4% w/w is optimum for the heterogeneous methanolysis. A yield of 90% was earlier reported when K-La was used as a promoter of ZSM-5 zeolite for the methanolysis of soybean oil (26).

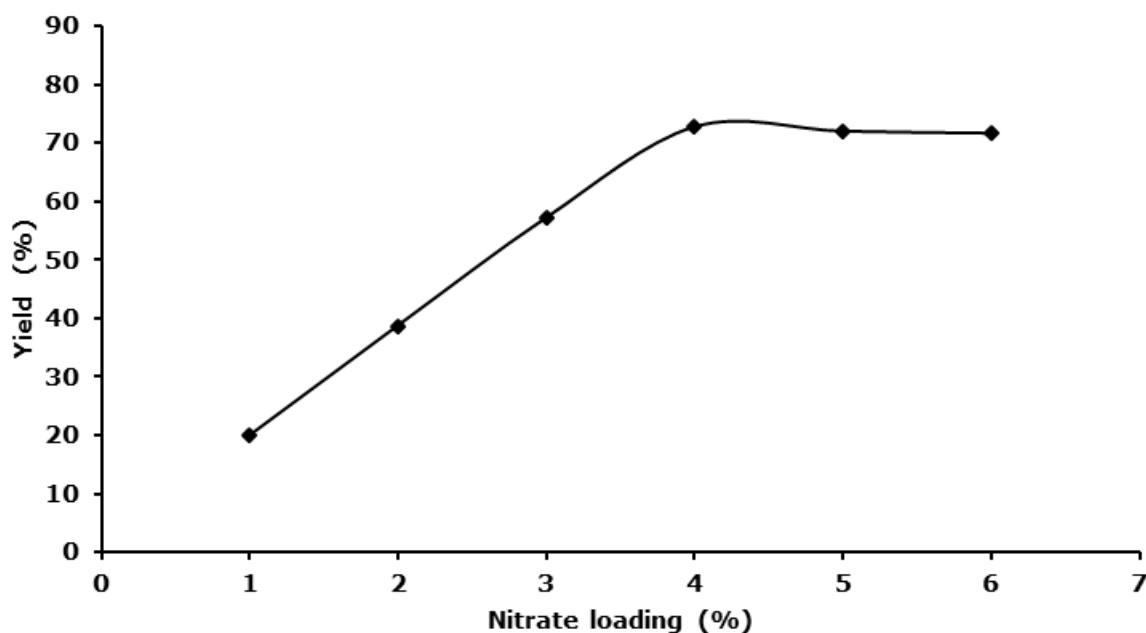


Figure 4. Effect of KNO_3 levels on the performance of the MgO-ZnO catalyst for the biodiesel synthesis. Mass of gmelina oil = 40 g, Mass of MgO-ZnO (0.8 g), temperature = 60 °C, reaction time = 4 h, methanol to oil molar ratio = 12:1, stirring speed = 600 rpm.

In the homogeneous methanolysis, the influence of NaOH (0.4 to 2%) was investigated at the optimum methanol-oil ratio. Increasing presence of NaOH from 0.4 to 1.2% enhanced the yield, with maximum yield (98.1%) corresponding to

1.2% NaOH (Figure 5). The decline in biodiesel yield above 1.2% NaOH (Figure 5) can be attributed to a high concentration of by-products. Therefore, a base catalyst loading of 1.2% was applied in the homogeneous methanolysis.

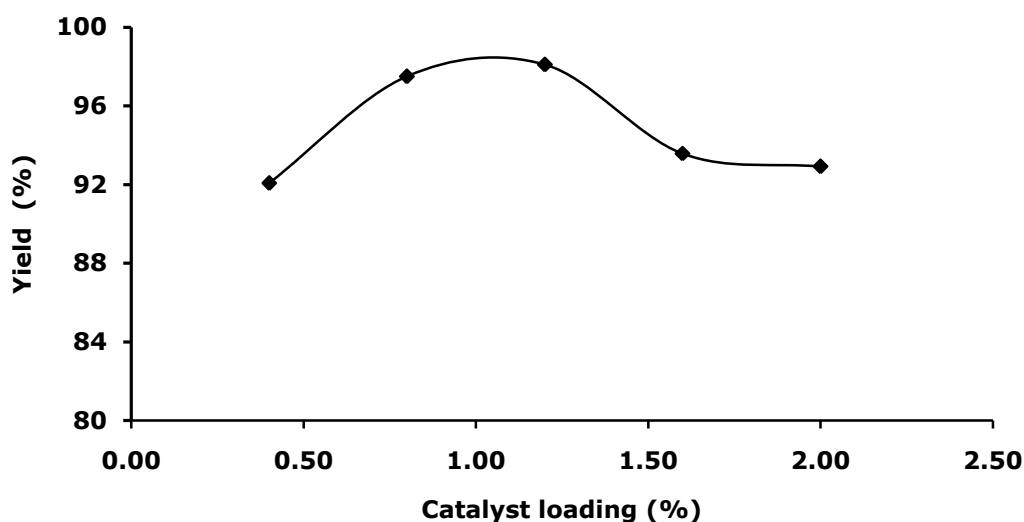


Figure 5. Effect of NaOH on biodiesel yield. Reaction time = 90 min, methanol-oil molar ratio = 9:1, temperature = 65 °C, stirring speed = 600 rpm, mass of gmelina oil = 40 g.

Reaction temperature is one of the most important parameters that influence biodiesel yield. The reaction temperature was investigated in a range of 45 to 70 °C for the solid catalyst and 45 to 65 °C for the NaOH mediated process (Figure 6). Biodiesel yield was enhanced until 65 (or 60) °C for the heterogeneous (or

homogeneous) process. This can be linked to corresponding enhancement of miscibility and mass transfer. Above this temperature biodiesel yield does not increase, likely due to the volatilisation of methanol and its decreasing polarity, hence the sodium methoxide population.

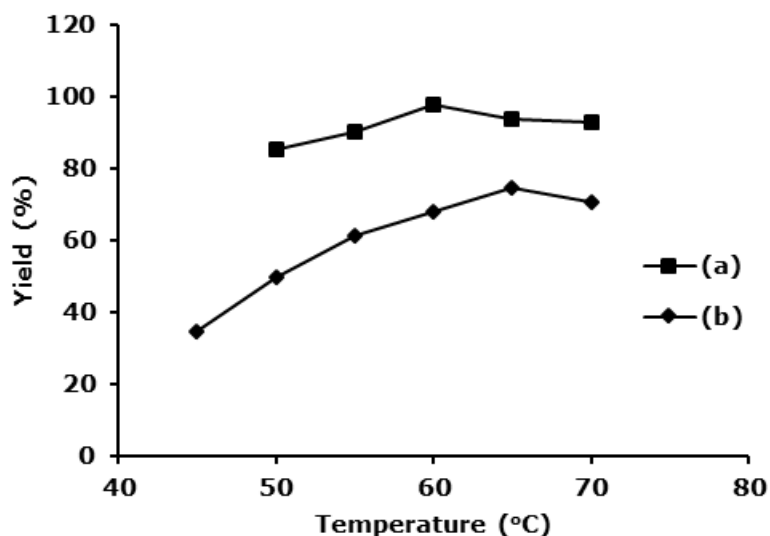


Figure 6. Effect of reaction temperature on biodiesel yield in presence of (a) 0.8 g of 4% w/w $\text{KNO}_3/\text{MgO-ZnO}$. Mass of gmelina oil = 40 g, methanol-oil molar ratio = 12:1, reaction time = 7 h, stirring speed = 600 rpm (b) 1.2% NaOH. Reaction conditions: methanol-oil molar ratio = 9:1, reaction time = 90 min, stirring speed = 600 rpm.

The influence of reaction time was studied between 2 and 7 h, at optimum temperature (60 °C), catalyst loading (0.8 g of 4 wt% $\text{KNO}_3/\text{MgO-ZnO}$), methanol-oil molar ratio (12:1) and at a constant stirring speed (600 rpm). As shown in Figure 7, the biodiesel yield increases progressively with increase in reaction time and reached its maximum (71.5%) at 7 h. This

catalyst was chosen as optimal for the biodiesel synthesis. The optimal catalyst is not very active (yield <90%) (15). However, it is not uncommon with yields of biodiesel yield to be lower than this threshold, especially with heterogeneous catalysts. A yield of 87.7% was obtained with ZSM-5 supported Ba-Sr nanocatalyst at optimum operating conditions (27).

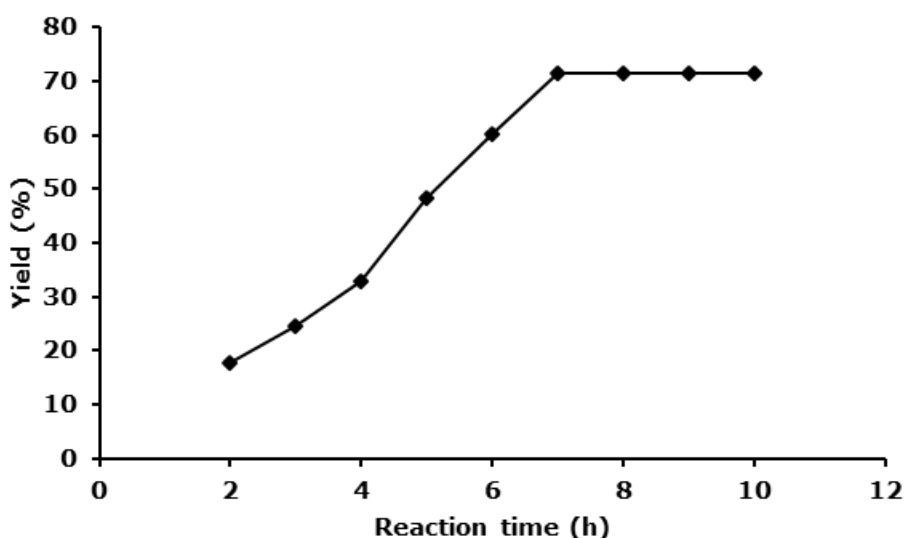


Figure 7. Effect of reaction time on biodiesel production over KNO_3 activated MgO-ZnO .

The influence of reaction time in this NaOH mediated methanolysis was performed in a range of 30 to 90 min at constant temperature (60 °C), methanol-oil molar ratio (9:1), catalyst loading

(1.2%), gmelina oil (40 g) and stirring speed (600 rpm). The results show an increase in biodiesel yield with an increase in reaction time up to 90 min with a maximum yield of 96.8% (Figure 8).

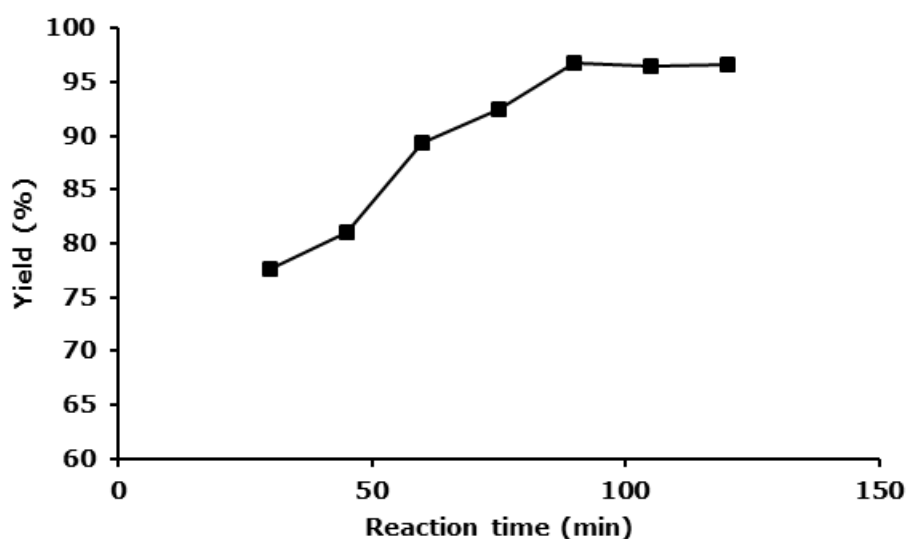


Figure 8. Effect of reaction time on biodiesel production using NaOH.

Oil characterisation

Prior to and after extraction of the gmelina oil, drying and pretreatment, acid value, free fatty acids and saponification values are given in Table 2. Gmelina oil was found to have high acid value (11.6 mg KOH/g) prior to pretreatment when compared to those from Karanja oil (5.06 mg

KOH/g) (28). The saponification value of the oil declined by 4%, while the free fatty acid (FFA) value and the acid value was lowered by 82%. The FFA value obtained after pretreatment (1.056%) implies a low tendency to undergo saponification.

Table 2. Properties of gmelina seed oil.

Property	Before pretreatment	After pretreatment
Acid value (mg KOH/g oil)	11.64	2.10
Free fatty acids (%)	5.85	1.06
Saponification value (mg KOH/g oil)	194	186

The fuel properties exhibited by gmelina oil, biodiesel (B100), the blends B20 and B50 and those of petrodiesel were determined (Table 3). Due to exceedingly high fuel properties such as cloud point (6 °C), flash point (126 °C), kinematic viscosity (11.91 mm²/s) and specific gravity, the gmelina oil must be upgraded or converted to another form prior to application as fuel. A comparison with petrodiesel shows the unsuitability of the gmelina oil for use as fuel. Upon methanolysis however, the biodiesel product and its blends exhibit properties consistent with those of ASTM standard. Specifically, the specific gravity (0.86) is more or less that of typical biodiesel (0.88) (29). The viscosity of the gmelina oil was reduced to 3.66 mm²/s, a value that is lower than that of Moringa

oleifera methyl esters (4.83 mm²/s) (30). Similarly, the specific gravity of gmelina oil is reduced down to acceptable values, by conversion to biodiesel blends B100, B50 and B20. The cloud point of the oil and B100 (-5 °C) nears that of typical cottonseed oil (-4 °C) (31). The B100 Furthermore, the biodiesel and its blends (Table 3) are inherently "sweet" (with S content << 0.5%) which is usual with biomass oils and consistent with green emissions. The sulphur content of B100 and gmelina oil is even lower than that of petrodiesel. The cetane number for B100 was determined to be 51.7 which complies with ASTM (23). The value measured in this study is slightly higher than that reported for castor biodiesel (48.9) (32).

Table 3. Fuel properties of gmelina oil, biodiesel and its blends with petrodiesel.

Fuel properties	Unit	Petrodiesel	Gmelina oil	B100	B50	B20	ASTM (23)
Kinematic viscosity @40°C	cSt	2.60	11.91	3.66	3.10	2.91	1.9-6.0
Sp. Gravity @27°C	kg/L	0.846	0.90	0.863	0.860	0.846	0.860-0.900
Flash point	°C	49	126	106	80	56	100-170
Combustion point	°C	59	125	96	91	65	-
Cloud point	°C	-5	6	2	-2	-5	-6 to 12
Sulphur content	%	0.167	0.012	0.0220	0.0929	0.100	-
Cetane number	°C	-	ND ^a	51.7	49.5	48.6	48-65

^aNot determined

Methanolysis products

The products of methanolysis were detected by GC-MS. The chromatographic peaks (Fig. 9) were interpreted using NIST107.LIB GC library.

There are fourteen peaks on the chromatogram, corresponding to different fatty acid methyl esters. These fatty acid methyl esters and their retention property are displayed in Table 4. Majority of the compounds have a base peak at $m/z = 74$ indicating a common fragment $[\text{CH}_2=\text{CHCH}_2\text{CH}_2]^+$. The compound petroselinic

acid methyl ester (or 6-octadecanoic acid methyl ester) eluted at 20 min retention time, has the broadest and most intense peak and accounts for about 62% of the fatty acid methyl esters yield of the methanolysis process. It was earlier noted from Table 4 that the cloud point of B100 is higher than petrodiesel, though within the acceptable range. This can be explained based on the waxing of the major product and other methyl esters which emerged at higher retention times (Table 4) at extremely low temperatures.

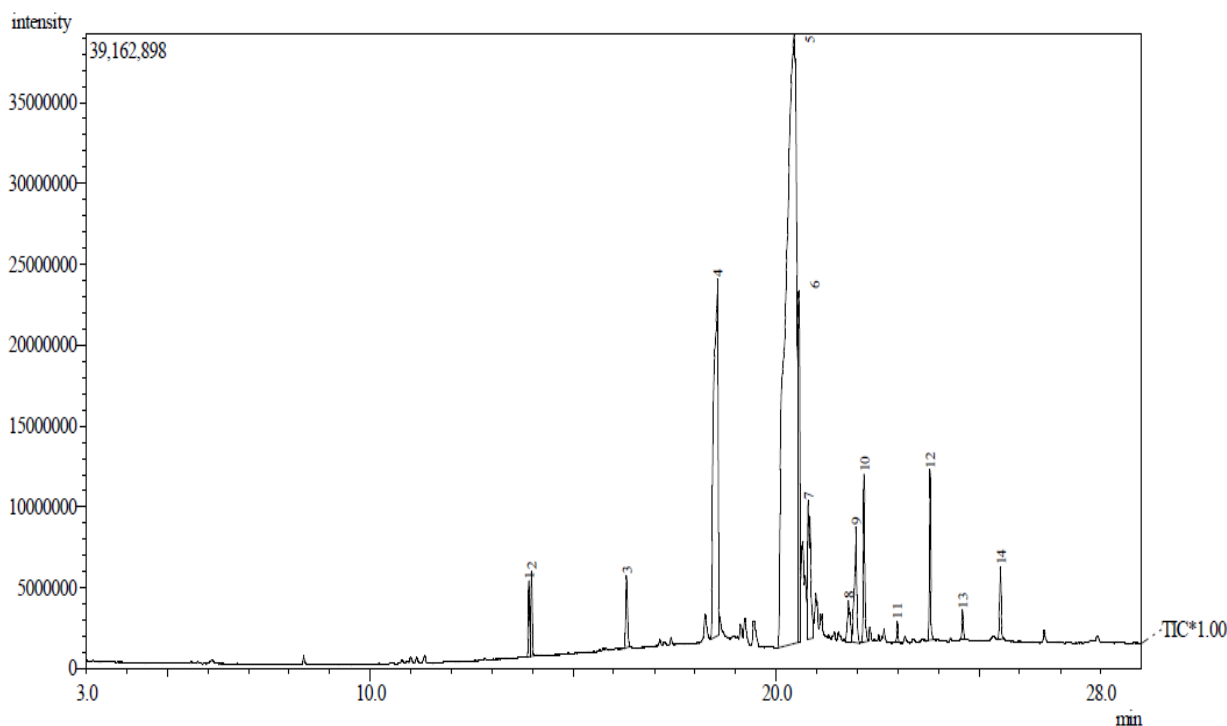


Figure 9. Elution peaks of fatty acid methyl esters with petroselinic acid methyl ester dominating the chromatogram.

Table 4. Chemical and common names of the fatty acid methyl ester (FAME) of the as-prepared biodiesel.

Peak No.	Retention time (min)	Peak area (%)	Assignment of peaks	C atoms
1	13.908	0.94	Dodecanoic (capric) acid methyl ester	C ₁₃
2	13.975	0.98	Tridecanoic acid methyl ester	C ₁₄
3	16.317	1.21	Tetradecanoic (myristic) acid methyl ester	C ₁₅
4	18.550	14.22	Hexadecanoic (or palmitic) acid methyl ester	C ₁₈
5	20.442	62.22	6-octadecanoic (or petroselinic) acid methyl ester	C ₁₉
6	20.567	6.37	Octadecanoic (or stearic) acid methyl ester	C ₁₉
7	20.792	3.97	Linolelaidic (or 9,12-Octadecadienoic) acid methyl ester	C ₁₉
8	21.783	1.18	5,8-octadecadienoic acid methyl ester	C ₁₉
9	21.958	2.41	9-octadecanoic (or elaidic) acid methyl ester	C ₁₉
10	22.167	2.39	Eicosanoic (arachidic) acid methyl ester	C ₂₁
11	22.983	0.26	Heptacosanoic acid methyl ester	C ₂₂
12	23.792	2.30	Docosanoic (or behenic) acid methyl ester	C ₂₃
13	24.592	0.39	Tricosanoic acid methyl ester	C ₂₄
14	25.525	1.17	Tetracosanoic (or lignoceric) acid methyl ester	C ₂₅

Reusability of the KNO₃ activated composite

Recovery of the synthesized catalyst was evaluated using 12:1 methanol to oil molar ratio, 65 °C reaction temperature, and reaction time of 7 h. After each run, the spent catalyst was recovered, washed with petroleum ether to remove the adsorbed materials. This catalyst was then reactivated for reuse by calcination in a muffle furnace for 2 h at 400 °C. The results

(Figure 10) showed that the catalyst can be reused for five consecutive runs while maintaining considerable methanolytic activity (above 50%). The decrease in biodiesel yield from 72.5% in the first cycle to 56.8% after five cycles may be attributed to deactivation of the catalyst sites caused by the various chemical species undergoing competitive adsorption and desorption.

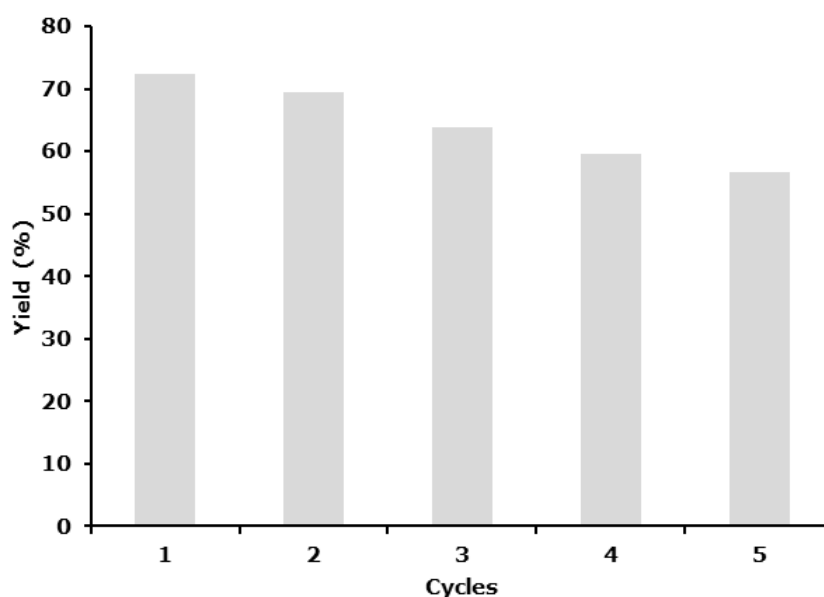


Figure 10. Effect of $K_{4.08}N_{0.73}Mg_{0.54}-ZnO_{2.38}$ recycling on biodiesel yield. Reaction conditions: Time = 7 h, temperature = 60 °C, catalyst loading = 0.8 g of 4% w/w $KNO_3/MgO-ZnO$, methanol-oil molar ratio = 12:1 and stirring speed = 600 rpm.

Transesterification kinetics

Generally, transesterification reactions proceed through three elementary steps comprising the conversion of triglyceride to diglyceride (the rate-limiting), diglyceride to monoglyceride and then finally monoglyceride to fatty acid methyl esters (FAME) and glycerol. The triglyceride conversion is traditionally first-order and can be used to evaluate the reaction rate constant (33). Basically, the logarithmic function of FAME is related to time by the equation:

$$\ln[\text{FAME}]_t - \ln[\text{FAME}]_0 = k't \quad (4)$$

Where $[\text{FAME}]_0$ = initial concentration of fatty acid methyl ester at time $t = 0$ and $[\text{FAME}]_t$ is the concentration at time t . The plot of $\ln[\text{FAME}]_t$ against t (Figure 11) for the heterogeneous system gives a straight line with a correlation coefficient (R^2) of 0.986 indicating consistency with pseudo-first-order. The slope of the plot which equals to the rate constant (k) of the heterogeneous process is $4.8 \times 10^{-3} \text{ min}^{-1}$. The corresponding rate constant for the NaOH base methanolysis was found to be $3.8 \times 10^{-3} \text{ min}^{-1}$.

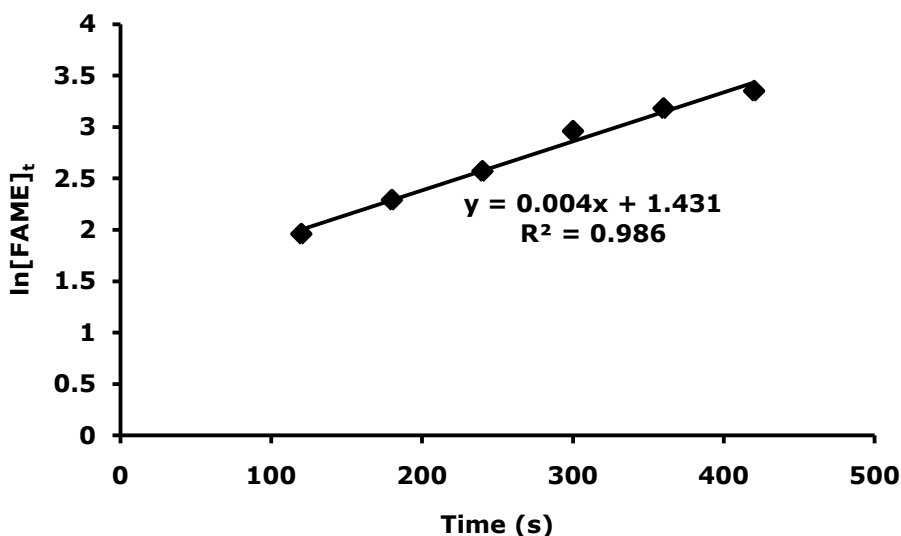


Figure 11. First-order kinetic plot of gmelina oil conversion over KNO_3 activated MgO-ZnO composite.

Activation parameters

Temperature dependence results permitted the estimation of energies of activation. The logarithmic function of the rate constant for the biodiesel production is related to activation energy by the Arrhenius equation (5).

$$\ln k = \ln A - \frac{E_a}{RT} \quad (5)$$

Where A is the Arrhenius factor (hr^{-1}), E_a is the activation energy (J/mol K), R is the molar gas constant (8.314 J/mol K) and T is the absolute temperature (K). Activation functions were obtained from the plot of $\ln k$ against $1/T$ (Figure 12). The activation energy and the pre-exponential factor for the $\text{K}_{4.08}\text{N}_{0.73}\text{Mg}_{0.54}\text{-ZnO}_{2.38}$ mediated biodiesel synthesis are 68.92 kJ/mol and $9.698 \times 10^7 \text{ min}^{-1}$, respectively, while the corresponding values for the NaOH-assisted process are 38.55 kJ/mol , $2.75 \times 10^4 \text{ min}^{-1}$.

The Eyring equation (expressed as Equation (6)) permits the estimation of other energies of activation (ΔG^* , ΔH^* , ΔS^*).

$$\ln\left(\frac{k}{T}\right) = -\left(\frac{\Delta H}{RT}\right) - \left[\ln\left(\frac{k_b}{h}\right) + \frac{\Delta S}{R}\right] \quad (6)$$

Where k_b is the Boltzmann constant ($1.38 \times 10^{-23} \text{ J/K}$) and h is the Planck's constant ($6.63 \times 10^{-34} \text{ Js}$) while other quantities have their usual meaning. A plot of $\ln\left(\frac{k}{T}\right)$ against the inverse of temperature ($1/T$) at 338 K as in Figure 13 gives a slope equal to $-\frac{\Delta H}{R}$ while the intercept provides $\frac{\Delta S}{R}$.

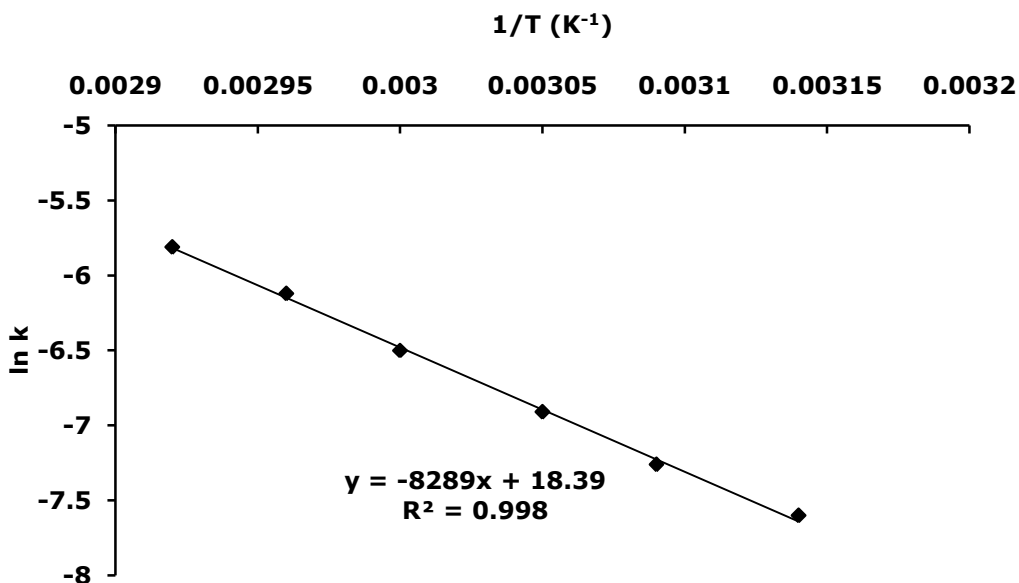


Figure 12. Arrhenius plot correlating lnk with 1/T for the conversion of gmelina oil to biodiesel over KNO₃ activated MgO-ZnO composite.

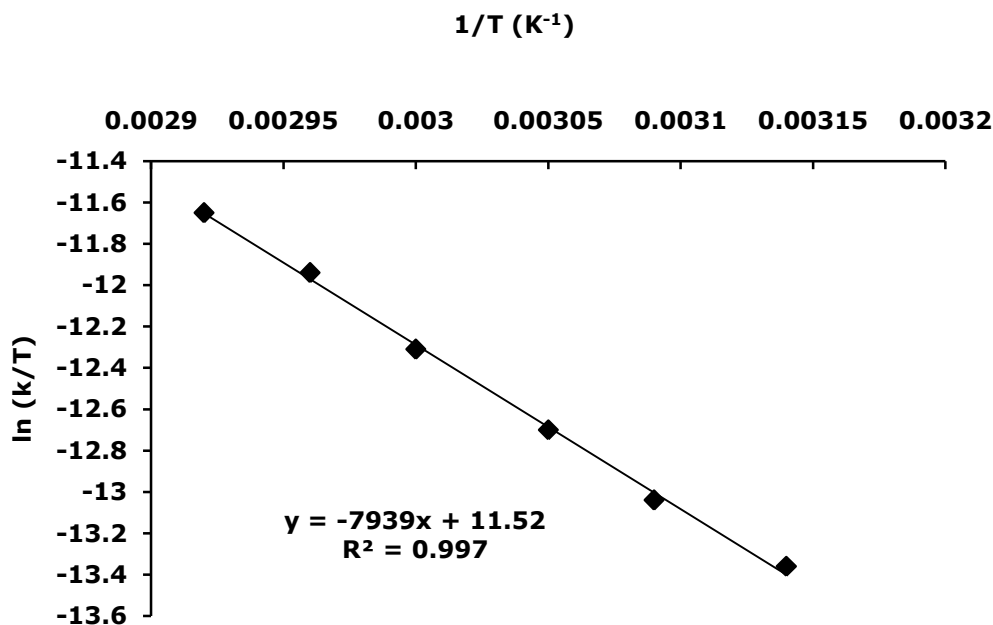


Figure 13. Eyring plot correlating ln(k/T) with 1/T for the conversion of gmelina oil to biodiesel over KNO₃ activated MgO-ZnO composite.

Table 5. Activation energies of gmelina methyl esters and reference values from selected literature.

Methyl esters*	ΔG (kJ/mol)	ΔH (kJ/mol)	ΔS (kJ/mol K)	Reference
GME	100.50	66.004	-0.102	This work
RME	105.6	139.5	-98.0	(34)
CME	96.128	36.124	-180.19	(35)
SPME	92.71	16.35	-232.83	(33)

*Gmelina methyl esters (GME), rapeseed methyl esters (RME), Chlorella methyl esters (CME), *Spirulina platensis* methyl esters (SPME).

The activation properties for gmelina biodiesel are presented in Table 5. Also in the same table for the sake of comparison are thermodynamic properties of the methyl esters of rapeseed, *Chlorella* and *Spirulina platensis*. The Gibbs free

energy, enthalpy and entropy of the gmelina methyl esters produced by the heterogeneous catalyst are 100.50 kJ/mol, 66.00 kJ/mol and -0.102 kJ/mol K. The corresponding activation properties of the NaOH base system are 92.14

kJ/mol, 34.23 kJ/mol and -0.174 kJ/mol K. The enthalpies of activation are within the range reported in various literature. As seen from the Table, the gmelina transesterification process is characterized by negative entropies of smaller magnitude which implies the formation or more ordered transient structures en route the formation of methyl esters (36).

CONCLUSIONS

Methyl esters were successfully produced from gmelina oil via methanolysis using NaOH and for the first time compared with KNO₃ activated MgO-ZnO. At optimal reaction condition, the biodiesel yields were significant for both the heterogeneous and homogeneous processes. Petroselinate or 6-octadecanoic acid ester was the major product and its fuel properties are within ASTM limits. It still remains a challenge to achieve a combination of high yield, low methanol-oil molar ratio and short reaction time with heterogeneous catalysts relative to the conventional base process.

ACKNOWLEDGEMENTS

The authors of this paper acknowledge the support of all of the staff of Quality Control Unit, Production, Programming and Quality Control Department, Kaduna Refinery and Petrochemical Company (KRPC), and Nigerian National Petroleum Corporation (NNPC).

REFERENCES

- Ullah Z, Bustam MA, Man Z. Biodiesel production from waste cooking oil by acidic ionic liquid as a catalyst. *Renewable Energy*. 2015; 77: 521-6.
- Sun K, Lu J, Ma L, Han Y, Fu Z, Ding J. A comparative study on the catalytic performance of different zeolites for biodiesel production. *Fuel*. 2015; 158: 848-54.
- Feyzi M, Shahbazi Z. Preparation, kinetic and thermodynamic studies of Al-Sr nanocatalysts for biodiesel production. *Journal of the Taiwan Institute of Chemical Engineers*. 2017; 71: 145-155.
- Ortiz-Martínez PA, Andreo-Martínez P, García-Martínez N, Pérez de le Ríos, Hernández-Fernández FJ, Quesada-Medina J. Approach to biodiesel production from microalgae under supercritical conditions by the PRISMA method. *Fuel Processing Technology*. 2019; 191: 211-222.
- Shahir VK, Jawahar CP, Suresh PR, Vinod V. Experimental Investigation on Performance and Emission Characteristics of a Common Rail Direct Injection Engine Using Animal Fat Biodiesel Blends. *Energy Procedia*, 2017; 117: 283-290.
- Goh BHH, Ong HC, Cheah MY, Chen W-H, Yu KL, Mahlia TMI. Sustainability of direct biodiesel synthesis from microalgae biomass: A critical review. *Renewable and Sustainable Energy Reviews*. 2019; 107: 59-74.
- Tural S. Zinc perchlorate hexahydrate catalyzed mono- and bis-transesterification of malonic esters. *Turkish Journal of Chemistry*. 2008; 32: 169-79.
- Alhassan FH, Rashid U, Taufiq-Yap YH. Biodiesel synthesis catalyzed by transition metal oxide: Ferric-manganese doped tungstated/molybdena nanoparticle catalyst. *Journal of Oleo Science*. 2014; 10: 1-8.
- Lam MK, Lee KT, Mohamed AR. Homogeneous, heterogeneous and enzymatic catalysis for transesterification of high free fatty acid oil (waste cooking oil) to biodiesel: A review. *Biotechnology Advances*. 2010; 28: 500-518.
- Mehra T., process optimization biodiesel production from cedar wood oil (*Cedrus deodara*) using response surface methodology, SAE Technical paper 2018-01-0665, 2018.
- Raita M, Laothanachareon T, Champreda V, Laosiripojana N. Biocatalytic esterification of palm oil fatty acids for biodiesel production using glycine-based cross-linked protein coated microcrystalline lipase. *Journal of Molecular Catalysis. B: Enzymatic*. 2011; 73: 74-9.
- Ramachandran K, Suganya T, Nagendra GN, Renganathan S. Recent developments for biodiesel production by ultrasonic assisted transesterification using different heterogeneous catalysts: A review. *Renewable & Sustainable Energy Reviews*. 2013; 22: 410-418.
- Istadi I, Prasetyo AP, Nugroho TS. Characterization of K₂O/CaO-ZnO catalyst for transesterification of soybean oil to biodiesel. *Procedia Environmental Science*. 2014; 23: 394-9.
- Abdulkareem-Alsultan G, Asikin-Mijan N, Lee HV, Taufiq-Yap YH. A new route for the synthesis of La-Ca oxide supported on nano activated carbon via vacuum impregnation method for one pot esterification transesterification reaction. *Chemical Engineering Journal*. 2016; 304: 61-71.
- Kesic Ž, Lukić I, Brkić D, Rogan J, Zdujić L, Liu H, Skala D. Mechanochemical preparation and characterization of CaO·ZnO used as catalyst for biodiesel synthesis. *Applied Catalysis, A: General*. 2012; 427: 58- 65.
- Kesic Ž, Lukić I, Zdujić L, Liu H, Skala D. Mechanochemical synthesis of CaO·ZnO·K₂CO₃ catalyst: Characterization and activity for methanolysis of sunflower oil. *Chemical Industry and Chemical Engineering Quarterly*. 2015; 21(1): 1-12.

17. Fuwape JA, Onyekwelu JC, Adekunle, VAJ. Biomass equations and estimation for *Gmelina arborea* and *Nauclea diderrichii* stands in Akure forest reserve. *Biomass & Bioenergy*. 2001; 21: 401-5.
18. Kansedo J, Lee KT. Process optimization and kinetic study for biodiesel production from nonedible sea mango (*Cerbera odollam*) oil using response surface methodology. *Chemical Engineering Journal*. 2013; 214: 157-64.
19. Šánek L, Pecha J, Kolomazník K, Bařinová M. Biodiesel production from tannery fleshings: Feedstock pretreatment and process modeling. *Fuel*. 2015; 148: 16-24.
20. Okoro LN, Fadila IS, Mukhtar L, Clifford N. Thermodynamic and viscometric evaluation of biodiesel and blends from olive oil and cashew nut oil. *Research Journal of Chemical Sciences*. 2011; 1(4): 90-7.
21. AOCS Methods Ca 5a-40, Official methods and recommended practices of the American Oil Chemists' Society. American Oil Chemists Society, Champaign IL, USA; 2000a.
22. AOCS Method Cd 3b-76, Official methods and recommended practices of the American Oil Chemists' Society, 5th Ed., American Oil Chemists Society, Champaign IL, USA; 2000b.
23. ASTM Method D6751-02 "Standard specification for biodiesel fuel (B100) blend stock for distillate fuels" ASTM International, West Conshohocken, PA, Pennsylvania, United States of America; 2002.
24. Das S, Khushalani D. Nonhydrolytic route for synthesis of ZnO and its use as a recyclable photocatalyst. *Journal of Physical Chemistry C*. 2010; 114: 2544-50.
25. Etacheri V, Roshan R, Kumar V. Mg-doped ZnO nanoparticles for efficient sunlight-driven photocatalysis. *ACS Applied Materials & Interfaces*. 2012; 4: 2717-25.
26. Feyzi M, Zinatizdeh AAL, Nouri P, Jafari F. Catalytic performance and characterization of promoted K-La/ZSM-5 nanocatalyst for biodiesel production. *Iranian Journal of Chemistry and Chemical Engineering*. 2018; 37(2): 33-44.
27. Feyzi M, Khajavi G. Investigation of biodiesel production using modified strontium nanocatalysts supported on the ZSM-5 zeolite. *Industrial Crops and Products*. 2014; 58: 298-304.
28. Meher LC, Naik SN, Das LM. Methanolysis of *Pongamia pinnata* (Karanja) oil for production of biodiesel, *Journal of Scientific and Industrial Research*. 2004; 63: 913-8.
29. Hoekman SK, Broch A, Robbins C, Cenicerós E, Natarajan M. Review of biodiesel composition, properties, and specifications. *Renewable and Sustainable Energy Reviews*. 2012; 16: 143- 69.
30. Rashid U, Anwar F, Moser BR, Knothe G. Moringa oleifera oil: A possible source of biodiesel. *Bioresource Technology*. 2008; 99: 8175-9.
31. Knothe G. "Designer" Biodiesel: Optimizing fatty ester composition to improve fuel properties. *Energy Fuels*. 2008; 22: 1358-64.
32. Berman P, Nizri S, Wiesman Z. Castor oil biodiesel and its blends as alternative fuel, *Biomass & Bioenergy*. 2011; 35: 2861-6.
33. Nautiyal P, Subramanian KA, Dastidar MG. Kinetic and thermodynamic studies on biodiesel production from *Spirulina platensis* algae biomass using single stage extraction-transesterification process. *Fuel*. 2014; 135: 228-34.
34. Astria DF, Ilvania CV, Fraderico AL, Heiddy MA, Vitor HM. Thermodynamic analysis of the kinetics reaction of the production of FAME and FAEE using Novazyme-435 as catalyst. *Fuel Processing Technology*. 2011; 92: 1007-11.
35. Ahmad AL, Mat Yasin NH, Derek CJC, Lim JK. Kinetic studies and thermodynamics of oil extraction and transesterification of *Chlorella* sp. for biodiesel production. *Environmental Technology*. 2014; 35: 881-7.
36. Engel T, Reid P. *Physical chemistry*. Pearson Education, San Fransisco; 2006.



A Green and Efficient Process for the Synthesis of Benzothiazinones using Phosphate Fertilizers MAP, DAP and TSP as Heterogeneous Catalysts

Imane Bahammou  , Badr Malek  , Tourya Ghailane  , Rachida Ghailane  ,
Said Boukhris  , Abdelaziz Souizi*  

Laboratory of Organic, Organometallic and Theoretical Chemistry, University Ibn Tofail, B.P.

Abstract: The aim of this work is to demonstrate the efficiency of the phosphate fertilizers mono-ammonium phosphate (MAP), di-ammonium phosphate (DAP), and triple-super phosphate (TSP) as a "green" heterogeneous catalyst for the synthesis of 2-aryl-2H-benzo[b][1,4]thiazin-3(4H)-ones via the C-S and C-N coupling process of *gem*-dicyano epoxide with α -aminothiophenol. To optimize the reaction conditions, the synthesis was conducted with a range of solvents, catalyst amounts, and particle sizes of the catalyst. Also, the recyclability potential of the catalysts was confirmed by using the recycled catalyst.

Keywords: Heterogeneous catalyst, phosphate fertilizer, MAP, DAP, TSP, Benzothiazinone.

Submitted: May 10, 2019. **Accepted:** August 09, 2019.

Cite this: Bahammou I, Malek B, Ghailane T, Ghailane R, Boukhris S, Souizi A. A Green and Efficient Process for the Synthesis of Benzothiazinones using Phosphate Fertilizers MAP, DAP and TSP as Heterogeneous Catalysts. JOTCSA. 2019;6(3):349-54.

DOI: <https://doi.org/10.18596/jotcsa.563093>.

*Corresponding author. E-mail: Souizi@yahoo.com. Tel: +212661183260.

INTRODUCTION

To date, benzothiazinone (BTZ) skeleton have been extensively used as pharmacophore group for the construction of numerous biologically active compounds such as anti-tubercular (1), antimicrobial (2), allosteric modulator (3), inhibitor of glycogen synthase kinase 3 β (3), monoamine oxidase B inhibitors (4), adenosine A2A receptor antagonists (4), antioxidant (5), anti-candida (6) and antitumor agents (7).

Currently, BTZ compounds were identified as a possible new class of acetylcholinesterase inhibitors for curing the symptoms of Alzheimer's disease (8).

In continuation of evaluation of BTZ's properties, Ghailane et al. (9) were able to classify some BTZ derivatives as anticorrosive agents for mild steel in 1M HCl based on quantum chemical studies and electrochemical measurements.

Given the importance of BTZ heterocyclic systems, they have been the object of several synthetic studies. For example, BTZ derivatives were successfully synthesized by the condensation of α -aminothiophenol with aryltrichlorocarbinol (10), or dibromonitroacrylates (11), from methyl 2-iodobenzoate and cyclic thiourea (12) or 2-mercaptoacetate and substituted 2-iodoanilines (13) via the Cu-catalyzed coupling processes. In attempts to establish a green approach to elaborate new derivatives of BTZ, Sharifi et al. (14) developed a green synthesis of various benzothiazinones via the condensation of 2-bromoalkanoates with α -aminothiophenol using ball milling and KF-Al₂O₃ support. Recently, new, facile, and regio-controlled methods to obtain BTZ derivatives by reacting α -aminothiophenol with different electron acceptor epoxides were reported (15). Therefore, the improvement of these methods in terms of reaction time, product purity and yield is highly desirable given environmental considerations.

MAP, DAP, and TSP are ones of the most important and popular members of phosphate fertilizers family due to their composition rich in nitrogen (from NH_4^+ (MAP, DAP)), phosphorus (from PO_4^{3-} (MAP, DAP, TSP)) and calcium (from Ca (TSP)). Nowadays, they prove to be eco-friendly, economically and highly active heterogeneous catalysts for Knoevenagel condensation (16), 2,3-dihydroquinazolin-4(1H)-one synthesis (17) and synthesis of 1-(benzothiazolylamino) methyl-2-naphthol derivatives (18).

As part of our previous efforts to valorize phosphate fertilizers (16) we describe herein a 'green' optimization of the one-pot synthesis of BTZ derivatives from *gem*-dicyano epoxide **1** as described by Ghailane et al. (15) using MAP, DAP and TSP fertilizers as novel heterogeneous and reusable catalysts.

EXPERIMENTAL

Chemicals and instruments

Chemicals were purchased from Fluka or Aldrich Companies. Catalysts MAP, DAP and TSP, were purchased from OCP group. They are marked as mention in our previous work (16). Mono-Ammonium Phosphate: MAP 11-52-00 - Binary Fertilizer, complex granule with Nitrogen: 11% N and Phosphorus: 52% P_2O_5 . Di-Ammonium Phosphate: DAP 18-46-00 - Binary Fertilizer, complex granule with Nitrogen: 18% N and Phosphorus: 46% P_2O_5 . Triple Super Phosphate: TSP 00-46-00 - Simple granule Fertilizer with Phosphorus: 46% P_2O_5 .

All known compounds were identified by comparing their melting points with literature data. Melting points were recorded on a Wagner & Munz HEIZBANK Kofler bench.

Separation of catalyst's particles according to their size

The catalyst was crushed and sieved on a mechanical sieve shaker to provide different size of catalyst particles. Three different powders of catalysts MAP, DAP and TSP were tested in this

work. The first (designated F_1) comprised catalyst powder in size range of 36-71 μm . The second (designated F_2) was of the size range between 71 and 90 μm . The last powder tested (designated F_3) comprised between 91 and 120 μm .

General experimental procedure for the phosphate fertilizers MAP, DAP and TSP catalyzed the one-pot synthesis of 2-(*p*-tolyl)-2*H*-benzo[*b*][1,4]thiazin-3(4*H*)-one, **3a**

Into a 25 mL round-bottomed flask equipped with a reflux condenser and mechanical stirrer were placed 2 mmoles of epoxide **1**, 2 mmoles of α -aminothiophenol **2** dissolved in 3 mL of acetonitrile. 10 mol% of catalyst was then added to the mixture. The latter was stirred for an appropriate time. The progress of the reaction was monitored by TLC, eluted with chloroform/petroleum ether (2:1). After completion of the reaction, the mixture was filtered to separate the catalyst. Then, the solvent of the filtrate was removed under vacuum, and the oily residue obtained was triturated with a mixture of diethyl ether and petroleum ether (9:1) to give 2-arylbenzothiazin-3-one as a solid which was collected and crystallized from ethanol.

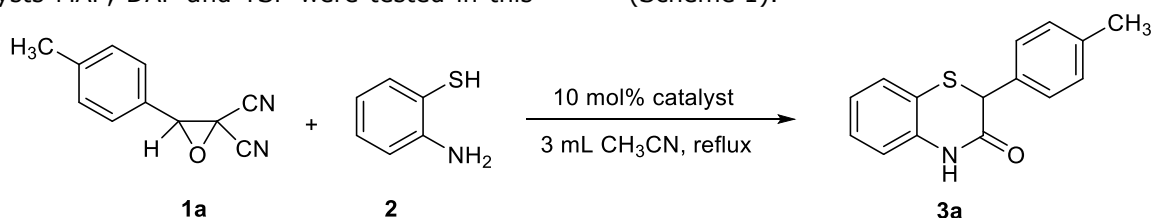
Recyclability studies on the catalysts

The catalyst separated from the mixture was rinsed with EtOH (2 \times 5 mL), dried at 70 $^\circ\text{C}$ for 6 hours and reused for subsequent catalytic reactions.

RESULTS AND DISCUSSION

Catalytic synthesis of BTZ

To obtain the optimal reaction conditions, one-pot synthesis of BTZ was carried out using MAP, DAP and TSP as heterogeneous catalysts. The reaction of epoxide **1a** with α -aminothiophenol was selected as a model reaction to produce 2-(*p*-tolyl)-2*H*-benzo[*b*][1,4]thiazin-3(4*H*)-one (**3a**). In the preliminary studies, the reaction was conducted following the conventional synthesis conditions earlier described (12) in the presence of 10 mol% of catalyst from fraction 1 (F_1) (Scheme 1).



Scheme 1: Synthesis of compounds **3a** in the presence of MAP, DAP or TSP catalysts.

Table 1: Catalytic test runs.

Entry	Catalyst	Time	Yield (%)
1	Neat	22 h	80
2	MAP	1 h 20	87
3	DAP	1 h	85
4	TSP	2 h	82

Influence of reaction parameters*Effects of reaction solvent*

After screening the potential activity of phosphate fertilizers MAP, DAP, and TSP, an optimized procedure for the preparation of 2-(*p*-tolyl)-2*H*-benzo[*b*]1,4]thiazin-3(4*H*)-one (**3a**) over these heterogeneous catalysts were therefore developed. Initially, the reaction was carried out in several solvents including MeCN, EtOH, AcOEt, CHCl₃ using 10 mol% of catalyst (F₁) (Table 2). As shown, the three catalysts tested were highly active and gave the desired BTZ **3a** in high yields within short reaction time in EtOH (Table 2, entries 4, 5 and 6). These results can be explained by the fact that EtOH contains polar molecules and an acidic hydrogen atom which is liable to establish a hydrogen bond with the oxygen atom of epoxide to facilitate the bi-nucleophilic attack of α -aminothiophenol.

Effects of catalysts' amount

The catalytic activities were then tested with a range of catalyst amounts (F₁), from 10 mol% up to 40 mol%, to determine the optimal catalyst loading for each catalyst. The reaction was conducted under otherwise identical reaction conditions in the presence of EtOH as a solvent. As can be seen, MAP, DAP and TSP catalysts exhibited high activities under a catalyst loading of 10 mol% and afforded the desired product within 40, 35, and 55 minutes, respectively, in high yields (Table 3, entries 1, 5 and 9). A further increase in the catalysts' amounts up to 40 mol% resulted in an extension of the reaction time with a slight decrease in the product yield, indicating the catalyst amount of 10 mol% to be optimal. This observation established the excellent catalytic activity of the recently developed catalysts.

Table 2: Optimization of the reaction solvent using MAP, DAP and TSP catalysts.

Entry	Catalyst (10 mol %)	Solvent (3 mL)	Time	Yield (%)
1	MAP	MeCN	1 h 20	87
2	DAP	MeCN	1h	85
3	TSP	MeCN	2h	82
4	MAP	EtOH	40 min	92
5	DAP	EtOH	35 min	89
6	TSP	EtOH	55 min	90
7	MAP	AcOEt	3 h 30	75
8	DAP	AcOEt	3 h	73
9	TSP	AcOEt	2h 50	65
10	MAP	CHCl ₃	3 h 10	63
11	DAP	CHCl ₃	3 h 40	60
12	TSP	CHCl ₃	4 h	55

Table 3: Optimization of the catalysts amount for the synthesis of 2-(*p*-tolyl)-2*H*-benzo[*b*][1,4]thiazin-3(4*H*)-one **3a**.

Entry	Catalyst	Catalyst loading (%)	Time	Yield (%)
1	MAP	10	40 min	92
2	MAP	20	55 min	91
3	MAP	30	1 h 10	85
4	MAP	40	1 h 25	82
5	DAP	10	35 min	89
6	DAP	20	45 min	88
7	DAP	30	1 h	85
8	DAP	40	1 h 15	83
9	TSP	10	55 min	90
10	TSP	20	1 h 05	85
11	TSP	30	1 h 20	83
12	TSP	40	1 h 35	79

Effects of catalysts' particle size

In the current study, we also focused on determining the effect of the catalysts' particle size in an attempt to compare the results with those obtained in our previous work (18). No remarkable influence of the catalyst particle size

on the catalysts activities was observed. The results prove our previous findings that the three phosphate fertilizers MAP, DAP and TSP can constantly show high catalytic activities even when their particle size increases.

Table 4: Screening of the effects of catalyst particle size on the catalytic activities of MAP, DAP and TSP for the synthesis of 2-(*p*-tolyl)-2*H*-benzo[*b*][1,4]thiazin-3(4*H*)-one **3a**.

Entry	Catalyst (10 mol%)	Particle size range	Time (min)	Yield (%)
1	MAP	36-71 μm	40	92
2	MAP	71-90 μm	40	93
3	MAP	90-120 μm	40	91
4	DAP	36-71 μm	35	89
5	DAP	71-90 μm	35	89
6	DAP	90-120 μm	40	88
7	TSP	36-71 μm	55	90
8	TSP	71-90 μm	55	88
9	TSP	90-120 μm	55	91

Control of the generality of the catalysts

To further screen the scope and the generality of our new catalysts, the reaction of α -aminothiophenol with various substituted epoxides for the synthesis of BTZ derivatives was studied under the optimized conditions using catalyst from fraction 1 (F_1). As shown in Table 5, almost all of the epoxide substrates with either

electron-withdrawing or electron-donating substitution furnished the corresponding adducts in high yields. It is noteworthy that the reaction time was extended to 45 min for MAP, 50 min for DAP and 1h for TSP when the epoxide was substituted with the nitro group (Table 5, Entries 7, 8 and 9).

Table 5. Synthesis of BTZ derivatives over phosphate fertilizers MAP, DAP and TSP under the optimized conditions.

Entry	R	1	Catalyst	Product	Time (min)	Mp (°C)	Yield (%)
1	CH ₃	1a	MAP	3a	40	198-199	92
2	CH ₃	1a	DAP	3a	35	198-199	89
3	CH ₃	1a	TSP	3a	55	198-199	90
4	Cl	1b	MAP	3b	25	186-187	96
5	Cl	1b	DAP	3b	30	186-187	93
6	Cl	1b	TSP	3b	40	186-187	94
7	NO ₂	1c	MAP	3c	45	202-203	92
8	NO ₂	1c	DAP	3c	50	202-203	85
9	NO ₂	1c	TSP	3c	60	202-203	90

Recyclability studies on the catalysts

In another study, the reaction of epoxide **1a** and α -aminothiophenol **2** was tested in the presence of recovered MAP, DAP and TSP to establish the reusability of the three catalysts developed for

the synthesis of 2-(*p*-tolyl)-2*H*-benzo[*b*][1,4]thiazin-3(4*H*)-one **3a**, the results are displayed in Table 6. To our delight, MAP, DAP and TSP catalysts were found to be reusable with consistency in activity up to four times.

Table 6. Recyclability of MAP, DAP and TSP catalysts.

Entry	Catalyst	Run number	Time(min)	Yield (%)
1	MAP	1	40	92
2	MAP	2	40	92
3	MAP	3	40	91
4	MAP	4	40	90
5	DAP	1	35	89
6	DAP	2	35	88
7	DAP	3	35	88
8	DAP	4	35	87
9	TSP	1	55	90
10	TSP	2	55	88
11	TSP	3	55	88
12	TSP	4	55	87

CONCLUSIONS

Through this study, we demonstrated the catalytic efficiency of the phosphate fertilizers MAP, DAP and TSP for the C-S and C-N coupling reactions. A "green" optimized procedure was therefore designed for the synthesis of 2-aryl-2*H*-

benzo[*b*][1,4]thiazin-3(4*H*)-ones from α -aminothiophenol and *gem*-dicyano epoxide.

ACKNOWLEDGEMENT

This study was financially supported by the Research Excellence Award Program of the

National Center for Scientific and Technical Research (CNRST-Rabat, Morocco).

REFERENCES

- Xiong L, Gao C, Shi YJ, Tao X, Rong J, Liu KL, Peng CT, Wang NY, Lei Q, Zhang YW, Yu LT, Wei YQ. Identification of a new series of benzothiazinone derivatives with excellent antitubercular activity and improved pharmacokinetic profiles. *RSC Adv.* 2018; 8:11163-76.
- Armenise D, Muraglia M, Florio MA, De Laurentis N, Rosato A, Carrieri A, Corbo F, Franchini C. 4H-1, 4-Benzothiazine, Dihydro-1, 4-benzothiazinones and 2-Amino-5-fluorobenzenethiol Derivatives: Design, Synthesis and in vitro Antimicrobial Screening. *Arch Pharm.* 2012; 345:407-16.
- Zhang P, Li S, Gao Y, Lu W, Huang K, Ye D, Li X, Chu Y. Novel benzothiazinones (BTOs) as allosteric modulator or substrate competitive inhibitor of glycogen synthase kinase 3 β (GSK-3 β) with cellular activity of promoting glucose uptake. *Bioorg Med Chem Lett.* 2014; 24:5639-43.
- Stöbel A, Schlenk M, Hinz S, Küppers P, Heer J, Gütschow M, Müller CE. Dual targeting of adenosine A2A receptors and monoamine oxidase B by 4 H-3, 1-benzothiazin-4-ones. *J Med Chem.* 2013; 56:4580-96.
- Kumar M, Sharma K, Samarth RM, Kumar A. Synthesis and antioxidant activity of quinolinobenzothiazinones. *Eur J Med Chem.* 2010; 45:4467-72.
- Borate HB, Maujan SR, Sawargave SP, Chandavarkar MA, Vaiude SR, Joshi VA, Wakharkar RD, Iyer R, Kelkar RG, Chavan SP, Kunte SS. Fluconazole analogues containing 2H-1, 4-benzothiazin-3 (4H)-one or 2H-1, 4-benzoxazin-3 (4H)-one moieties, a novel class of anti-Candida agents. *Bioorg Med Chem Lett.* 2010; 20:722-5.
- Kamel MM, Ali HI, Anwar MM, Mohamed NA, Soliman AM. Synthesis, antitumor activity and molecular docking study of novel Sulfonamide-Schiff's bases, thiazolidinones, benzothiazinones and their C-nucleoside derivatives. *Eur J Med Chem.* 2010; 45:572-80.
- Berwaldt GA, Gouvêa DP, da Silva DS, das Neves AM, Soares MS, Azambuja JH, Spanevello RM, Cunico W. Synthesis and biological evaluation of benzothiazin-4-ones: a possible new class of acetylcholinesterase inhibitors. *J Enzyme Inhib Med Chem.* 2019; 34:197-203.
- Ghailane T, Balkhmima RA, Ghailane R, Souizi A, Tourir R, Touhami ME, Marrakchi K, Komiha N. Experimental and theoretical studies for mild steel corrosion inhibition in 1 M HCl by two new benzothiazine derivatives. *Corros Sci.* 2013; 76:317-24.
- Willardsen JA, Dudley DA, Cody WL, Chi L, McClanahan TB, Mertz TE, Potoczak RE, Narasimhan LS, Holland DR, Rapundalo ST, Edmunds JJ. Design, synthesis, and biological activity of potent and selective inhibitors of blood coagulation factor Xa. *J Med Chem.* 2004; 47:4089-99.
- Makarenko SV, Kovalenko KS, Vershinina YS, Berestovitskaya VM. One-pot synthesis of substituted 1,3-benzothiazole and 1,4-benzothiazinone from dibromonitroacrylates. *Russ J Org Chem.* 2014; 50:83-6.
- Chen D, Wu J, Yang J, Huang L, Xiang Y, Bao W. Cascade syntheses of aza[2,1-b][1,3]-benzothiazinone heteropolycyclic compounds from cyclic thiourea catalyzed by Cu(I). *Tetrahedron Lett.* 2012; 53:7104-7.
- Huang W-S, Xu R, Dodd R, Shakespeare WC. Facile synthesis of 1, 4-benzothiazin-3-ones from Cu-catalyzed coupling of 2-iodoanilines and 2-mercaptoacetate. *Tetrahedron Lett.* 2013; 54:5214-6.
- Sharifi A, Ansari M, Darabi HR, Abaee MS. Synergistic promoting effect of ball milling and KF-alumina support for the green synthesis of benzothiazinones. *Tetrahedron Lett.* 2016; 57: 529-32.
- Ghailane T, Saadouni M, Boukhris S, Habbadi N, Hassikou A, Kerbal A, Garrigues B, Souizi A. Regio-controlled synthesis of 1,4-benzothiazinones. *Heterocycles.* 2011; 83:357-63.
- Bahammou I, Esaady A, Boukhris S, Ghailane R, Habbadi N, Hassikou A, Souizi A. Direct use of mineral fertilizers MAP, DAP, and TSP as heterogeneous catalysts in organic reactions. *Mediterr J Chem.* 2016; 5:615-23.
- Merroun Y, Chehab S, Ghailane T, Boukhris S, Ghailane R, Habbadi N, Hassikou A, Lakhrissi B, Souizi A. An effective method to synthesize 2,3-dihydroquinazolin-4(1H)-One using phosphate fertilizers (MAP, DAP and TSP) as green heterogeneous catalysts. *J Turk Chem Soc Sect A Chem.* 2018; 5:303-16.
- Zimou O, Malek B, Elhallaoui A, Ghailane T, Ghailane R, Boukhris S, Habbadi N, Hassikou A, Souizi A. Valorization of the Phosphate Fertilizers Catalytic Activity in 1-(Benzothiazolylamino) Methyl-2-Naphthol Derivatives Synthesis. *Bull Chem React Eng Catal.* 2019; 14:238-46.



Evaluation of Changes in the Biological Activity of *Onosma Sericeum Willd (Boraginaceae)* Based on Collection Time and Extraction Solvent, and Determination of Its Mineral and Trace Element Composition

Selda Doğan Çalhan^{1*}  , Mustafa Gündoğan²  

¹Mersin University, Faculty of Pharmacy, Department of Pharmaceutical Biotechnology, 33169 Mersin, Turkey.

²Mersin University, Faculty of Pharmacy, Department of Pharmaceutical Technology, 33169 Mersin, Turkey.

Abstract: In this study, total phenol, flavonoid, and free radical scavenging activity of *Onosma Sericeum Willd (Boraginaceae)*, a plant grown in Turkey and traditionally used for wound healing, were determined by using spectrophotometric methods. Its cytotoxic effect on breast cancer cells (MCF-7) was investigated. Furthermore, mineral and trace element composition of the plant roots, collected in different times, was determined by using inductively coupled plasma mass spectroscopy (ICP-MS). *Onosma Sericeum Willd*, which was collected in Besni region, Adiyaman in May, June and July and dried properly, was extracted by using different solvents in the study. Total phenol content of the extracts was calculated by using the Folin-Ciocalteu method in gallic acid equivalent as 58.42±0.13–93.34±0.68 mg (GAE)/g. The flavonoid content was calculated as 21.79±1.3–60.33±0.36 mg (KUE)/g in quercetin equivalent by using the aluminum chloride method. Free radical scavenging activity was measured spectrophotometrically by using the 2,2-diphenyl-1-picrylhydrazyl (DPPH) assay. DPPH radical scavenging activity rates were found to be in the range of 60.27±0.06–78.60±0.21% in the form of % inhibition. It was observed that extracts which were prepared by using ethanol produced the cytotoxic effect on the MCF-7 cancer cells depending on the dosage. It was concluded that the rates of phenol, flavonoid, free radical scavenging activity, and cytotoxic effect differed based on the solvent used for extraction and the time of plant collection. Moreover, trace element and mineral composition of the plant samples, collected in different times, were determined.

Keywords: Boraginaceae, phenolic species, antioxidant activity, wound healing, element composition.

Submitted: July 01, 2019. **Accepted:** August 25, 2019.

Cite this: Doğan Çalhan S, Gündoğan M. Evaluation of Changes in the Biological Activity of *Onosma Sericeum Willd (Boraginaceae)* Based on Collection Time and Extraction Solvent, and Determination of Its Mineral and Trace Element Composition. JOTCSA. 2019;6(3):355–64.

DOI: <https://doi.org/10.18596/jotcsa.585036>.

***Corresponding author. E-mail:** seldadgn@gmail.com.

INTRODUCTION

Mankind has sought ways of coping with diseases since the beginning of the world, and this adventure is still ongoing. One of the primary sources used by people in this process is plants. Archeological research indicates that herbal medicine dates back to the ancient times. Increased knowledge of plants over time and positive outcomes of the treatment of diseases brought along the concept of medication. Therefore, the first medications were herbal drugs. Considering the plant diversity and

population worldwide, and the possibility of finding dozens of active substances with pharmaceutical efficacy in every plant, we come to realize how an endless world we live in. Hence, knowledge that has been acquired and learned for centuries has resulted in the cooperation of different disciplines in this area.

Turkey hosts a wide variety of plant species due to its geographical location and diverse climate. One of them is the family Boraginaceae. Spread in the tropical, subtropical and temperate regions of the world, the family is represented

by 154 genus and 2500 species. The primary regions where the family shows greatest diversity are Iran-Turan and the Mediterranean. The family is also present in the Central and North America. Growing in different regions of Turkey, the family Boraginaceae includes 357 taxons, consisting of 34 genera, 325 species, 16 subspecies and 16 variants. Phytochemical analyses indicate that the family Boraginaceae, rich in naphthoquinone, includes alkannin-shikonin and their derivatives (1). In pharmacological activity studies, it is acknowledged that these are strong candidates with pharmaceutical potential thanks to their antimicrobial, antifungal and anti-inflammatory activity as well as anticancer effects with the inhibition of topoisomerase I and topoisomerase II (2). The genus *Onosma* L. is the largest one in the family Boraginaceae (3,4). The word *Onosma* derives from the Greek word "onos" and "osmê", and Latin word "osma". It means "scent, fragrance", and locally known as "emzik otu" or "yalancı hava civa" in Turkish.

Because of the considerable use of the *Onosma* species particularly in traditional medicine,



significant research has been conducted on them for many years. Traditional use of the *Onosma* species among local people in Turkey includes the treatment of bronchitis, tonsillitis and hemorrhoid (5). It was found that root extract of the *Onosma argentatum* comprises bioactive compounds with antioxidant and antimicrobial effects such as deoxyshikonin, acetylshikonin, 3-hydroxy-isovalerylshikonin and 5,8-O-dimethyl acetylshikonin (6,7). It was reported that *Onosma echioides* extract helps diminishing the growth of tumors and oxidative stress (8). Ozer et al. stated that *Onosma heterophyllum* (Griseb) has enzyme inhibitory and antioxidant activities (9).

It is well known that some species under the family Boraginaceae (*Onosma Sericeum* Willd., *Onosma Microcarpum* Steven ex D.C.) produce wound healing effects in traditional application, and are used for the treatment of burns (10). *Onosma Sericeum* Willd in particular is used in diverse areas such as food and textile thanks to the red pigments in its roots (11).



Figure 1. *Onosma Sericeum* Willd.

Onosma sericeum, the subject of this study, has been used to treat injuries and burns in Adiyaman for many years. It is known that mostly cream formulations, prepared with the roots of the plant, help treatment, without leaving scars. As is well-known, natural and/or synthetic molecules have been used for a long time for treatment in the process of healing injuries, in which many different variables are at play. Among them, especially plants and plant extracts attract a great deal of attention. Plants are frequently used in healing injuries due to their phenolic compounds and antioxidant properties in particular. It is known that polyphenols and antioxidants, considered as bioactive compounds, have antiinflammatory and anticarcinogenic effects (12). Another important point about plants is the time of collection, because the amount and composition

of bioactive compounds may vary depending on the time they are collected. Another aim of this study was to explore the mineral and trace element composition of the *Onosma Sericeum* Willd, in addition to its biological activities, which has been the subject of few studies. Determining the mineral and trace element composition of the plant is vital for both identifying its positive effects on metabolic processes and human health, and for detecting potential toxic effects on plants with increasing environmental pollution. This is because element levels are affected by pesticide residues, industrial pollution and automobile exhaust to which the plant is exposed where it grows (13,14).

In light of this information, the *Onosma Sericeum* Willd, a member of the family Boraginaceae, was collected in May, June and

July, extracted by using different solvents, and total phenolic, flavonoid content and free radical scavenging activity of the extracts were determined. Cytotoxic effect of different extracts on the MCF-7 breast cancer cell was investigated. Trace element and mineral composition of the plant which was gathered in different times was also identified.

MATERIALS AND METHODS

Collection and Identification of Plant Material

Specimens of the *Onosma Sericeum Willd (Boraginaceae)* used in the study were gathered in Besni district of Adiyaman, Turkey in May, June and July 2018. The plant was identified by Assoc. Prof. Rıza Binzet from the Department of Biology of the Faculty of Arts and Sciences, Mersin University. After properly dried, roots of the plant were used throughout the study.

Materials

Methanol and ethanol, used as extraction solvents in the study, were procured from Merck. Folin-Ciocalteu phenol reagent, 2,2-diphenyl-1-picrylhydrazyl (DPPH), ascorbic acid, and gallic acid were obtained from Sigma. Sodium carbonate was procured from Tekkim. Quercetin, aluminum chloride (Fluka), sodium nitrite (Merck) and sodium hydroxide were supplied by Sigma. Nitric acid (65%, Merck), hydrochloric acid (37%, Merck), hydrogen peroxide (30%, Merck), and dimethyl sulfoxide (99.9%, Merck) were used in experimental work. Cell culture applications used fetal bovine serum (Sigma), Trypsin-EDTA solution (Sigma), Penicillin-Streptomycin solution (Sigma), Thiazolyl blue tetrazolium bromide (MTT) (98%, Sigma) and RPMI 1640 medium (Sigma). The MCF-7 breast cancer cells were procured from ATCC (catalogue number: HTB-22). All the chemicals used in the study were of analytical grade, and 18.2 mΩ of distilled water needed throughout the research was obtained through the Milli-Q A10 water purification system.

Instruments

All spectrophotometric measurements were conducted by using a Shimadzu UV-1601 spectrophotometer. Element and mineral composition was analyzed by using the Agilent 7500ce Inductively Coupled Plasma-Mass Spectrometry (ICP-MS). CEM Mars 240/50 microwave system was used to digest the samples on the ICP-MS. Thermal shaking water bath was used for plant extraction. The study also used Heidolph Reaxtop vortex and Heidolph Laborota 4000 efficient evaporator.

Extraction Procedure

5 g of crushed plant roots was obtained, and mixed with 25 mL of ethanol (EtOH), methanol (MeOH), and boiled water, respectively. It was kept in shaking water bath for 1 hour. This procedure was repeated 3 times. Later, the

extracts were filtered with white filter paper and evaporated at maximum 40 °C by using a rotary evaporator. Dried extracts were dispersed by using solvents, and stock solutions were prepared and filtered through 0.45 μm membrane filters. The stock solutions were stored under suitable conditions to be used in determining biological activity and trace element/mineral composition. Nine different extracts which were collected in May, June and July were named as May EtOH, May MeOH, May water, June EtOH, June MeOH, June water, July EtOH, July MeOH and July water.

Total Phenolic Content Analysis

Total phenolic content of the extracts was determined spectrophotometrically by using the Folin-Ciocalteu method (15). 100 μL of sample/extract sample was mixed with 7900 μL of distilled water and 500 μL of Folin-Ciocalteu's reagent in a test tube (10%, v/v in water). The mixture was vortexed and allowed to stand to incubate in the dark at room temperature for 2 minutes. After that, 1.5 mL of Na₂CO₃ (20%) solution (w/v) was added to the mixture, and it was vortexed again. After the mixture was kept in the dark at room temperature for 2 hours, absorbance of the resulting blue solutions was measured by using the UV spectrophotometer at 765 nm wavelength. Gallic acid was used as standard. Results were expressed as average of the three measurements, in mg GAE/g dry weight.

Total Flavonoid Content Analysis

Total flavonoid content of the extracts was determined spectrophotometrically through the aluminum chloride/sodium nitrite method (16). After 500 μL of extract sample, diluted to a certain extent, was placed in a test tube with 3 mL of distilled water, 0.3 mL of aqueous NaNO₂ solution (5%) was added, and the mixture was vortexed. After 5 minutes, 0.3 mL of aqueous AlCl₃ solution (10%) was added to the mixture. Then, by adding 2 mL of 1 M NaOH after 1 minute, the final volume of the mixture was completed to 10 mL, with distilled water. This final mixture was vortexed again, and its absorbance was measured at 510 nm. Results were expressed as the average of the three measurements, in mg Quercetin/g dry weight.

DPPH-Free Radical Scavenging Activity

Free radical scavenging activity of the extracts was assessed spectrophotometrically through the DPPH method (17). 100 μL of the root extract and ascorbic acid solution with different concentrations, used as standard, was mixed with 2.9 mL of 80 μM DPPH solution, freshly prepared in methanol. The mixture was vortexed and kept in the dark for 1 hour to incubate. After this procedure, absorbance of each mixture was measured at 517 nm. The results are given as average of the three measurements, in % inhibition (Equation 1).

$$\% \text{ Inhibition} = \frac{(\text{Abs}_{\text{control}} - \text{Abs}_{\text{sample}})}{\text{Abs}_{\text{control}}} \times 100 \quad (\text{Eq. 1})$$

Cytotoxic Effect

The MTT (3-(4,5-dimethylthiazolyl-2)-2,5-diphenyltetrazolium bromide) assay, a colorimetric method, is based on the principle of the reduction of tetrazolium salt to colored formazans. Cell viability is assessed by dying the cells at various levels with the MTT according to their mitochondrial activity. After the formazan crystals are dissolved, reading is made at 570 nm wavelength. The present study used the method proposed by Turan et al. (18) with some modification. In the present study, the MCF-7 cells were seeded into 4 plates containing 96 wells, with 10^4 cells in each well. Water was placed in the outermost wells of the plates to adjust moisture balance. Nine samples (May EtOH, May MeOH, May water, June EtOH, June MeOH, June water, July EtOH, July MeOH, July water) were administered to the MCF-7 breast cancer cells in 3 different concentrations (50µg/

mL, 100 µg/mL, 200 µg/mL). The procedure was repeated 10 times for each concentration (n=10). After 24 hours, the extracts in the cells were taken from the wells and mixed with the MTT solvent. The cells were kept for incubation at 37 °C, with 5% CO₂. The plates were wrapped with aluminum foil to prevent the entrance of light. The cells were taken out after being kept in incubation for 5 hours, the medium over them was removed, and 200 µL of dimethyl sulfoxide was added to each well. In this way, unsolved formazan crystals were also dissolved. After waiting for 15 minutes, they were measured by using an ELISA set at 570 nm wavelength. Outer wells which did not contain any cells were introduced as empty. IC50 value and cell viability was calculated by using the absorbance rates and the formula in Equation 2.

$$\text{Relative cell viability (\%)} = \text{OD570 of the treated sample} / \text{OD570 of the control} \quad (\text{Eq. 2})$$

To count the viable cells, Cedex XS (Roche, Mannheim, Germany) was used. This device distinguishes between viable and non-viable cells with high precision, by providing information about cell concentration and viability based on the trypan blue exclusion method, in a semi-automatcal manner. 20 µL of resuspended cells were taken and added to 0.2 mL of Eppendorf tube. The cells were mixed with 20 µL of trypan blue solution (0.4%), diluted with distilled water which helps to distinguish between viable and non-viable cells (Roche, Mannheim, Germany). After this mixture was homogenized through pipetting, 20 µL of it was put in the Smart Slides chamber, special slide of the device (Roche, Mannheim, Germany). Later, the sample was placed on the Cedex XS cell counter in the chamber, and the cells were counted by using the software of the device.

Determination of Mineral and Trace Element Composition

0.5 g of the plant roots which were collected in May, June and July was obtained, and digested using the heat controlled microwave system. For this procedure, 12 mL of nitric acid-hydrochloric acid mixture and 1 mL of hydrogen peroxide were used. Digestion process took 30 minutes at 175 °C. The system settings of the device were optimized to 239 PSI and 720 w. After the resulting acidic solution was diluted properly, measurements were made through the ICP-MS. Operating parameters of the ICP-MS device are given in Table 1.

Statistical Analysis

The results were calculated by taking the average of the three measurements and standard deviation (mean±SD). Repeated Measures Analysis of Variant was used for

comparing more than two dependent averages (in different times). Contrast process was used to determine in which time intervals the difference occurred. The statistical significance level was set at 0.05 in all analyses. The data was analyzed by using SPSS 21.

Table 1. Operating Conditions of ICP MS.

Parameter	Value
RF power	1500 W
Sampling Depth	8.8mm
Flow Rates of Plasma Gas	15 L/min
Flow Rates of Carrier Gas	0.9 L/min
Flow Rates of Auxiliary Gas	1 L/min
Integration Time	0.60 s

RESULTS AND DISCUSSION

It is known that the genus *Onosma*, including the *Onosma Sericeum Willd*, the subject of the present study, is used in traditional treatment, especially in healing wounds (19, 20). Studies conducted on the *Onosma* roots found alkannin/ shikonin derivatives displaying biological activity and these structures have healing, anti-inflammatory, anti-tumor, anti-thrombotic, and anti-microbial properties (21-23). For this reason, it is highly important and necessary to carry out biological activity research on this genus. Thus, this study investigated the biological activity of the *Onosma Sericeum Willd* species, which is not studied as much as the other *Onosma* species, depending on collection time and extraction solvent. The study also determined its element composition which plays significant roles and/or has toxic effects in biological processes.

In the study, *Onosma Sericeum Willd* was collected in Besni region, Adiyaman in May, June

and July 2018, and its roots were extracted by using ethanol, methanol, and water. The total phenol, flavonoid content and DPPH radical scavenging activity of the extracts were determined. The cytotoxic effect of the extracts on the MCF-7 cells was investigated through the MTT method. Trace element and mineral composition of the plant samples, collected in different periods, was determined through the ICP-MS after the samples were digested using microwave.

Total phenol was determined by Folin-Ciocalteu reactive using the spectrophotometric method. A calibration graphic was created by preparing gallic acid solutions in specific concentrations (used as standard) and the amount of sample in the extract was calculated in gallic acid equivalent as 58.42 ± 0.13 - 93.34 ± 0.68 mg(GAE)/g by taking into consideration $y = 0.001x + 0.0033$, $R^2 = 0.9901$ regression equation and dilution.

The total flavonoid content was determined through the spectrophotometric method by using the aluminum chloride/sodium nitrite method. A calibration graphic was created by preparing quercetin solutions in specific concentrations (used as standard), and the amount of sample in the extract was calculated in quercetin equivalent as 21.79 ± 1.3 - 60.33 ± 0.36 mg(KUE)/g by taking into consideration $y = 0.0002x + 0.0078$, $R^2 = 0.9717$ regression equation and dilution.

The DPPH radical scavenging activity rates of the extracts were given in % inhibition which is used as the indicator of antioxidant activity. Calculations were carried out based on $y = -0.0038x + 0.7616$ regression equation and Equation 1. According to the results, it was found that the % inhibition rates were in the range of 60.27 ± 0.06 - 78.60 ± 0.21 %.

All the results are given as the average of the three measurements and with standard deviation rates (Table 2).

Table 2. Total phenol, flavonoid, and % inhibition rates of the *Onosma Sericeum Willd* extract.

	PHENOL CONTENT* mg GAE/g	FLAVONOID CONTENT *mg KUE/g	RADICAL SCAVENGING ACTIVITY*% Inhibition
May EtOH	93.34±0.68	60.33±0.36	60.27±0.06
May MeOH	70.46±1.31	46.79±0.95	62.13±0.21
May Water	62.36±0.13	24.5±1.65	78.60±0.22
June EtOH	75.01±1.31	40.54±0.95	67.37±0.11
June MeOH	68.19±1.31	32.21±0.95	61.09±0.27
June Water	60.46±0.13	23.25±1.25	73.82±0.22
July EtOH	70.08±0.47	42.42±0.95	66.87±0.38
July MeOH	59.78±0.26	31.58±1.30	60.81±0.23
July Water	58.42±0.13	21.79±1.30	73.75±0.62

* The results were given based on dry weight and as the average of three measurements.

An assessment of the results indicated that the rates of phenol, flavonoid, and free radical scavenging activity differed according to collection time and extraction solvent, and the difference between the averages was statistically significant. A statistically significant difference was found in the phenol content between May EtOH, June EtOH, and July EtOH ($p = 0.001$). Accordingly, it was determined that the difference was between May and June ($p = 0.001$), May and July ($p = 0.001$), and June and July ($p = 0.036$) periods. It was observed that there was a statistically significant difference ($p = 0.011$) in the phenol content between May MeOH, June MeOH, and July MeOH ($p = 0.011$); and this difference was between May and July ($p = 0.004$), and June and July ($p = 0.007$) periods. A statistically significant difference ($p < 0.001$) was also observed in the phenol content between May Water, June Water, and July Water. It was concluded that this difference ($p = 0.002$) was between May and July ($p < 0.001$), and June and July ($p < 0.001$) periods. Moreover, a statistically significant

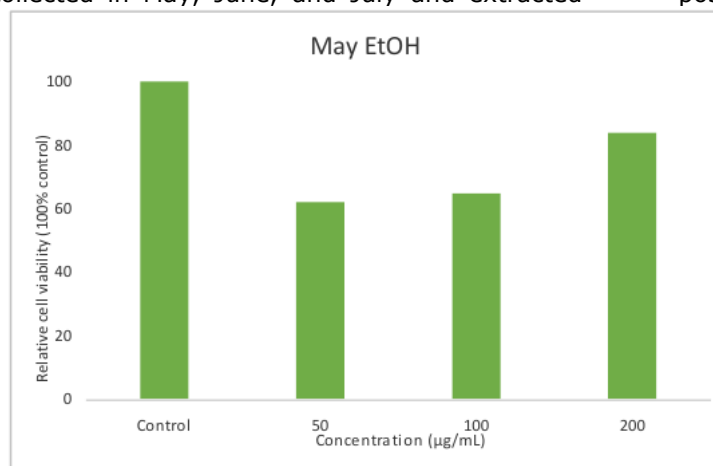
difference ($p < 0.001$) was identified in the flavonoid content between May EtOH, June EtOH, and July EtOH, which was found to be between May and June ($p = 0.001$) and May and July ($p = 0.001$). There was a statistically significant difference in the flavonoid content between May MeOH, June MeOH, and July MeOH ($p = 0.004$). The difference was observed between May and June ($p = 0.003$) and May and July ($p = 0.006$) periods. The difference in the flavonoid content between May Water, June Water, and July Water ($p = 0.011$) was also statistically significant. Accordingly, this difference was between May and July ($p = 0.006$), and June and July ($p = 0.020$) periods. Another statistically significant difference was identified in the radical scavenging activity rates between May EtOH, June EtOH, and July EtOH ($p < 0.001$). The difference was between May and June ($p = 0.001$) and May and July ($p < 0.001$) periods. There was a statistically significant difference ($p = 0.009$) in the radical scavenging activity rates between May MeOH, June MeOH, and July MeOH. The difference was between May and

June ($p=0.015$) and May and July ($p=0.001$) periods. Finally, a statistically significant difference was found in the radical scavenging activity rates between May Water, June Water, and July Water ($p=0.002$), which was between May and July ($p<0.001$) periods.

In a study by Mazandarani et al. (24) in 2011, phenolic and flavonoid contents were detected in different extraction solvents of the *Onosma Dichroanthum Boiss* (ethanol, methanol, acetone). According to the results of this study, the total phenol concentration varied between 4.5 ± 0.7 and 125.6 ± 3.01 mgGAE/g, and flavonoid concentration was between 9.8 ± 3 and 41 ± 2.3 mgKUE/g, which is compatible with the results of the present study.

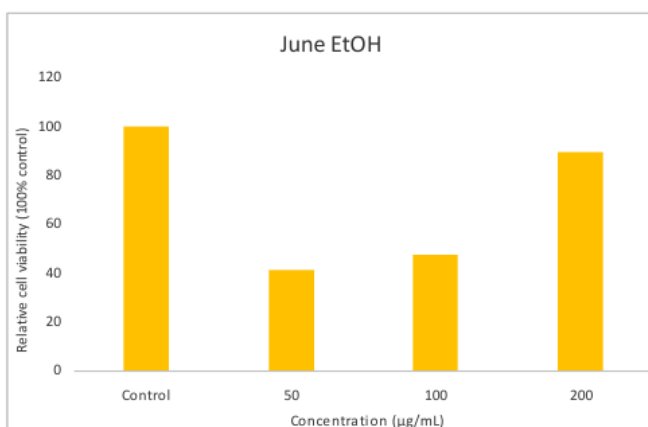
In a biological activity study conducted as result of the extraction of the *Onosmatauricum* with ethyl acetate, methanol and water, the phenolic and flavonoid concentrations were determined as $40.88 \mu\text{molGAEs/g}$ and $7.40 \mu\text{molRES/g}$, respectively. This finding is also compatible with the results of the present study (25). The cytotoxic effect of the samples which were collected in May, June, and July and extracted

by using ethanol, methanol, and water, respectively, on the MCF-7 cells was investigated through the MTT test (3-(4,5-dimethylthiazol-2-yl)-2,5 -diphenyltetrazolium bromide), a colorimetric method. 24 hours after adding the extract, the % relative cell viability of the MCF-7 cells was determined by using the Equation 2. It was found that the extracts prepared with methanol and water did not have any cytotoxic effect on the cancer cells; on the contrary, these samples triggered the growth of these cells (Relative cell viability >100). In addition, it was found there was a significant cytotoxic effect, depending on the dosage, on the samples collected in May, June, and July and extracted with ethanol (Figure 2-4). Cell viability decreased in all concentrations compared to the control group. The concentration which decreased the cell viability most was 50 $\mu\text{g/mL}$. The more the concentration increased, the more the cytotoxic effect on the cancer cells decreased. It is considered that the plant has a positive impact on cell growth due to its wound healing property, and it produced cytotoxic effect on the cancer cells in low concentrations while it affected the growth of cancer cells positively in high concentrations.



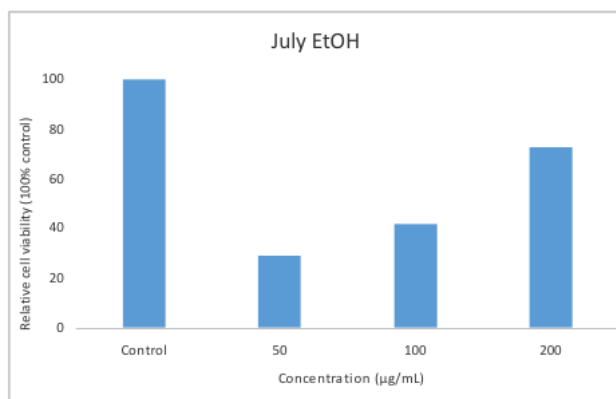
Conc $\mu\text{g/mL}$	Relative cell viability (%)
May EtOH 50	62.13 \pm 11.33
May EtOH 100	64.58 \pm 12.39
May EtOH 200	83.79 \pm 11.83

Figure 2. Cell viability (%) for May EtOH 50 $\mu\text{g/mL}$, 100 $\mu\text{g/mL}$, and 200 $\mu\text{g/mL}$.



Conc $\mu\text{g/mL}$	Relative cell viability (%)
June EtOH 50	40.92 \pm 6.81
June EtOH 100	47.47 \pm 15.3
June EtOH 200	89.55 \pm 20.77

Figure 3. Cell viability (%) for June EtOH 50 $\mu\text{g/mL}$, 100 $\mu\text{g/mL}$, and 200 $\mu\text{g/mL}$.



Conc µg/mL	Relative cell viability (%)
July EtOH 50	28.76±11.31
July EtOH 100	41.75±15.56
July EtOH 200	72.71±17.07

Figure 4. Cell viability (%) for July EtOH 50µg/mL, 100 µg/mL, and 200 µg/mL.

In a study investigating the cytotoxic effects of the Alkanna, another significant species in the family Boraginaceae (26), five different cancer cell lines were used. Also using the MCF-7 cancer cells, the study assessed cytotoxic effects through the MTT analysis. Some of the findings demonstrated that the more the extract concentration decreased, the more cytotoxic effect increased. The study emphasized that the more the purity of biologically active substances creating cytotoxic effect increased, the more the amount of concentration, in which it was active, decreased. These results are consistent with the rates obtained in the present study. Moreover, the study reported that roots of the plant displayed higher cytotoxic effect than ground surface parts.

The present study revealed that the extract producing cytotoxic effect on the cancer cells was prepared in ethanol for all months. It was determined whether the dosage made any statistical difference for all months. A

statistically significant difference was identified between May EtOH 50 µg/mL, June EtOH 50 µg/mL, and July EtOH 50 µg/mL ($p < 0.001$). This difference was between May and June ($p < 0.001$), May and July ($p < 0.001$), and June and July ($p < 0.001$) periods. The difference between May EtOH 100 µg/mL, June EtOH 100 µg/mL, and July EtOH 100 µg/mL was statistically significant ($p = 0.001$). Accordingly, the difference was between May and June ($p = 0.003$) and May and July ($p = 0.001$) periods. However, there was no statistically significant difference between May EtOH 200 µg/mL, June EtOH 200 µg/mL, and July EtOH 200 µg/mL ($p = 0.565$).

After the *Onosma Sericeum Willd*, collected in May, June and July, was digested using the microwave, its trace element and mineral composition was defined. The results are given as the average of three measurements (Table 3).

Table 3. Total content of metals (ppb) in dried *Onosma Sericeum Willd*.

	May	June	July
B	9944±1.594	16328±4.598	2262.4±3.196
Na	9600±0.002	9600±0.003	13600±0.012
Mg	47200±0.013	67200±0.019	7200±0.046
Al	4217.6±0.818	5449.6±1.834	9056±6.908
P	42040±9.444	78200±2.244	41288±2.255
K	909600±0.191	1267200±0.240	912000±0.540
Ca	508000±0.043	939200±0.151	1233600±0.748
Cr	1114.4±0.271	1504.8±0.623	1695.2±1.516
Mn	2238.4±0.309	4124±0.965	2818.4±1.659
Fe	12000±0.001	13600±0.004	15200±0.013
Co	nd	nd	nd
Ni	234.4±0.037	357.6±0.023	339.2±0.157
Cu	1388±0.057	1807.2±0.135	1915.2±0.814
Zn	3107.2±0.037	2702.4±0.085	5067.2±2.124
As	395.2±0.105	356±0.132	362.4±0.322
Se	661.6±0.407	278.4±0.162	195.2±0.239
Cd	nd	nd	nd
Sn	1549.6±0.200	1887.2±0.043	1600±0.861
Ba	4338.4±0.323	10680±1.738	11392±5.653
Pb	nd	nd	nd

nd: not detected

As it is seen in Table 3, the concentration values of toxic elements such as cobalt, cadmium and lead could not be determined as they were below 1ppb. Nickel, arsenic, and selenium were relatively in low concentrations, and they were at proximate levels in three periods when the plant was collected. Among the toxic elements, only the concentration rate of aluminum was higher compared to nickel, arsenic and selenium. It was identified that all the other elements were essential and had higher concentration rates than other toxic elements.

CONCLUSION

The use of plants for therapeutic purposes is as old as the human history. In fact, mostly plant and plant extracts were used for medical purposes until the discovery of synthetic drugs. In this process until the present day, the idea that synthetic drugs have greater potential harmful effects has led people to use drugs of natural origin. Interest in natural products has increased gradually with the promotion of print and visual media. One of the significant disadvantages of this deep interest is the idea that natural products have no harmful or side effects. However, it is vital that herbal products are procured from reliable sources using proper methods, and recommended and administered by competent persons. Otherwise, it might result in serious mortality and morbidity. Besides, the data on plants, particularly those with traditional use, must be built on a scientific foundation. In addition to all these, the area where the plant grows, collection time, soil and climate conditions might change the quantity of bioactive components and composition of the plant. Moreover, it is necessary to carry out toxicity studies while determining the dosage to be used. It is a fact that antioxidant activity which plays a significant role especially in healing the wounds depends on the quantity of phenolic and flavonoid species. Thus, the present study investigated the changes in the biological activity of the *Onosma Sericeum* Willd, traditionally used and known for its therapeutic properties among public, depending on collection time and extraction solvent. Its cytotoxic effect on the MCF-7 was also investigated. The highest cytotoxic effect was detected in the extracts containing ethanol which also had high phenolic, flavonoid and radical scavenging activity rates. At the same time, the study assessed trace element/mineral composition which plays a significant role in understanding biological processes. The results demonstrated that biological activity changed depending on collection time and extraction solvent. Although the family Boraginaceae has drawn the attention of many researchers due to its bioactive species, studies on the *Onosma Sericeum* Willd, a member of this family, are considerably limited. In this sense, we believe that our study will make a contribution to the relevant literature. In

continuation of this study, the researchers intend to carry out the isolation of bioactive compounds belonging to this species, assessment of their biological activities, and assessment of possible cytotoxic effects on different cells.

ACKNOWLEDGEMENTS

The authors thank Assoc. Prof. Dr. Rıza Binzet from the Department of Biology at the Faculty of Arts and Sciences, Mersin University for the botanical identification of the plant. We also thank the Department of Biostatistics and Medical Informatics, Faculty of Medicine, Mersin University and Specialist Asena Ayça Özdemir for their contributions in performing statistical analyses.

REFERENCES

1. Vukic MD, Vukovic NL, Djelic GT, Popovic S, Zaric MM, Baskic DD, Krstic GB, Tesevic VV, Kacaniova MM. Antibacterial and cytotoxic activities of naphthoquinone pigments from *Onosma Visianii* Clem. EXCLI Journal. 2017;16:73-88.
2. Ozgen U, Ikbal M, Hacimuftuoglu A, Houghton P.J, Gocer F, Dogan H, Coskun M. Fibroblast growth stimulation by extracts and compounds of *Onosma argentatum* roots. J Ethnopharmacol. 2006;104:100-3.
3. Binzet R, Orcan N. A New species of *Onosma* (Boraginaceae) from Southern Turkey. Missouri Botanical Garden Press. 2007;17(1): 8-10.
4. Akçin ÖE, Aktaş T, Altıntaş MY. *Myosotis Alpestris* F.W.Schmidt (Boraginaceae) türünün anatomik özellikleri. Ordu Univ. J. Sci. Tech. 2013;3(1): 61-8.
5. Tosun A, Akkol EK, Bahadır Ö, Yesilada E. Evaluation of anti-inflammatory and antinociceptive activities of some *Onosma* L. Species growing in Turkey. J Ethnopharmacol. 2008;120:378-81.
6. Ozgen U, Coskun, M, Kazaz, C, Secen, H. Naphthoquinones from the roots of *Onosma argentatum* Hub.-Mor (Boraginaceae). Turk J Chem. 2004;28: 451-4.
7. Ozgen U, Houghton, PJ, Ogundipe, Y, Coskun, M. The Antioxidant and antimicrobial activities of *Onosma argentatum* and *Rubiaperegrina*. Fitoterapia. 2003;74: 682-5.
8. Sharma S, Khan, K, Sultana, S. Effect of *Onosma echiodes* on DMBA/croton oil mediated carcinogenic response, hyperproliferation and oxidative damage in murine skin. Life Sci. 2004;75(20): 2391-410.

9. Ozer MS, Kirkan B, Sarikurkcu C, Cengiz M, Ceylan O, Atılğan N, Tepe B. *Onosmaheterophyllum*: Phenolic composition, enzyme inhibitory and antioxidant activities. *Ind Crops Prod.* 2018;111:179-84.
10. Sezik E, Yeşilada E, Tabata M, Honda G, Takaishi Y, Fujita T, Tanaka T, Takedau Y. Traditional medicine in Turkey VIII. Folk medicine in East Anatolia; Erzurum, Erzincan, Ağrı, Kars, Iğdır Provinces. *Econ. Bot.* 1997;51(3):195-211.
11. Gharematrossian S, Popov Y, Ghorbanli M, Safaeian S, Iranbakhsh A. Phytochemical and morphological evidences for Shikonin production by plant cell cultures of *Onosmasericum Willd.* *Braz. Arch. Biol. Technol.* 2016; 59: 1-7.
12. Dziri S, Hassen I, Fatnassi S, Mrabet Y, Casabianca H, Hanchi B. Phenolic constituents, antioxidant and antimicrobial activities of rosygarlic (*Allium roseum* var. *odoratissimum*). *J Funct Foods.* 2012; 4(2): 423-32.
13. Baye H, Hymete A. Lead and cadmium accumulation in medicinal plants collected from environmentally different sites. *Bull Environ Contam Toxicol.* 2010; 84(2): 197-201.
14. Pytlakowska K, Kita A, Janoska P, Połowniak M, Kozik V. Multi-element analysis of mineral and trace elements in medicinal herbs and their infusions. *Food Chem.* 2012; 135(2): 494-501.
15. Slinkard K, Singleton VL. Total phenols analysis: Automation and comparison with manual methods. *Am. J. Enol. Vitic.* 1977;28: 49 - 55.
16. Kim DO, Jeong SW, Lee CY. Antioxidant capacity of phenolic phytochemicals from various cultivars of plums, *Food Chem.* 2003;81(3): 321 - 6.
17. Floegel A, Kim DO, Chung SJ, Koo SI, Chun OK. Comparison of ABTS/DPPH assays to measure antioxidant capacity in popular antioxidant-rich US foods. *J Food Compost Anal.* 2011;24: 1043-8.
18. Turan I, Demir S, Aliyazıcıoğlu R, Aliyazıcıoğlu Y. Evaluation of antioxidant and cytotoxic properties of *Primula vulgaris* Leaf Extract. *KSU J. Nat. Sci.* 2017; 20(4): 361-7.
19. Cadirci E, Suleyman H, Aksoy H, Halici Z, Ozgen U, Koc A. Effects of *Onosma armeniacum* root extract on ethanol-induced oxidative stress in stomach tissue of rats. *Chem Biol Interact.* 2007;170(1):40-8.
20. Binzet R, Akçin ÖE. The anatomical properties of two *Onosma* L. (Boraginaceae) species from Turkey. *J Med Plant Res.* 2012; 6(17): 3288-94.
21. Papageorgiou VP, Assimopoulou AN, Ballis AC. Alkannins and shikonins: a new class of wound healing agents. *Curr Med Chem.* 2008;15:3248-67.
22. Wang L, Li F, Liu X, Chen B, Yu K, Wang MK. Meroterpenoids and a naphthoquinone from *Arnebiaeuchroma* and their cytotoxic activity. *Planta Med.* 2015;81:320-6.
23. Naz S, Ahmad S, AjazRasool S, AsadSayeed S, SiddiqIR. Antibacterial activity directed isolation of compounds from *Onosma hispidum*. *Microbiol Res.* 2006;161:43-8.
24. Mazandarani M, Moghaddam PZ, Baiat H, Zolfaghari MR, Ghaemiand EA, Hemati H. Antioxidant activity, phenol, flavonoid and anthocyanin contents in various extracts of *Onosma dichroanthum* Boiss. in north of Iran Masoumeh. *Iran. J. Plant Physiol.* 2011; 1(3): 169 - 76.
25. Kirkan B, Sarikurkcu C, Ozer MS, Cengiz M, Atılğan N, Ceylan O, Tepe B. Phenolic profile, antioxidant and enzyme inhibitory potential of *Onosma tauricum* var. *Tauricum*. *Ind Crops Prod.* 2018; 125:549-55.
26. Bıçkıcı Ş. Bazı Alkanna türlerinin biyoaktivite rehberli izolasyon yöntemi kullanılarak çeşitli kanser hücreleri üzerindeki sitotoksik etkilerinin in vitro ortamda taranması [Master of Science Thesis]. [İzmir]:Ege University;2006.



Synthesis of Polysulfone Based Amphiphilic Graft Copolymers by a 'Grafting to' Approach

Mustafa Ciftci*  

¹Bursa Technical University, Faculty of Engineering and Natural Sciences, Department of Chemistry, 16310, Bursa, Turkey.

Abstract: Synthesis of amphiphilic polysulfone graft copolymers by "Click" chemistry is described. First, a commercial PSU was chloromethylated to give chloro-functional PSU (PSU-Cl). Subsequently, chloride groups were converted into azide moieties by nucleophilic substitution. Hydrophilic poly(*N,N*-dimethylacrylamide) (PDMA) side chains were then attached via a "grafting to" approach by using copper-catalyzed azide-alkyne cycloaddition (CuAAC). Precursor polymer and the final amphiphilic copolymers were characterized by proton nuclear magnetic resonance (¹H NMR), fourier-transform infrared spectroscopy (FT-IR), gel permeation chromatography (GPC) and contact angle measurements.

Keywords: Polysulfone, grafting to, graft copolymers, amphiphilic materials.

Submitted: August 19, 2019. **Accepted:** August 28, 2019.

Cite this: Ciftci M. Synthesis of Polysulfone Based Amphiphilic Graft Copolymers by a 'Grafting to' Approach. JOTCSA. 2019;6(3):365-72.

DOI: <https://doi.org/10.18596/jotcsa.606191>.

*Corresponding author. E-mail: mustafaciftcis@gmail.com.

INTRODUCTION

Based on their outstanding properties, such as superb thermal and chemical stability, mechanical strength, and resistance to radiation degradation (1, 2), polysulfones (PSU) have been widely employed in numerous industrial applications such as food processing, fuel cells, and electronics (3, 4). Moreover, based on their biocompatible and non-degradable nature, they have also been used in bio-applications including bioreactors, hemodialysis, etc. (5, 6). However, their poor tracking resistance and weathering properties remains as the major challenges limit their even wider utilization (7). Not only to overcome these problems, but also to fulfill the necessities of the application, functionalization of suitable PSU precursors have gained growing interest recently (8). Using functional comonomers through the polymerization or post-modification approaches are the two main approaches utilized for this purpose. However, the latter method, in which the desired functionalities are incorporated to the PSU chains, appears to be a more powerful approach, since polymerizations may be inhibited in the direct

polymerization case as a result of limited functional-group tolerance of the polymerization procedures (9).

The post-modification concept has made a great progress by the development of "Click Chemistry" (10). Basically, click chemistry term covers the chemical approaches with several advantageous properties including high yields, tremendous orthogonality and selectivity (11). Although here exist different type of click reactions including Diels-Alder and thiol-ene reactions, the pioneering approach, copper-catalyzed azide-alkyne cycloaddition (CuAAC) has gained broad interest and has been extensively utilized for the preparation of numerous complex macromolecular structures (12). For instance, it has been established that many macromolecular architectures such as graft/block and star copolymers, polymeric networks, functional polymers and hyperbranched polymers can be prepared by CuAAC click reactions (13). Moreover, CuAAC has been also demonstrated to be a powerful tool for the modification/functionalization of different polymeric materials (14, 15).

Amphiphilic polymeric materials have been the basis of different bio-applications ranging from drug delivery systems to membranes (16-18). As a result of their unique chemical structure, they form polymeric micelles with a hydrophobic core and hydrophilic shell where the core act as a reservoir for hydrophobic drugs and the hydrophilic part stabilizes the core by serving as an interface between aqueous phase and the hydrophobic domain. This exceptional property makes them perfect materials for encapsulation and delivery of hydrophobic drugs (19, 20). Among the various polymers employed as hydrophilic domains for amphiphilic polymers, poly(*N,N*-dimethylacrylamide) (PDMA) is one of the most widely used one due to their hydrophilic in the absence of ionic functionalities and inertness to biomolecules (21, 22).

In the current study, a "grafting to" approach is described for the synthesis of PSU-based graft copolymers through CuAAC. PDMA was purposely chosen as the side chain to obtain amphiphilic polysulfone graft copolymers. Thus, the obtained polymer scaffold is believed to be a suitable candidate for biomedical applications and drug delivery systems.

EXPERIMENTAL SECTION

Materials

Polysulfone (PSU, Udel® P-1700, Solvay), paraformaldehyde (95%, Merck), tin(IV) chloride (98%, Alfa Aesar), trimethylsilyl chloride ($\geq 99.0\%$, Aldrich), sodium azide (97%, Aldrich), *N,N'*-dicyclohexylcarbodiimide (DCC, 99%, Aldrich), 4-(dimethylamino)pyridine (DMAP, 98%, Aldrich), propargyl alcohol (99%, Aldrich), copper (I) bromide (98%, Acros), *N,N,N',N'',N'''*-pentamethyldiethylene triamine (PMDETA, 99%, Aldrich), *N,N*-dimethylacrylamide (99%, Aldrich), *N,N*-dimethylformamide (DMF, $\geq 99.8\%$, Merck), and methanol (100%, VWR) were used as received. Alkyne functional RAFT agent (RAFT-alkyne) was synthesized according to previous literature (23).

Characterization

^1H NMR spectra were recorded on a Bruker Advance III, 300 MHz spectrometer at room temperature in CDCl_3 with tetramethylsilane as an internal standard. Molecular weights and distributions were determined by GPC using Viscotek GPC max system including a pump module (GPC max, Viscotek, Houston, TX) and a refractive index (RI) detector (VE 3580, Viscotek). In the analyses, 1 mL/min flow rate and 50 μL injection volume were used with autosampler system. The calibration of RI detector was done by narrow molecular weight polystyrene standards. Two columns (LT5000L, Mixed, Medium Organic 300 \times 8 mm and LT3000L, Mixed, Ultra-Low Organic 300 \times 8 mm) with a guard column (TGuard, Organic Guard Column 10

\times 4.6 mm) were used for the tetrahydrofuran eluent at 35 °C. Viscotek OmniSEC Omni01 software was used to analyze the data. Fourier transformed infrared spectroscopy (FTIR) studies were performed by using a Perkin-Elmer Spectrum Two Spectrometer (Lambda 25, Waltham, MA) equipped with a diamond attenuated total reflectance (ATR) device at ambient temperature.

Chloromethylation of polysulfones

PSU-Cl was synthesized by following a literature protocol. Briefly, PSU (10 g, 0.25 mmol) was dissolved in chloroform (300 mL) by using an ultrasonic bath and then paraformaldehyde (29 mL, 225 mmol) and trimethylsilyl chloride (29 mL, 225 mmol) were added. After stirring for a while, tin(IV) chloride (0.26 mL, 2.25 mmol) was added and the mixture was stirred at room temperature for 72 hours. At the end of the given time, the product was precipitated by pouring into excess methanol. Then, the precipitate was filtered and dried in a vacuum oven at room temperature.

Azidation of polysulfones

PSU-Cl was synthesized by following a literature protocol. Briefly, PSU (10 g, 0.25 mmol) was dissolved in chloroform (300 mL) by using ultrasonic bath and then paraformaldehyde (29 mL, 225 mmol) and trimethylsilyl chloride (29 mL, 225 mmol) were added. After stirring for a while, tin(IV) chloride (0.26 mL, 2.25 mmol) was added and the mixture was stirred at room temperature for 72 hours. End of the given time, the product was precipitated into excess methanol. Then, the precipitate was filtered and dried in a vacuum oven at room temperature.

Synthesis of alkyne functional PDMA (PDMA-alkyne)

PDMA-alkyne was synthesized by reversible addition-fragmentation chain-transfer (RAFT) polymerization according to previous literature. Briefly, DMA (50 eq.), RAFT agent (1 eq.), and AIBN (0.01) were dissolved in DMSO. After deoxygenation by purging with N_2 , the mixture was heated at 60 °C. After given time the reaction was terminated by cooling to 0 °C and exposed to air. The mixture was dissolved in a large excess of DCM and extracted twice by distilled water. The organic phase removed by reduce pressure, the concentrated mixture was precipitated in ten-fold excess of Et_2O and dried under reduced pressure.

Click Reactions

In a typical click reaction, azide functional PSU (50 mg), PDMA-alkyne (3×10^{-4} mol), catalyst ($\text{Cu}^{\text{I}}\text{Br}$, 3×10^{-4} mol), ligand (PMDETA, 6×10^{-4} mol), and 4 mL of toluene were placed in a Schlenk tube. The reaction mixture was degassed by three freeze-pump-thaw cycles and stirred at room temperature for 24 h. After the click reaction, the reaction mixture was passed through a column filled with neutral alumina to

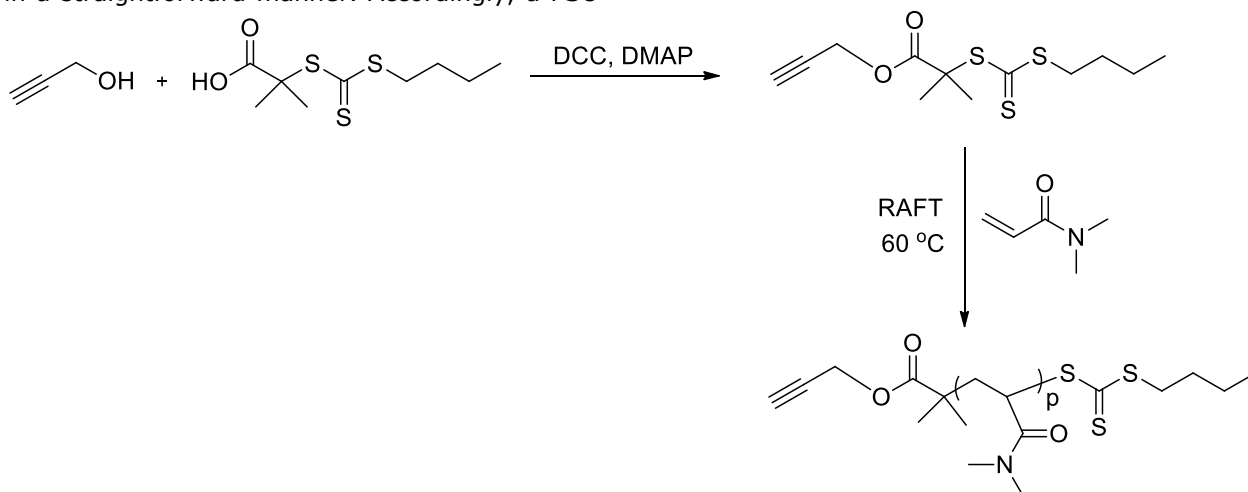
remove the copper salt, 10-fold excess of methanol and dried under reduced pressure.

RESULTS AND DISCUSSION

Among the various potential approaches that could be employed for the synthesis of PSU graft copolymers, CuAAC appeared to be the most appropriate one for numerous motives. In addition to its orthogonality and excellent yields, the procedure is also compatible the functional groups existing in the PSU backbone.(24) Thus, it enables the attachment of the desired side chains in a straightforward manner. Accordingly, a PSU

with pendant chloro-groups was prepared by using a chloromethylation procedure. Then, chloro- units were converted into azide groups by a nucleophilic substitution reaction using NaN_3 to give the azide-functional PSU (PSU- N_3).

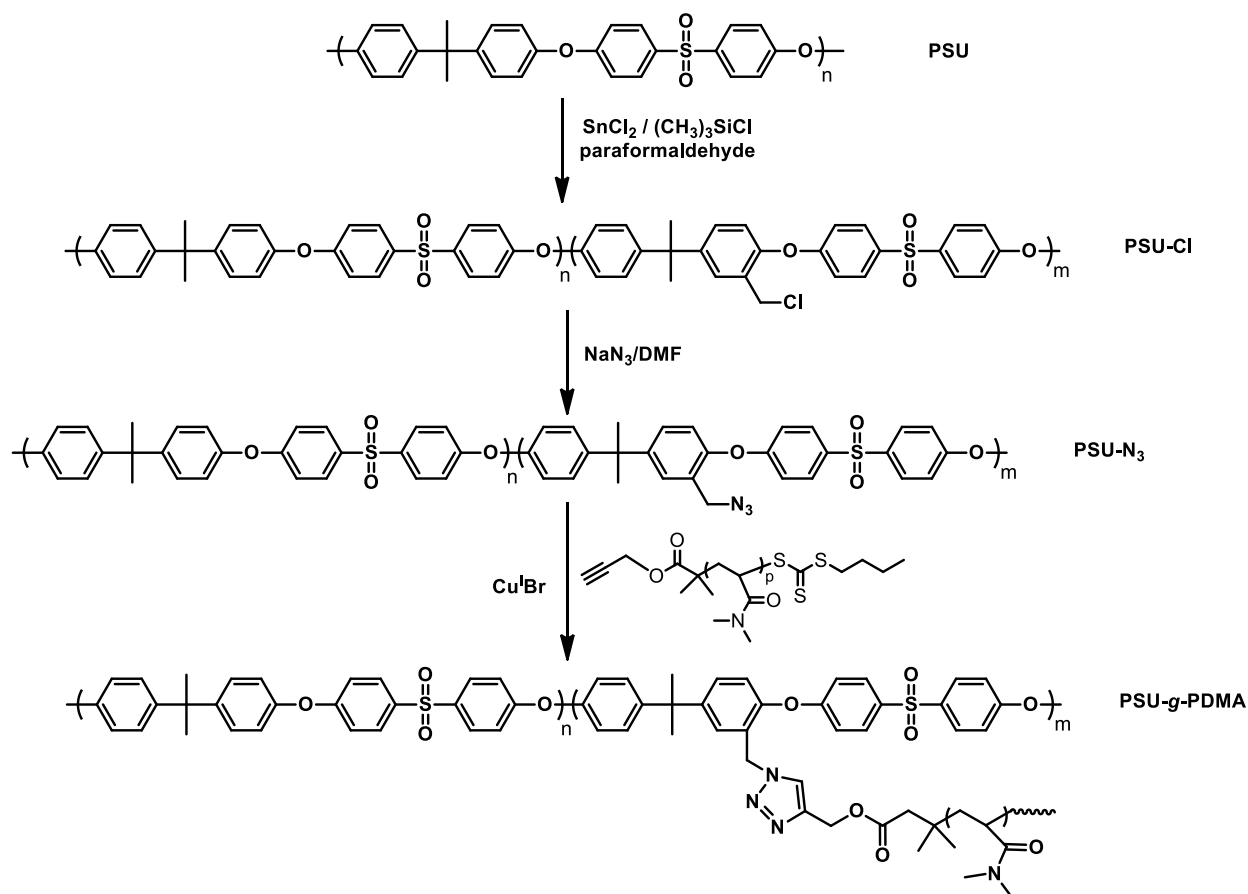
On the other hand, alkyne functional PDMA (PDMA- alkyne) was prepared following a literature procedure with slight changes (Scheme 1). Accordingly, an alkyne functional RAFT agent was synthesized by esterification reaction, which was then used to mediate RAFT polymerization of DMA to access the anticipated PDMA-alkyne.



Scheme 1: Synthetic route to PDMA-alkyne.

Finally, the PDMA chains were grafted to the PSU main chain via CuAAC reactions to give the desired amphiphilic polysulfone graft copolymers.

Overall process for the synthesis of graft copolymers is summarized in Scheme 2.



Scheme 2: Overall process for synthesis of PSU-*g*-PDMA copolymers by CUAAC.

As can be seen from Table 1, molecular weights, and thus, hydrophilicities of the formed graft copolymers could be manipulated by using

different PDMA-alkyne with diverse molecular weights.

Table 1: "Grafting to" of PDMA to PSU-N₃^a.

Sample	M_n (g mol ⁻¹) ^b	M_w/M_n ^b	WCA (°)
PSU- <i>g</i> -PDMA-1 ^c	39 300	1.77	72
PSU- <i>g</i> -PDMA-2 ^d	46 100	1.79	65

^a $M_n(\text{PSU-N}_3) = 30,200 \text{ g mol}^{-1}$, $M_w/M_n = 1.74$, ^b Determined by GPC, ^c PDMA-1 ($M_n = 1,300 \text{ g mol}^{-1}$, $M_w/M_n = 1.09$) was used as the antagonist click component, ^d PDMA-2 ($M_n = 2,100 \text{ g mol}^{-1}$, $M_w/M_n = 1.09$) was used as the antagonist click component.

Each step of the process was followed by ¹H-NMR analysis. The degree of the chloromethylation was determined as 10 mol% by comparison of the integration area of -CH₂Cl protons of the chloromethyl at $\delta = 4.55 \text{ ppm}$ with the aromatic signals of PSU backbone (Figure 1). Subsequent to the azide substitution, the mentioned methylene signals were entirely shifted to $\delta =$

4.35 confirming quantitative azidation. The successful click process was also confirmed as can be seen from the spectra of the graft copolymer. Thus, a new signal appeared, in addition to the aromatic peaks of PSU segment, around $\delta = 2.87$ corresponding to characteristic signals of -CH₃ moieties of PDMA.

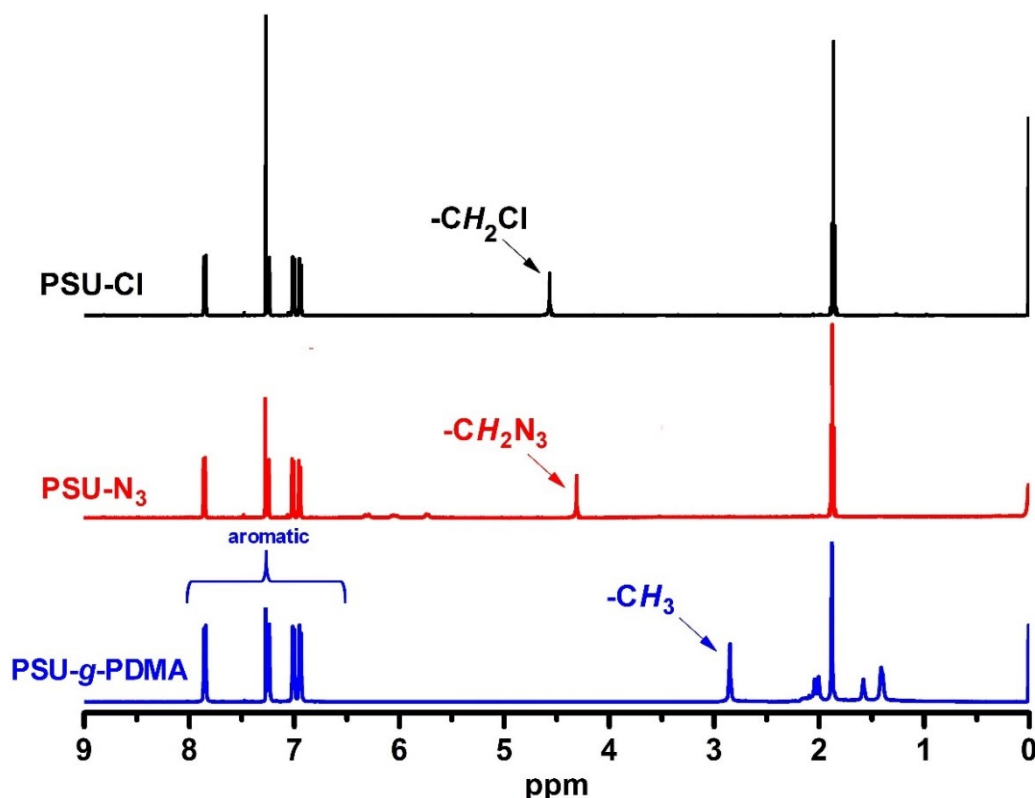


Figure 1: ^1H NMR spectra of PSU-Cl, PSU- N_3 and PSU-*g*-PDMA.

FT-IR results also confirmed both azidation and grafting processes (Figure 2). After the azidation, the typical $-\text{N}_3$ peak around 2120 cm^{-1} was clearly detectable. On the other hand, the spectrum of the graft copolymer displays the distinguishing

carbonyl bands (1720 cm^{-1}) of the PDMA segment in addition to the aromatic stretching bands of PSU units at 1590 and 1480 cm^{-1} . Moreover, the complete disappearance of $-\text{N}_3$ signal represents the quantitative yield of the click reaction.

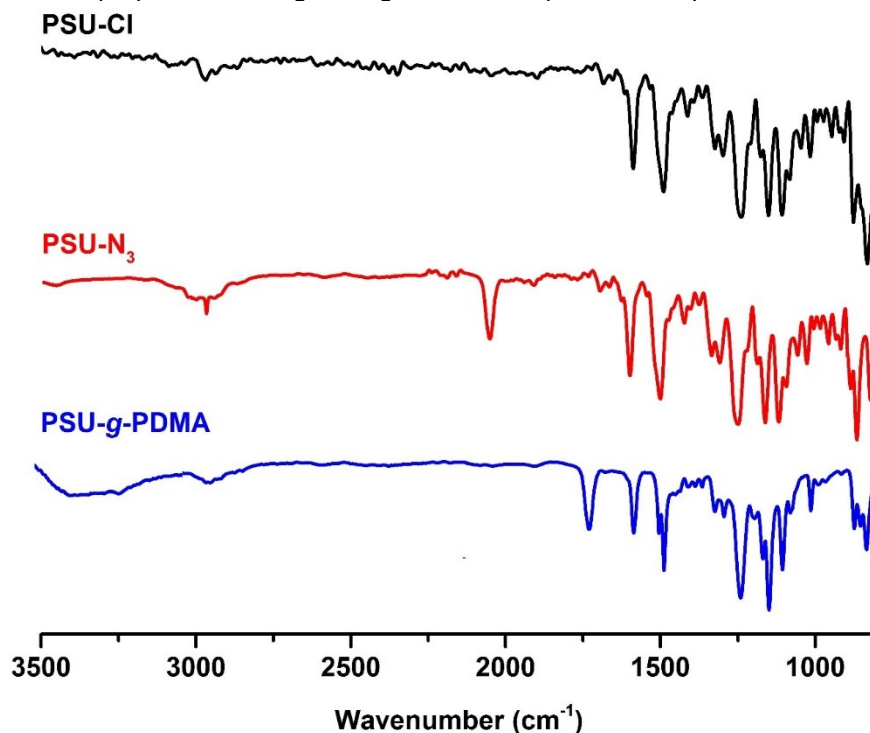


Figure 2: FT-IR spectra of PSU-Cl, PSU- N_3 and PSU-*g*-PDMA.

The GPC curves of the precursor polymer and its corresponding graft copolymer analogues are illustrated in Figure 3. The obvious shift of the

graft copolymers towards higher molecular weight region (lower elution volumes), indicates successful grafting.

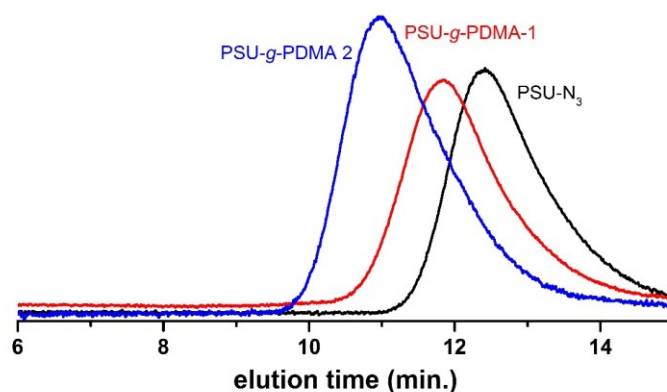


Figure 3: GPC traces of PSU-N₃, PSU-*g*-PDMA-1 and PSU-*g*-PDMA-2.

Hydrophilicity of the graft copolymers were investigated by demonstrated by water contact angle (WCA) measurements. The WCA results of the pristine PSU and corresponding graft copolymer analogues are presented in Figure 4. WCAs of graft copolymers were lower (72° and

65°) then the precursor PSU (81°) as expected. Moreover, as can deduced from the higher WCA of PSU-*g*-PDMA-1 that bears a shorter hydrophilic PDMA side chain compared to PSU-*g*-PDMA-2, the WCAs decreased with the increase of the PDMA side chain content in the structure.



Figure 4. Shapes of water drops on thin films of PSU-N₃ (left), WCA: 83°, PSU-*g*-PDMA-1 (middle), WCA: 72° and PSU-*g*-PDMA-2 (right), WCA: 65°.

In summary, amphiphilic polysulfone graft copolymers, with different hydrophilicities were obtained. In the process, chloro-functional PSUs were synthesized from a commercial PSU then azide groups were then incorporated to the polymer chain. Subsequently, alkyne functional PDMA, prepared by RAFT polymerization by using functional RAFT agent, were attached via CuAAC to give the amphiphilic polysulfone-*g*-poly(*N,N*-dimethylacrylamide) (PSU-*g*-PDMA) copolymers. The obtained graft copolymers possessing hydrophobic PSU main chain and hydrophilic PDMA side chains appear as suitable candidates for various application especially biomedical applications.

REFERENCES

1. Barth C, Goncalves MC, Pires ATN, Roeder J, Wolf BA. Asymmetric polysulfone and

polyethersulfone membranes: effects of thermodynamic conditions during formation on their performance. *Journal of Membrane Science*. 2000;169(2):287-99.

2. Watanabe S, Kobayashi A, Kakimoto M-A, Imai Y. Synthesis and characterization of new aromatic polyesters and polyethers derived from 1,2-bis(4-hydroxyphenyl)-1,2-diphenylethylene. *Journal of Polymer Science*. 1994;32(5):909-15.

3. Hickner MA, Ghassemi H, Kim YS, Einsla BR, McGrath JE. Alternative Polymer Systems for Proton Exchange Membranes (PEMs). *Chemical Reviews*. 2004;104(10):4587-612.

4. Noshay A, Robeson LM. Sulfonated Polysulfone. *Journal of Applied Polymer Science*. 1976;20(7):1885-903.

5. Park JY, Acar MH, Akthakul A, Kuhlman W, Mayes AM. Polysulfone-graft-poly(ethylene glycol) graft copolymers for surface modification of polysulfone membranes. *Biomaterials*. 2006;27(6):856-65.
6. Yoon K, Hsiao BS, Chu B. Formation of functional polyethersulfone electrospun membrane for water purification by mixed solvent and oxidation processes. *Polymer*. 2009;50(13):2893-9.
7. Higuchi A, Shirano K, Harashima M, Yoon BO, Hara M, Hattori M, et al. Chemically modified polysulfone hollow fibers with vinylpyrrolidone having improved blood compatibility. *Biomaterials*. 2002;23(13):2659-66.
8. Dizman C, Tasdelen MA, Yagci Y. Recent advances in the preparation of functionalized polysulfones. *Polymer International*. 2013;62(7):991-1007.
9. Dizman C, Demirkol DO, Ates S, Torun L, Sakarya S, Timur S, et al. Photochemically prepared polysulfone/poly(ethylene glycol) amphiphilic networks and their biomolecule adsorption properties. *Colloids and Surfaces B-Biointerfaces*. 2011;88(1):265-70.
10. Kolb HC, Finn MG, Sharpless KB. Click chemistry: Diverse chemical function from a few good reactions. *Angewandte Chemie-International Edition*. 2001;40(11):2004-21.
11. Binder WH, Sachsenhofer R. 'Click' chemistry in polymer and materials science. *Macromol Rapid Commun*. 2007;28(1):15-54.
12. Tron GC, Pirali T, Billington RA, Canonico PL, Sorba G, Genazzani AA. Click chemistry reactions in medicinal chemistry: Applications of the 1,3-dipolar cycloaddition between azides and alkynes. *Medicinal Research Reviews*. 2008;28(2):278-308.
13. Tasdelen MA, Yagci Y. Light-Induced Click Reactions. *Angewandte Chemie-International Edition*. 2013;52(23):5930-8.
14. Ciftci M, Kahveci MU, Yagci Y, Allonas X, Ley C, Tar H. A simple route to synthesis of branched and cross-linked polymers with clickable moieties by photopolymerization. *Chemical Communications*. 2012;48(82):10252-4.
15. Murtezi E, Ciftci M, Yagci Y. Synthesis of clickable hydrogels and linear polymers by type II photoinitiation. *Polymer International*. 2015;64(5):588-94.
16. Gustafsson J, Ljusberg-Wahren H, Almgren M, Larsson K. Submicron particles of reversed lipid phases in water stabilized by a nonionic amphiphilic polymer. *Langmuir*. 1997;13(26):6964-71.
17. Nishikawa T, Nishida J, Ookura R, Nishimura SI, Wada S, Karino T, et al. Honeycomb-patterned thin films of amphiphilic polymers as cell culture substrates. *Materials Science & Engineering C-Biomimetic and Supramolecular Systems*. 1999;8-9:495-500.
18. Acik G, Altinkok C. Polypropylene microfibers via solution electrospinning under ambient conditions. 2019;136(45):48199.
19. Geyik C, Ciftci M, Demir B, Guler B, Ozkaya AB, Gumus ZP, et al. Controlled release of anticancer drug Paclitaxel using nano-structured amphiphilic star-hyperbranched block copolymers. *Polymer Chemistry*. 2015;6(30):5470-7.
20. Selecı M, Selecı DA, Ciftci M, Demirkol DO, Stahl F, Timur S, et al. Nanostructured Amphiphilic Star-Hyperbranched Block Copolymers for Drug Delivery. *Langmuir*. 2015;31(15):4542-51.
21. Haraguchi K, Farnworth R, Ohbayashi A, Takehisa T. Compositional effects on mechanical properties of nanocomposite hydrogels composed of poly(N,N-dimethylacrylamide) and clay. *Macromolecules*. 2003;36(15):5732-41.
22. Trossarelli L, Meirone M. Solution properties of poly(N,N-dimethylacrylamide). *Journal of Polymer Science*. 1962;57(165):445-52.
23. Lu D, Jia Z, Monteiro MJ. Synthesis of alkyne functional cyclic polymers by one-pot thiol-ene cyclization. *Polymer Chemistry*. 2013;4(6):2080-9.
24. Toiserkani H, Yilmaz G, Yagci Y, Torun L. Functionalization of Polysulfones by Click Chemistry. *Macromolecular Chemistry and Physics*. 2010;211(22):2389-95.



Synthesis and Characterization of Some New 4-Methyl-5-Imidazole Carbaldehyde Derivatives

Ersin Orhan^{1*}  , Mahmut Kose²  , Demet Alkan²   and Leyla Öztürk²  

¹Department of Chemistry, Faculty of Arts and Science, Düzce University, 81620, Düzce, Turkey.

²Department of Chemistry, Faculty of Arts and Science, Bülent Ecevit University, 67100, Zonguldak, Turkey.

Abstract: Imidazole is a common and important heterocyclic fragment of many biologically important molecules. 5-imidazole-carbaldehydes containing mono- (N-1) methyl (or aryl) analogs are commonly used as building blocks in medical chemistry. In this study, starting from 4-methyl-1H-imidazole-5-carbaldehyde, the N-1 atom of the imidazole ring is derived with different alkyl groups. In addition, both N atoms of the starting imidazole-carbaldehyde were methylated to give 5-carbaldehyde-1,3,4-trimethyl-3-imidazolium salt. The salt which possess quite reactive carbaldehyde group could be used as a precursor for synthesis of other imidazolium derivatives. Furthermore, 4-methyl-5-imidazole carbaldehyde was converted into the benzoxazole, benzothiazole and benzoimidazole by a two-step reaction over the aldehyde group. These new compounds could display some biological activities.

Keywords: Imidazole, imidazolium derivatives, biologically active imidazole.

Submitted: January 22, 2019. **Accepted:** September 05, 2019.

Cite this: Orhan E, Kose M, Alkan D, Öztürk L. Synthesis and Characterization of Some New 4-Methyl-5-Imidazole Carbaldehyde Derivatives. JOTCSA. 2019;6(3):373-82.

DOI: <https://doi.org/10.18596/jotcsa.530757>.

*Corresponding author. E-mail: ersinorhan@duzce.edu.tr.

INTRODUCTION

Imidazole ring is one of the most basic groups of biologically important compounds. Many biologically active compounds containing the imidazole ring have been synthesized. Imidazole derivatives are used for the development of antifungal, antibacterial, anticancer, and antimalarial drugs. Until now, many drug and drug candidate isomers,

containing imidazole and mono-N-alkylated imidazole rings, have been synthesized. For example, ipronidazole is a drug developed as an anti-protozoal agent (1). Nimorazole, a heterocyclic N-alkyl substituted compound, is an effective antimicrobial drug in parasites of the genus trichomonas, synthesized in 1970 (2). The imidazole derivative known under the trade name of moxidazole is an antimicrobial drug acting with trichomonas parasites.

Another imidazole derivative that is effective against the *Trichomonas* parasites is flunidazole (3-6). Imidazole derivatives also have been used in the development of drugs for the treatment of ulcers. For example, the imidazole derivative known as Cimetidine is a highly effective drug in the treatment of ulcers (7). Highly complex imidazole-based drugs containing the imidazole group have also been developed. For example, the imidazole derivative known as dazadol, is used as an anti-depressant (8). The drug called cimicoxib, which exhibits anti-inflammatory properties, is also an imidazole derivative (9). The imidazole derivative, Cipralisant, synthesized in recent years, has been found to be effective in attention deficit syndrome on animal studies. This compound is probably thought to be good for Alzheimer's disease (10-12). Imidazolium derivatives have begun to work in recent years. James H. Davis, Jr. et al. synthesized the first biologically active ionic liquid crystalline imidazolium cation starting from miconazole which exhibit antifungal properties (13). Azami et al. have synthesized many 1,3-dialkyl imidazolium derivatives and some of these compounds have antibacterial properties (14). In another study, imidazolium derivatives containing long alkyl chains on the N atom were synthesized and these compounds were found to have quite good antimicrobial activity on gram-negative, gram-positive bacteria and fungi (15). Donald D. Ourth et al. isolated and elucidated its structure of 1,3-methylimidazolium derivatives which occurred naturally; this compound showed a broad-spectrum antiviral properties for insects. This compound also contemplated that can be used in HIV-1 and HSV viruses seen in humans (16-18). Jadwiga Zabielska-Matejuk et al. have synthesized several 1,3-dialkylimidazolium derivatives and studied their antifungal properties to protect wood materials. The synthesized imidazolium salts have been found to inhibit the growth of fungus, in particular *Sclerophoma pityophila* (19-27).

5-Imidazole-carbaldehyde and its mono- (N-1) alkyl or aryl analogs are often used in medicine as drug building blocks, but their dialkyl (N-1 and N-3) analogs are less visible in the literature. In this work, new imidazole derivatives were synthesized from 4-methyl-5-imidazole carbaldehyde by alkylation of N atom

or condensation of carbonyl group with appropriate reagents.

EXPERIMENTAL

General

The starting chemicals were commercially purchased from Merck, Aldrich, Acros Organics, and ABCR.

The ^1H NMR spectra were recorded on Bruker 400 MHz spectrometers for samples in DMSO and CDCl_3 . The signals are expressed as parts per million down fields from $(\text{CH}_3)_4\text{Si}$, used as an internal standard. IR spectra were measured using a Jasco FT-IR-300E spectrometer. Electrospray ionization mass spectra were obtained in positive ion mode on a AB SCIEX LC - MS/MS spectrometer. Column chromatographic isolation was performed on Merck Kieselgel 60 (70-230 mesh) using ethyl acetate and n-hexane as the eluent. An analytical thin-layer chromatography was performed on Merck pre-coated silica gel 60 GF-254 with 0.25-mm thick TLC plates.

1,4-dimethyl-imidazole-5-carbaldehyde (1)

NaH (60%, 2.179 g, 0.0908 mol) in dry THF (120 mL) was added to 4-methyl-5-imidazole carbaldehyde (5 g, 0.0454 mol) at room temperature for 30 min. Methyl iodide (5.65 mL, 0.0908 mol) was then added and mixed at room temperature for 20 hours. As a result of the reaction, the mixture had solid and liquid phases. The THF phase was isolated, then the solid phase was washed several times with CHCl_3 , then the organic phases were combined. The remaining precipitate was dissolved in water and extracted again with CHCl_3 . Then all the organic phases were combined and the solvent was evaporated. The resulting brownish-yellow oily substance was purified by column chromatography using ethyl acetate over silica gel. Isomer **1** was obtained as a yellow oily solid (3.32 g, 59%). ^1H NMR (400 MHz, DMSO): δ_{H} 2.46 (3H, s, CH_3), 3.60 (3H, s, CH_3), 7.73 (1H, s, imidazole C-H), 9.76 (1H, s, CHO).

1-Benzyl-4-methyl-imidazole-5-carbaldehyde (2)

4-Methyl-5-imidazole carbaldehyde (1 g, 9.08 mmol) was treated with NaH (60%, 720 mg, 18.16 mmol) in dry DMF (120 mL) at room temperature for 5 min. Benzyl chloride (1.36

mL, 11.8 mmol) was then added and mixed at room temperature for 20 h. After that saturated sodium carbonate solution (25 mL) was added to the mixture, extracted by addition of 30 mL of water and extraction with ethyl acetate (3 x 30 mL). The combined extracts were filtered after being dried over sodium sulfate. The solvent was removed on the rotary evaporator. The resulting brownish-yellow oily substance was purified by column chromatography using ethyl acetate over silica gel. Yellow oily solid (0.76 g, 42%). Mixture of isomers **2a** and **2b** ^1H NMR (400 MHz, CDCl_3): d_{H} 2.30 (3H, s, CH_3), 2.38 (3H, s, CH_3), 4.41 (2H, s, N- CH_2), 4.67 (2H, s, N- CH_2), 7.30-7.62 (10H, m, Ar-H), 9.79 (1H, s, CHO), 9.83 (1H, s, CHO).

1-(2-phenylethyl)-4-methyl-imidazole-5-carbaldehyde (3)

4-Methyl-5-imidazole carbaldehyde (0.5 g, 4.5 mmol) was treated with NaH (60%, 220 mg, 5.5 mmol) in dry DMF (120 mL) at room temperature for 5 min. It was allowed to mix. 2-Phenylethylbromide (0.7 mL, 5 mmol) was then added and mixed at room temperature for 20 h. Saturated sodium carbonate solution (25 mL) was then added to the mixture, extracted by addition of 25 mL of water and extraction with ethyl acetate (2 x V). The combined extracts were filtered after being dried over sodium sulfate. The solvent was removed on the rotary evaporator. The resulting brownish-yellow oily substance was purified by column chromatography eluting with ethyl acetate over silica gel. It was seen from the ^1H NMR spectrum that this compound was an isomeric mixture in approximately equal proportions. Yellow oily solid (0.48 g, 49%). Mixture of isomers **3a** and **3b** ^1H NMR (400 MHz, CDCl_3): d_{H} 2.27 (3H, s, CH_3), 2.41 (3H, s, CH_3), 2.93 (2x2H, t, 2x CH_2), 4.05 (2H, t, N- CH_2), 4.40 (2H, t, N- CH_2), 6.94-7.25 (10H, m, Ar-H), 9.82 (1H, s, CHO), 9.85 (1H, s, CHO). IR (ATR, v/cm^{-1}): 3127, 2923-2852, 1662, 1610. ESI-MS: m/z = 215 (**M**) $^+$; Calcd. for $\text{C}_{13}\text{H}_{14}\text{N}_2\text{O}$: 214.11.

1-(2-Chlorobenzyl)-4-methyl-imidazole-5-carbaldehyde (4)

4-Methyl-5-imidazole carbaldehyde (1 g, 9 mmol) was treated with NaH (60%, 720 mg, 18 mmol) in dry DMF (120 mL) at room temperature for 5 min. It was allowed to mix. 2-chlorobenzyl bromide (1.53 mL, 10 mmol)

was then added and mixed at room temperature for 1 day. Saturated sodium carbonate solution (25 mL) was then added to the mixture extracted by the addition of about 25-30 mL of water and extraction with ethyl acetate (3 x 40 mL). The combined extracts were filtered after being dried over sodium sulfate. The solvent was removed on the rotary evaporator. The resulting brown-yellow oily substance was purified by column chromatography eluting with ethyl acetate over silica gel. Yellow oily solid was observed as a mixture of products in ^1H NMR (0.82 g, 39%). Main product **4a** (%85): ^1H NMR (400 MHz, CDCl_3): d_{H} 2.42 (3H, s, CH_3), 5.48 (2H, s, CH_2), 6.90-7.48 (5H, m, Ar-H), 9.73 (1H, s, CHO). By-product **4b** (%15): ^1H NMR (400 MHz, CDCl_3): d_{H} 2.37 (3H, s, CH_3), 4.66 (2H, s, CH_2), 6.90-7.48 (5H, m, Ar-H), 9.85 (1H, s, CHO). IR (ATR, v/cm^{-1}): 3111, 2851, 1661, 1543. ESI-MS : m/z = 235(**M**) $^+$; Calc. for $\text{C}_{12}\text{H}_{11}\text{ClN}_2\text{O}$: 234.05.

1-(3-Chlorobenzyl)-4-methyl-imidazole-5-carbaldehyde (5)

4-Methyl-5-imidazole carbaldehyde (1 g, 9 mmol) was treated with NaH (60%, 720 mg, 18 mmol) in dry DMF (120 mL) at room temperature for 5 min. It was allowed to mix. 3-Chlorobenzyl bromide (1.4 mL, 10 mmol) was then added and mixed at room temperature for 1 day. Saturated sodium carbonate solution (25 mL) was then added to the mixture extracted by addition of 25 mL of water and extraction with ethyl acetate (3 x 40 mL). The combined extracts were filtered after being dried over sodium sulfate. Solvent was removed on the rotary evaporator. The resulting oily substance was purified by column chromatography eluting with ethyl acetate over silica gel. Yellow oily solid (0.71 g, 33%). It was found from the ^1H NMR results that the material was isolated as an isomeric mixture. Main product **5a** (%71): ^1H NMR (400 MHz, CDCl_3): d_{H} 2.43 (3H, s, CH_3), 5.36 (2H, s, CH_2), 6.98-7.54 (5H, m, Ar-H), 9.74 (1H, s, CHO). By-product **5b** (%29): ^1H NMR (400 MHz, CDCl_3): d_{H} 2.34 (3H, s, CH_3), 4.95 (2H, s, CH_2), 6.98-7.54 (5H, m, Ar-H), 9.88 (1H, s, CHO). IR (ATR, v/cm^{-1}): 3088, 2936, 2841, 1659, 1598. ESI-MS : m/z = 235(**M**) $^+$; Calc. for $\text{C}_{12}\text{H}_{11}\text{ClN}_2\text{O}$: 234.05.

5-formyl-1,3,4-trimethyl-imidazolium tetrafluoroborate (6)

1,4-dimethyl-1H-imidazole-5-carbaldehyde (1 g, 8.77 mmol) and trimethyloxonium tetrafluoroborate (1.55 g, 0.0105 mol) were stirred in dry ethyl acetate (15 mL) for 2 hours at room temperature. The solvent was removed on the rotary evaporator. Due to the fact that the product is highly polar, the organic phase could not be extracted and also could not be purified by chromatography. The mixture was further left to rinse in a mixture of ethanol and chloroform. ¹H NMR analysis was performed on pure white crystals and the expected product was observed to be formed. ¹H NMR (400 MHz, DMSO): δ_{H} 2.59 (3H, s, CH₃), 3.79 (3H, s, N-CH₃), 4.00 (3H, s, N-CH₃), 9.14 (1H, s, imidazolium C-H), 9.94 (1H, s, CHO).

2-((4-methyl-1H-imidazole-5-yl)methyleneamino)phenol (8)

4-methyl-1H-imidazole-5-carbaldehyde (1 g, 9.082 mmol), 2-aminophenol (0.99 g, 9.082 mmol) was refluxed in 95% EtOH for 1 day. The reaction mixture was allowed to crystallize with EtOH. A light yellow solid 4.3.1 (0.81 g, 44%) was obtained. Compound **8** was found to have very little impurity from the ¹H NMR spectrum. ¹H NMR (400 MHz, DMSO): δ_{H} 2.38 (3H, s, CH₃), 6.8-7.07 (4H, m, Ar-H), 7.45 (1H, s, N=C-H), 7.83 (1H, s, imidazole C-H), 8.73 (1H, s, Ar-OH), 12.61 (1H, broad s, N-H).

2-((4-methyl-1H-imidazole-5-yl)methyleneamino)benzenethiol (9)

4-Methyl-5-imidazole carbaldehyde (1 g, 9.082 mmol) and 2-aminothiophenol (1.137 g, 9.082 mmol) were refluxed in EtOH (20 mL) for 1 hour. The reaction was followed by TLC (50% EtOAc / n-Hexane). The reaction was continued until the starting material was finished in the TLC. When the reaction mixture was allowed to cool, it was immediately observed that light cream crystals began to form. A quantity of the obtained solid light cream matter (1.494 g) was observed to be **12** by ¹H NMR analysis **9** as well as part of the material being converted to ring closure reaction. It was detected from the ¹H NMR spectrum that the ratio of **9** to **12** was 79:21.

Main product **9** (%79): ¹H NMR (400 MHz, DMSO): δ_{H} 2.16 (3H, s, CH₃), 3.38 (1H, s, SH), 6.48-6.59 (3H, m, Ar-H), 6.61-6.97 (2H, m,

Ar-H), 7.45 (1H, s, imidazole C-H), 8.02 (1H, s, N=C-H), 11.93 (1H, broad s, N-H).

By-product **12** (%21): ¹H NMR (400 MHz, DMSO): δ_{H} 2.66 (3H, s, CH₃), 7.34-7.48 (2H, d.t., 2xAr-H), 7.70 (1H, s, imidazole C-H), 7.90- 8.04 (2H, d.d., 2xAr-H), 12.56 (1H, broad s, N-H).

2-((4-methyl-1H-imidazole-5-yl)methyleneamino)aniline (10)

1-2-diaminobenzene (1.178 g, 10.9 mmol) with 4-methyl-5-imidazolecarbaldehyde (1 g, 9.082 mmol) was refluxed in 20 mL EtOH for 1 day. The reaction was extracted by TLC (20% EtOH, EtOAc), the product was observed to be lower in TLC as it was more polar than imidazole. The solvent was removed and the remaining mixture was purified by flash column chromatography on silica gel using n-hexane, ethyl acetate and EtOH. (The solvent polarity for the separation was 20% acetate-n-hexane and the temperature was increased to 50% EtOH / EtOAc mixture). The fractions of the product were collected and the solvent was removed to give the target compound **10** as a light brown solid (1.66 g, 90%).

It was determined that there is an isomeric mixture of **10** from ¹H NMR spectrum. The isomeric mixture may possibly be an E/Z mixture around -N=CH-. The isomeric ratios were found to be 63% for the main isomer and 37% for the other isomer. ¹H NMR (400 MHz, DMSO): δ_{H} 2.56 (3H, s, CH₃), 2.65 (3H, s, CH₃), 7.10-7.59 (8H, m, Ar-H), 7.48 (1H, s, imidazole C-H), 7.71 (1H, s, imidazole C-H), 7.82 (2H, s, N=C-H), 12.25 (2H, broad s, N-H).

2-((4-methyl-1H-imidazole-5-yl)methyleneamino)benzo[d]oxazole (11)

2-((4-methyl-1H-imidazol-5-yl)methyleneamino)phenol (**8**) (0.6 g, 2.28 mmol) and lead tetraacetate (1.32 g, 2.98 mmol) were dissolved in acetic acid (12 mL) at 45-50 °C for 24 hours. The reaction was monitored by TLC (25% EtOH / EtOAc); TLC was observed to walk faster because it is less polar than the starting material of the product. The reaction mixture was basified in ice bath with about 20 mL of 10% NaOH. The organic extracts were extracted with chloroform and the organic phase was dried over sodium sulfate. The mixture was separated by column chromatography on silica gel using n-hexane,

ethyl acetate, and EtOH. (The solvent polarity for the separation was 5% ethyl acetate-n-hexane and eluted to 25% EtOH / EtOAc mixture). Compound **11** was isolated as a pale yellow solid (0.41 g, 69%). ^1H NMR (400 MHz, DMSO): δ_{H} 2.63 (3H,s, CH₃), 7.35 (2H, m, 2xAr-H), 7.72 (2H, m, 2xAr-H), 7.83 (1H, s, imidazole C-H). IR (ATR, ν/cm^{-1}): 3379, 1642. ESI-MS : $m/z = 200(\text{M})^+$; Calcd. for C₁₁H₉N₃O:199.07.

2-(4-methyl-1H-imidazole-5-yl)benzo[d]thiazole (12)

Compound **9** (0.6 g, 2.764 mmol) and lead tetraacetate (1.2 g, 2.764 mmol) were stirred in acetic acid (10 mL) at 45-50 °C for 1 day. After termination of the reaction, the mixture was basified in ice bath with about 20 mL of NaOH. The organic material was extracted with chloroform and the organic phase was dried over sodium sulfate. The solvent was removed and the residue was chromatographed on silica gel in a mixture of ethyl acetate-n-hexane (1: 1). Compound **12** was obtained as a yellow solid (0.348 g, 30%). ^1H NMR (400 MHz, DMSO): δ_{H} 2.66 (3H,s, CH₃), 7.33-7.48 (2H, d.t., 2xAr-H), 7.71 (1H, s, imidazole C-H), 7.91- 8.05 (2H, d.d., 2xAr-H), 12.58 (1H, broad s, N-H). IR (ATR, ν/cm^{-1}): 3054, 3015, 2937-2838-2711, 1603. ESI-MS : $m/z = 216(\text{M})^+$; Calcd. for C₁₁H₉N₃S:215.05.

2-(4-methyl-1H-imidazole-5-yl)-1H-benzimidazole (13)

2-((4-methyl-1H-imidazole-5-yl)methyleneamino)aniline (**10**) (1.1281 g, 5.63 mmol) and lead acetate (2.49 g, 5.63 mol) in glacial acetic acid (20 mL) was added for 24 hours at 35-40 °C. It was basified with 10% NaOH. Extraction with chloroform was performed. (3xV) and the organic phase was dried over sodium sulfate. Crystallization yielded **13** as a light yellow solid (0.66 g, 59%). ^1H NMR (400 MHz, DMSO): δ_{H} 2.55 (3H,s, CH₃), 7.14 (2H, m, 2xAr-H), 7.39 (1H, s), 7.58 (2H, m, 2xAr-H), 7.80 (1H, s, imidazole C-H), 12.45 (1H, broad s, N-H). IR (ATR, ν/cm^{-1}): 3127, 2922, 2852, 1606. ESI-MS : 293.1(**M**)⁺; Calcd. for C₁₁H₁₀N₄:198.09.

RESULTS AND DISCUSSION

The alkylation reaction of 4-methyl-5-imidazole carbaldehyde is shown in Figure 1. The acidic N-H hydrogen in the imidazole ring was first ionized with strong base NaH and then converted to the corresponding primary alkyl halides (N-alkylation) by reaction with the S_N2 type reaction.

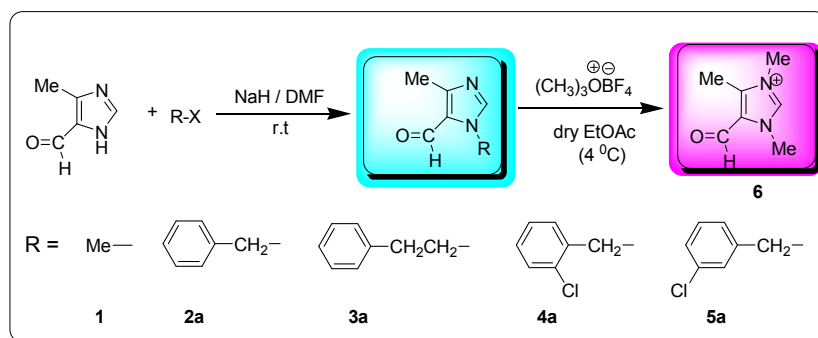


Figure 1. The alkylation reaction of 4-methyl-5-imidazole carbaldehyde.

An isomeric mixture or polyalkylation can be expected because of the presence of two N atoms on the imidazole ring. As a result of the reaction with Me-I, very pure N-methylated imidazole derivative was obtained. ^1H -NMR

analyses showed that there was only one isomer **1** for this compound. In the Me-I reaction, although more than two equivalents of Me-I was taken, multiple alkylation has not been detected.

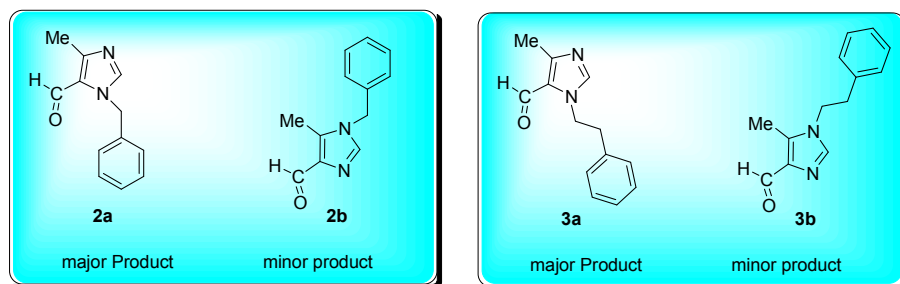


Figure 2. Isomeric mixtures of **2a**, **2b** and **3a,3b**.

The second reaction of this section is the reaction with benzyl chloride (PhCH_2Cl). Among the alkyl halides used, only benzyl chloride is less reactive than the others (other alkyl halides are alkyl bromides and iodides). From the benzyl chloride reaction, the product was impure and is also an isomeric mixture. However, when the alkylation reaction was carried out with sterically more hindered alkyl group, such as 2-phenylethyl bromide, isomeric mixture (**3a** and **3b**) were obtained (Figure 2). The $^1\text{H-NMR}$ analysis showed that the isomeric mixture almost in the vicinity of 50:50. When alkylation reactions were carried out with 2-chlorobenzyl bromide or 3-chlorobenzyl bromide, which are structurally very similar with benzyl chloride, the reaction proceeded smoothly and expected products (**4a** and **5a**) were obtained. In all alkylation reactions, except Me-I, the product was obtained both as a low yield and as an isomeric mixture; for instance, the alkylation reaction of 4-methyl-5-

imidazole carbaldehyde with 2-chlorobenzyl bromide or 3-chlorobenzyl bromide gave about 30% yield and the products were isomeric mixture (**4a** / **4b** and **5a** / **5b**). But from the similar reaction with Me-I, only one isomer with higher yield (60%) was obtained.

The isomeric mixtures of **4a** and **4b** or **5a** and **5b**, could not be separated completely by column chromatography (Figure 3). ^1H NMR analysis indicated that the major isomer was **4a** and the minor isomer was **4b** and the ratio of the two isomers was 85:15. Similar way, the ^1H NMR spectroscopy showed that the **5a** is major and the **5b** is minor and isomer ratio is 71/29. It is not surprising that, although the isomeric mixture is not observed in the reaction with MeI, the alkyl halides with a large R group causes isomerization. This can be attributed to the steric effect of the carbaldehyde group adjacent to the N-H group.

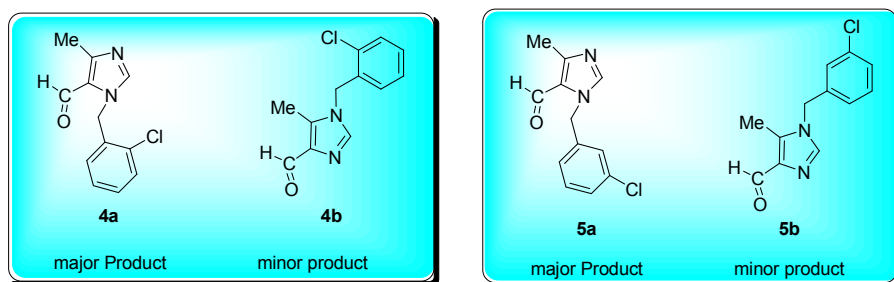


Figure 3. Isomeric mixtures of **4a**, **4b** and **5a,5b**.

4-Methyl-5-imidazole carbaldehydes (N-R) were tried to convert to their imidazolium salts using $(\text{CH}_3)_3\text{O}^+\text{BF}_4^-$, from this reaction only N-

Me isomer **1** gave desired imidazolium salt **6**, but other isomers (N-R) for example **5a** could not converted to **7**(figure 4).

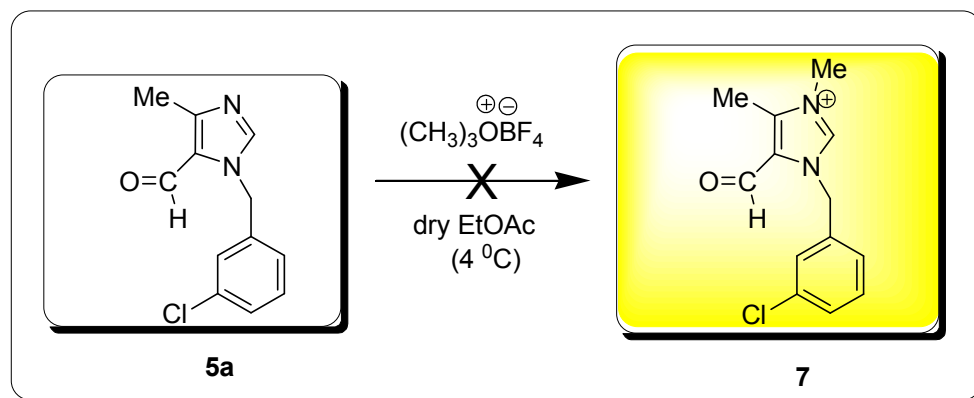


Figure 4. Unsuccessful synthesis of compound **7**.

Synthesis of benzoxazole, benzothiazole and benzimidazole derivatives from 4-methyl-5-imidazole carbaldehyde

In the literature, benzoxazole, benzothiazole and benzimidazole derivatives were synthesized from less reactive carbonyl compounds with 2-aminophenol, 2-aminobenzenethiol and 1,2-diaminobenzene etc via two step Schiff base reaction and their antimicrobial effects were investigated (28-32). Therefore, it was thought that the basic starting material used in this study, 4-methyl-5-imidazole carbaldehyde, could react with 2-aminophenol, 2-aminobenzenethiol, and 1,2-diaminobenzene. Thus, synthesis of benzoxazole, benzothiazole and benzimidazole

derivatives containing imidazole rings has been tried to synthesize by a two-step reaction as shown in Figure 5. The intermediate products (**8**, **9** and **10**), obtained as a result of the first step shown in Figure 5, were isolated as an isomeric mixture or with some impurities (analyzed by ^1H NMR spectroscopy). The isomerization (cis / trans isomers) may be derived from the $-\text{N}=\text{CH}-$ double bond. Further reaction of the intermediates gave new benzoxazole, benzothiazole and benzimidazoles (**11**, **12** and **13**) as pure compounds.

In addition, compounds 1, 2, 12 and 13 were synthesized by different methods from the literature (33-35).

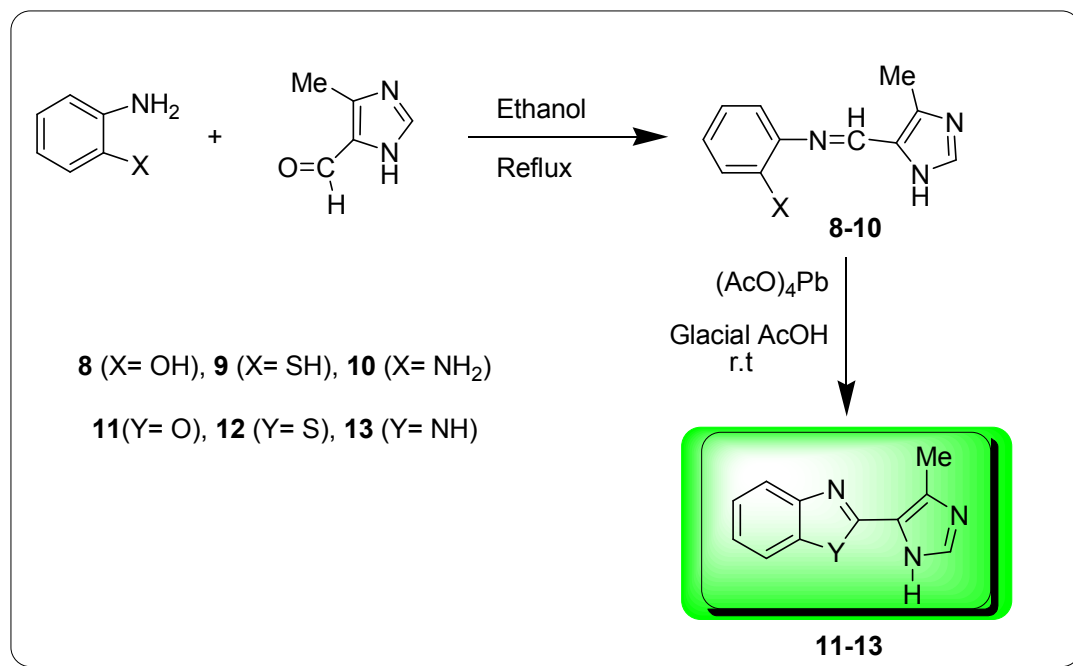


Figure 5. Synthesis of benzoxazole, benzothiazole and benzimidazole derivatives containing imidazole ring.

CONCLUSIONS

In this work, the N-1 atom on the imidazole ring of the starting 4-methyl-1H-imidazole-5-carbaldehyde were derivatized with different alkyl groups. In addition, both N atoms of the starting imidazole-carbaldehyde were methylated to give 5-carbaldehyde-1,3,4-trimethyl-3-imidazolium salt. The salt which possess quite reactive carbonyl group could be used for synthesis of other imidazolium derivatives. Furthermore, 4-methyl-5-imidazole carbonyl was converted into the benzoxazole, benzothiazole and benzimidazoles by a two-step reaction over the aldehyde group. These new compounds could display some biological activities.

ACKNOWLEDGMENTS

The authors are grateful to the Zonguldak Bülent Ecevit University (Grant No.: BAP 2014-72118496-06) and Düzce University (Grant No.: 2012.05.03.097) for the financial aid of this study.

REFERENCES

- Butler K, Howes HL, Lynch JE and Pirie DK. Nitroimidazole Derivatives. Relationship between Structure and Antitrichomonal Activity. *J. Med. Chem.* 1967;10(5):891-7.
- a) Giraldi PN, Mariotti V, Namini G, Tosolini GP, Dradi E, Logemann W, de Carnevi I, Monti G. *Arzneimittelforsch.* 1970; 20,52 b) Heeres J, Mostmans JH and Maes R, German Patent, 1975;2:429,755.
- Rufer C, Kessler HJ, Schroeder E. Chemotherapeutic nitroheterocycles 6. Substituted 5-aminomethyl-3-(5-nitro-2-imidazolylmethyleneamino)-2-oxazolidinones. *J. Med. Chem.* 1971; 14(2):94-6.
- Arton., Netherlands Patent, 1965, 6413814; *Chem. Abstr.*, 1965, 63, 18097b
- Godefroi EF, Van Cutsem J, Van Der Eycken CAM, Janssen PAJ. *Med. Chem.* 1967;10:1160.

6. Godefroi EF, Heeres J, Van Cutsem J, Janssen PAJ. Preparation and antimycotic properties of derivatives of 1-phenethylimidazole. *J. Med. Chem.* 1969;12 (5):784-91.
7. Durant GJ, Emmett JC, Ganellin CR, Miles PD, Parsons ME, Prain HD, White GR. Cyanoguanidine-thiourea equivalence in the development of the histamine H₂-receptor antagonist, cimetidine. *J. Med. Chem.* 1977;20 (7):901-6.
8. Walter LA. German Patent. 1969;1: 905, 353; *Chem. Abstr.*, 1970; 72, 317904.
9. Almansa C, Alfón J, de Arriba AF, Cavalcanti FL, Escamilla I, Gómez LA, Miralles A, Soliva R, Bartrolí J, Carceller E, Merlos M, García-Rafanell J. Synthesis and Structure-Activity Relationship of a New Series of COX-2 Selective Inhibitors: 1,5-Diarylimidazoles. *J. Med. Chem.* 2003;46 (16):3463-75.
10. Liu H, Kerdesky FA, Black LA, Fitzgerald M, Henry R, Ebenshade TA, Hancock AA, Bennani YL. An efficient multigram synthesis of the potent histamine H₃ antagonist GT-2331 and the reassessment of the absolute configuration. *J. Org. Chem.* 2004;69(1):192-4.
11. Nallan L, Bauer KD, Bendale P, Rivas K, Yokoyama K, Hornéy CP, Pendyala PR, Floyd D, Lombardo LJ, Williams DK, Hamilton A, Sebti S, Windsor WT, Weber PC, Buckner FS, Chakrabarti D, Gelb MH, Voorhis WCV. Protein Farnesyltransferase Inhibitors Exhibit Potent Antimalarial Activity. *J. Med. Chem.* 2005;48(11):3704-13.
12. Berezin M, Achilefu S. Novel synthon for incorporating 1,3-dimethyl-imidazolium group into molecular architecture. *Tetrahedron Letters.* 2007;48(7):1195-9.
13. Davis Jr JH, Forrester KJ, Merrigan T. Novel organic ionic liquids (OILs) incorporating cations derived from the antifungal drug miconazole. *Tetrahedron Letters.* 1998;39(49):8955-8.
14. Hu B, Malamas M, Ellingboe J, Largis E, Han S, Mulvey R, Tillett J. New oxadiazolidinedione derivatives as potent and selective human β_3 agonists. *Bioorganic & Medicinal Chemistry Letters.* 2001;11(8): 981-4.
15. Demberelnyamba D, Kim K-S, Choi S, Park S-Y, Lee H, Kim C-J, Yoo I-D. Synthesis and antimicrobial properties of imidazolium and pyrrolidinium salts. *Bioorganic & Medicinal Chemistry.* 2004;12(5):853-7.
16. Ourth DD. Antiviral activity against human immunodeficiency virus-1 in vitro by myristoylated-peptide from *Heliothis virescens*. *Biochemical and Biophysical Research Communications.* 2004;320(1):190-6.
17. Orhan E, Garci A, Tina R, Saudani M, Dyson PJ, Therrien B. Cytotoxic double arene ruthenium metalla-cycles that overcome cisplatin resistance. *Journal of Organometallic Chemistry,* 2016;803: 39-44.
18. Orhan E, Garci A, Riedel T, Dyson PJ, Therrien B. Cytotoxicity of arene ruthenium metalla-rectangles incorporating bispyridyl diimide linkers. *Journal of Organometallic Chemistry,* 2016; 815-816: 53-8.
19. Zabielska-Matejuk J. Antifungal properties of new quaternary ammonium compounds in relation to their surface activity. *Wood Sci Technol.* 2005;39(3):235-43.
20. Reiter LA. Synthesis of 4(5)-acyl-, 1-substituted 5-acyl- and 1-substituted 4-acyl-1H-imidazoles from 4-aminoisoxazoles. *J. Org. Chem.* 1987;52(13):2714-26.
21. Koch P, Ansideri F. 2-Alkylsulfanyl-4(5)-aryl-5(4)-heteroarylimidazoles: An Overview on synthetic Strategies and Biological Activity. *Arch. Pharm. Chem. Life Sci.* 2017;350(12): e1700258.
22. Beyer C, Wagenknecht H-A. Synthesis of Spiropyrans As Building Blocks for Molecular Switches and Dyads. *J. Org. Chem.* 2010;75(8):2752-5.
23. Küçükbay H, Durmaz R, Orhan E, Günel S. Synthesis, antibacterial and antifungal activities of electron-rich olefins derived

benzimidazole compounds. *Il Farmaco*. 2003;58(6):431-7.

24. Akkurt M, Öztürk S, Küçükbay H, Orhan E, Büyükgüngör O. 1-Ethyl-3-(2-phenylethyl) benzimidazole-2-selone. *Acta Crystallographica Section E: Structure Reports Online*. 2004;60(7):o1263-o1265.

25. Akkurt M, Yıldırım SO, Orhan E, Küçükbay H, Büyükgüngör O. 1-Methoxyethyl-5-nitrobenzimidazole. *Acta Crystallographica Section E: Structure Reports Online*. 2005;61(9):o2804-5.

26. Yıldırım SO, Akkurt M, Küçükbay H, Orhan E, Büyükgüngör O. 6-Nitro-1-(2-phenylethyl)1H-benzimidazole. *Acta Crystallographica Section E: Structure Reports Online*. 2005;61(7):o2038-9.

27. Küçükbay H, Günal S, Orhan E, Durmaz R. Synthesis and Antimicrobial Activities of Some Transition Metal Benzimidazole Complexes. *Asian Journal of Chemistry*. 2010;22(9):7376.

28. Abdel-Magid AF, Carson KG, Harris BD, Maryanoff CA, Shah RD. Reductive Amination of Aldehydes and Ketones with Sodium Triacetoxyborohydride. Studies on Direct and Indirect Reductive Amination Procedures. *J. Org. Chem.* 1996;61(11):3849-62.

29. Gwaltney SL, O'Connor SJ, Nelson LTJ, Sullivan GM, Imade H, Wang W, Hasvold L, Li Q, Cohen J, Gu W-Z, Tahir SK, Bauch J, Marsh K, Ng S-C, Frost DJ, Zhang H, Muchmore S, Jakob CG, Stoll V, Hutchins C, Rosenberg SH, Hing. Aryl tetrahydropyridine inhibitors of farnesyltransferase: bioavailable analogues with improved cellular potency.

Bioorganic & Medicinal Chemistry Letters. 2003;13:1363-6.

30. Pinar Ş, Akkurt M, Küçükbay H, Orhan E, Büyükgüngör O. Bis[1-(but-2-enyl)-5-nitro-1H-benzimidazole-κN³]dichlorocobalt(II), *Acta Crystallographica Section E: Structure Reports Online*. 2006;62(7):m1663-5.

31. Akkurt M, Karaca S, Küçükbay H, Orhan E, Büyükgüngör O. 1-Benzyl-3-(2-phenethyl)benzimidazolium bromide monohydrate, *Acta Crystallographica Section E: Structure Reports Online*. 2005;61(8):o2452-4.

32. Akkurt M, Karaca S, Küçükbay H, Orhan E, Büyükgüngör O. Dichlorobis[1-(2-ethoxyethyl)-1H-benzimidazole-κN³]nickel(II), *Acta Crystallographica Section E: Structure Reports Online*. 2004;61(1):m41-3.

33. Hubball W, Pyman FL. Glyoxaline-4(5)-formaldehyde. *Journal of the Chemical Society*, 1928; 21-32.

34. Reiter LA. Synthesis of 4(5)-Acyl-, 1-Substituted 5-Acyl-, and 1-Substituted 4-Acyl-1H-imidazoles from 4-Aminoisoxazoles. *J. Org. Chem.*, 1987; 52(13): 2714-26.

35. Gilbert JG, Addison AW, Palaniandavar M and Butcher RJ. Synthesis of Some Benzimidazole-, Benzothiazole- and Pyridine Derived Chelating Agents. *Journal of Heterocyclic Chemistry*, 2002;39(2):399-404.



Experimental and modeling study of polyphenols in *Olea europaea* leaves through ultrasound-assisted extraction

Selin Şahin*  

Istanbul University-Cerrahpaşa, Engineering Faculty, Department of Chemical Engineering, 34320 Avcılar, Istanbul, Turkey.

Abstract: Olive tree (*Olea europaea*) leaves were extracted by ultrasound-assisted extraction (UAE). The attention was focused on the yield of extract and its polyphenols, and extraction kinetics to contribute to the application of the extraction process industrially. Samples were extracted with water, ethanol, methanol, and their aqueous solutions (50%, v/v) under temperature values ranging from 30 to 50 °C. Additionally, the temperature interval changed between 30 and 80 °C, when water was used as the solvent. Backing the solvents with water enhanced the polyphenolic yield. Total phenolic content (TPC) from water extracts decreased after a certain temperature point, as a result of the problems of degradation. The second-order model was followed for characterizing the kinetic of the UAE process of TPC from olive leaves under various solvents and temperatures. Major phenolic component was also quantified for each solvent system by means of High Performance Liquid Chromatography (HPLC).

Keywords: Agro-industrial by-products; mathematical model; olive leaves; polyphenols extraction.

Submitted: January 04, 2019. **Accepted:** September 10, 2019.

Cite this: Şahin S. Experimental and modeling study of polyphenols in *Olea europaea* leaves through ultrasound-assisted extraction. JOTCSA. 2019;6(3):383-94.

DOI: <https://doi.org/10.18596/jotcsa.508113>.

*Corresponding author. E-mail: selins@istanbul.edu.tr.

INTRODUCTION

Olive tree (*Olea europaea*) is grown to produce table olives and olive oil, and the leaves, its abundant wastes, are traditionally used for therapeutic purposes. Olive leaf is a substantial by-product of tree pruning and fruit harvesting. Recent scientific studies have reported that phenolic extracts from all parts (such as fruit, leaves, pomace, and even olive tree extracts) of the olive crop have remarkable antioxidant activity (1-5).

Olive plantation in Mediterranean countries counts about 98% (corresponding to 8 ha) of the world's cultivation. Olive leaf obtained from pruning is estimated to be 25 kg per olive tree, accounting for approximately 10% of the total weight of the olives from the olive oil industries. So, this huge amount of waste by-product should be valorized for both economic and ecological points. Due to its beneficial effects to health, interests in this by-product have been increasing in many

researchers and commercial organizations (6,7). Generally, medical properties of this natural material is mostly attributable to oleuropein, which is its predominant phenolic ingredient (8–10). Oleuropein is a phenolic

secoiridoid compound, and has a formula similar to the forms of dimethyl oleuropein (sketched in ChemDraw, see Figure 1) such as ligstroside, oleuroside, and verbascoside.

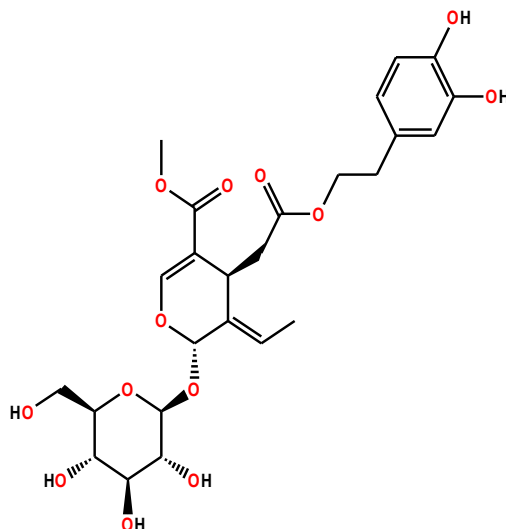


Figure 1. Molecular structure of oleuropein.

Since various biological activities of plant extracts and their phytochemical content have been reported, the study of higher plants with known ethnobotanical knowledge has attracted the attention of researchers. Due to the transition from disease-based products to products that promote healthy living, phytochemicals have high commercial value in local and global markets. In addition, the prevalence of chronic diseases that cannot be treated with conventional drugs has transformed the phytochemical industry into an approaching industrial sector. However, a common trap associated with this sector is that the production of these phytochemicals is often carried out by various conventional methods, resulting in high losses and low yields. In order to make the phytochemical industries suitable and profitable, various transformations with appropriate processes such as planting and harvesting, raw material preparation and high-added value production are required. Furthermore, the process technology for successful modernization of phytochemical processes needs to be optimized for the purpose of extraction and product formulation. In this respect, the modeling of the kinetics of a process is a beneficial engineering tool for controlling the

process for industrial applications through optimization and simulation (11).

Ultrasound technology has not been developed recently (12). Sound waves having frequencies greater than 20 kHz can move within a material and may include expansion and compression cycles during movement in the environment. The frequency between 18 and 40 kHz range was considered to be an excellent source of energy to support ultrasound-assisted extraction (UAE). UAE is much more rapid than conventional extraction methods due to the high contact surface area between the solid matrix and liquid solvent. High frequency sound energy can separate phytochemicals from plant materials by means of cavitation. The formation and collapse of cavitation or microscopic bubbles creates a tremendous amount of energy, such as heat, pressure, and mechanical shear. Thus, it increases mass transfer and facilitates solvent diffusion to the cell (13, 14). In this sense, special attention has been given to the use of UAE in the recovery of bio-active compounds from diverse natural sources. The related cavitation has a great effect on extraction efficiency and its kinetics. Therefore, it enhances the penetration

potential of the solvent to the cell matrix and favors mass transfer. In the UAE process, sonication can disturb walls of the bioactive cells by improving the release of target content. UAE is cheaper and easier to extract fine chemicals from natural raw materials comparing to other advanced methods such as microwave and supercritical CO₂ (15). UAE has been suggested as an advanced separation method with better recovery of the target bioactive components with less energy and solvent consumption (16, 17).

In this study, olive leaves were extracted by means of UAE under several conditions. The kinetic description of the UAE process was carried out by second-order kinetic model with respect to total phenolic content (TPC) extraction. Effect of extraction temperature was also investigated as well as solvent type. Finally, the most distinguished phenolic compound of the olive leaf extract was also quantified by means of high performance liquid chromatography (HPLC).

MATERIAL AND METHODS

Material

Olive leaf samples were collected from Kaş in Mediterranean area of Turkey. Leaf samples belong to *Tavşan yüreği* cultivar of olives. The samples collected in November (2013), where the leaves have the highest period in terms of phenolic matter (18). The leaves were dried at ambient conditions in dark. After 4 days, the samples were stored at plastic bags kept in the dark until grinding for the extraction. The moisture of the leaf sample was nearly 16 % of the total leaf weight.

Ethanol, methanol, acetonitrile, and formic acid were purchased from Merck (Darmstadt, Germany), while Folin-Ciocalteu, gallic acid, and sodium carbonate were procured from Sigma-Aldrich (St. Louis, MO).

Ultrasound-Assisted Extraction

Extraction process was carried out in a sonicator (Protech) with 50 Hz of frequency under several temperature values (30, 40, 50, 60, 70, and 80 °C). A specific amount of leaf samples were added into the selected solvents (water, ethanol, methanol, and their 50% aqueous solutions (v/v)), respectively. The beaker containing the material and the solvent was kept in an ice bath to maintain the temperature constant. A centrifuge (Nüve, CN 180) was used to separate the heterogeneous mixture for 15 min of time at 5000 rpm. Aqueous olive leaf extracts were dried in a rotary evaporator (Buchi, Switzerland) under vacuum.

Folin-Ciocalteu Method

The procedure developed by Malik and Bradford (2006) was exploited for the quantification of total polyphenolic content of the extract samples (19). UV-spectrophotometry (PG Instruments, T60/Leicestershire, England) was used as described in detail by Şahin and Samli (2013) (20). Results were given as gallic acid equivalence per gram of dried leaf (mg GAE/g DL).

HPLC

Extracts obtained under optimum conditions by each solvent system were also analyzed by High Performance Liquid Chromatography (HPLC). The gradient elution program used in this method is shown in Table 1.

Table 1. Gradient program and analysis conditions applied in HPLC.

Conditions	Program		
	Time (sec)	A (%)	B (%)
Agilent 1260 (Agilent, Waldbronn, ABD) (model)			
Agilent Eclipse Plus C18 RRHD 18 (3 mm x 5 mm; 1,8 µm) (column)	0.0	100	0
Mobile phase A: Water + 0.1% formic acid (v/v)	0.5	100	0
Mobile phase B: Acetonitrile + 0.1% formic acid (v/v)			
276 nm (wavelength)	7.0	60	40
1 mL/min (flow rate)	7.1	0	100
40 °C (column temperature)	8.6	0	100
20 µL (injection volume)	8.7	100	0

Kinetics of UAE

Kinetic description of olive leaf extraction by means of UAE was held by second-order kinetic model as stated below (Qu *et al.*, 2010):

$$\frac{dC_t}{dt} = k(C_e - C_t)^2 \quad (1)$$

The linearized form of the equation 1 is stated as given below:

$$\frac{t}{C_t} = \frac{1}{kC_e^2} + \frac{t}{C_e} \quad (2)$$

where:

C_t = Concentration of TPC at time t (mg/g)

C_e = Concentration of TPC when the equilibrium is attained (mg/g)

t = Extraction time (min)

k = Rate constant (g/mg·min)

When t approaches to 0, initial extraction rate can be expressed as h (mg/g·min):

$$h = kC_e^2 \quad (3)$$

If h is substituted into Eq. 2, C_t can be stated as follows:

$$C_t = \frac{t}{(1/h) + (t/C_e)} \quad (4)$$

Statistical analysis

Analysis of variance (ANOVA) statistical test was utilized through Tukey's test of InStat® software (GraphPad, San Diego, CA, USA) to analyze the means of three replicate outputs.

Reliability of the mathematical model was evaluated by some indicators such as correlation coefficient (R^2/r^2) and the root-mean-square deviations ($rmsd$):

$$rmsd = \sqrt{\frac{\sum_{i=1}^n (C_{i,exp} - C_{i,cal})^2}{n}} \quad (5)$$

n = number of the experiments

$C_{i,exp}$ = concentration value of experiment i

$C_{i,cal}$ = calculated concentration value of the i

RESULTS AND DISCUSSIONS

Effect of the type of solvent

Table 2 indicates the influence of solvent type under several temperature values on the extract yield and TPC of each olive leaf extract obtained by UAE as a function of time.

Table 2. Change of the extract yield and TPC of the olive leaf extracts as a function of time with various solvent types under different temperatures.

Solvent (v/v)	T (°C)	Time (minute)	Extract yield* (mg/g DL)	TPC** (mg GAE/g DL)
50 % EtOH	30	20	194.74 ± 6.50	20.78 ± 0.45
		30	202.55 ± 9.01	24.56 ± 1.20
		40	255.00 ± 9.81	25.18 ± 1.68
		50	254.98 ± 8.25	27.11 ± 1.88
		60	263.06 ± 7.51	28.71 ± 2.39
	40	20	202.24 ± 9.82	28.78 ± 1.29
		30	220.01 ± 8.41	31.09 ± 1.45
		40	257.60 ± 5.21	31.54 ± 2.00
		50	270.71 ± 5.60	32.53 ± 2.40
		60	281.20 ± 6.74	32.84 ± 1.11
50	20	277.57 ± 7.71	32.43 ± 1.11	
	30	298.09 ± 6.45	34.50 ± 3.32	
	40	301.79 ± 9.46	36.80 ± 1.45	
	50	320.91 ± 7.55	37.33 ± 3.01	
	60	322.33 ± 7.01	37.38 ± 1.75	
50 % MeOH	30	20	172.44 ± 5.12	26.18 ± 1.38

Solvent (v/v)	T (°C)	Time (minute)	Extract yield* (mg/g DL)	TPC** (mg GAE/g DL)	
100 % EtOH	30	30	201.98 ± 6.66	28.70 ± 0.58	
		40	233.03 ± 8.45	31.03 ± 0.28	
		50	234.09 ± 9.01	33.28 ± 0.70	
		60	234.48 ± 5.01	35.20 ± 1.96	
	40	20	188.14 ± 4.21	38.55 ± 1.65	
		30	229.89 ± 8.02	40.30 ± 2.29	
		40	255.98 ± 9.78	42.72 ± 3.25	
		50	277.31 ± 9.90	43.40 ± 1.28	
	50	60	279.07 ± 4.00	43.87 ± 3.04	
		20	242.04 ± 6.12	44.11 ± 1.76	
		30	257.57 ± 4.30	46.97 ± 2.06	
		40	288.99 ± 6.13	49.22 ± 2.48	
	60	50	303.88 ± 7.13	51.01 ± 2.85	
		60	310.26 ± 7.50	51.78 ± 3.03	
		30	20	81.89 ± 3.51	9.79 ± 0.5
			30	100.91 ± 5.06	10.99 ± 1.75
40	124.07 ± 4.45		12.00 ± 2.03		
50	130.21 ± 5.55		13.60 ± 2.32		
40	60	132.89 ± 4.44	15.15 ± 1.00		
	20	127.56 ± 5.50	16.24 ± 1.5		
	30	131.87 ± 4.12	18.09 ± 2.89		
	40	134.65 ± 6.77	18.97 ± 3.01		
50	50	145.00 ± 4.99	20.06 ± 2.21		
	60	147.53 ± 5.33	20.28 ± 1.51		
	20	160.72 ± 7.50	20.99 ± 2.50		
	30	172.90 ± 4.54	23.25 ± 1.78		
60	40	172.87 ± 4.33	23.57 ± 2.75		
	50	173.00 ± 7.10	24.14 ± 2.75		
	60	176.42 ± 7.44	24.46 ± 2.02		
	30	20	171.89 ± 5.09	26.53 ± 3.02	
30		188.45 ± 6.06	27.91 ± 3.30		
40		199.96 ± 7.06	30.00 ± 1.45		
50		255.98 ± 6.77	30.71 ± 2.06		
40	60	266.89 ± 6.50	31.42 ± 1.50		
	20	196.88 ± 3.64	30.87 ± 3.02		
	30	242.22 ± 7.79	33.01 ± 3.12		
	40	254.61 ± 7.03	36.45 ± 2.85		
50	50	274.59 ± 6.84	38.40 ± 1.98		
	60	284.04 ± 5.51	39.89 ± 3.00		
	20	252.44 ± 6.16	38.49 ± 3.00		
	30	277.65 ± 7.67	41.70 ± 2.45		
60	40	296.64 ± 4.55	42.36 ± 1.99		
	50	312.98 ± 5.78	42.96 ± 2.07		
	60	328.82 ± 7.02	43.07 ± 3.50		
	Water	20	178.65 ± 4.79	12.30 ± 2.50	
30		187.98 ± 8.03	14.18 ± 1.88		
40		192.87 ± 7.16	14.95 ± 2.78		
50		200.00 ± 8.01	16.01 ± 3.14		
40	60	207.15 ± 4.00	17.24 ± 2.50		
	20	201.34 ± 7.77	16.99 ± 1.78		

Solvent (v/v)	T (°C)	Time (minute)	Extract yield* (mg/g DL)	TPC** (mg GAE/g DL)
		30	206.23 ± 8.30	18.91 ± 3.05
		40	211.09 ± 4.73	21.25 ± 1.89
		50	218.78 ± 5.79	22.01 ± 2.01
		60	217.04 ± 6.00	22.84 ± 2.06
50	50	20	200.89 ± 5.44	18.70 ± 1.50
		30	207.56 ± 6.78	20.95 ± 0.98
		40	212.37 ± 6.00	22.87 ± 0.88
		50	218.83 ± 7.11	24.24 ± 1.08
		60	220.13 ± 4.51	26.40 ± 2.01
60	60	20	209.35 ± 6.88	19.24 ± 2.35
		30	216.38 ± 6.44	22.24 ± 2.08
		40	228.26 ± 6.51	25.07 ± 2.11
		50	234.92 ± 6.42	28.01 ± 2.71
		60	246.40 ± 6.00	30.67 ± 3.10
70	70	20	226.73 ± 4.89	21.14 ± 1.33
		30	240.57 ± 5.00	23.02 ± 1.77
		40	252.34 ± 3.01	25.46 ± 1.48
		50	255.91 ± 5.78	25.65 ± 1.86
		60	254.86 ± 6.11	25.75 ± 2.50
80	80	20	226.59 ± 7.77	22.32 ± 2.03
		30	236.71 ± 5.78	23.46 ± 3.01
		40	255.12 ± 7.99	25.19 ± 2.14
		50	254.98 ± 8.78	25.86 ± 1.13
		60	257.91 ± 9.00	25.96 ± 3.00

* Data are expressed as the mean (n=3) ± S.D

** Data are expressed as the mean (n=9) ± S.D

Both extract yield and TPC in all solvent systems rose steadily with time. Generally, after 40 minutes, the slow extraction was found out by a low rise in the yields. Hence, 60 minute is accepted as the equilibrium time in the relevant process (Table 2). EtOH gave the poorest extract yield, whereas MeOH showed the greatest performance. Water did not produce the highest yields, even though it is the most polar one among the selected solvents. This might be a matter of mass transfer, where water's comparatively higher viscosity leads to lower yields. On the other hand, the 50% MeOH treatment showed the highest yield of TPC, due to the fact that addition of water into the solvent gives rise to open the pores in the plant matrix by increasing the diffusion of the phenolics into the solvent. On the other hand, MeOH itself also assists for disruption of the targeted ingredients from the plant material (15, 21). Additionally, water's high dielectric constant also might be the another reason since that

increases the polarity of MeOH-water mixture (22).

Effect of temperature

Figure 2 represents the effect of temperature on the extract yield and TPC of each olive leaf extract obtained by UAE through various solvents. More precisely, the figure exhibits the comparative extract yield and TPC of extractions at the 60th minute (at equilibrium), respectively. Both extract yield and TPC of all solvents increased by temperature. Rather, the same trend was observed for each solvent with respect to both extract yield and TPC. However, for water, the TPC of the extracts started to decrease after a certain temperature point (60 °C) and reached the equilibrium at 70 °C. This might be explained by degradation owing to the hydrolysis and oxidation of the antioxidant ingredients (23). This might be ascribed to the enzyme polyphenol oxidase, which degrade polyphenols in water extracts, whereas they are not active in alcohol medium. On the

other hand, consuming much longer unreasonable condition with respect to temperature is also obvious to be an economical points.

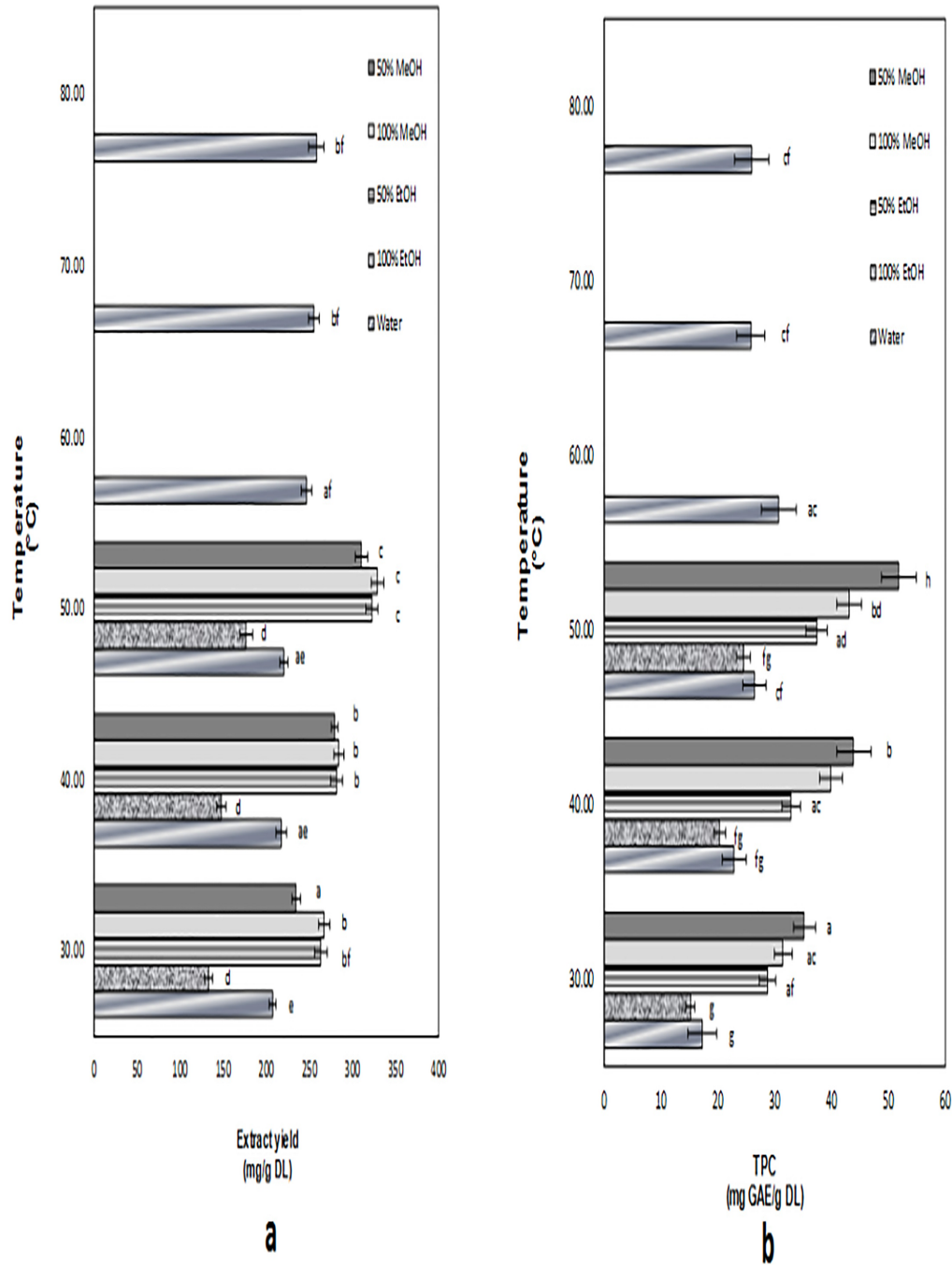


Figure 2. Effect of temperature on the extract amount (a) and TPC (b) depending on the solvent type. Data are expressed as the mean (n=3) ± S.D. Values for each column not sharing a common letter were significantly different from each cultivar at $P < 0.05$.

The extracts obtained by 50% MeOH and EtOH solutions and pure MeOH at 50 °C shared the highest yield with the values of 310.26, 322.33 and 328.82 mg/g DL, which are not significantly different at $P>0.05$ (Figure 2a). On the other hand, the 50% EtOH extracts at 30, 40 and 50 °C gave the statistically the same poorest yields (at $P>0.05$). The maximum TPC was extracted by 50% MeOH solution at 50°C with the quantity of 51.78 mg GAE/g DL (Figure 2b). As seen in the same figure, there was no significant difference ($P>0.05$) between the lowest values of TPC obtained by pure EtOH and water at 30, 40 and 50°C.

Kinetic study of the extraction process

Table 3 presents the initial extraction rate (h), the equilibrium concentration (C_e), the second-order extraction rate constant (k) and the correlation coefficient (R^2), which were calculated from the slopes plotted by t/C_t against t (Eq.2). The second-order kinetic model equation was used to calculate the predictive values of TPC under the concerned experimental conditions. The relationship between the actual findings and the calculated

results of the kinetic model for different conditions are also shown with the correlation coefficient (r^2) and root-mean-square deviation ($rmsd$) in Table 3.

Generally, the kinetic parameters of the UAE of olive leaf polyphenols increased with temperature as expected. The kinetic values were found higher for the pure MeOH extracts, which are consistent with the results of the related experiments. The values of correlation coefficients obtained with the kinetic model were extremely high ($R^2=0.9555-0.9994$) for each UAE experiment with different solvents under several temperature values. Consequently, second-order kinetic equation has been found to be convenient to describe the kinetics of UAE of olive leaves.

Depending on the high correlation coefficient ($r^2=0.9332-0.9930$) and the low root mean squared deviation ($rmsd=0.1229-1.7875$) in all the experiments, the second-order kinetic model used in this study shows to be an appropriate model for the relevant system.

Table 3. Values for h , k , C_e and R^2 of the second-order kinetic model of UAE through various solvent types under different temperatures. r^2 and $rmsd$ of the experimentally obtained values of the TPC versus the calculated values using the kinetic model for each condition of extraction.

Solvent (v/v)	T (°C)	h (mg/g.min)	k (g/mg.min)	C _e (mg/g)	R ²	Relationship between the experimental and calculated data	
						rmsd	r ²
50% EtOH	30	2.56	0.0021	34.72	0.9949	0.5286	0.9332
	40	8.08	0.0065	35.21	0.9992	0.1229	0.9930
	50	8.01	0.0048	40.82	0.9989	0.2592	0.9607
50% MeOH	30	3.07	0.0017	42.74	0.9953	0.6213	0.9672
	40	10.38	0.0047	46.95	0.9987	0.6982	0.9718
	50	8.07	0.0028	57.14	0.9997	0.8745	0.9894
100% EtOH	30	0.77	0.0017	21.37	0.9555	0.4874	0.9678
	40	2.67	0.0049	23.31	0.9994	0.6347	0.9824
	50	5.64	0.0081	26.39	0.9992	0.3645	0.9674
100% MeOH	30	5.16	0.0043	34.84	0.9992	0.4093	0.9692
	40	4.00	0.0018	47.39	0.9969	0.7845	0.9633
	50	13.99	0.0067	45.66	0.9995	1.7875	0.9581

	30	1.39	0.0031	21.19	0.9941	0.2859	0.9730
	40	2.11	0.0027	27.86	0.9983	0.2571	0.9859
Water	50	1.99	0.0018	32.89	0.9920	1.1361	0.9540
	60	1.57	0.0008	44.05	0.9845	0.6680	0.9741
	70	3.93	0.0046	29.33	0.9966	1.6563	0.9505
	80	4.83	0.0059	28.65	0.9989	0.5339	0.9632

Major polyphenol of the extract

As seen in Figure 3, oleuropein remarkably surpasses of all phenolic compounds in olive leaf extract. Oleuropein has been verified to

be the major polyphenolic compound of olive leaf. Many pharmacological effects of olive leaf are also attributed to this component (7).

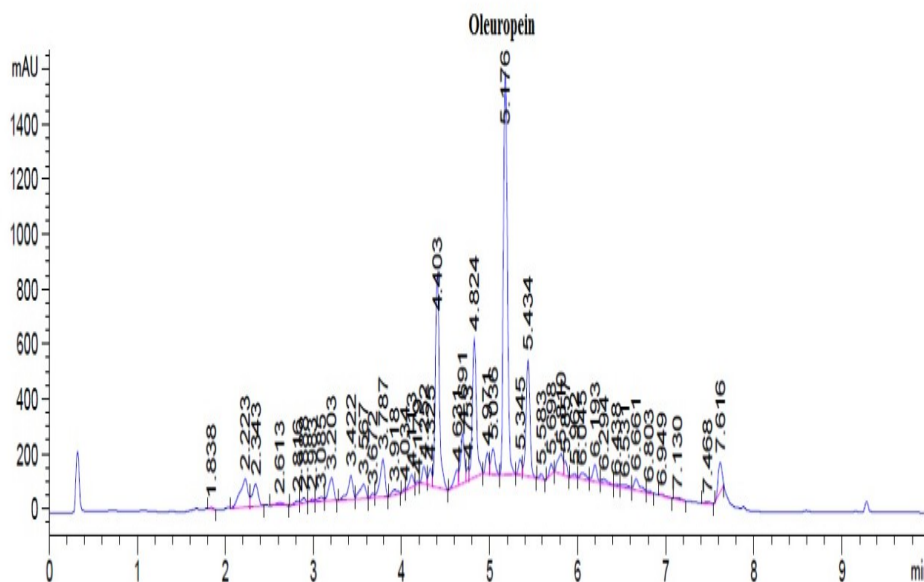


Figure 3. HPLC chromatogram of olive leaf extract obtained under optimum extraction conditions by means of 50% (v/v) methanol.

Figure 4 demonstrates the oleuropein contents of olive leaf extracts obtained under optimum conditions by each solvent system. It was found to be between 8.69 and 31 mg per gram of dried leaf. This output is consistent with the reported results (24).

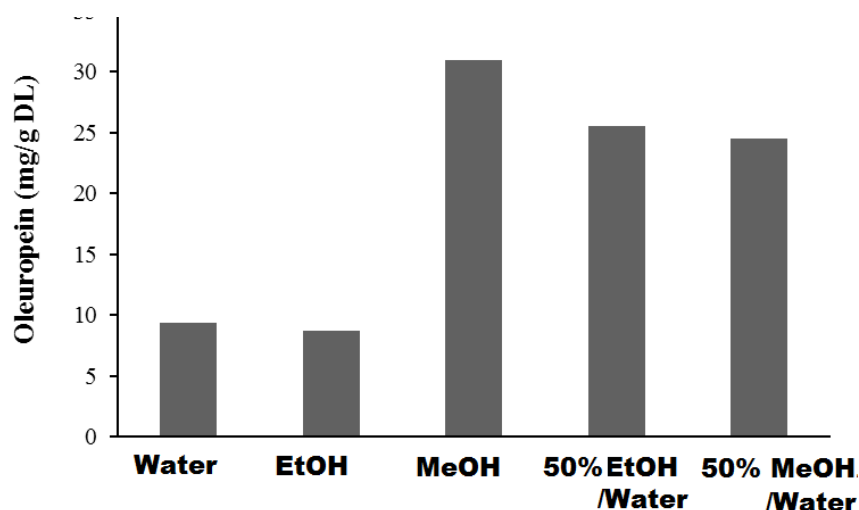


Figure 4. Oleuropein quantity of olive leaf extracts depending on the solvent.

CONCLUSION

Addition of water to alcohol improved the extraction of bioactive ingredients. TPC from water extracts decreased after a certain temperature point, as a result of degradation problems. Second-order kinetic equation has been found to be adequate to represent the experimental outcome for the ultrasound-assisted extraction of biologically active ingredients from olive leaves.

REFERENCES

1. Brahmi F, Mechri B, Dhibi M, Hammami M. Variations in phenolic compounds and antiradical scavenging activity of *Olea europaea* leaves and fruits extracts collected in two different seasons. *Industrial Crops and Products*. 2013; 49: 256–264.
2. Salido S, Pérez-Bonilla M, Adams RP, Altarejos J. Phenolic Components and Antioxidant Activity of Wood Extracts from 10 Main Spanish Olive Cultivars. *Journal of Agricultural and Food Chemistry*. 2015; 63: 6493–6500.
3. Talhaoui N, Taamalli A, Gómez-Caravaca AM, Fernández-Gutiérrez A, Segura-Carretero A. Phenolic compounds in olive leaves: Analytical determination, biotic and abiotic influence, and health benefits. *Food Research International*. 2015; 77: 92–108.
4. Elhussein EAA, Şahin S. Drying behaviour, effective diffusivity and energy of activation of olive leaves dried by microwave, vacuum and oven drying methods. *Heat and Mass Transfer*. 2018; 54: 1901–1911.
5. Şahin S, Samli R, Tan ASB, Barba FJ, Chemat F, Cravotto G, Lorenzo JM. Solvent-Free Microwave-Assisted Extraction of Polyphenols from Olive Tree Leaves: Antioxidant and Antimicrobial Properties. *Molecules*. 2017; 22: 1056.
6. Bouaziz M, Sayadi S. Isolation and evaluation of antioxidants from leaves of a Tunisian cultivar olive tree. *European Journal of Lipid Science and Technology*. 2005; 107: 497–504.
7. Şahin S, Bilgin M. Olive tree (*Olea europaea* L.) leaf as a waste by-product of table olive and olive oil industry: a review. *Journal of the Science of Food and Agriculture*. 2018; 98: 1271–1279.
9. Şahin S, Elhussein E, Bilgin M, Lorenzo JM, Barba FJ, Roohinejad S. Effect of drying method on oleuropein, total phenolic content, flavonoid content, and antioxidant activity of olive (*Olea europaea*) leaf. *Journal of Food Processing and Preservation*. 2018; 42: e13604.
10. Şahin S, Sayım E, Bilgin M. Effect of olive leaf extract rich in oleuropein on the quality of virgin olive oil. *Journal of Food Science and Technology*. 2017; 54: 1721–1728.

11. Bilgin M, Şahin S. Effects of geographical origin and extraction methods on total phenolic yield of olive tree (*Olea europaea*) leaves. *Journal of the Taiwan Institute of Chemical Engineers*. 2013; 44: 8–12.
12. Soria AC, Villamiel M. Effect of ultrasound on the technological properties and bioactivity of food: a review. *Trends in Food Science and Technology*. 2010; 21: 323–331.
13. Novak I, Janeiro P, Seruga M, Oliveira-Brett AM. Ultrasound extracted flavonoids from four varieties of Portuguese red grape skins determined by reverse-phase high-performance liquid chromatography with electrochemical detection. *Analytica Chimica Acta*. 2008; 630: 107-115.
14. Joana Gil-Chávez G, Villa JA, Fernando Ayala-Zavala J, Basilio Heredia J, Sepulveda D, Yahia EM, González-Aguilar GA. Technologies for Extraction and Production of Bioactive Compounds to be Used as Nutraceuticals and Food Ingredients: An Overview. *Comprehensive Reviews in Food Science and Food Safety*. 2013; 12: 5–23.
15. Wang L, Weller CL. Recent advances in extraction of nutraceuticals from plants. *Trends in Food Science and Technology*. 2006;17: 300–312.
16. Esclapez MD, García-Pérez JV, Mulet A, Cárcel JA. Ultrasound-Assisted Extraction of Natural Products. *Food Engineering Reviews*. 2011; 3: 108–120.
17. Leighton TG. What is ultrasound? Progress in biophysics and molecular biology. 2007; 93: 3–83.
18. Şahin S, Saeed N, Malik A, Perez JL, Brockington JE. Seasonal Changes of Individual Phenolic Compounds in Leaves of Twenty Olive Cultivars Grown in Texas. *Journal of Agricultural Science and Technology B*. 2012; 2: 242–247.
19. Malik NSA, Bradford JM. Changes in oleuropein levels during differentiation and development of floral buds in “Arbequina” olives. *Scientia Horticulturae*. 2006; 110: 274–278.
20. Şahin S, Şamlı R. Optimization of olive leaf extract obtained by ultrasound-assisted extraction with response surface methodology. *Ultrasonic Sonochemistry*. 2013; 20: 595–602.
21. Lang Q, Wai CM. Supercritical fluid extraction in herbal and natural product studies — a practical review. *Talanta*, 2001; 53: 771–782.
22. Spigno G, De Faveri DM. Microwave-assisted extraction of tea phenols: A phenomenological study. *Journal of Food Engineering*. 2009; 93: 210–217.
23. Co M, Zettersten C, Nyholm L, Sjöberg PJR, Turner C. Degradation effects in the extraction of antioxidants from birch bark using water at elevated temperature and pressure. *Analytica Chimica Acta*. 2012; 716: 40–48.
24. Alañón ME, Ivanović M, Gómez-Caravaca AM, Arráez-Román D, Segura-Carretero A. Choline chloride derivative-based deep eutectic liquids as novel green alternative solvents for extraction of phenolic compounds from olive leaf. *Arabian Journal of Chemistry*. 2018; in press, doi:10.1016/J.ARABJC.2018.01.003.



Synthesis, spectroscopic, thermal, and structural properties of cyano-bridged metal complexes containing tetracyanonickelate(II) building blocks with 4-aminomethylpyridine

Dursun Karaağaç*  

Ulubatlı Hasan Anatolian High School, 16320, Bursa, Turkey.

Abstract: New cyano-bridged metal complexes with chemical formulas $[\text{Fe}(\text{NH}_3)_2(\text{ampy})\text{Ni}(\text{CN})_4]_n$, $[\text{Co}(\text{H}_2\text{O})_2(\text{ampy})\text{Ni}(\text{CN})_4]_n$ and $[\text{Ni}(\text{NH}_3)_2(\text{ampy})\text{Ni}(\text{CN})_4]_n$ (ampy = 4-aminomethylpyridine, hereafter abbreviated as Fe-Ni-ampy, Co-Ni-ampy and Ni-Ni-ampy) were obtained in the form of powders and examined by vibrational (infrared and Raman) spectroscopy, thermal (TG, DTG and DTA), and elemental analysis techniques. The infrared and Raman spectra of the complexes were performed in the range of $4000\text{--}400\text{ cm}^{-1}$ and $4000\text{--}250\text{ cm}^{-1}$, respectively. General information about the structural features of synthesized complexes was obtained by considering the changes in the cyano group and characteristic peaks of ampy. The cleavage of the $\nu(\text{CN})$ stretching bands in the infrared spectrum of the complexes shows that the terminal and bridge cyano groups are in the structure. Considering the variations in the vibrational frequencies of the cyano group and ampy ligand in the spectrum of the complexes, the Ni atom is in a square plane geometry with four cyano groups and two of these cyano groups are the bridge and the other two are terminal. In addition, the metal atoms [Fe(II), Co(II) or Ni(II)] are linked to the ring and amino nitrogen atoms of two symmetric ampy ligands, the two ammonia (two aqua ligands for Co-Ni-ampy) ligands and the two bridging cyano groups, and show a distorted octahedral geometry. The thermal degradation of the complexes was also studied between 30 and 950 °C using TG, DTG, and DTA techniques.

Keywords: Tetracyanonickelate(II), 4-aminomethylpyridine, Cyano-bridged complex, Vibration spectra, Thermal analysis.

Submitted: August 14, 2018. **Accepted:** September 13, 2019.

Cite this: Karaağaç D. Synthesis, spectroscopic, thermal, and structural properties of cyano-bridged metal complexes containing tetracyanonickelate(II) building blocks with 4-aminomethylpyridine. JOTCSA. 2019;6(3):395–400.

DOI: <https://doi.org/10.18596/jotcsa.453521>.

***Corresponding author. E-mail:** ddkaraagac@hotmail.com. Tel.: +90 224 3661101; fax: +90 224 3669696.

INTRODUCTION

Metal organic lattice framework structures (MOFs) are formed by binding by organic linkers of metal centers and these formed structures can be of one-, two-, and three-dimensional. MOFs have extraordinary high surface areas and most of them allow the permanent porous structures to be formed (1-3). Different sizes of porous structures

can be formed with changes of metal and organic linkers. Because of these porous structures, MOFs are the subject of many areas of work, including applications such as gas storage (4, 5), iodine adsorption (6), magnetic materials (7), ion exchange materials (8) and conductivity (9).

The cyano, azide and nitrile short bridge ligands are highly preferred ligands in the binding of transition

metals. By using cyano donor atoms, the cyano anion can either provide monodentate (C-) or bidentate (C-, N-) coordination. Cyano acts as a bridging ligand by binding to metal atoms through both carbon and nitrogen atoms or a terminal ligand by binding from carbon atoms to metal atoms. With this feature, the cyano ligand can produce different polymeric species (7, 10, 11).

The cyano anion is used as a bridging ligand between metal centers and additionally different neutral organic molecules such as 4-aminomethylpyridine, imidazole, and pyridine can be obtained metal organic lattice framework structures. In these structures, octahedral Fe, Co, or Ni, square pyramidal $[\text{Ni}(\text{CN})_5]^{3-}$, square-planar $[\text{Ni}(\text{CN})_4]^{2-}$, tetrahedral $[\text{Cd}(\text{CN})_4]^{2-}$, trigonal $[\text{Cu}(\text{CN})_3]^{2-}$ and linear $[\text{Ag}(\text{CN})_2]^-$ cyanometallics are used as main building blocking entities (12, 13). Between these building blocks, the square-planar $[\text{Ni}(\text{CN})_4]^{2-}$ cyanometallics were intensively studied (14-19). The cyano groups in the $[\text{Ni}(\text{CN})_4]^{2-}$ may exhibit two different arrangements in cyano-bridged metal complexes by acting as both a bridging and terminal ligands. In this case, 1D, 2D and 3D cyano-bridged complexes can be obtained.

We reported tetracyanometallate(II) complexes with 4-aminomethylpyridine (20-24). As a part of our continuing work on cyano-bridged metal complexes, cyano-bridged metal complexes of the type $[\text{M}(\text{NH}_3)_2(\text{ampy})\text{Ni}(\text{CN})_4]_n$, and $[\text{Co}(\text{H}_2\text{O})_2(\text{ampy})\text{Ni}(\text{CN})_4]_n$ [ampy = 4-aminomethylpyridine; M = Fe(II) or Ni(II)] were synthesized using cyano, 4-aminomethylpyridine, two ammonia (two aqua ligands for Co-Ni-ampy) ligands. Structural properties of the resulting complexes were illuminated by vibrational (infrared and Raman) spectroscopy, elemental and thermal analysis methods.

EXPERIMENTAL

Materials

Iron(II) chloride tetrahydrate ($\text{FeCl}_2 \cdot 4\text{H}_2\text{O}$, 99%), cobalt(II) chloride tetrahydrate ($\text{CoCl}_2 \cdot 4\text{H}_2\text{O}$, 98%), nickel(II) chloride hexahydrate ($\text{NiCl}_2 \cdot 6\text{H}_2\text{O}$, 97%), potassium cyanide (KCN, 96%) and 4-aminomethylpyridine ($\text{C}_6\text{H}_9\text{N}_2$, 97%) were purchased from commercial sources.

Syntheses of the complexes

The cyano-bridged metal complexes were synthesized in three stages; in the 1st stage $\text{K}_2[\text{Ni}(\text{CN})_4] \cdot \text{H}_2\text{O}$, in the 2nd stage $\text{M}[\text{Ni}(\text{CN})_4] \cdot \text{H}_2\text{O}$ [M = Fe(II), Co(II) or Ni(II)] and in the final stage $[\text{M}(\text{NH}_3)_2(\text{ampy})\text{Ni}(\text{CN})_4]_n$, and $[\text{Co}(\text{H}_2\text{O})_2(\text{ampy})\text{Ni}(\text{CN})_4]_n$ [ampy = 4-aminomethylpyridine; M = Fe(II) or Ni(II)]. The $\text{K}_2[\text{Ni}(\text{CN})_4] \cdot \text{H}_2\text{O}$ complexes were prepared

according to literature (25). 1 mmol (0.259 g) of tetracyanonickelate(II) was dissolved in distilled water, and 1 mmol of the metal(II) chloride ($\text{FeCl}_2 \cdot 4\text{H}_2\text{O} = 0.199$ g, $\text{CoCl}_2 \cdot 4\text{H}_2\text{O} = 0.202$ g and $\text{NiCl}_2 \cdot 6\text{H}_2\text{O} = 0.238$ g) was dissolved in distilled water and added to the stirring tetracyanonickelate(II) solution and then, the $\text{M}[\text{Ni}(\text{CN})_4] \cdot \text{H}_2\text{O}$ [M = Fe(II), Co(II) or Ni(II)] has been obtained. The colors of $\text{Fe}[\text{Ni}(\text{CN})_4] \cdot \text{H}_2\text{O}$, $\text{Co}[\text{Ni}(\text{CN})_4] \cdot \text{H}_2\text{O}$ and $\text{Ni}[\text{Ni}(\text{CN})_4] \cdot \text{H}_2\text{O}$ are brown, pink and pale blue, respectively. A mixture of $\{\text{Fe}[\text{Ni}(\text{CN})_4] \cdot \text{H}_2\text{O} = 0.237$ g, 1 mmol, $\text{Co}[\text{Ni}(\text{CN})_4] \cdot \text{H}_2\text{O} = 0.240$ g, 1 mmol or $\text{Ni}[\text{Ni}(\text{CN})_4] \cdot \text{H}_2\text{O} = 0.239$ g, 1 mmol} in water (10 mL), ampy (2 mmol, 0.216 g) dissolved in ethanol (10 mL) and ammonia for Fe-Ni-ampy and Ni-Ni-ampy (2 mmol, 0.034 g) was stirred at 40 °C for 4 h in a temperature-controlled bath. The resulting complexes were filtered and washed with distilled water and ethanol respectively, and dried in air. These complexes were analyzed for C, H, and N, and the results obtained: Anal. Found (Calcd.) (%) for brown $\text{C}_{10}\text{H}_{14}\text{N}_8\text{FeNi}$ ($M_w = 360.81$ g/mol) : C, 33.45 (33.29); H, 3.68 (3.91); N, 30.76 (31.06); for pink $\text{C}_{10}\text{H}_{12}\text{N}_6\text{O}_2\text{CoNi}$ ($M_w = 365.87$ g/mol) : C, 33.54 (32.83); H, 3.79 (3.31); N, 21.89 (22.97); for pale blue $\text{C}_{10}\text{H}_{14}\text{N}_8\text{Ni}_2$ ($M_w = 363.66$ g/mol) : C, 32.13 (33.03); H, 4.39 (3.88); N, 30.41 (30.81).

Measurements

The synthesized complexes were analyzed for C, H, and N with a LECO CHN-932 analyzer at the Middle East Technical University Central Laboratory in Ankara, Turkey. The infrared spectra were recorded as KBr pellets between 4000 and 400 cm^{-1} (2 cm^{-1} resolution) on a Perkin Elmer 100 FT-IR spectrometer, which was calibrated using polystyrene and CO_2 bands. Raman spectrum of the synthesized complexes were recorded between 4000 and 250 cm^{-1} on a Bruker Senterra Dispersive Raman apparatus using 785 nm laser excitation. Thermal analysis curves of the obtained complexes were performed in a static air atmosphere at a heating rate of 10 K min^{-1} in the temperature region 30-950 °C using Perkin Elmer Diamond TG/DTA thermal analyzer instrument.

RESULTS AND DISCUSSION

Ligand vibrations

The infrared spectrum of the ampy ligand is shown in Figure S1. The infrared and Raman spectra of the obtained cyano-bridged metal complexes are given in Figures S2-S7. The infrared vibration frequencies of the ampy (liquid) and the vibration (Infrared and Raman) frequencies of the obtained cyano-bridged metal complexes together with the vibrational assignments of the ampy ligand according to (26) are presented in Table 1. Asymmetric and symmetric stretching vibrations and deformation vibrations of the free ammonia ligand are found in

the 3400-3000 cm^{-1} and 1650-550 cm^{-1} regions, respectively (27). In the infrared spectrum of Fe-Ni-ampy and Ni-Ni-ampy, the $\nu(\text{NH}_3)$ and $\delta(\text{NH}_3)$ vibration frequencies are identified at 3381 cm^{-1} and 1661 cm^{-1} for Fe-Ni-ampy, at 3381 and 1672 cm^{-1} for Ni-Ni-ampy, respectively. In general, the $\nu(\text{OH})$ and $\delta(\text{HOH})$ vibration frequencies appear in the 3560-3200 and 1700-1600 cm^{-1} regions, respectively (27, 28). The aqua ligand of Co-Ni-ampy displays a sharp peak of $\nu(\text{OH})$ at 3544 cm^{-1} . In the infrared spectrum of Co-Ni-ampy, the $\delta(\text{HOH})$ bending vibration of the aqua ligand was also found at 1695 cm^{-1} .

The ampy ligand has unpaired electrons on the nitrogen atom. The ampy ligand which has these electron pairs can coordinate as monodentate or bidentate ligand to metal atoms. When the coordination takes place via the amino nitrogen atom of the ampy ligand, the N-H bond is weakened and the NH_2 stretching frequencies are lowered. In this case, the M-N bond is stronger, whereas the N-H bond is weaker. Furthermore, if the NH_2 group of the ampy ligand makes a hydrogen bond, the N-H stretching frequencies are further reduced. In addition, the out of plane bending frequencies of NH_2 shift to higher frequency region (27, 29, 30). As presented in Table 2, symmetric and asymmetric wavenumbers of the $\nu(\text{N-H})$ belonging to the NH_2 group in the ampy ligand are found at 3367 and 3292 cm^{-1} . In the infrared spectrum of the complexes, the strong vibration bands at 3346 and 3274 cm^{-1} for Fe-Ni-ampy, at 3346 and 3292 cm^{-1} for Co-Ni-ampy and at 3346 and 3274 cm^{-1} for Ni-Ni-ampy are identified as the stretching vibrations belonging to the NH_2 group. The $\nu(\text{N-H})$ belonging to the NH_2 group of the ampy in the obtained complexes are lower than those of the free ampy ligand. The band identified at 1602 cm^{-1} in the infrared spectrum of the free ampy determined as the out-of-plane bending vibration of NH_2 and observed at a higher frequency according to the free ampy ligand in the spectrum of the complexes. Shifts in the NH_2 stretching and bending vibration frequencies are sensitive to metal. On the other hand, when the ampy ligand is linked to metal atoms from the ring nitrogen atom, there are significant shifts in the ring stretching and the deformation vibration frequencies. Especially, the increase in ring stretching frequencies is observed (17, 23, 31). The ring stretching modes of the free ampy ligand, $\nu(\text{skeletal})$ assigned as the strong and sharp bands at 1220, 1088, 1065 and 994 cm^{-1} in the infrared spectrum of the free ampy. In the complexes, the metals are N-bonded (ring) since the $\nu(\text{skeletal})$ of the free ligand is shifted to higher frequencies around 3-40 cm^{-1} . Other significant bands of the free ampy ligand are the $\nu(\text{CH})$ at 3070 and 2991 cm^{-1} , the $\nu(\text{CH})$ at 2991 cm^{-1} and 2898 cm^{-1} , the $\nu(\text{CC})$ at 1560 cm^{-1} , the $\delta(\text{CH}_2)$ at 1496 and 1446 cm^{-1} , the $\text{t}(\text{CH}_2)$ at 877

cm^{-1} and $\text{r}(\text{NH}_2)$ at 591 cm^{-1} . In the complexes, these vibration bands show upward or downward shifts in frequency according to those of the free ampy ligand. Therefore, infrared and Raman spectra show that the ampy ligand in the obtained complexes is N-bonded from both ring nitrogen atom of pyridine and NH_2 group.

Vibrations (infrared and Raman) of the $[\text{Ni}(\text{CN})_4]^{2-}$ group

The vibrational assignments and frequencies of the tetracyanonickelate(II) in the complexes are included in Table 1. The assignments of vibrational bands belonging to vibrations (infrared and Raman) of the tetracyanonickelate(II) in the obtained complexes are performed using that of the solid $\text{Na}_2[\text{Ni}(\text{CN})_4]$ salt presented by McCullough *et al.*, (32). The distinctive band in the cyano-bridged metal complexes is the vibration band of the cyano group. The $\nu(\text{CN})$ stretching vibration band of the cyano group gives a strong and sharp peak in the range of 2200-2000 cm^{-1} and can be easily determined in the spectrum of the complexes. The $\nu(\text{CN})$ stretching vibration frequency of free cyano ligand in ionic KCN is determined at 2080 cm^{-1} (27). When the cyano ligand is coordinated to a metal atom from the carbon atom, the $\nu(\text{CN})$ stretching vibration frequency is undergoes a blue-shift. In this case, the M-CN type terminal property is seen in the complexes (23, 33-35). If the cyano ligand is bound to two separate metal atoms from both the carbon and the nitrogen atom, $\nu(\text{CN})$ stretching vibration occurs more blue shift and the M-CN-M' type bridge forms in the complexes. Both terminal and bridge property of cyano ligand in the cyano-bridged metal complexes is intensively observed (23, 33-35). The terminal Ni-CN of obtained complex $\text{K}_2[\text{Ni}(\text{CN})_4]\cdot\text{H}_2\text{O}$ exhibits a distinctive peak at 2120 cm^{-1} in the infrared spectra. In the infrared spectrum of the cyano-bridged metal complexes, the $\nu(\text{CN})$ stretching vibration frequency is observed at 2124 cm^{-1} (for Fe-Ni-ampy), 2123 cm^{-1} (for Co-Ni-ampy) and 2125 cm^{-1} (for Ni-Ni-ampy). The $\nu(\text{CN})$ stretching vibration frequencies in the complexes M-Ni-ampy ([Fe(II), Co(II) or Ni(II)]) are closer that of the terminal Ni-CN. M-CN-M' type bridge in the cyano complexes can easily be determined with infrared spectroscopy. According to this, the $\nu(\text{CN})$ stretching vibration in obtained cyano-bridged metal complexes were determined at 2162 and 2143 cm^{-1} (for Fe-Ni-ampy), 2160 cm^{-1} (for Co-Ni-ampy), 2162 and 2143 cm^{-1} (for Ni-Ni-ampy). Bridge $\nu(\text{CN})$ stretching vibration wavenumbers in obtained cyano-bridged metal complexes are usually identified at higher frequencies due to kinematic binding, which is a mechanical limitation upon the bridging cyano ligand bound to the second metal (13, 17, 27). The cleavage of the $\nu(\text{CN})$ supports the presence of bridges and terminal cyano groups in the cyano-bridged metal complexes. In the resulting

complexes, the A_{1g} and B_{1g} cyano stretching modes are observed at 2186 and 2169 cm^{-1} (for Fe-Ni-ampy), 2187 cm^{-1} (for Co-Ni-ampy), 2187, 2170 and 2150 cm^{-1} (for Ni-Ni-ampy). This data show that the A_{1g} and B_{1g} modes are observed to have higher wavenumbers in the region of 9–27 cm^{-1} in obtained cyano-bridged metal complexes. In addition, the modes originating from $\nu(\text{NiCN})$ and

$\delta(\text{NiCN})$ vibrations for the obtained cyano-bridged metal complexes are determined between 600 and 400 cm^{-1} . In the infrared spectrum of M-Ni-ampy [M(II) = Fe(II), Co(II) or Ni(II)], the modes found at 557 and 429 cm^{-1} in Fe-Ni-ampy, 557 and 438 cm^{-1} in Co-Ni-ampy, 555 and 429 cm^{-1} in Ni-Ni-ampy are expressed as the $\nu(\text{NiCN})$ and $\delta(\text{NiCN})$ vibrations, respectively.

Table 1 The vibrational wavenumbers of the tetracyanonickelate(II) group in M-Ni-ampy (cm^{-1}).

Assignments (32)	$\text{K}_2[\text{Ni}(\text{CN})_4]\cdot\text{H}_2\text{O}$	Fe-Ni-ampy	Co-Ni-ampy	Ni-Ni-ampy
A_{1g} , $\nu(\text{CN})$	(2160) vs	(2186) s, (2169) vs	(2187) vs	(2187) s, (2170) vs
B_{1g} , $\nu(\text{CN})$	(2137) m	(2150) vs	-	(2150) vs
E_{u} , $\nu(\text{CN})$	2120 vs	2162 s, 2143 s, 2124 vs	2160 vs, 2126 m	2163 s, 2143 s, 2125 s
$\nu(^{13}\text{CN})$	2084 vw	2087 vw	2097 vw	2084 vw
E_{u} , $\nu(\text{NiC})$	542 w	557 w	557 w	555 m
A_{2u} , $\pi(\text{NiCN})$	443 w	468 vw	486 w	472 vw
E_{u} , $\delta(\text{NiCN})$	414 vs	429 s	438 s	429 s

ν ; valence, δ ; in-plane, π ; out-of-plane, s; strong, m; medium, w; weak, sh; shoulder, v; very. The vibrational frequencies in the Raman spectrum are enclosed in parentheses.

As a result, the ampy ligand acts as a bridge ligand between metals, while the cyano ligand acts as a terminal and bridging ligand. In this case, it is

considered that the structures of the complexes according to the obtained spectral data are as shown in Figs. 1 and 2.

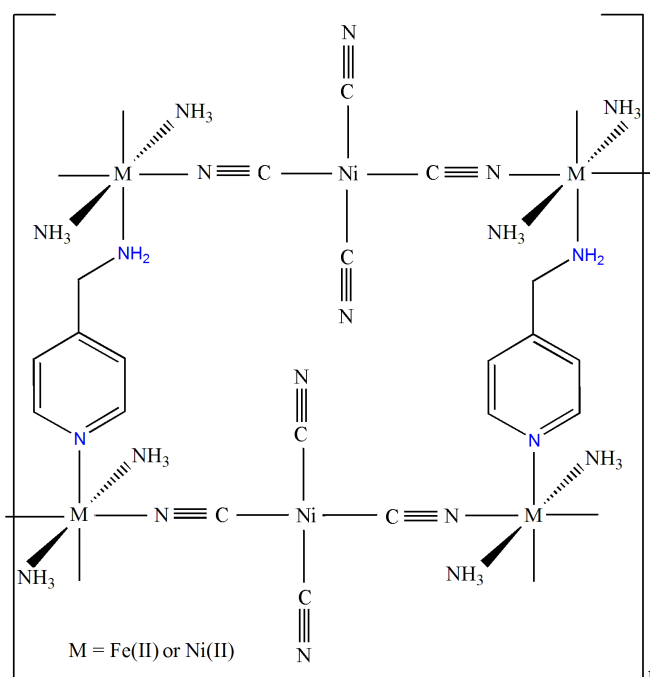


Figure 1. Representation of molecular structures of Fe-Ni-ampy and Ni-Ni-ampy.

Table 2. The vibrational wavenumbers of the liquid ampy and the ampy in the complexes (cm⁻¹).

Assignment (26)	ampy (liquid)	Fe-Ni-ampy		Co-Ni-ampy		Ni-Ni-ampy	
		Infrared	Raman	Infrared	Raman	Infrared	Raman
v(NH ₂)	3367 vs	3346 s	3354 w	3346 s	3346 vw	3346 s	3353 vw
v(NH ₂)	3292 s	3274 s	3291 w	3292 s	3271 vw	3274 s	3292 w
v(NH ₂)	3197 sh	3188 m	3200 vw	3197 sh	3190 vw	3188 m	3200 vw
v(CH)	3070 s	3090 w	3088 w	3073 m	3078 vw	3091 w	3088 w
v(CH)	2991 s	2972 w	2983 vw	2972 w	2964 vw	2971 w	2982 vw
v(CH ₂)	2898 s	2936 w	2946 w	-	-	2935 w	2946 vw
v(CH ₂)	2849 s	2829 vw	2847 vw	2855 sh	-	2851 vw	2842 vw
v(C=N)	1652 sh	1661 vw	1666 vw	1695 w	1681 vw	1671 vw	1668 vw
δ(NH ₂)	1602 vs	1612 s	1625 w	1618 s	1627 w	1612 s	1625 w
v(CC)	1560 vs	1582 m	1592 vw	1563 m	1586 vw	1582 m	1595 vw
δ(CH ₂)	1496 s	1505 w	1516 vw	1506 w	1509 vw	1505 w	1516 vw
δ(CH ₂)	1446 s	1457 vw	1468 vw	-	1451 vw	1457 m	1452 vw
ω(CH)	1416 vs	1423 s	1434 vw	1428 s	1437 vw	1424 s	1434 w
t(CH)	1387 s	1376 w	1373 vw	1369 w	1363 vw	1375 w	1371 vw
t(NH ₂)	1287 m	1324 w	1335 vw	1322 vw	1332 vw	1324 w	1333 vw
v(skeletal)	1220 s	1249 s	1254 w	1227 m	1223 w	1249 s	1255 w
v(skeletal)	1088 m	1094 w	1104 vw	1093 w	1091 w	1094 m	1092 w
v(skeletal)	1065 s	1072 w	1084 w	1072 w	-	1072 w	-
v(skeletal)	994 vs	1014 s	1026 m	1017 s	1034 w	1015 s	1027 m
t(CH ₂)	877 vs	874 vw	885 vw	876 vw	898 vw	874 vw	886 vw
r(CH ₂), ω(NH ₂)	822 sh	819 w	831 w	852 vw	862 vw	819 w	832 w
r(NH ₂)	667 w	646 m	680 w	689 vw	679 w	646 m	680 w
r(NH ₂)	591 s	615 w	621 vw	563 w	535 w	615 m	612 vw

v; stretching, δ; deformation, ω; wagging, t; twisting, r; rocking, s; strong, m; medium, w; weak, sh; shoulder, v; very.

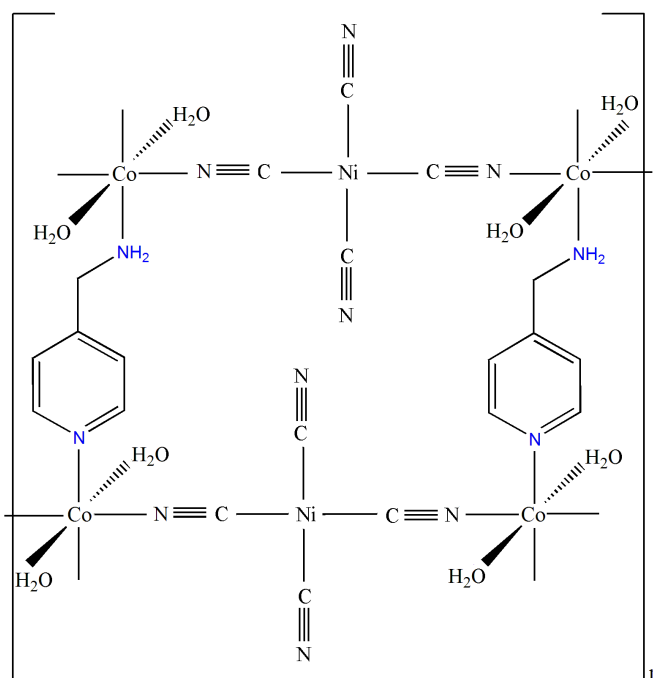


Figure 2. Representation of molecular structures of Co-Ni-ampy.

Thermal Analysis

Thermal decompositions of the synthesized complexes were investigated by TG, DTA, and DTG methods in a static areal atmosphere at 30-950 °C temperature range. Thermal analyses of the synthesized complexes are given in Figures S8-S10. Thermal degradation of the complexes began at approximately 150, 30 and 180 °C for Fe-Ni-ampy, Co-Ni-ampy, and Ni-Ni-ampy, respectively. As seen in Figures S8-S10, TG, DTA, and DTG curves of Fe-Ni-ampy, Co-Ni-ampy, and Ni-Ni-ampy are similar to each other and thermal decomposition of the complexes occurs in two stages. In the first stage, two ammonia ligands between 65 and 174 °C [Found (Calcd.) (%) = 9.46 (9.43)] for Fe-Ni-ampy, between 65 and 213 °C [Found (Calcd.) (%) = 9.83 (9.36)] for Ni-Ni-ampy and two aqua ligands between 30 and 101 °C [Found (Calcd.) (%) = 9.88 (9.85)] for Co-Ni-ampy are released from the structure of the complexes. In the second stages, the loss of the one ampy ligand and the four cyano ligands take place between 174 °C and 628 °C for Fe-Ni-ampy ($DTA_{max} = 413$ °C), 101 and 910 °C for Co-Ni-ampy ($DTA_{max} = 353$ °C) and 213 °C and 685 °C for Ni-Ni-ampy ($DTA_{max} = 346$ °C). The remaining products after the loss of the ligands were found to be *FeO* and *NiO* for Fe-Ni-ampy, *CoO* and *NiO* for Co-Ni-ampy and $2(NiO)$ for Ni-Ni-ampy [Found (Calcd.) (%) = 40.20 (40.61) for Fe-Ni-ampy, 37.14 (40.89) for Co-Ni-ampy and 39.13 (41.07) for Ni-Ni-ampy].

CONCLUSIONS

In this article, we have prepared and reported new cyano-bridged metal complexes with chemical formulas $[M(NH_3)_2(ampy)Ni(CN)_4]_n$, and $[Co(H_2O)_2(ampy)Ni(CN)_4]_n$ [ampy = 4-aminomethylpyridine; M = Fe(II) or Ni(II)]. According to the spectral data obtained from the complexes, the coordination environment of the M(II) atoms is coordinated to the octahedral geometry by the ring and amino nitrogen atoms of two symmetric ampy ligands, two nitrogen atoms of two ammonia ligands (two oxygen atoms of two aqua ligands for Co-Ni-ampy) and two symmetric nitrogen atoms of the cyano groups, while the Ni(II) atom is coordinated to the square-plane geometry by the four carbon atoms of the cyano groups. In addition, it has been concluded that cyano ligand along with ring nitrogen and NH_2 group of the ampy is involved in the formation of complexes. The spectral properties reveal that the complexes are composed of two dimensional networks. When the thermal properties of the complexes are examined, the two ammonia ligands (two aqua ligands for Co-Ni-ampy) are first released from the unit formula of the complexes, then an ampy and four cyano groups are released. In addition, the thermal degradation of the complexes between 30 and 950 °C are in good agreement with elemental analysis results.

ACKNOWLEDGMENT

I would like to thank Prof. Dr. Güneş Süheyla Kürkçüoğlu for her support in the writing of this article.

REFERENCES

1. Wong-Ng W, Culp J, Siderius D, Chen Y. Synthesis and synchrotron X-ray characterization of two 2D Hoffman related compounds $[\text{Ni}(\text{p-Xylylenediamine})_n\text{Ni}(\text{CN})_4]$ and $[\text{Ni}(\text{p-tetrafluoroxlylenediamine})_n\text{Ni}(\text{CN})_4]$. *Solid State Sci.* 2018;81:12-8.
2. Wong-Ng W, Williamson I, Lawson M, Siderius D W, Jeffrey T, Culp J F. Electronic structure, pore size distribution, and sorption characterization of an unusual MOF, $\{[\text{Ni}(\text{dpbz})][\text{Ni}(\text{CN})_4]\}_n$, dpbz=1,4-bis(4-pyridyl)benzene. *J. Appl. Phys.* 2018;123(24):245105.
3. Lu W, Wei Z, Gu Z-Y, Liu T.F, Park J, Park J, Tian J, Zhang M, Zhang Q, Gentle T, Boscha M, Zhou H C. Tuning the structure and function of metal-organic frameworks via linker design. *Chem. Soc. Rev.* 2014;43(16):5561-93.
4. Li Y, Liu Y, Wang Y, Leng Y, Xie L, Li X. Hydrogen storage properties of $[\text{M}(\text{Py})\{\text{Ni}(\text{CN})_4\}]$ (M=Fe, Co, Ni). *Int. J. Hydrogen Energy.* 2007;32(15):3411-5.
5. Culp JT, Natesakhawat S, Smith MR, Bittner E, Matranga C, Bockrath B. Hydrogen storage properties of rigid three-dimensional hofmann clathrate derivatives: The effects of pore size. *J. Phys. Chem.* 2008;112(17):7079-83.
6. Massasso G, Rodríguez-Castillo M, Long J, Haines J, Devautour-Vinot S, Maurin G, Grandjean A, Onida B, Donnadiou B, Larionova J, Guérina C, Guari Y. Molecular iodine adsorption within Hofmann-type structures $\text{M}(\text{L})[\text{M}'(\text{CN})_4]$ (M=Ni, Co; M'=Ni, Pd, Pt): impact of their composition. *Dalton Trans.* 2015;44(44):19357-69.
7. Černák J, Orendáč M, Potočňák I, Chomič J, Orendáčová A, Skoršepa J, Feher A. Cyanocomplexes with one-dimensional structures: preparations, crystal structures and magnetic properties. *Coord. Chem. Rev.* 2002;224(1-2):51-66.
8. Kämper M, Wagner M, Weiß A. Krypton-und Xenon-Einschlußverbindungen komplexer Metallcyanide. *Angew. Chem.* 1979;91(6):517-8.
9. Gapud A, Weber A, Alexander J, Pham L, Khan A, Leatherbury R I, Reyes A P, Lumata L L, Kuhns P L, Valente E J, Sykora R E. New quasi-one-dimensional tetracyanidoplatinate, $\text{Cs}_4[\text{Pt}(\text{CN})_4](\text{CF}_3\text{SO}_3)_2$: Synthesis, structure, and physical characterization. *J. Phys. Chem. Solids.* 2014;75(3):447-52.
10. Çetinkaya F, Kürkçüoğlu G S, Yeşilel O Z, Hökelek T, Dal H. One-dimensional cyano-bridged heterometallic (Cu/Ni and Cu/Pd) complexes with 1-ethylimidazole. *Polyhedron* 2012;47(1):126-33.
11. Potocnak I, Vavra M, Cizmar E, Tibenská K, Orendáčová A, Steinborn D, Wagner C, Dušek M, Fejfarová K, Fejfarová H, Muller C, Orendáč M, Feher A J. Low-dimensional compounds containing cyano groups. XIV. Crystal structure, spectroscopic, thermal and magnetic properties of $[\text{CuL}_2][\text{Pt}(\text{CN})_4]$ complexes (L=ethylenediamine or N,N-dimethylethylenediamine). *J. Solid State Chem.* 2006;179:1965-76.
12. Nemeč I, Herchel R, Boča R, Svoboda I, Trávníček Z, Dlháň L, Matelková K, Uess H. Heterobimetallic assemblies of Ni(II) complexes with a tetradentate amine ligand and diamagnetic cyanidometallates. *Inorg. Chim. Acta.* 2011;366(1):366-72.
13. Ouyang L. The use of Tetracyanozincate (II) in the preparation of supramolecular coordination polymers: Department of Chemistry-Simon Fraser University; 2007.
14. Sayın E, Kürkçüoğlu G S, Yeşilel O Z, Hökelek T. 1D cyanide complexes with 2-pyridinemethanol: Synthesis, crystal structures and spectroscopic properties. *J. Mol. Struct.* 2015;1101:73-81.
15. Karaağaç D, Kürkçüoğlu G S, Yeşilel O Z, Hökelek T, Dal H. Synthesis and crystal structure of cyano-bridged three dimensional polyheteronuclear complex. *Z. Kristallogr.* 2012;227(9):639-45.
16. Karaağaç D, Kürkçüoğlu G S. Syntheses, spectroscopic and thermal analyses of the hofmann-type metal(II) tetra-cyanonickelate(II) pyridazine complexes: $\{[\text{M}(\text{pdz})\text{Ni}(\text{CN})_4] \cdot \text{H}_2\text{O}\}_n$ (M=Zn(II) or Cd(II)). *Bull. Chem. Soc. Ethiop.* 2015;29(3):415-22.
17. Kartal Z. Synthesis, spectroscopic, thermal and structural properties of $[\text{M}(\text{3-aminopyridine})_2\text{Ni}(\mu\text{-CN})_2(\text{CN})_2]_n$ (M(II)=Co and Cu) heteropolynuclear cyano-bridged complexes. *Spectrochim. Acta, Part A.* 2016;152:577-83.
18. Parlak C, Alver Ö, Şenyel M. Vibrational spectroscopic study on some Hofmann type clathrates: $\text{M}(\text{1-Phenylpiperazine})_2\text{Ni}(\text{CN})_4 \cdot 2\text{G}$ (M=Ni, Co and Cd; G=aniline). *J. Mol. Struct.* 2009;919(1-3):41-6.

19. Černák J, Abboud K A. Three different bonding modes of cyano groups in the coordination polymer $[\text{Cu}(\text{en})_2(\text{H}_2\text{O})][\text{Cu}(\text{en})_2\text{Ni}_2\text{Cu}_2(\text{CN})_{10}] \cdot 2\text{H}_2\text{O}$ (en is 1,2-diaminoethane). *Acta Crystallogr., Sect. C: Cryst. Struct. Commun.* 2002;58(3):m167-m170.
20. Karaağaç D, Kürkçüoğlu G S, Hökelek T, Yeşilel O Z, Süzen Y. Two dimensional cyano-bridged heteropolynuclear complex containing Pd...n interactions. *Z. Kristallogr.* 2013;228(2):100-5.
21. Karaağaç D, Kürkçüoğlu G S, Yeşilel O Z, Hökelek T. Two dimensional cyano-bridged heterometallic coordination polymers containing metal... n interactions. *Spectrochim. Acta, Part A.* 2014;121:196-204.
22. Karaağaç D, Kürkçüoğlu G S, Yeşilel O Z. Two dimensional heteronuclear complexes with cyanide and 4-aminomethylpyridine ligands. *J. Mol. Struct.* 2014;1074:339-48.
23. Karaağaç D, Kürkçüoğlu G S, Yeşilel O Z, Taş M. Syntheses, thermal analyses, crystal structures, FT-IR and Raman spectra of 2D $[\text{Zn}(\text{NH}_3)_2(\mu\text{-ampy})\text{M}'(\mu\text{-CN})_2(\text{CN})_2]_n$ ($\text{M}'=\text{Ni}(\text{II}), \text{Pd}(\text{II})$ or $\text{Pt}(\text{II})$) complexes. *Polyhedron.* 2013;62:286-92.
24. Karaağaç D, Kürkçüoğlu G S, Yeşilel O Z, Hökelek T, Süzen Y. Syntheses, crystal structures, spectroscopic and thermal analyses of 3- and 4-aminomethylpyridinium tetracyanometalate (II) complexes. *Inorg. Chim. Acta.* 2013;406:73-80.
25. Karaağaç D, Kürkçüoğlu GS. Syntheses, spectroscopic and thermal analyses of cyanide bridged heteronuclear polymeric complexes: $[\text{M}(\text{L})_2\text{Ni}(\text{CN})_4]_n$ (L=N-methylethylenediamine or N-ethylethylenediamine; M=Ni(II), Cu(II), Zn(II) or Cd(II)). *J. Mol. Struct.* 2016;1105:263-72.
26. Niven M L, Percy G C. The infrared spectra ($3500\text{-}140\text{ cm}^{-1}$) of the 2, 2'-bipyridine, 2-aminomethylpyridine and ethylenediamine adducts and the sodium tris-compounds of cobalt(II), nickel(II) and zinc(II) acetylacetonates. *Transit. Metal Chem.* 1978;3(1):267-71.
27. Nakamoto, K. *Infrared and Raman Spectra of Inorganic and Coordination Compounds*, applications in coordination, Wiley and Sons, New York, 2009.
28. Cabral O V, Giannerini T, Felcman J. Fourier-transform infrared spectrum of aspartate hydroxo-aqua nickel(II) complex and DFT-B3LYP/3-21G and 6-311G structural and vibrational calculations. *J. Spectrochim. Acta, Part A.* 2005;61(1-2):337-45.
29. Kürkçüoğlu G S, Hökelek T, Aksel M, Yeşilel O Z, Dal H. Cyano-bridged heteropolynuclear Ni(II), Cu(II) and Cd(II) complexes, $[\text{M}(\text{deten})_2\text{Ni}(\mu\text{-CN})_2(\text{CN})_2]_n$. *J. Inorg. Organomet. Polym. Mater.* 2011;21(3):602.
30. Akyüz S. An infrared spectroscopic study of dianiline-metal(II) tetracyanometalate complexes. *J. Mol. Struct.* 1980;68:41-9.
31. Akalin E, Akyüz S. Experimental and theoretical vibrational spectroscopic investigation of Zn(II) halide complexes of 3-aminopyridine and 3-chloropyridine. *J. Mol. Struct.* 2011;993(1-3):390-6.
32. McCullough R, Jones L, Crosby G. An analysis of the vibrational spectrum of the tetracyanonickelate(II) ion in a crystal lattice. *Spectrochim. Acta* 1960;16(8):929-44.
33. Smékal Z, Čísařová I, Mroziński J. Cyano-bridged bimetallic complexes of copper(II) with tetracyanonickelate(II). Crystal structure of $[\text{Cu}(\text{dpt})\text{Ni}(\text{CN})_4]$. *Polyhedron* 2001;20(28):3301-6.
34. Černák J, Abboud K, Chomič J, Meisel M W, Orendáč M, Orendáčová A, Feher A. $\text{Ni}(\text{tn})_2\text{Ag}_2(\text{CN})_4$ and $\text{Cu}(\text{tn})_2\text{Ag}_2(\text{CN})_4$ (tn=1,3-diaminopropane): preparation, crystal structure, magnetic and spectral properties. *Inorg. Chim. Acta* 2000;311(1):126-32.
35. Potočňák I, Vavra M, Čížmár E, Dušek M, Müller T, Steinborn D. Low-dimensional compounds containing cyano groups. XIX. Crystal structure, spectroscopic, thermal and magnetic properties of $\{[\text{Cu}(\text{tn})_2]_3[\text{Pt}(\text{CN})_4]_2\}[\text{Pt}(\text{CN})_4]$ (tn=1,3-diaminopropane) complex. *Inorg. Chim. Acta* 2009;362(11):4152-7.

Synthesis, spectroscopic, thermal, and structural properties of cyano-bridged metal complexes containing tetracyanonickelate(II) building blocks with 4-aminomethylpyridine

Dursun Karağaç

Ulubatlı Hasan Anatolian High School, 16320, Bursa, Turkey.

Supplementary file

This file contains the figures originally in the article, and moved to this file.

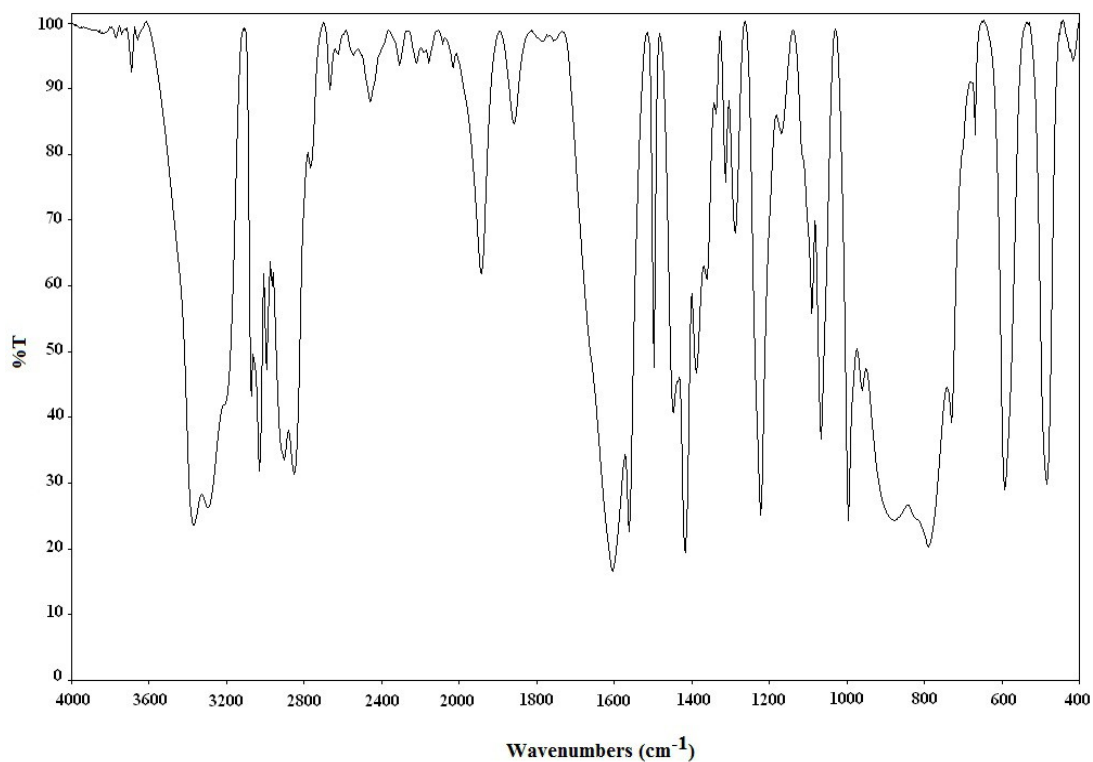


Figure S1. The infrared spectrum of the ampy ligand.

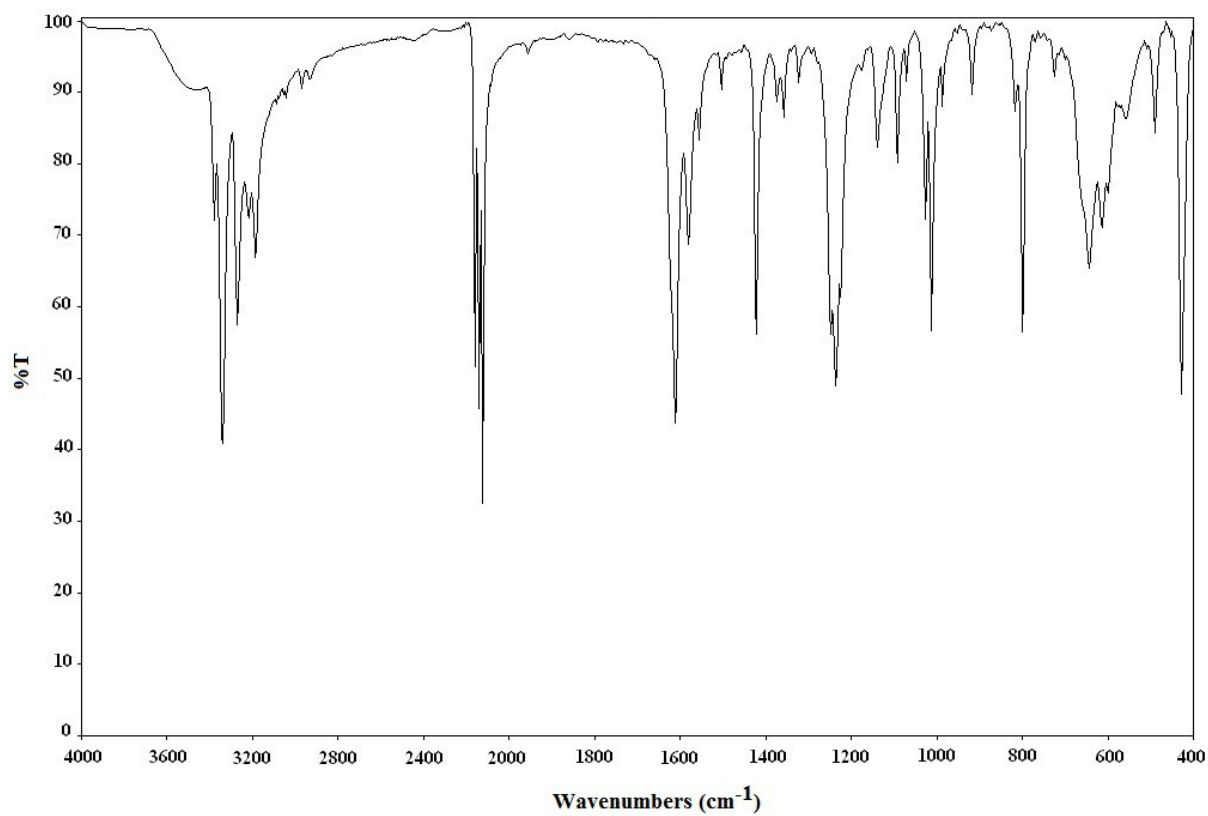


Figure S2. The infrared spectrum of Fe-Ni-ampy.

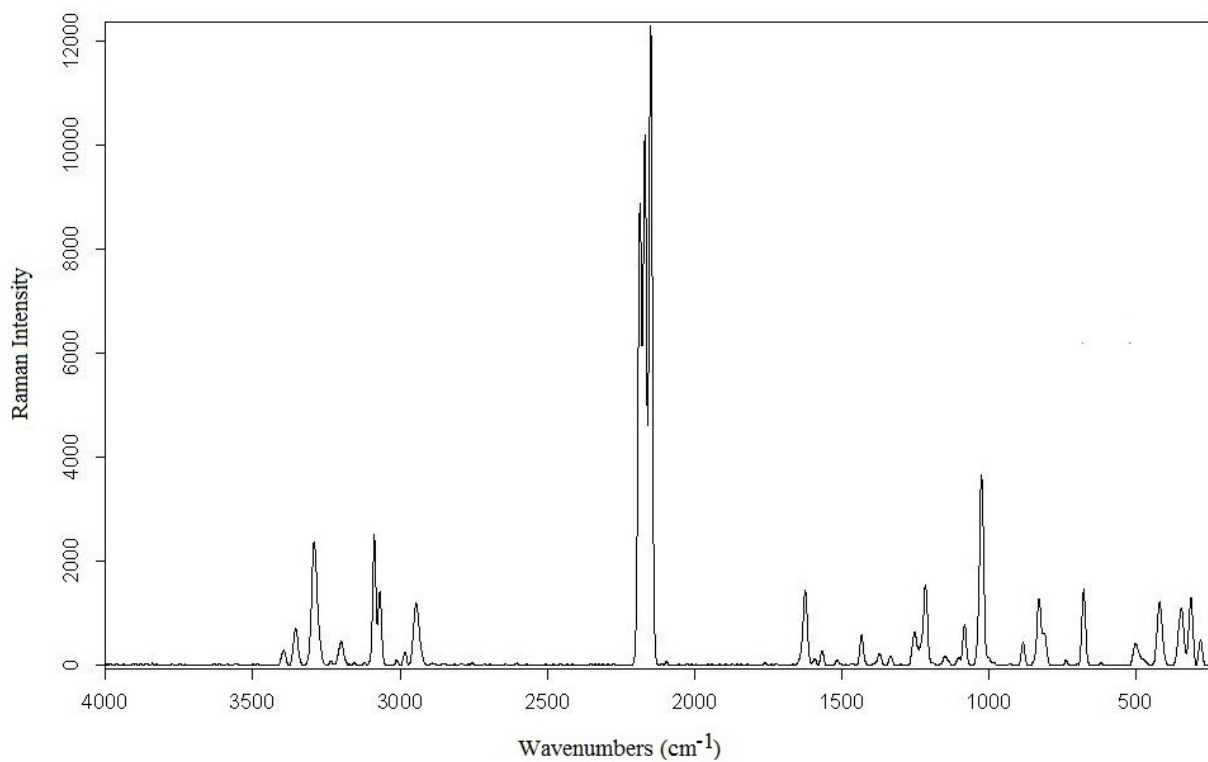


Figure S3. The Raman spectrum of Fe-Ni-ampy.

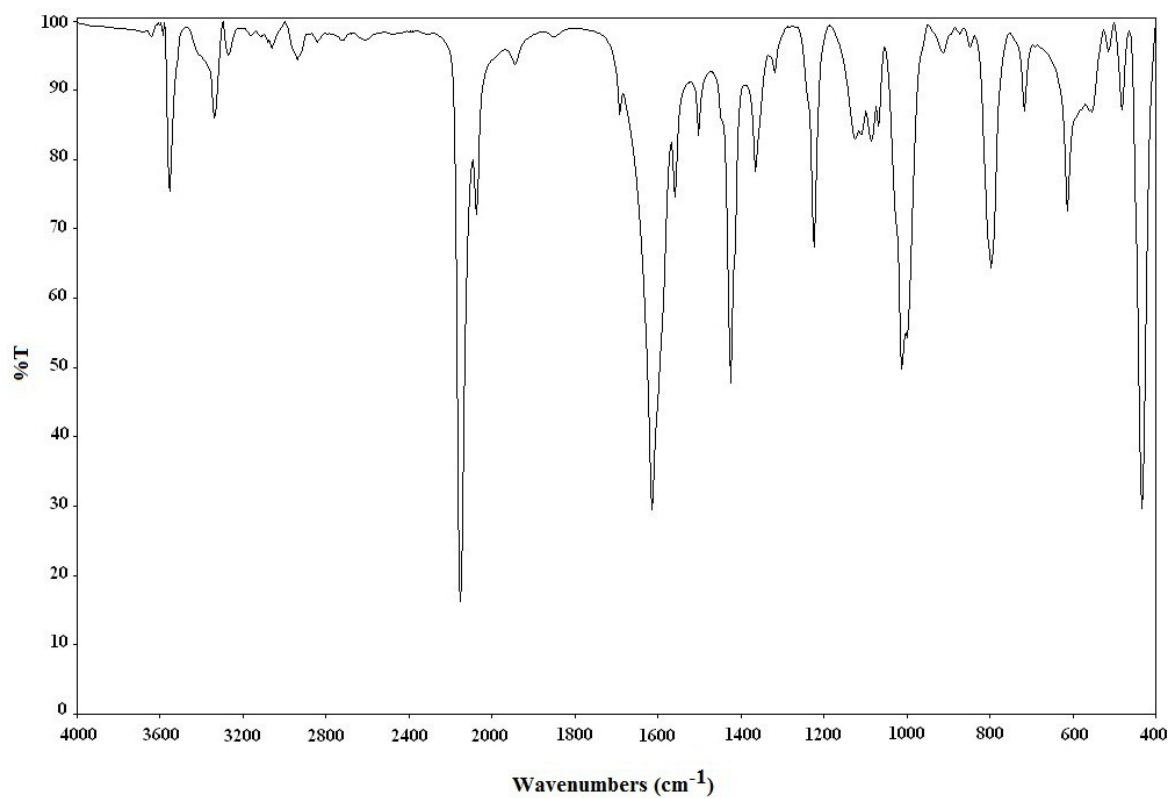


Figure S4. The infrared spectrum of Co-Ni-ampy.

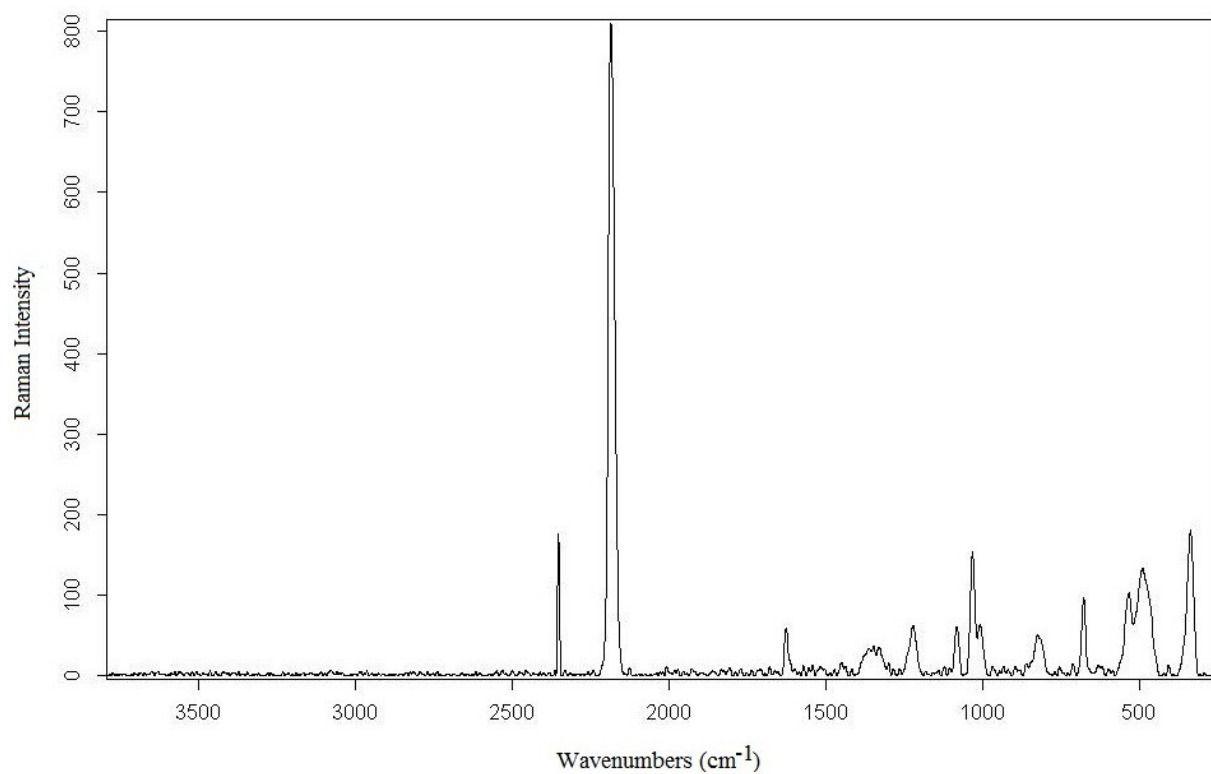


Figure S5. The Raman spectrum of Co-Ni-ampy.

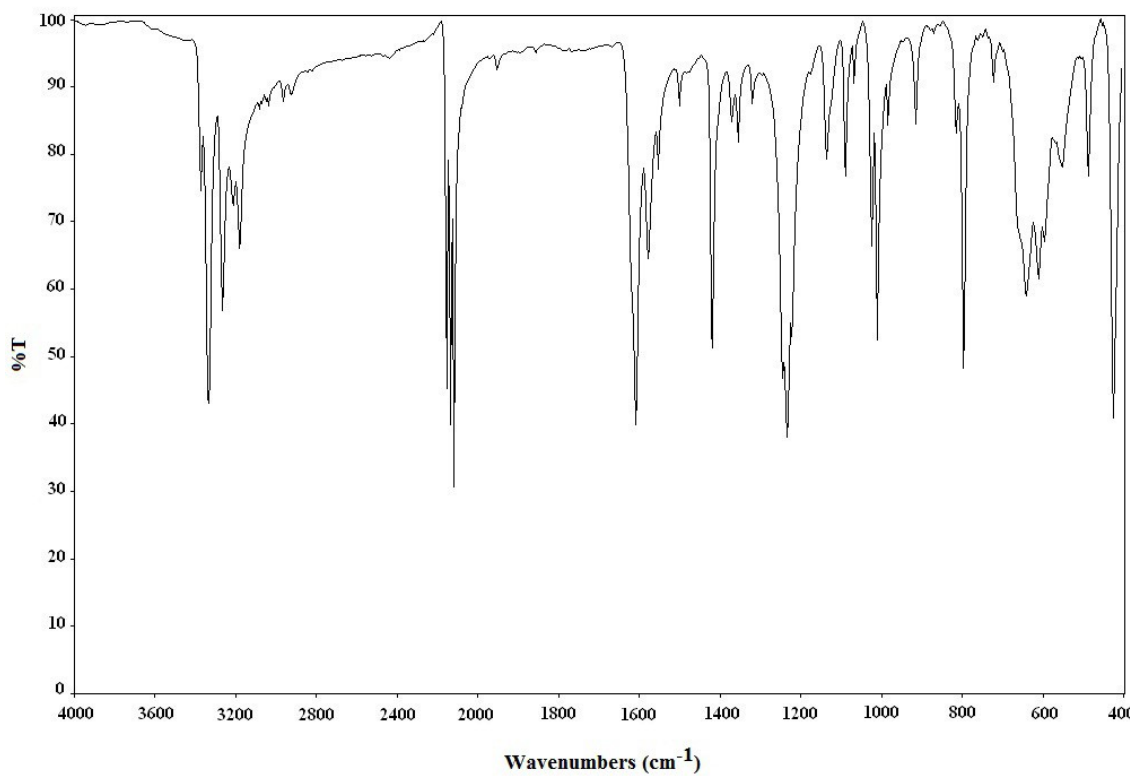


Figure S6. The infrared spectrum of Ni-Ni-ampy.

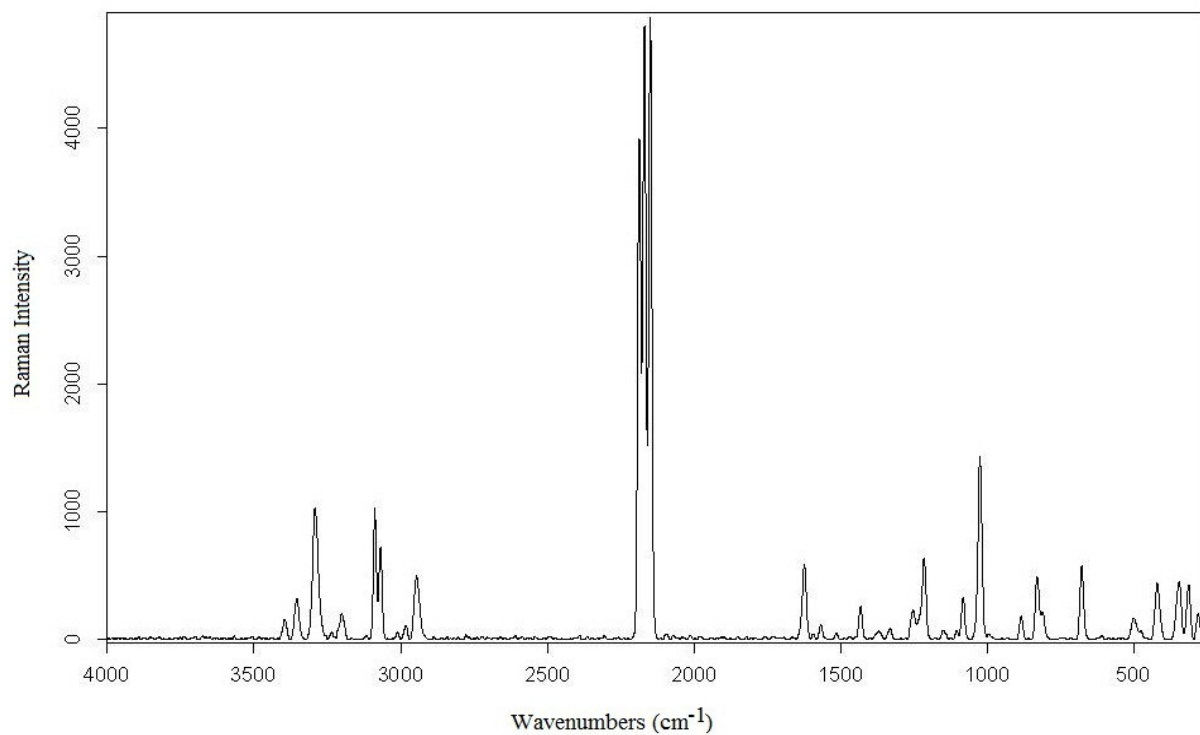


Figure S7. The Raman spectrum of Ni-Ni-ampy.

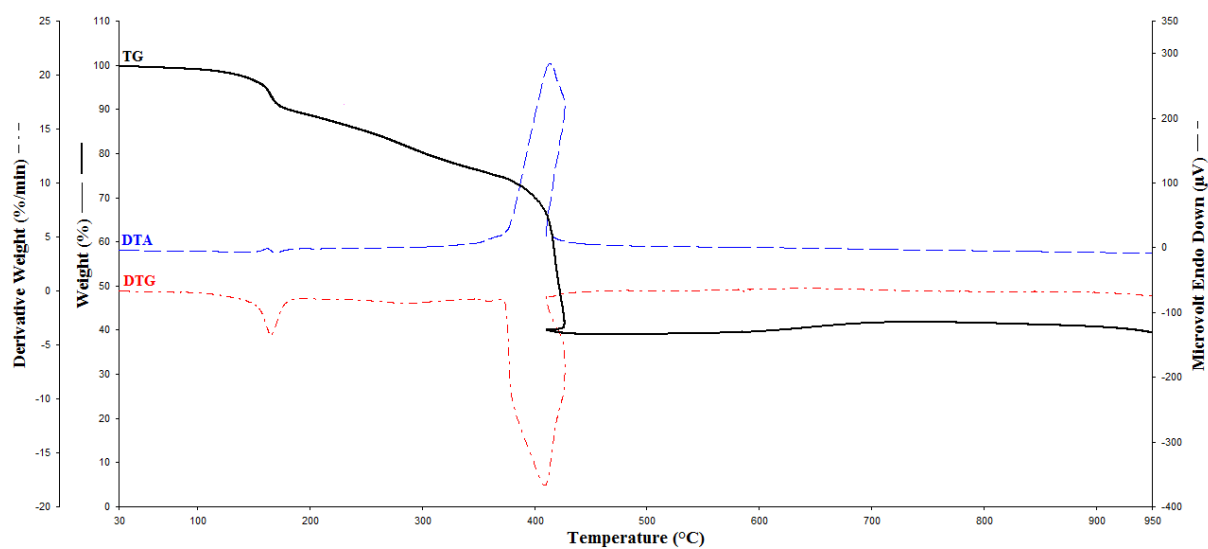


Figure S8. The thermal curves of Fe-Ni-ampy.

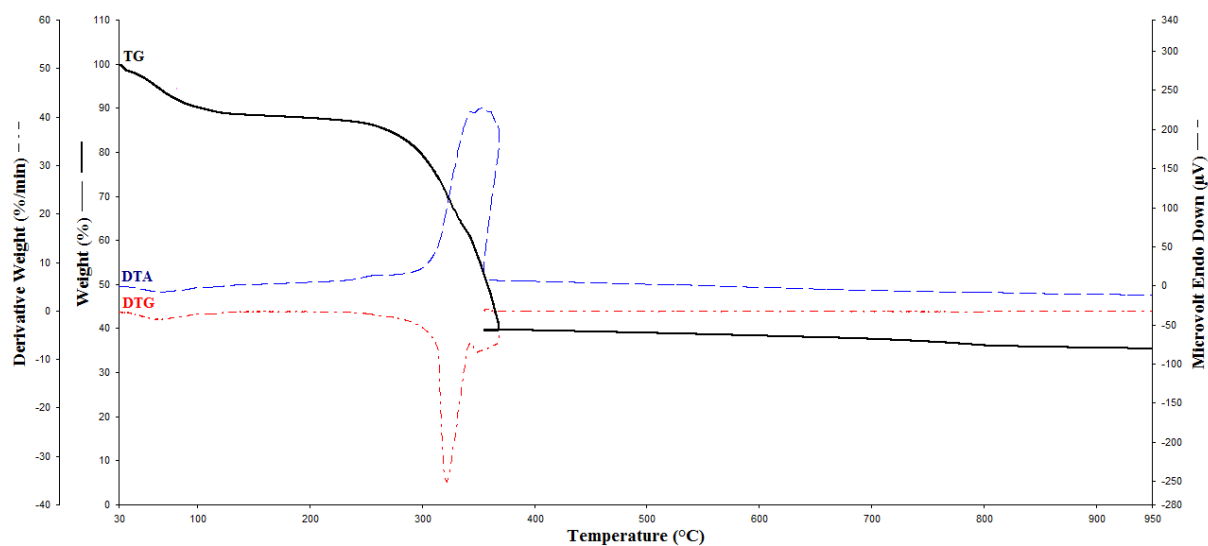


Figure S9. The thermal curves of Co-Ni-ampy.

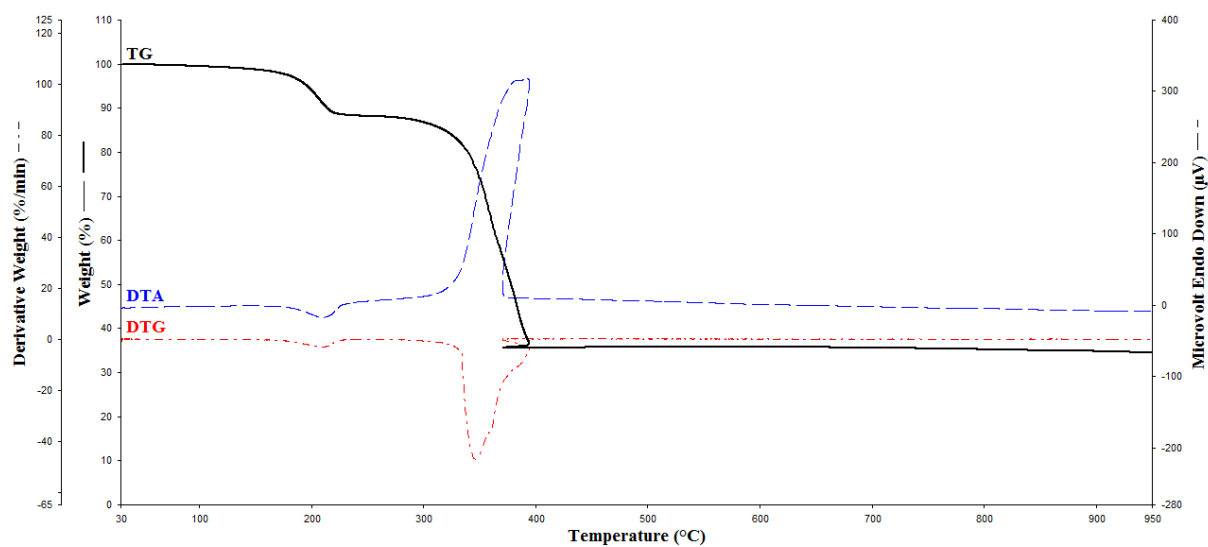


Figure S10. The thermal curves of Ni-Ni-ampy.



Green Synthesis of Antioxidant Silver and Platinum Nanoparticles Using Ginger and Turmeric Extracts and Investigation of Their Catalytic Activity

Muradiye SAHIN^{1*}  , Ilkay Hilal GUBBUK²  

1-Graduate School of Natural Sciences, Selcuk University, 42003, Selcuklu/Konya, Turkey

2- Department of Chemistry, Selcuk University, Campus, 42075, Konya, Turkey

Abstract: Antioxidant silver nanoparticles (AgNPs) and platinum nanoparticles (PtNPs) were synthesized by using ginger and turmeric extracts with green method in this work. Thus these nanoparticles synthesized were characterized by UV-Vis spectroscopy, SEM-EDX and FTIR. The UV-Visible spectra of the AgNPs revealed a characteristic surface plasmon resonance peak at 420-425 nm and the UV-Visible spectra of the PtNPs revealed a characteristic surface plasmon resonance peak at 234-240 nm. The synthesized AgNPs and PtNPs acted as a catalyst to the degradation of dyes (rhodamine B, methyl orange, and methylene blue) with sodium borohydride (NaBH₄). Green synthesized antioxidant silver nanoparticles effectively degraded the dyes nearly 4-10 min. and green synthesized antioxidant platinum nanoparticles effectively degraded the dyes nearly 15-24 min. of exposure time.

Keywords: Platinum nanoparticles, catalysis, silver nanoparticles, antioxidants, dyes.

Submitted: December 14, 2018. **Accepted:** April 06, 2019.

Cite this: Şahin M, Gubbuk I. Green Synthesis of Antioxidant Silver and Platinum Nanoparticles Using Ginger and Turmeric Extracts and Investigation of Their Catalytic Activity. JOTCSA. 2019;6(3):403–10.

DOI: <https://doi.org/10.18596/jotcsa.497440>.

*Corresponding author. E-mail: muradiyeok_40@hotmail.com.

INTRODUCTION

Noble metal nanoparticles such as silver and platinum have emerged as promising antimicrobial agents and catalytic elements so have been greatly applied in the cosmetic, medical, textile and food industries (1). Catalysts of metal nanoparticles such as silver are efficient for various reactions. Silver have earned significant caution due to their inimitable electronic properties and high Fermi potential (2, 3).

Over the last few years, herb-welded biologically synthesis of the nanoparticles are earned overage significance because of their inexpensive and environmentally approach (4-7). The applications of AgNPs and PtNPs in medicine, optoelectronics, optics, and catalysis are well

known and has received great attention due to the surface strong absorption in the visible region which can be easily monitored by UV-visible spectrophotometer (8). Moreover, these NPs have been gaining significant research interest due to their unique shape and size-dependent optical, antimicrobial and catalytic properties (9).

In this work, silver and platinum nanoparticles are synthesized, for the first time, using ginger and turmeric antioxidant extracts as a reducing agent for the first time. Antioxidants limit the deleterious effects of oxidative reactions so they can involve scavenging free radicals followed by the stabilization of nanoparticles.

Organic dyes are a major class environmental pollutant in various industries, particularly textiles. The organic dyes can cause many

diseases such as blood diseases, cancer, renal and hepatic damage for living beings (10). These dyes generate tons of wastewater. Clean and usable water is a prerequisite for life. Nanoparticles provide remediation and treatment in water (11). In order to remove dyes such as methyl orange (MO), methylene blue (MB) and rhodamine B (RB) faster from water, catalytic potential role of the synthesized AgNPs and PtNPs' in the presence of sodium borohydride (NaBH_4) is investigated in this study.

EXPERIMENTAL SECTION

Preparation of the extract

Ginger and turmeric powders were purchased from the haberdasher. To obtain ginger and turmeric extracts, 1 g of the particular powder was added to 50 mL of distilled water. The mixture was stirred continuously at 25°C for 5 hours. After grinding, the solution was filtered through a filter paper. Then all extracts were stored at room temperature to be used for biosynthesis of silver and platinum nanoparticles from silver nitrate or chloroplatinic acid.

Synthesis of silver and platinum nanoparticles

In order to investigate the effect of antioxidant extracts on the synthesis of AgNPs and PtNPs, each extract was mixed with silver nitrate (AgNO_3) or chloroplatinic acid ($\text{H}_2[\text{PtCl}_6] \cdot \text{H}_2\text{O}$). Each extract (7 mL) was added to 0.01 M 50 mL of AgNO_3 or ($\text{H}_2[\text{PtCl}_6] \cdot \text{H}_2\text{O}$). The solutions were left at room temperature under magnetic stirring for the completion of the synthesis. Reduction of silver ions (Ag^+) to silver (Ag^0) was completed around 3-5 min. and formation of nanoparticles was visually identified by color change and followed the UV-Vis spectral analysis. Reduction of platinum ions (Pt^{4+}) to platinum (Pt^0) was

completed around 12-15 min. and was followed by the color change of the solution from yellow to brownish-yellow to deep black.

Catalytic study

The reduction of methyl orange (MO), methylene blue (MB) and rhodamine B (RB) by sodium borohydride (NaBH_4) in the existence of each AgNPs and each PtNPs as a heterogeneous catalyst at 25 °C was conducted. 1 mL of the NaBH_4 solution ($1 \times 10^{-2} \text{ mol L}^{-1}$) is mixed with 1 mL of dyes ($1 \times 10^{-5} \text{ mg L}^{-1}$). 0.5 mL antioxidant silver or platinum nanoparticles was added to this mixture and then the UV-VIS spectra have been recorded at regular intervals of time. The degradation of all dyes are shown by the decolorization of the solution to colorless. The concentrations of the MO, RB and MB dyes were quantified by measuring the absorption band at 465, 564 and 664 nm, respectively.

RESULT AND DISCUSSION

Characterization

Silver and platinum nanoparticles fabricated from ginger and turmeric extracts as a reducing agent have been examined for their heterogeneous catalytic activity reaction. The reduction of both extract metal ion solutions was quantitative and identified by a change in color from yellow to brown and orange to dark brown for ginger and turmeric respectively. The phenols and the other compounds in the antioxidant extracts provide in efficient reduction of silver and platinum salts to nanoparticles (12,13). Figure 1 showed that the UV visible spectra of the AgNPs revealed a characteristic surface plasmon resonance peak at 420-425 nm and the UV-Visible spectra of the PtNPs revealed a characteristic surface plasmon resonance peak at 234-240 nm.

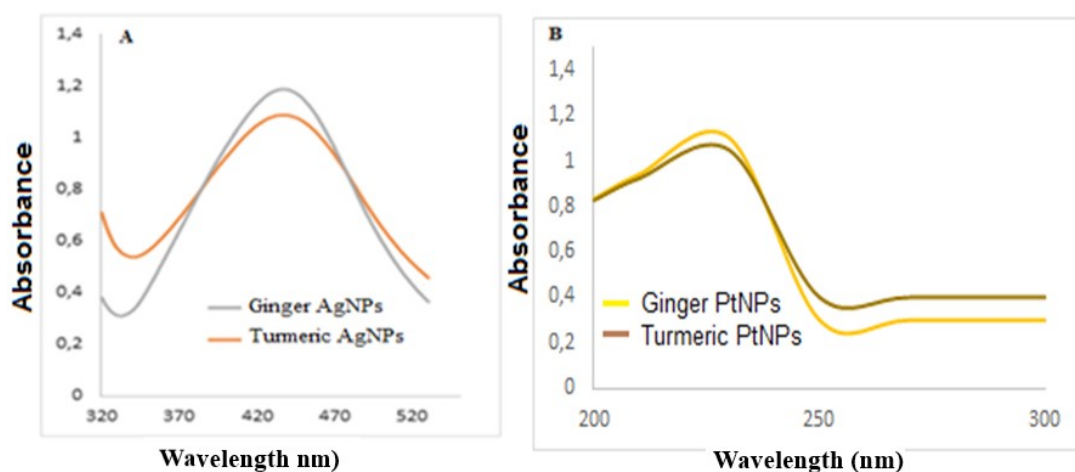


Figure 1. UV-Vis. spectra of A) AgNPs and B) PtNPs.

The FTIR spectra of ginger silver nanoparticles (Gng-AgNPs) and turmeric silver nanoparticles (Trm-AgNPs) were shown in Figure 2. The bands at 1566 cm^{-1} proved that C=C double bond or aromatic annulus or C=O carboxyl groups. The bands at 1026 cm^{-1} proved that -CN- amine

groups. The IR bands at 1307 cm^{-1} proved the presence of geminal methyl (14-16).

The FTIR spectra of ginger platinum nanoparticles (Gng-PtNPs) and turmeric platinum nanoparticles (Trm-PtNPs) were shown in Figure 3.

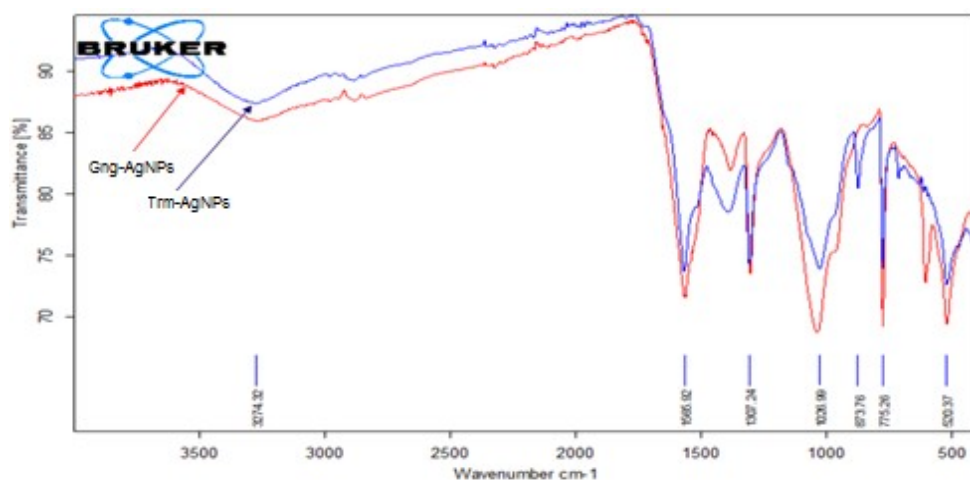


Figure 2. ATR-FTIR spectra of Gng-AgNPs (red line) and Trm-AgNPs (blue line).

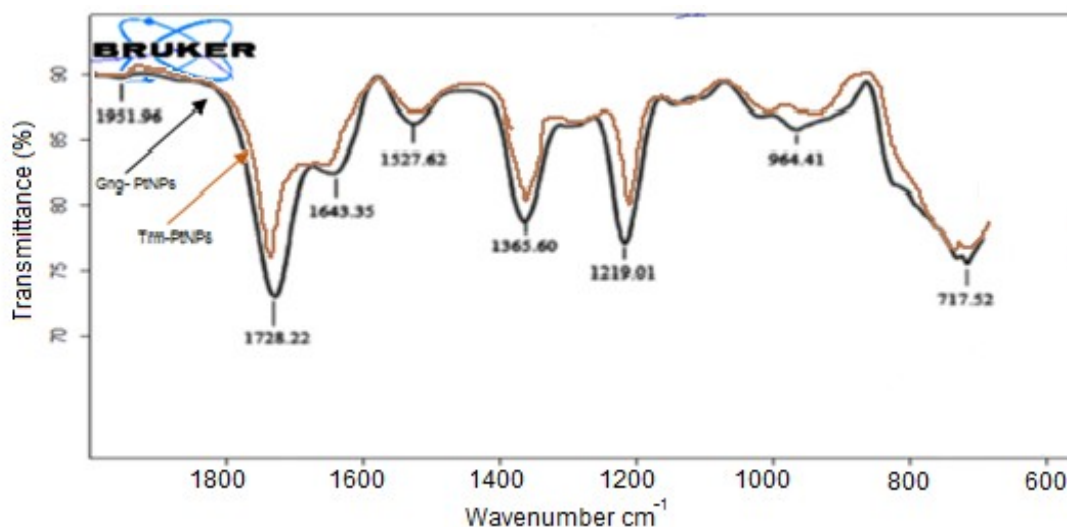


Figure 3. ATR-FTIR spectra of Gng-PtNPs (black line) and Trm-PtNPs (brown line).

The crystalline nature of the silver nanoparticles was confirmed by SEM and EDX pattern as shown in Figure 4. Also, elemental analysis was obtained using the SEM-EDX combination. An EDX spectroscopy was used to approve the existence of silver nanoparticle. The EDX view evidently confirmed the existence of silver nanoparticles by

demonstration of a violent spectra within fundamental elements. Ag, Mg, Al, Fe etc. were observed in the EDX analysis samples which were concluded that these could be caused by antioxidant extract.

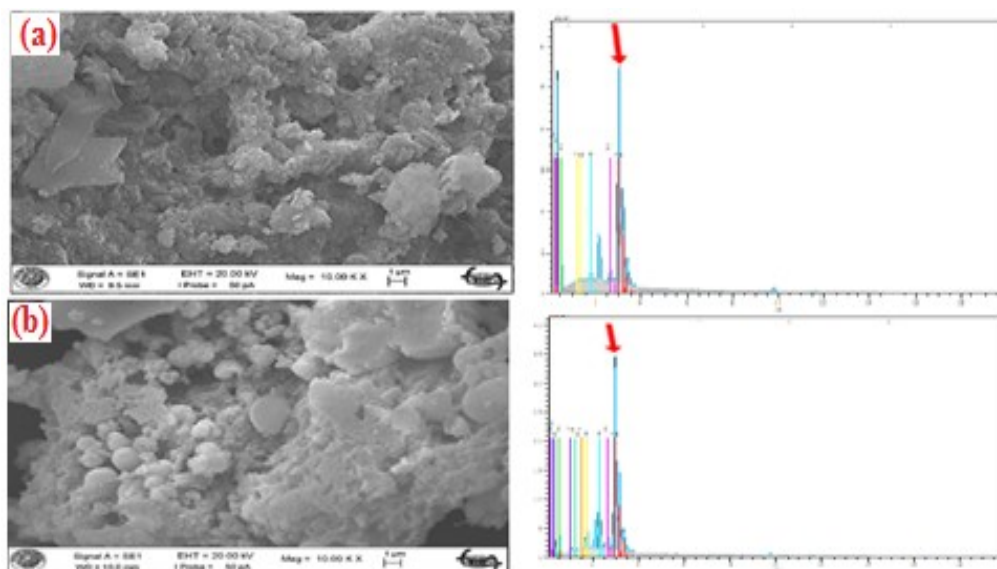


Figure 4. SEM images and EDX results of *Gng-AgNPs* (a) and *Trm-AgNPs* (b).

Catalytic study

The reduction of methyl orange (MO), Rhodamine B (RB) and methylene blue (MB) by sodium borohydride (NaBH_4) in the existence of each *AgNPs* or each *PtNPs* as a heterogeneous catalyst at 25 °C was conducted. 1 mL of NaBH_4 solution ($1 \times 10^{-2} \text{ mol L}^{-1}$) is mixed with 1 mL of dyes

($1 \times 10^{-5} \text{ mg L}^{-1}$). 0.5 mL antioxidant silver or platinum nanoparticles was added to this mixture and then the UV-Vis spectra have been recorded at regular intervals of time. The degradation of all dyes are shown by the decolorization of the solution to colorless.

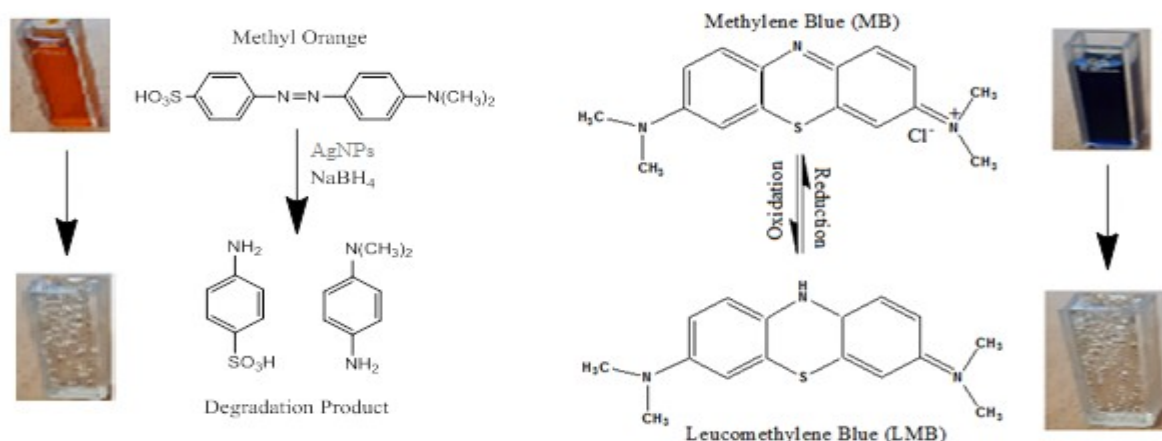


Figure 5. Degradation mechanism of the MB and MO and color change.

All dyes can be reduced by both nanoparticles to nontoxic species and the reduction rate is very fast. Antioxidant silver nanoparticles with higher

catalytic activity than platinum nanoparticles can speed up the reduction rate of dyes, thus increasing the degradation capacity.

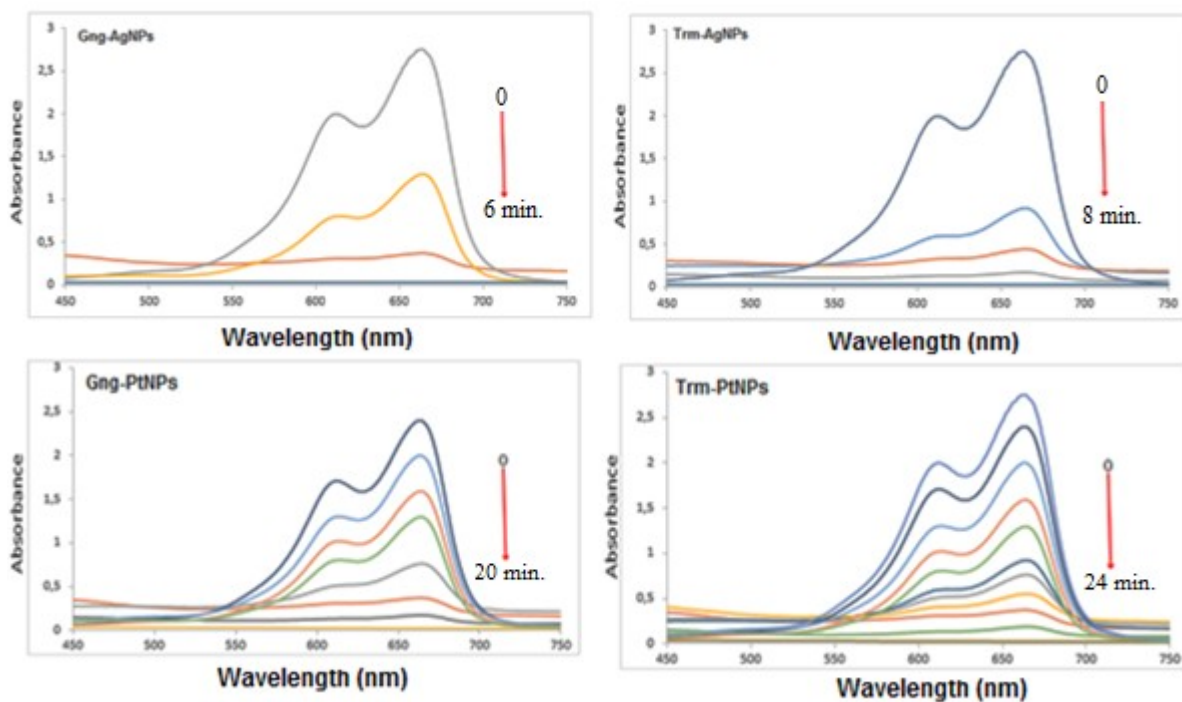


Figure 6. UV-Vis. spectra of the catalytic reduction of Methylene Blue.

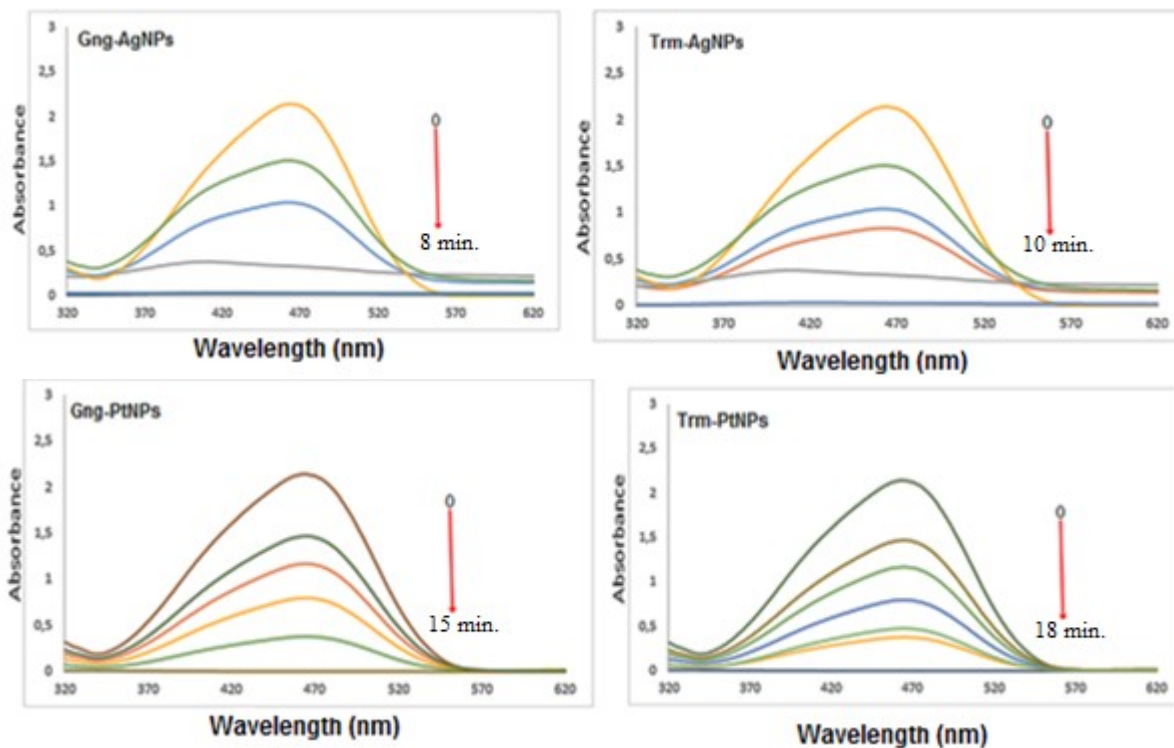


Figure 7. UV-Vis. spectra of the catalytic reduction of Methyl Orange.

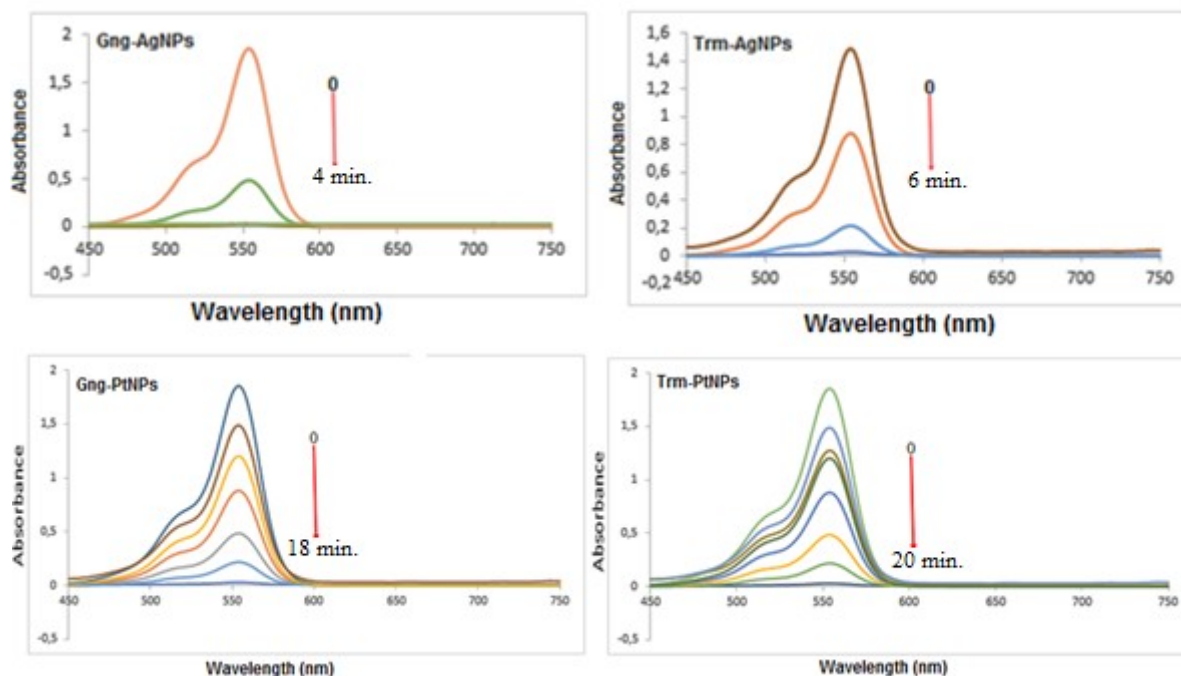


Figure 8. UV-Vis. spectra of the catalytic reduction of Rhodamine B.

CONCLUSION

Antioxidant silver and platinum nanoparticles were prepared successfully via a facile, simple, economic, and eco-friendly route from ginger and turmeric extracts. The UV-Vis, FTIR, SEM, EDX spectroscopic analyses confirmed the formation of nanoparticles. The catalytic feature of the *Gng-AgNPs*, *Gng-PtNPs*, *Trm-AgNPs* and *Trm-PtNPs* in degrading RB, MB and MO to their end products in the presence of NaBH_4 at room temperature were studied.

Antioxidant silver and platinum nanoparticles in the existence of NaBH_4 catalyze the degradation reaction, which leads to the removal of RB, MB and MO. Absorbance became almost zero in the case of all of dyes. Thus *Gng-AgNPs*, *Gng-PtNPs*, *Trm-AgNPs* and *Trm-PtNPs* provided a good electron transfer that catalyzes the reactions by reducing the activation energy. Also, as a reducing agent, NaBH_4 , was not capable to reduce RB, MB and MO in absence of a catalyst, indicating the efficacy of *Cnm-AgNPs*, *Gng-PtNPs*, *Trm-AgNPs* and *Trm-PtNPs*. Therefore, it was concluded that *antioxidant silver and platinum nanoparticles* significantly reduce the color of RB, MB and MO dyes in the existence of NaBH_4 , but antioxidant silver nanoparticles with higher catalytic activity than platinum nanoparticles can speed up the reduction rate of dyes, thus increasing the degradation capacity.

REFERENCES

1. Shao Y, Wu CH, Wu TT, Yuan CH, Chen SG, Ding T, et al. Green synthesis of sodium alginate-silver nanoparticles and their antibacterial activity. *Int J Biol Macromol.* 2018;111:1281-92.
2. Sintubin L, De Windt W, Dick J, Mast J, van der Ha D, Verstraete W, et al. Lactic acid bacteria as reducing and capping agent for the fast and efficient production of silver nanoparticles. *Appl Microbiol Biot.* 2009;84(4):741-9.
3. Wang MM, Zhang WJ, Zheng XS, Zhu PZ. Antibacterial and catalytic activities of biosynthesized silver nanoparticles prepared by using an aqueous extract of green coffee bean as a reducing agent. *Rsc Adv.* 2017;7(20):12144-9.
4. Raja S, Ramesh V, Thivaharan V. Green biosynthesis of silver nanoparticles using *Calliandra haematocephala* leaf extract, their antibacterial activity and hydrogen peroxide sensing capability. *Arabian J. Chem.* 2017;10:253-61.
5. Padalia H, Moteriya P, Chanda S. Green synthesis of silver nanoparticles from marigold flower and its synergistic antimicrobial potential. *Arabian J. Chem.* 2015;8: 732-41.
6. Velayutham K, Rahuman AA, Rajakumar G, Roopan SM, Elango G, Kamaraj C, Marimuthu S, SanthoshKumar T, Iyappan M, Siva C. Larvicidal activity of green synthesized silver nanoparticles using bark aqueous extract of *Ficus racemosa*

against *Culex quinquefasciatus* and *Culex gelidus*. *Asian Pac. J. Trop. Med.* 2013;6:95-101.

7. Kumar DA, Palanichamy V, Roopan SM. Green synthesis of silver nanoparticles using *Alternanthera dentata* leaf extract at room temperature and their antimicrobial activity. *Spectrochim. Acta A* 2014;127:168-171.

8. Edison TJI, Sethuraman MG. Instant green synthesis of silver nanoparticles using *Terminalia chebula* fruit extract and evaluation of their catalytic activity on reduction of methylene blue. *Process Biochemistry* 2012;47:1351-7.

9. Baruah B, Gabriel GJ, Akbashev MJ, Booher ME. Facile Synthesis of Silver Nanoparticles Stabilized by Cationic Polynorbornenes and Their Catalytic Activity in 4 Nitrophenol Reduction. *Langmuir* 2013;29:4225-30.

10. Veisi H, Azizi S, Mohammadi P. Green synthesis of the silver nanoparticles mediated by *Thymbra spicata* extract and its application as a heterogeneous and recyclable nanocatalyst for catalytic reduction of a variety of dyes in water. *J Clean Prod.* 2018;170:1536-43.

11. Sowmya T, Lakshmi GV. Antimicrobial and Catalytic Potential of *Soymida febrifuga* Aqueous

Fruit Extract-Engineered Silver Nanoparticles. *Bionanoscience.* 2018;8:179-95.

12. Harborn, JB. *Introduction to Ecological Biochemistry*, 3rd ed. London Academic Press. 1988;356.

13. Vidhu VK, Philip D. Catalytic degradation of organic dyes using biosynthesized silvernanoparticles. *Micron* 56. 2014;54-62.

14. Lopez-Miranda JL, Vazquez M, Fletes N, Esparza R, Rosas G. Biosynthesis of silver nanoparticles using a *Tamarix gallica* leaf extract and their antibacterial activity. *Mater. Lett.* 2016;176:285-9.

15. Karimzadeh I, Aghazadeh M, Ganjali MR, Norouzi P, Shirvani-Arani S, et al. A novel method for preparation of bare and poly(vinylpyrrolidone) coated superparamagnetic iron oxide nanoparticles for biomedical applications, *Mater. Lett.* 2016;179:5-8.

16. Khan ZUH, Khan A, Shah A, Wan P, Chen Y, et al. Enhanced photocatalytic and electrocatalytic applications of green synthesized silver nanoparticles, *J. Mol. Liq.* 2016;220:248-57.



Bioactivities of Phaeophytin *a*, α -Amyrin, and lupeol from *Brachystelma togoense* Schltr

Abiche Ekalu^{a*}  , Rachael Gbekele-Oluwa Ayo^b  , James D. Habila^b   and Ibrahim Hamisu^b  

^a Department of Chemistry, Nigerian Army School of Education, Ilorin, Kwara, Nigeria

^b Department of Chemistry, Ahmadu Bello University Zaria, Kaduna, Nigeria

Abstract: Phaeophytin *a*, α -amyrin and lupeol isolated from *Brachystelma togoense* were screened against *S. aureus*, *E. coli*, *S. pneumoniae*, *S. typhi*, and *C. albicans* using Ciprofloxacin and Terbinafine as standards. The results showed that these phytochemicals displayed antimicrobial activity against the tested organisms with the zone of inhibition from 12 – 27 mm. The result of minimum inhibitory concentration (MIC) showed that phaeophytin *a* was most active against *C. albicans* (0.09 mg/mL). The minimum bactericidal concentration (MBC) showed that phaeophytin *a* and lupeol were most active against *S. aureus*, *S. pneumoniae* and *S. typhi* (0.37 mg/mL). The result of minimum fungicidal concentration (MFC) showed that phaeophytin *a* was most active against *C. albicans* (0.1875 mg/mL). The activities of these phytoconstituents in *B. togoense* justified ethnomedicinal uses of the plant to treat various ailments.

Keywords: Bioactivity, Phaeophytin *a*, α -amyrin and lupeol, *Brachystelma togoense* Schltr

Submitted: May 30, 2019. **Accepted:** September 17, 2019.

Cite this: Ekalu A, Gbekele-Oluwa Ayo R, Habila J, Hamisu I. Bioactivities of Phaeophytin *a*, α -Amyrin, and lupeol from *Brachystelma togoense* Schltr. JOTCSA. 2019;6(3):411–8.

DOI: <https://doi.org/10.18596/jotcsa.571770>.

***Corresponding author. Address:** Department of Chemistry, Nigerian Army School of Education, Ilorin, Kwara, Nigeria. **E-mail:** ekalumiracle@gmail.com.

INTRODUCTION

Medicinal plants are used in developing countries as alternative medical treatments and phytochemicals isolated from these plants have shown *in vitro* and *in vivo* biological activity (1). Previously, humans have used natural products, such as plants, animals, microorganisms, and marine organisms, in medicines to alleviate and treat various diseases.

These natural products have a unique chemical diversity, which results in diversity in their

biological activities and drug-like properties (2). The use of medicinal plants for the treatment of diseases dates back to the history of human life, as the use of plants was their only choice of treatment (3). The World Health Organization (WHO) defines traditional medicinal plants as natural plant materials which are used at least or in the absence industrial processing for the treatment of diseases at a local or regional scale. Traditional herbal medicine has been used for thousands of years because it is natural and causes relatively fewer complications (3). There is a promising future of

medicinal plants as many plants around the world, and most of them are not investigated yet for their medical activities and their hidden potential of medical activities could be useful in the treatment of present and future studies (4).

Brachystelma was first described by Robert Brown in 1822. The genus *Brachystelma* R. Br. (Apocynaceae: Asclepiadoideae) is represented by about 100-120 species (5). *Brachystelma* is chiefly distributed in South Africa, South-East Asia, and Australasia (6). A total of 18 species are known in India (7) and out of them, 3 species are in Maharashtra. *Brachystelma togoense* is distributed on partially degraded hill slopes and open hill tops among grasses. It is an erect perennial herb, growing up to 30 cm, recorded from Ghana to Nigeria, in lowlands to montane situations. The tuber is said to be edible raw (8). The leaves are green in color, opposite, decussate, sessile or subsessile, linear to lanceolate to narrowly elliptic, 3-8 x 0.4-1 cm, acute, and margin ciliate. Tubers of *Brachystelma* species are known to be eaten as a food supplement in rural areas when there is a food shortage. Many of the tuberous *Brachystelma* are known to be used medicinally for the treatment of headache, stomach ache, and colds in children. In China, *Brachystelma edule* tubers are edible and the plant is used for the treatment of coughs and reduction of phlegm (9).

The secondary metabolites, phaeophytin *a*, α -amyrin, and lupeol, were previously isolated from the CH₂Cl₂ and MeOH extracts of *B. togoense*. The structures were elucidated using ¹H, ¹³C and 2D NMR. The presence of phaeophytin *a*, α -amyrin, and lupeol in *B. togoense* justified the use of the plant for medicinal purpose in Nigeria (10). The aim of this study is to carry out antimicrobial studies of the phaeophytin *a*, α -amyrin, and lupeol isolated from the aerial parts of *B. togoense*.

MATERIALS AND METHODS

Chemicals

The chemicals used for this study are CH₂Cl₂, MeOH, EtOH, DMSO, and EtOAc. All the chemicals were of analytical grade.

Material

Collection of plant

The stem bark of *Brachystelma togoense* was collected in April 2018 from Benue State, Nigeria. The plant was identified by the plant taxonomist Mallam Sanusi Namadi and a voucher specimen (no. 25856) is retained in the Biological Science Department, Ahmadu Bello University, Zaria-Nigeria.

Extraction and isolation

The air-dried *B. togoense* was manually reduced to powder using a mortar and pestle. Exactly 1000 g of the powdered plant material was extracted on a shaker (labcon sw39, 136 rpm) at room temperature (at 25 °C) using 100% dichloromethane (CH₂Cl₂) for 72 h. The extracts were concentrated using a rotary evaporator (Rotavapor R-215) at 40 °C resulting in a brown gum-like texture (32.0 g). The same procedure was used for methanol (MeOH) which yielded a brown gum-like texture (36.0 g). The CH₂Cl₂ and MeOH extracts were then separated by flash chromatography (Biotage SP1) over silica gel using three solvents. Firstly, an n-hexane/ CH₂Cl₂, gradient starting with 100% hexane and gradually increasing the polarity to 100% CH₂Cl₂. Secondly, CH₂Cl₂/ EtOH/EtOAc from a 100% CH₂Cl₂ to 50% EtOH/ EtOAc and to 100% EtOH/ EtOAc to yield various fractions (fr. 1-100). Fr.20 was spotted on the TLC plate using 100% CH₂Cl₂ and appeared a pure compound 1 (51.0 mg). The same procedure was repeated for the MeOH extract yielding compounds 2 (32.0 mg) and 3 (28.0 mg) which were spotted as pure compounds using CH₂Cl₂ /EtOH/ EtOAc (7:3) from fr.30. The structures of phaeophytin *a* (1), α -amyrin (2) and lupeol (3) are shown in Figure 1.

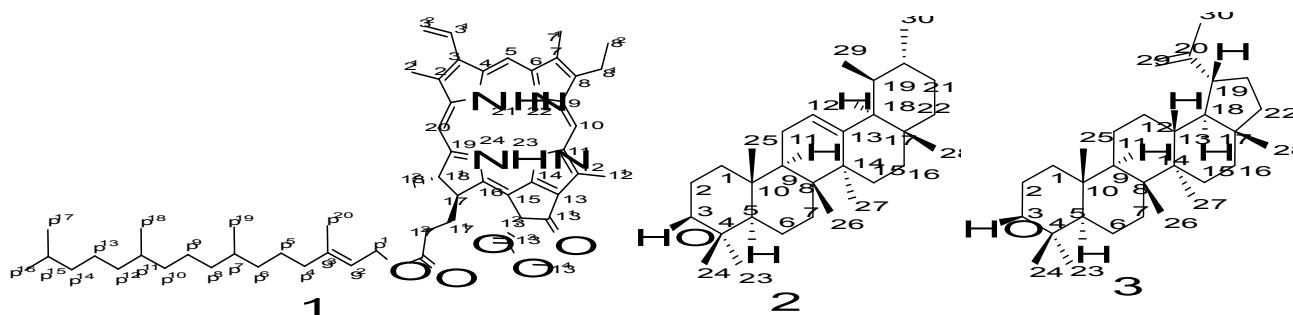


Figure 1. Structures of phaeophytin a (1), α -amyrin (2) and lupeol (3).

Antimicrobial screening of the isolates

The antimicrobial activities of the isolates were determined using some pathogenic microorganisms. The microorganisms were obtained from the Department of Medical Microbiology, Ahmadu Bello University Teaching Hospital, Zaria, Nigeria. All isolates were checked for purity and maintained in slants of blood agar. The antimicrobial activities of the isolates were evaluated by the broth dilution assay as described previously for the bacteria and Mueller Hinton broth assay for the fungi (11). The microorganisms tested were as follows: *Staphylococcus aureus*, *Streptococcus pneumoniae*, *Escherichia coli*, *Salmonella typhi*, and *Candida albicans*.

Determination of Zone of Inhibition

Solutions of 6.0 mg of the compounds were prepared using 10.0 mL dimethyl sulfoxide (DMSO). This solution was used to check the antimicrobial activity of the compound. A control experiment was also set up using DMSO.

The standardized inocula of the isolates were uniformly streaked onto freshly prepared Mueller Hinton agar plates with the aid of a sterile swab stick. Using a sterile cork borer (6 mm in diameter), 5 appropriately labelled wells were punched into each agar plate. An aliquot of 0.3 mL of the appropriate isolate concentration was placed in each well and then allowed to diffuse into the agar. An extra plate was streaked with the isolate and Ciprofloxacin (10 μ g/disc) was placed on it. The plates were incubated at 37 °C for 24 h. While for the fungi, Sabouraud dextrose broth was used and the incubation period was 30 °C and 48 h. The antimicrobial activities were expressed as diameter (mm) of inhibition zones produced by the plant extracts.

Minimum Inhibition Concentration (MIC)

The minimum inhibition concentrations of the isolates were carried out on the test microbes using the broth dilution method as outlined by the Clinical and Laboratory Standards Institute (CLSI) (12). Mueller Hinton broth was prepared as follows: 10.0 mL was dispensed into tubes and was sterilized at 121 °C for 15 minutes and allowed to cool. The McFarland turbidity standard scale 0.5 was prepared to give turbidity of the solution. Normal saline was prepared, 10.0 mL was dispensed into a sterile test tube and the test microbes were inoculated and incubated at 37 °C for 24 hours. Dilution of the test microbes was done in the normal saline until the turbidity matched that of the McFarland turbidity scale by visual comparison at this point the test microbe has a concentration of about 1.5×10^8 cfu/mL. Two-fold serial dilution of the extracts in the sterilized broth was made to obtain the concentrations of 3.00 mg/mL, 1.50 mg/mL, 0.75 mg/mL, 0.37 mg/mL, 0.18 mg/mL and 0.09 mg/mL. The initial concentration was obtained by dissolving 6.0 mg of the isolate in 10 mL of the sterile broth. Having obtained the different concentrations of the extracts in the sterile broth, 0.3 mL of the standard inoculum of the test microbe in the normal saline was then inoculated into the different concentrations. Incubation was made at 37 °C for 24 h, after which each test tube of the broth was observed for turbidity (growth). The lowest concentration of the isolate in which the broth shows no turbidity was recorded as the Minimum Inhibition Concentration (MIC).

Determination of Minimum Bactericidal Concentration/Minimum Fungicidal Concentration (MBC/MFC)

This was carried out to determine whether the microorganisms could be completely killed or their growth could only be inhibited. The minimum

bactericidal concentration of the isolates was determined as outlined by the CLSI on the nutrient agar plates. Minimum bactericidal concentrations were determined by assaying the test tube contents of the MIC determinations. A loopful of the content of each tube was inoculated by

streaking on a solidified nutrient agar plate and then incubated at 37 °C for 24 h for bacterial and 30 °C for 48 h for fungi. The lowest concentration of the subculture with no growth was considered as minimum bactericidal concentration/ minimum fungicidal concentration.

Table 1. Diameter of Zone Of Inhibition (mm) of Phaeophytin *a*.

Microorganisms	Concentration (mg/mL)				Ciprofloxacin (10x10 ⁻⁶)	Terbinafine (30x 10 ⁻⁶)
	3	1.5	0.75	0.375		
<i>S. aureus</i>	21	19	16	14	25	
<i>E. coli</i>	20	17	14	12	33	
<i>S. pneumoniae</i>	20	17	14	12	20	
<i>S. typhi</i>	19	17	15	13	19	
<i>C. albicans</i>	27	24	21	20		33

Table 2. Diameter of Zone Of Inhibition (mm) of α-amyrin.

Microorganisms	Concentration (mg/mL)				Ciprofloxacin (10x10 ⁻⁶)	Terbinafine (30x 10 ⁻⁶)
	3	1.5	0.75	0.375		
<i>S. aureus</i>	18	16	15	14	25	
<i>E. coli</i>	20	18	16	13	34	
<i>S. pneumoniae</i>	18	14	13	12	20	
<i>S. typhi</i>	19	16	15	14	18	
<i>C. albicans</i>	22	19	16	14		33

Table 3. Diameter of Zone Of Inhibition (mm) of lupeol.

Microorganisms	Concentration (mg/mL)				Ciprofloxacin (10x10 ⁻⁶)	Terbinafine (30x 10 ⁻⁶)
	3.0	1.5	0.75	0.375		
<i>S. aureus</i>	19	16	14	13	25	
<i>E. coli</i>	20	18	16	16	35	
<i>S. pneumoniae</i>	22	18	15	13	20	
<i>S. typhi</i>	20	18	16	15	20	
<i>C. albicans</i>	21	18	15	13		33

Table 4. Minimum Inhibitory Concentration (MIC)

Microorganisms	Concentration(mg/mL)		
	Phaeophytin <i>a</i>	α-amyrin	lupeol
<i>S. aureus</i>	0.18	0.37	0.37
<i>E. coli</i>	0.18	0.37	0.37
<i>S. pneumoniae</i>	0.18	0.37	0.18
<i>S. typhi</i>	0.18	0.37	0.18
<i>C. albicans</i>	0.09	0.37	0.18

Table 5. Minimum Bactericidal Concentration (MBC).

Microorganisms	Concentration(mg/mL)		
	Phaeophytin a	α -amyrin	lupeol
<i>S. aureus</i>	0.37	0.75	0.75
<i>E. coli</i>	0.75	0.75	0.75
<i>S. pneumoniae</i>	0.75	0.75	0.37
<i>S. typhi</i>	0.75	0.75	0.37

Table 6. Minimum Fungicidal Concentration (MFC).

Microorganism	Concentration(mg/mL)		
	Phaeophytin a	α -amyrin	lupeol
<i>C. albicans</i>	0.18	0.75	0.37

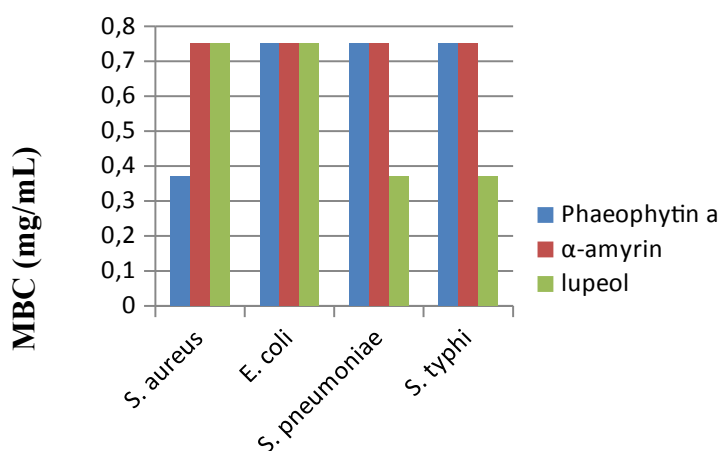


Figure 2. Graphical representation of Minimum Inhibitory Concentration (MIC) of the isolates against the microorganisms.

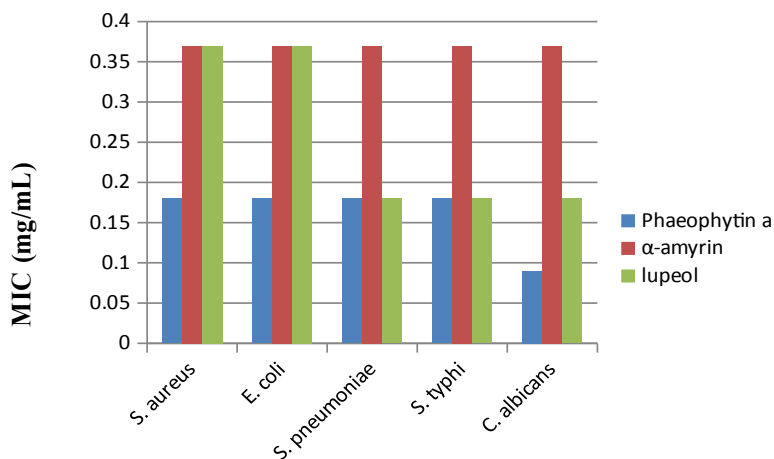


Figure 3. Graphical representation of the Minimum Bactericidal Concentration (MBC) of the isolates against the microorganisms.

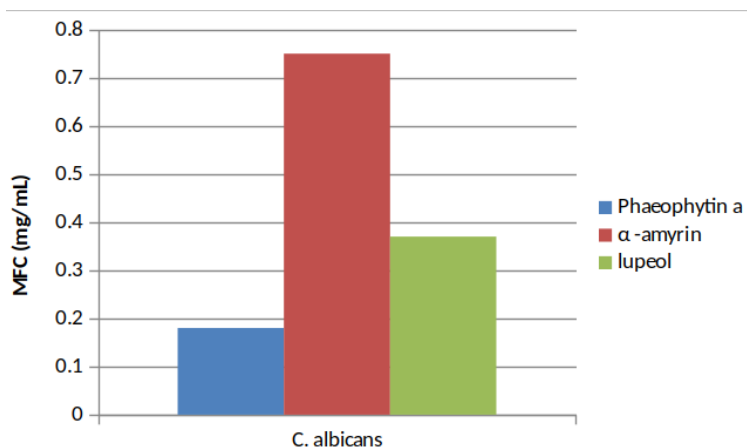


Figure 4. Graphical representation of the Minimum Fungicidal Concentration (MFC) of the isolates against the fungus.

RESULTS AND DISCUSSION

This study was carried out to investigate the *in vitro* antimicrobial activities of the phytoconstituents in *B. togoense* so as to justify its ethnomedicinal uses in the treatment of various ailments. The results of the antimicrobial studies showed that the compounds exhibited remarkable activity at 3.0 mg/mL against the five microorganisms tested. These phytochemicals displayed antimicrobial activity against the tested organisms with the zone of inhibition at various concentrations used ranging between 12 – 27 mm (Tables 1, 2 and 3). The MIC (Table 4 and Figure 2) showed that Phaeophytin *a* inhibited the growth of the microorganisms between 0.09- 0.18 mg/mL. That of α -amyrin was observed at 0.37 mg/mL while lupeol showed MIC between 0.37-0.75 mg/mL. The MBC (Table 5 and Figure 3) showed that Phaeophytin *a* killed the microbes between 0.37-0.75 mg/mL. That of α -amyrin was observed at 0.75 mg/mL while lupeol showed MBC between 0.37-0.75 mg/mL against these microbes. The result of MFC (Table 6 and Figure 4) showed that phaeophytin *a*, α -amyrin and lupeol stopped the growth of the microbes at 0.18 mg/mL, 0.75 mg/mL and 0.37mg/mL, 0.18 mg/mL respectively.

Phaeophytin *a* was most potent against *C. albicans* (0.09 mg/mL). The MBC showed that Phaeophytin *a* and lupeol were the most potent against *S. aureus*, *S. pneumoniae* and *S. typhi* (0.37 mg/mL) which confirmed the antimicrobial activity of lupeol

(13). Phaeophytin had exhibited *in vitro* antimicrobial action against fungal and bacterial standard strains (14). This confirmed the potency of Phaeophytin *a* in this study against the microorganisms tested. The result of MFC showed that Phaeophytin *a* was most potent against *C. albicans* (0.1875 mg/mL) confirmed that phaeophytin *a* possess strong antimicrobial activity against *C. albicans* (ATCC 90028) and *C. albicans* (ATCC 76615) (14). Phaeophytin *a* had also exhibited antimicrobial action against various microorganisms tested (15). α - and β -amyrin and amyrin acetate derivatives have exhibited potential antifungal activity against *Candida* spp (16). The pentacyclic triterpenoids, α -amyrin and β -amyrin, and lupeol have showed antibacterial activity against *S. aureus* and *E. coli* (17). In general, α -, β -amyrin have proved to be active by reducing bacterial viability < 20 % (18). α - and β -amyrin had inhibited the growth of *Bacillus subtilis*, *Staphylococcus aureus*, *Enterococcus faecium* and *Staphylococcus saprophyticus* (19).

CONCLUSION

Phaeophytin *a*, α -amyrin, and lupeol isolated from *Brachystelma togoense* were screened against *S. aureus*, *E. coli*, *S. pneumoniae*, *S. typhi*, and *C. albicans* using Ciprofloxacin and Terbinafine as standards. The results of activity of these isolates supported the ethnomedicinal uses of this plant in the treatment of skin infections, abdominal

disorders, gonorrhoea, cough, cold, and typhoid fever. Though isolation and characterization of these compounds have been reported (10), this is the first report of antimicrobial activity of this genus. The activities of these phytoconstituents in *B. togoense* justified ethnomedicinal uses of the plant.

ACKNOWLEDGMENTS

The authors wish to thank the Natural Products Research Group, University of Surrey, UK for the bench work opportunity.

REFERENCES

- Höfling J, Anibal PC, Obando-Pereda G, A T Peixoto I, Furlatti VF, Foglio M, et al. Antimicrobial potential of some plant extracts against *Candida* species. *Brazilian Journal of Biology* [Internet]. 2010;70:1065–8. Available from: <http://www.scielo.br/pdf/bjb/v70n4/a22v70n4.pdf>
- Yuan H, Ma Q, Ye L, Piao G. The Traditional Medicine and Modern Medicine from Natural Products. *Molecules*. 2016;21(229):1–3.
- Jamshidi-kia F, Lorigooini Z, Amini-khoei H. Medicinal plants: Past history and future perspective. *Journal of Herbmmed Pharmacology*. 2018;7(1):1–7.
- Dar RA, Shahnawaz M, Qazi PH. General overview of medicinal plants: A review. *The Journal of Phytopharmacology*. 2017;6(6):349–51.
- Bruyns P V. Three New Species of *Brachystelma* (Apocynaceae, Asclepiadoideae, Ceropegieae) from South Tropical and Southern Africa. Vol. 19. SPIE; 2009. 5 p.
- Ollerton J, Masinde S, Meve U, Picker M, Whittington A. Fly pollination in *Ceropegia* (Apocynaceae: Asclepiadoideae): biogeographic and phylogenetic perspectives. *Annals of Botany*. 2009;103(9):1501–14.
- Britto SJ, Bruyns P V. Three new species of *Brachystelma* from Tamil Nadu, India. *Haseltonia*. 2016;(22):48–54.
- Kew Royal Botanical Gardens. Electronic Plant Information Centre (ePIC) [Internet]. 2019 [cited 2019 Feb 7]. Available from: <http://epic.kew.org/index.htm>
- Prasad K, Prasanna P V., Meve U, Rao MS, Thulasaiah T. *Brachystelma annamacharyae* sp. nov. (Apocynaceae) from the Seshachalam hills of Andhra Pradesh (India). *Nordic Journal of Botany*. 2016;34(3):360–3.
- Ekalu A, Ayo RG, Habila JD, Hamisu I. Phaeophytin and Triterpenoids from *Brachystelma togoense* Schltr, a Nigerian Medicinal Herb. *Asian Journal of Chemical Sciences*. 2019;6(1):1–5.
- Niaz SI, Zhang P, Shen H, Li J, Chen B, Chen S, et al. Two new isochroman derivatives penisochromanes A and B from ascidian-derived fungus *Penicillium* sp. 4829. *Natural Product Research* [Internet]. 2018;6419(May):1–7. Available from: <https://doi.org/10.1080/14786419.2018.1470173>
- CLSI. Testing, Clinical and Laboratory Standards Institute, 32. 27 th. 2017.
- Gallo M, Miranda bullet, Sarachine J. Biological activities of lupeol. In: *International Journal of Biomedical and Pharmaceutical Sciences*. 2009. p. 46–66.
- Gomes RA, Teles YCF, Pereira F de O, Rodrigues LA de S, Lima E de O, Agra M de F, et al. Phytoconstituents from *Sidastrum micranthum* (A. St.-Hil.) Fryxell (Malvaceae) and antimicrobial activity of pheophytin a. *Brazilian Journal of Pharmaceutical Sciences* [Internet]. 2015;51:861–7. Available from: http://www.scielo.br/scielo.php?script=sci_arttext&pid=S1984-82502015000400861&nrm=iso
- Yen KH, Nyokat N, Kutoi CJ, Hamzah AS, Lim IF. Chemical Constituents of *Artocarpus odoratissimus* from Sarawak. 2017;7(08):137–41.
- Johann S, Soldi C, Lyon JP, Pizzolatti MG, Resende MA. Antifungal activity of the amyridin derivatives and in vitro inhibition of *Candida albicans* adhesion to human epithelial cells. 2007;45:148–53.
- Keawsa-ard S, Liawruangrath B, Kongtaweelert S. Bioactive Compounds from *Mesua ferrea* Stems. 2015;42(1):185–95.
- Díaz-ruiz G, Hernández-vázquez L, Luna H, Wachter-rodarte MC, Navarro-ocaña A. Growth

Ekalu A et al. JOTCSA. 2019; 6(3): 411-418.

RESEARCH ARTICLE

Inhibition of Streptococcus from the Oral Cavity by α -Amyrin Esters. 2012;(Figure 1):12603-11.

19. Kiplimo JJ, Koorbanally NA, Chenia H. Triterpenoids from Vernonia auriculifera Hiern exhibit antimicrobial activity. 2011;5(8):1150-6.



ASSESSMENT OF GROUNDWATERS' QUALITY WITH DEPTH of 8-60 m IN THE ARBËRIA NEIGHBOURHOOD OF GJILAN MUNICIPALITY, KOSOVO

Valdrin M. Beluli ^{1*}  

¹University of Tirana, Faculty of Natural Sciences, Department of Industrial Chemistry, Boulevard Zogu I, Tirana, Albania.

Abstract: Gjilan is one of the largest cities in the Republic of Kosovo. Groundwater samples with a depth of 8-60 m have been taken in this neighbourhood Arbëria, where the samples were taken in three different areas. These groundwaters are used as drinking water and to ascertain that these groundwaters comparing with the WHO regulation. Parameters analysed are: nitrites (NO₂-N), nitrates (NO₃-N), ammonia (NH₃-N), chlorides (Cl⁻), bicarbonates (HCO₃⁻), alkaline (A-HCl), carbonic strength (CS), NTU, pH, and conductivity in water (CW). The results of this study display the quality of these groundwaters based on the WHO regulation. Some groundwaters are not in accordance with WHO water quality regulations. The groundwaters we have analysed in three areas of the Arbëria neighbourhood in Gjilan Municipality, based on the analysis confirm very well, showing that the land of this neighbourhood has strong layers of lime.

Keywords: Groundwater, hydrogenochemical, neighbourhood, WHO.

Submitted: December 08, 2018. **Accepted:** September 24, 2019.

Cite this: Beluli V. ASSESSMENT OF GROUNDWATERS' QUALITY WITH DEPTH of 8-60 m IN THE ARBËRIA NEIGHBOURHOOD OF GJILAN MUNICIPALITY, KOSOVO. JOTCSA. 2019;6(3):419-28.

DOI: <https://doi.org/10.18596/jotcsa.493909>.

***Corresponding author. E-mail:** valdrin.beluli@hotmail.com.

INTRODUCTION

The vast majority of groundwater comes from rains and melting of ice. Water fills the spaces between stones and soil forming aquifers (water reservoirs). Groundwater can be considered as one of the hidden resources. Groundwater may contain natural impurities or pollutants regardless of human activity (1). Groundwater is an important water resource and a major factor for maintaining the regional ecological environment, which plays a significant role in ensuring water, food, economic, and ecological security (2). The chemical composition of groundwater is the product of the long-term interaction between groundwater and the surrounding environment. During the evolution of a groundwater system, different hydrogenochemical processes result in

groundwaters having different chemical compositions (3).

Well water quality and their suitability for drinking were discussed through physico-chemical parameters. Well water was taken in different depths and analysed for pH, conductivity in water (CW), nephelometric turbidity unit (NTU), bicarbonates (HCO₃⁻), carbonic strength (CS), alkaline (A-HCl), chlorides (Cl⁻), nitrites (NO₂-N), nitrates (NO₃-N), and ammonia (NH₃-N).

pH is a very important parameter in water quality (4). Turbidity results from the scattering of light in water by organic and inorganic particles; however, high turbidity usually is caused by suspended inorganic particles, particularly

sediments (5). Conductivity of water (CW), also, known as specific conductivity, represents the ability of water to convey electricity, and is related to the concentration of ionised substances in water (6).

Ammonia (NH₃-N) is present in groundwater very often. Its presence in water describes its formation as the result of the reduction of organic substances containing nitrogen, deamination of amines, etc. The main source of nitrite ions (NO₂-N), in water is the process of mineralisation of organic matter and nitrification from bacteria. Nitrites are much more toxic than ammonia and nitrates (7). In our case, some groundwater contains high amounts of NO₂ and their values are not in accordance with WHO, etc. Concentration of nitrates in groundwater often reaches alarming values. The concentration of NO₃-N higher than 10 mg/L in water is a cause for the methemoglobinemia of children, a disease characterised by cyanosis and blue skin colour. NO₃-N deactivates haemoglobin by transforming into methaemoglobin, a form that cannot make oxygen transport. This illness hits hard babies up to three months after birth. Chlorides are inorganic anions that are most commonly found in natural and contaminated waters and mainly come from natural minerals and industrial pollution. In drinking waters such as groundwater, salty taste is derived from the presence of high amounts of Cl⁻ (1). Water hardness considers the amount of mineral salts dissolved in water or water capability to form a stone scale. The water hardness indicator is of great importance for determining the use of drinking water and for industrial purposes (4). The largest number of European countries rely more on surface water than on groundwater. In many countries, groundwater is used as the main source of water for public use because such processing and water supply costs are relatively low, while water is of high quality, etc. The parameters analysed in groundwaters are based on WHO criteria.

EXPERIMENTAL

Chemicals

Some of the reagents used for groundwater analysis: Nitri Ver 3 (HACH®), Nitra Ver 5 (HACH®), 0.01 M HCl, K₂CrO₄ 0.257 mol/L, AgNO₃ 0.01 M, methyl orange, phenolphthalein, 0.1 M HCl, Ammonia Salicylate reagent (HACH®), Ammonia Cyanurate reagent (HACH®).

Physico - Chemical parameters and methods analysis

Absorption spectrophotometry in the ultraviolet and visible region is based on the electromagnetic radiation absorption of molecules

in the UV spectra of 160–400 nm and Vis 400–780 nm range. UV-Vis radiation absorption causes the excitation of the electrons of chemical bonds by passing the molecules to higher energy levels (8). The absorption of UV-Vis radiation from complex molecules and inorganic salts of transitional metals, as well as of lanthanides and actinides, causes the molecule to move from its basal to its excited state (9). The HACH® Model DR/2010 Spectrophotometer is a microprocessor-controlled single-beam instrument for colorimetric testing in the laboratory or in the field. The instrument is precalibrated for over 120 different colorimetric measurements and allows convenient calibrations for user-entered and future HACH® methods (10).

The pH and CW are defined in the groundwater sampling areas so that the results are as accurate and realistic as those waters. The pH is determined with a WTW 3010 type instrument, while CW is determined with WTW Cond 3110 at μS/cm. NTU results were obtained in labs shortly after laboratory sampling. The instrument used was the 2100N ISC Turbidimeter HACH® (*ISO Method 7027*).

In aquatic environments, total ammonia exists in two chemical forms, unionised ammonia and ionised ammonium (NH₃-N). Nowadays, there is increasing attention and a significant number of studies that are focusing on nitrogen to gain more knowledge about the factors that are influencing its different transformation pathways (11).

NH₃-N concentration was determined using in first step Ammonia Salicylate reagent and in second step using Ammonia Cyanurate reagent (Nitrogen Ammonia Test 0 – 0.50 mg/L, *Method 8155*) and the absorbance level was then measured using a spectrophotometer (HACH® DR/ 2010, USA) at λ = 655 nm.

NO₂-N concentration was determined using Nitri Ver 3 reagent (Nitrite Test 2 - 150 mg/L, *Method 8153*) and the absorbance level was then measured using a spectrophotometer (HACH® DR 900, USA). Nitrate (NO₃-N) concentration was determined using Nitra Ver 5 reagent (Nitrate Test 0-30 mg/L, *Method 8039*) and the absorbance level was then measured using a spectrophotometer (HACH® DR / 2010, USA) at λ = 500 nm.

The water sample alkalinity is the measurement of its capacity to neutralise the acids. Water accumulation is mainly due to weak acid salts. We took 100 mL of the analysed sample, added 4 drops of phenolphthalein and if the 100 mL solution gets purple, then water has bases as a

result of pH above 8.3, and if it does not get purple, then 2 to 3 drops of methyl orange is added, which gives yellow colour. It is titrated with 0.01 M HCl until the solution gets orange and the amount of titre used is written (7).

The determination of chlorides was carried out in an Erlenmeyer flask containing 100 mL of water sample (adjust pH 7–10 if necessary). With the addition of 1 mL of (K_2CrO_4 ($C = 0.257$ mol/L)) the sample turned to a yellowish colour. Titration was done with silver nitrate ($AgNO_3$ ($C = 0.01$ mol/L)) and it stopped at the moment when the solution gets light red colour. The value of the chlorides in the sample was calculated according to Eq. 1 (12):

$$Cl^- \text{ mg/L} = 35.453 \cdot M \cdot \frac{(V_1 - V_2)}{V_s} \quad (1)$$

where V_1 is the volume of the titre for the sample (mL), V_2 is the volume of the titre for blank sample (mL), M is molarity of $AgNO_3$ 0.01 M, and V_s is the volume of the sample used (100 mL in our case).

Carbonate strength (CS) is defined as the alkalinity to methyl orange. A volume of 100 mL water sample was transferred to a 500 mL Erlenmeyer flask and 2–3 drops of methylene chloride were added. The titration was performed with standard HCl solution ($C = 0.01$ mol/L) until the colour changed to orange. The analysis results were calculated in German degrees ($^\circ dH$) water hardness scale according to E. 2 (12):

$$CS \text{ (}^\circ dH\text{)} = 2.8 \cdot V_{HCl} \cdot C_{HCl} \quad (2)$$

2.8 is a constant, V_{HCl} is the consumed volume of HCl, and the concentration of HCl is 0.1 mol/L.

RESULTS AND DISCUSSION

The location of the analysed samples

To analyse a large-scale neighbourhood is a challenge. We have analysed 15 groundwaters in the Arbëria neighbourhood in municipality of Gjilan, where the distance from one sample to the other sample is about 100-200 m and the depth of the groundwaters are 8 to 60 m. Before sampling the waters, sampling planning has been carried out to divide into three sampling areas such as Area 1, Area 2 and Area 3, see Figure 1.



Figure 1. Research areas of groundwaters within the depth of 8-60 m in neighbourhood Arbëria in municipality of Gjilan.

Transporting samples to the laboratory

First, we have cleaned the glass bottles and sterilised them well in order to be in a level of purity, then started collecting 1000 mL water samples and in each area were taken 5 samples

in deep wells of 8-60 m. The water samples were transported from 15 locations to a laboratory with a temperature of 4-5 $^\circ C$. The water is taken from taps that have been connected with groundwater and before the samples are taken,

the water flow should be within a 15-minute time interval. The samples were taken according to EPA / 600 / R-94/205.

Results for the pH

pH is a very important parameter in groundwaters, surface waters, and atmospheric waters. In our case, the pH does not express any degradation as a parameter and is in accordance with the WHO regulation. In area 1, pH ranges from 7.1-7.45 in depths of 8-60 m, see Table 1. In Area 2, pH in groundwaters with depth of 8-30 m is 7.39-7.81, while in area 3 pH in groundwaters with depth of 25-40 m is 7.2-7.8, see Table 1. pH in area 2 is slightly higher compared to Areas 1 and 3.

Results for the conductivity water (CW)

Electrical conductivity in water, also known as specific conductivity, is the ability of water to convey electricity, and is related to the concentration of ionised substances in water (7). If the electrical conductivity in the water is too high, then this indicates that in that sample the water contains many minerals. In the CW water chemistry is an important parameter that is carried out at the place where the samples are taken. CW in groundwaters where we have obtained values in the deposits in the three areas is not presented as a problem in the three areas analysed (Figure 1). In Area 1, where the sampling depth was 8-60 m, which CW is 867-1673 $\mu\text{S}/\text{cm}$ as seen in Table 3. In a groundwater with a depth of 18 m, the CW is slightly high and is not in compliance with WHO allowed values. see Table 1. Groundwaters in area 2 with a depth of 8-30 m, CW value is from 471-1448 $\mu\text{S}/\text{cm}$ and these groundwaters are in accordance with WHO, see Table 1, also in Area 3 where groundwater with depth of 25-40 m CW included in 920-1400 $\mu\text{S}/\text{cm}$, see Table 1. Meaning that even in Area 3 conductivity is in accordance with WHO rules. Groundwaters have always been found to possess a higher conductivity than surface water (lakes, rivers etc).

Results for Nephelometric turbidity unit (NTU)

Turbidity is a measurement of the influence of suspended solids on an aqueous solution's ability to transmit light (13). In the groundwaters from the evidence of scientific research it has concluded that in the groundwaters it is difficult to achieve a high turbidity, eventually if there is extreme contamination near an underground water, etc. In Area 1 of groundwaters with depth of 8-60 m, the value of NTU is not high which is 0.75-3.54 and is in accordance with the WHO regulation, while in area 2 (Figure 1), where groundwaters with depth 8-30 m, the NTU are from 0.44 to 0.65, these NTU values that are

analysed are in accordance with WHO. In Area 3, NTU in groundwaters with depth of 25-40 m is 0.5-3.1, see Table 1. NTU values in the three areas analysed are in accordance with WHO.

Results for chlorides (Cl^-)

Chlorides (Cl^-) are present in both fresh and salty water, and are essential elements of life. High chloride concentrations in fresh water can harm aquatic organisms by interfering with osmoregulation, the biological process by which they maintain the proper concentration of salt and other solutes in their bodily fluids (14). Chlorides in groundwaters often are higher than surface water because water is always in contact with the various layers of soil which may contain different ions. Groundwaters in Area 1 with depth of 8-60 m, there is no high concentration of chlorides is 26.2-55 mg/L, see Table 1. In Area 2, groundwaters with depth of 8-30 m, the concentration of Cl^- in this area is 12.6-49.4 mg/L. In Area 3, the concentration of Cl^- in groundwaters with depth of 25 -60 m is 22-60 mg/L, see Table 1. In Area 3 (Figure 1) the concentration of Cl^- is higher compared to Area 2 and Area 1, see Table 1. In all groundwater samples, the concentration of Cl^- is in accordance with WHO.

Results for Alkalinity

Alkalinity is determined by volume through class titrations or potentiometric titrations (6). The alkaline in these waters are in accordance with the WHO regulation and this appearance a positivity in these groundwaters that we have analysed. In Area 1, the amount of alkalinity in groundwaters with depth of 8-60 m is 6.39-8.57 HCl/ mL, while in area 2 the amount of alkalinity is 4.2-8.6 HCl/mL in the groundwaters' depths of 8-30 m, see Table 1. In Area 3, groundwaters with a depth of 25-40 m, the amount of alkalinity is 4.73-8.46 HCl/mL, see Table 1. In the three areas analysed (Figure 1), all values obtained in this groundwater are in accordance with the WHO regulation for this parameter, see Table 1.

Results for bicarbonates (HCO_3^-)

The amount of bicarbonate (HCO_3^-) often expresses great concern in groundwaters, because limestone layers can be found in the interior, etc. In Area 1, the concentration of HCO_3^- in groundwaters with depth of 8 - 60 m is 390.4 -523.2 mg/L, so in two groundwaters of this area are not in accordance with the WHO regulation. In area 2, groundwaters with a depth of 8-30 m of HCO_3^- is 256.2-524.6 mg/L. In Area 3, groundwaters with a depth of 25-40 m of HCO_3^- is within 289-516.5 mg/L, see Table 1. The concentration of HCO_3^- in those groundwaters that is not accordance with WHO:

(i). In groundwater with a depth of 8 m in Area 1, the concentration of HCO_3^- is 523.2 mg/L. This concentration indicates that it is not in accordance with the WHO regulation because it is more than 23.2 mg/L, see Table 1. In addition, in this area there is another groundwater that is not in accordance with the WHO regulation, which is in depth of 9 m, where the concentration of HCO_3^- is 518.5 mg/L. This indicates that the concentration of 18.5 mg/L is more than the WHO allowed regulation, see Table 1.

(ii). In Area 2, there is only a groundwater that is not in accordance with the WHO. The depth of this groundwater reaches up to 12 m where the concentration of HCO_3^- is 524.6 mg/L, so according to this value, the concentration of 24.6 mg/L is above the WHO allowed value, see Table 1.

(iii). Also, in Area 3, groundwater with a depth of 30 m and other groundwater with a depth of 40 m are not in accordance with WHO. In groundwater with a depth of 30 m, the concentration of HCO_3^- is 516.5 mg/L, so according to this concentration in this groundwater there are more than 16.5 mg/L HCO_3^- , see Table 1. In groundwater with a depth of 40 m, the concentration of HCO_3^- is 501.9 mg/L, see Table 1 and compare with WHO criteria for these parameters that have been analysed in three areas.

Results for nitrites (NO_2^- - N) and nitrates (NO_3^- - N)

Nitrates (NO_3^-) and nitrites (NO_2^-) are frequently present in plants, soils and waters; since their chemistries are practically indissociable, one rarely is found without the other. If in excessive levels, these ions can have an adverse impact on public health and ecological systems. NO_3^- is the foremost toxic agent, but the fairly inert nitrate is easily reduced to nitrite by bacterial action in the soil or within the digestive system (15). With the development of agriculture, the use of artificial fertilisers increases, which means that the consumption of nitrates increases, while the phosphate consumption remains the same. There is a risk of NO_3^- , because approximately 10% of fertilisers and pesticides are removed from the soil surface (16). In Area 1, the concentration of NO_3^- -N in groundwaters with a depth of 8-60 m does not contain a high concentration, where values are within 3-7.1 mg/L, while in Area 2 the concentration of NO_3^- -N is within 1.9-35 mg/L in groundwaters with depth of 8-30 m, see Table 1. In Area 3, groundwaters with depth of 25-40 m does not display a high concentration of NO_3^- -N, where values are within 1.9-8.9 mg/L. The concentration of NO_3^- -N which is not in accordance with WHO regulation:

(i). In Area 2, groundwater with a depth of 8 m (Figure 1) possesses a very high concentration of nitrate up to 35 mg/L, see Table 1. This concentration is too high for a groundwater, containing more than 25 mg/L as compared to WHO regulation. This groundwater is not in accordance with WHO, see Table 1.

Nitrites (NO_2^- -N) usually display many complications in groundwater, where these waters are open in the ex-agricultural land, as in our study.

The nitrites in our case in the groundwater with a depth of up to 60 m have been proved to be present in most groundwaters, the concentration of NO_2^- -N in some groundwaters is not in accordance with WHO. In Area 1, NO_2^- -N in groundwaters with depth of 8 - 60 m, the concentration of NO_2^- -N is 0.001-0.008 mg/L, see Table 1. In Area 2, in groundwaters with depth of 8 - 30 m, the concentration of NO_2^- -N is 0.003-0.008 mg/L, while in Area 3, the NO_2^- -N quantity is within 0.002-0.009 mg/L, see Table 1. The concentration of NO_2^- -N in groundwaters in the Arbëria neighbourhood that are not in accordance with the WHO regulation:

(i). In Area 1, groundwater with a depth of 8 m, NO_2^- -N is 0.008 mg/L, see Table 1 and this concentration is high compared to WHO, see Table 1. In this groundwater NO_2^- -N is more than 0.003 mg/L compare to the permissibility up to 0.005 mg/L.

(ii). In Area 2, groundwater with a depth of 12 m displays an obstacle in this water because the concentration of NO_2^- -N is 0.008 mg/L, this concentration of NO_2^- -N is not in accordance with the WHO. So, in this groundwater the concentration of NO_2^- -N is more than 0.003 mg/L compare to the permissible concentration up to 0.005 mg/L, see Table 1.

(iii). In Area 3, groundwater with depths of 30 m, 32 m and 40 m, the value of NO_2^- -N is high, see Table 2. In groundwater with a depth of 30 m the concentration of NO_2^- -N is 0.007 mg/L and this value display in one consistent with the WHO regulation and this indicates that it is not in accordance, see Table 1. In groundwater with a depth of 30 m, the concentration of NO_2^- -N is 0.006 mg/L, this value is not in accordance with the WHO because in this water is more than 0.001 mg/L, while in groundwater with a depth of 40 m, the concentration of NO_2^- -N is 0.009 mg/L, this value is out of regulation or better to say it is not in accordance with the WHO regulation, because it contains more than 0.004 mg/L, see Table 1.

Results for ammonia (NH₃-N)

Nowadays, there is increasing attention and a significant number of studies that are focusing on nitrogen to gain more knowledge about the factors that are influencing its different transformation pathways (7). Amount of ammonia (NH₃-N) in groundwater with depth of 8-60 m reaches the concentration of 0-0.09 mg/L in Area 1, see Table 1. These concentrations are in accordance with WHO. In Area 2, in groundwater with a depth of 8-30 m, NH₃-N is 0-0.08 mg/L, this chemical parameter in this area is in accordance with the WHO, see Table 1. Area 3 (Figure 1), in groundwater with depths of 25-30 m, NH₃-N quantities is 0-0.03 mg/L and these values do not indicate any risk, see Table 1. In Area 3, all results obtained in this groundwaters are in accordance with WHO, see Table 1. In Area 1, NH₃-N is present with a higher concentration compared to Areas 2 and 3.

Results for carbonic strength

Water hardness is considered to be a disadvantageous parameter in the use of water for urban purposes and factories (due to the formation of lacquer layers in the steam pipes). But it should be said that drinking water should have a moderate hardness value because in these cases the solubility of the toxic metals is lower and the water represents a higher buffering effect on acidic compounds. In addition, medium-medium water presents a better taste as well as evidence that it is better for health in particular in reducing cases of some heart disease (6). Natural water which has a high amount of soluble calcium and magnesium salts is called strong water (17).

The carbonic strength (CS) in the groundwaters we have analysed in three different areas (Figure 1) is a bit high, but this creates a benefit for reason that reduces heart disease, also the third toxic metals. In Area 1, groundwaters with a depth of 8-60 m, the amount of CS is 21.67-40.02 °dH, see Table 1. In Area 2, the amount of CS is 12.53-37.07 °dH in the groundwaters with depth of 8-30 m, while in Area 3 in groundwaters with depth of 25-40 m, the amount of CS includes values 20.64-36.47 °dH. Carbonic strength (CS) in groundwaters with depths of 8-60 m which are not in accordance with the WHO regulation:

(i). In Area 1, all groundwaters entered the category of strong water according to WHO, while the very high CS value in this area is at a depth of 18 m which reaches up to 40.02 °dH. This value is not in accordance with WHO, see Table 1.

(ii). In Area 2, all groundwaters entered the category of strong water according to the German °dH degree. In groundwater with a depth of 30 m, the value of CS is 37.07 °dH, this value is not in tune because this groundwater entered the category of very strong water, see Table 1.

(iii). Also, in area 3, groundwaters entered the category of strong waters. In groundwater with a depth of 32 m, where the value of CS is 36.47 °dH, as well as in groundwater with a depth of 40 m value of CS is 31.2 °dH, see Table 1. In these two high groundwaters mentioned in area 3, they entered the category of groundwater with high hardness according to the German scale and this two groundwaters are not in accordance with WHO, see Table 1.

If the water contains large amounts of bicarbonate, this will determine the hardness of the CS rather than the general hardness (GH). In this case, after determining the total hardness (GH), it equals the carbonate strength.

The health side effects that may have some underground water in the three study areas of the Arbëria neighbourhood

One current challenge in geochemistry is determining the genesis and particularly the geochemical processes controlling the chemical compositions of mineral waters, which are often generated in complex hydrogeological systems (18).

Arterial hypertension, affecting about one billion people worldwide, is the most prevalent modifiable risk factor for cardiovascular diseases and related disability (19). In many cases, groundwater has caused many health problems due to the scarcity of chemical knowledge. In our case, some groundwaters containing HCO₃⁻ that are not in accordance with WHO and can cause health problems (Figure 2) due to the formation of alkalosis.

Normal arterial blood pH is restricted to a very narrow range of 7.35 to 7.45. A person who has a blood pH below 7.35 is considered to be in acidosis (actually, "physiological acidosis," because blood is not truly acidic until its pH drops below 7), and a continuous blood pH below 7.0 can prove fatal. Acidosis has several symptoms, including headache and confusion, and the individual can become lethargic and easily fatigued. A person who has a blood pH above 7.45 is considered to be in alkalosis, and a pH above 7.8 is fatal. Some symptoms of alkalosis include cognitive impairment (which can progress to unconsciousness), tingling or numbness in the

extremities, muscle twitching and spasm, nausea, and vomiting. Both acidosis and alkalosis can be caused by either metabolic or respiratory disorders. Metabolic alkalosis is the opposite of metabolic acidosis. It occurs when the blood is too alkaline (pH above 7.45) due to too much bicarbonate (called primary bicarbonate excess), see Table 2. A transient excess of bicarbonate in the blood can follow ingestion of excessive amounts of bicarbonate, citrate, or antacids for conditions such as stomach acid reflux—known as heartburn. Cushing's disease, which is the chronic hypersecretion of adrenocorticotrophic hormone (ACTH) by the anterior pituitary gland, can cause chronic metabolic alkalosis. The over secretion of ACTH results in elevated aldosterone levels and an increased loss of potassium by urinary excretion. Other causes of metabolic alkalosis include the loss of hydrochloric acid from the stomach through vomiting, potassium depletion due to the use of diuretics for hypertension, and the excessive use of laxatives (20).

Nitrogen compounds are formed in the air by lightning or discharged into it from industrial processes, motor vehicles, and intensive agriculture (21). Nitrites in the water supply system can also reach due to their frequent use as a corrosion inhibitor during industry water

processing. When the nitrite ions reach the stomach, the high concentration of hydrochloric acid in the stomach turns nitrite into nitrous acid (HNO_2) which reacts with secondary amines from the digestive tract and forms *N*-nitrosoamine. *N*-nitrosoamines are known as carcinogenic substances (1).

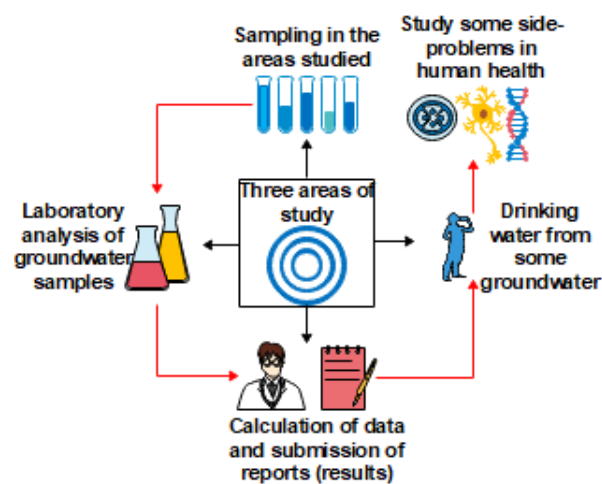


Figure 2. Scientific description of chemical problems in groundwaters with depths of (8-60) m in Arbëria neighbourhood in municipality of Gjilan.

Table 1. Physico-chemical results of groundwaters with depth 8-60 m in the Arbëria neighbourhood in Gjilan Municipality.

Area	Depth (m)	pH	NTU	CW µS/cm	Cl ⁻ mg/L	A ⁻ mL HCl 0.1	HCO ₃ ⁻ mg/L	CS °dH	NO ₂ -N mg/L	NO ₃ -N mg/L	NH ₃ -N mg/L
Area 1	8	7.19	3.54	1400	55	8.57	523.2	23.21	0.008	7.1	0.05
	9	7.45	0.75	1076	46	8.5	518.5	21.67	0.002	5.6	0.06
	12	7.32	1.62	867	26.2	6.39	390.4	21.79	0.002	5.9	0.02
	18	7.4	1.15	1693	55	7.1	433.1	40.02	0.004	4	0.09
	60	7.1	1.66	1037	28	8.1	494.1	26.27	0.001	3	0
Area 2	8	7.57	0.65	920	39	5.6	341.6	23.08	0.003	5	0.04
	12	7.74	4.52	1170	45.2	8.6	524.6	29.35	0.008	5	0.06
	18	7.51	0.44	978	65	7.78	292	25.27	0.003	6.9	0
	30	7.39	0.45	471	49.4	4.26	260.1	12.53	0.004	1.9	0.01
	30	7.81	0.51	1448	12.6	4.2	256.2	37.07	0.003	3.4	0.08
Area 3	25	7.3	1.5	920	43	4.73	289	24.08	0.002	7.3	0.03
	30	7.31	3.1	1230	29	8.46	516.5	20.64	0.007	8.7	0
	30	7.12	2.99	1310	22	7.05	430.1	21.94	0.004	8.1	0
	32	7.2	0.45	1295	60	6.54	399.1	36.47	0.006	1.9	0
	40	7.8	0.5	1400	59	8.22	501.9	31.2	0.009	8.9	0.01
WHO reference values		7.2 to 7.8	5	1500	250	10.5	250 to 500	18 to 30	0.005	10 (Method 8039)	0.5

Table 2. Types of Acidosis and Alkalosis

	pH	PCO ₂	HCO ₃ ⁻
Metabolic acidosis	↓	N, then ↓	↓
Respiratory acidosis	↓	↑	N, then ↑
Metabolic alkalosis	↑	N, then ↑	↑
Respiratory alkalosis	↑	↓	N, then ↓

Reference values (arterial): pH: 7.35–7.45; pCO₂: male: 35–48 mm Hg, female: 32–45 mm Hg; total venous bicarbonate: 22–29 mM. N denotes normal; ↑ denotes a rising or increased value; and ↓ denotes a falling or decreased value.

CONCLUSION

The quality and quantity of water for human during history has been a vital factor in determining the welfare. The results obtained on the basis of laboratory analysis conclude that in the neighbourhood Arbëria the water is not of

good quality in some areas due to the high concentrations of NO₂-N and HCO₃⁻ ions and these values of these ions send us in a direction that the waters in this neighbourhood are included a high CS at the German °dH scale. During the analysis we have concluded that there is a high carbonic strength (CS) in the three

research areas, and this happened when the water comes into contact with the underground lime layers by dissolving them. In conclusion we can say that water quality is not very good due to the carbon strength exceeding the allowed drinking norm and this is dangerous for direct consumption and for use in the field of industry. The reason why these waters are not suitable for human organs is that these waters after use will cause problems over time in the digestive system, cardiovascular problems etc. NO₂-N in these groundwaters express a great concern because nitrites are very toxic. After receiving the results, we immediately informed the users of these groundwater where their parameters were not in accordance with the WHO regulation. In some groundwaters of the three analysed areas it is proved that those parameters that are not in accordance can cause major problems of normal metabolism.

List of symbols and abbreviations

CW – conductivity water, NTU – nephelometric turbidity unit, CS – carbonic strength, EDTA – ethylenediaminetetraacetic acid, GH – general hardness, WHO – World Health Organisation, A – Alkalinity, ACTH - adrenocorticotrophic hormone.

REFERENCES

1. Korça B, Analiza Kimike e Ujit, Universiteti i Prishtinës [Water Chemical Analysis, University of Pristina], Prishtinë . 2013: 91–92, 95, 97, 100, 105, 108.
2. Ting X, Dengming Y, Baisha W, Wuxia B, Pierre D, Fang L, Wang Y, Jun M. "The Effect Evaluation of Comprehensive Treatment for Groundwater Overdraft in Quzhou County, China. *Water*. 2018; 10:1-18, <https://doi.org/10.3390/w10070874>
3. Liting X, Linxian H, Xinyu H, Lizhi Y ,Guangyao Ch, Junxiang X, Henghua Zh. Groundwater Hydrochemical Zoning in Inland Plains and its Genetic Mechanisms. *Water*. 2018; 10: 1-18 <https://doi.org/10.3390/w10060752>
4. Aliu M, Teknologjia e Ujit, Universiteti i Mitrovicës [Water Technology, University of Mitrovica]. 2017: 23, 52
5. Denby S, Lloyd Jeffrey S, Koenings Jacqueline P, Laperriere D, Effects of Turbidity in Fresh Waters of Alaska. 1987; 7: 18-33 [https://doi.org/10.1577/1548-8659\(1987\)](https://doi.org/10.1577/1548-8659(1987))
6. Çullaj A, Kimi Mjedis, Universiteti i Tiranës [Chemistry Environment, University of Tirana], Tiranë. 2005: 13, 171
7. Daci N.M, Daci-Ajvazi M.N, Shkenca e Mjedisit, Akademia e Shkencave dhe e Arteve të Kosovës [Environmental Science, Academy of Sciences and Arts of Kosovo], Prishtinë. 2014: 87, 230, 249-255
8. Vasjari M, Shehu A, Baraj B, Çullaj A, Metodot Instrumentale të Analizës, Universiteti i Tiranës [Instrumental Methods of Analysis, University of Tirana], Tiranë. 2013: 52
9. Lazo P, Çullaj A, Metoda të Analizës Instrumentale, Universiteti i Tiranës [Instrumental Analysis Methods, University of Tirana], Tiranë. 2017: 59
10. DR/2010 Spectrophotometer instrument manual, general description, USA. 1999: 15.
11. Leoni B, Patelli M, Soler V, Nava V, Ammonium Transformation in 14 Lakes along a Trophic Gradient. *Water*. 2018; 10: 1-13. <https://doi.org/10.3390/w10030265>
12. Beluli V.M. Influence of Urbanization and Industries on the Pollution of Rivers of Gjilan Municipality, Kosovo. 2018; 67: 517-525. <https://doi.org/10.15255/KUI.2018.007>
13. Arnold E, Toran L, Effects of Bank Vegetation and Incision on Erosion Rates in an Urban Stream. *Water*. 2018; 10: 1-16. <https://doi.org/10.3390/w10040482>
14. Molly H, Elizabeth H, Linda G, Chlorides in Fresh Water, The University of Rohde, Island. 2012: 1-4
15. Almeida X. MG, Serra A, Silveira CM, Moura JJ, Nitrite Biosensing via Selective Enzymes—A Long but Promising Route. *Sensors*. 2010; 10: 1-26, <https://doi.org/10.3390/s101211530>
16. Liu C-W, Sung Y, Chen B-C, Lai H-Y. Effects of Nitrogen Fertilizers on the Growth and Nitrate Content of Lettuce (*Lactuca sativa* L.). *International Journal of Environmental Research and Public Health*. 2014; 11 (4): 4427-4440.

17. Rexhepi R. Nj, Mbrojtja e ambientit për jetë më të mirë [Protecting the environment for a better life], Prishtinë. 2006: 17
18. Shestakova A, Guseva N, Kopylova Y, Khvashevskaya A, Polya DA, Tokarev I. Geothermometry and Isotope Geochemistry of CO₂-Rich Thermal Waters in Choygan, East Tuva, Russia. Water. 2018; 10(6):729. <https://doi.org/10.3390/w10060729>
19. Tetti M, Monticone S, Burrello J, Matarazzo P, Veglio F, Pasini B, Jeunemaitre X, Mulatero P. Liddle Syndrome: Review of the Literature and Description of a New Case. International Journal of Molecular Sciences. 2018; 19(3):812. <https://doi.org/10.3390/ijms19030812>
20. URL-1. <https://courses.lumenlearning.com/suny-ap2/chapter/disorders-of-acid-base-balance/> (20.03.2019)
21. URL-2. https://www.who.int/water_sanitation_health/dwq/chemicals/nitratenitrite2ndadd.pdf (21.03.2019)



Anticancer Activities of Even-Numbered Monoketo Eicosanoic Acid Anilides and Semicarbazones

Hülya Çelik Onar^{1*}  , Fatma Ceren Anlaş²  , Hasniye Yaşa¹  ,
Fulya Üstün Alkan²  , Belma Hasdemir¹   and Tülay Bakirel²  

¹ Istanbul University-Cerrahpaşa Engineering Faculty, Chemistry Department, Organic Chemistry Division, Avcılar/İstanbul/Turkey.

² Istanbul University-Cerrahpaşa Veterinary Faculty, Pharmacology and Toxicology Department, Avcılar/İstanbul/Turkey.

Abstract : This work was carried out on the cytotoxic activity of semicarbazone and anilide derivatives of ketoeicosanoic acids on canine mammary tumor cell line (CMT-U27). Five semicarbazone compounds (**1-5**) and five anilide compounds (**6-10**) were used in this study. 8-Semicarbazone eicosanoic acid (**3**) was shown to be cytotoxic. In contrast, 10-keto eicosanoic acid anilide (**9**) has been shown to be less cytotoxic towards CMT-U27 cell line.

Keywords: Anilide, Semicarbazone, Fatty Acid, Canine mammary tumor, MTT Assay.

Submitted: June 28, 2019. **Accepted:** September 24, 2019.

Cite this: Çelik Onar H, Anlaş F, Yaşa H, Üstün Alkan F, Hasdemir B, Bakirel T. Anticancer Activities of Even-Numbered Monoketo Eicosanoic Acid Anilides and Semicarbazones. JOTCSA. 2019;6(3):429–32.

DOI: <https://doi.org/10.18596/jotcsa.583845>.

*Corresponding author. E-mail: hcelikonar@gmail.com.

INTRODUCTION

In recent years, pharmaceutical industry has been focused on the development of new innovative drugs for cancer therapy, due to cancer represents an important health problem at a global level. Many natural and synthetic compounds are in charge of affecting selectively specific organs and tissues within a biological system. Particularly heterocyclic compounds are being studied as anticancer reagents. Among such compounds, Schiff bases are important functional groups in terms of biological activities as antimicrobial (1-3), anti-inflammatory (4,5), analgesic (6,7), and pesticidal agents (8,9).

Keto-fatty acids are stable compounds. High molecular weight keto-fatty acids constitute the structure of plant waxes. There are many literature reports on the biological activity of fatty acids. For example, antibacterial effects of C₁₂-C₁₈

saturated and unsaturated fatty acids have been observed (10). As another one, it has been suggested that surfactants prepared from fatty acids have a skin irritation-reducing effect. They show good biodegradability and low toxicity, so they are defined as environmentally friendly (11). Amides and anilides are also important in pharmaceutical, agrochemical industries, and are used as protecting groups in organic synthesis (12,13). It has been proved that some of the fatty acid amides and anilides synthesized have good activity against gram-positive bacteria (14). The anticancer activities of vanillin semicarbazone have been reported against Ehrlich Ascites Carcinoma (EAC) (15).

In this study, anilide and semicarbazone derivatives of (4-12) monoketo C₂₀ fatty acids were examined as anti-cancer agent on canine mammary tumor cell line (CMT-U27) and the effect of the position of the keto group were also,

too. Canine mammary tumors (CMTs) are most frequent neoplasia in female dogs, as well as considered as a suitable model for human breast cancer.

MATERIAL AND METHODS

(4-12) Monoketo eicosanoic acid anilides and semicarbazones synthesis

In previous work, 4-, 6-, 8-, 10- and 12-keto C₂₀ esters were synthesized by Blaise reaction with high purity by Çelik and Özeriş. These esters were hydrolyzed to the corresponding carboxylic acids. Then semicarbazone and anilide derivatives of keto acids were obtained (16).

Cell line and reagents

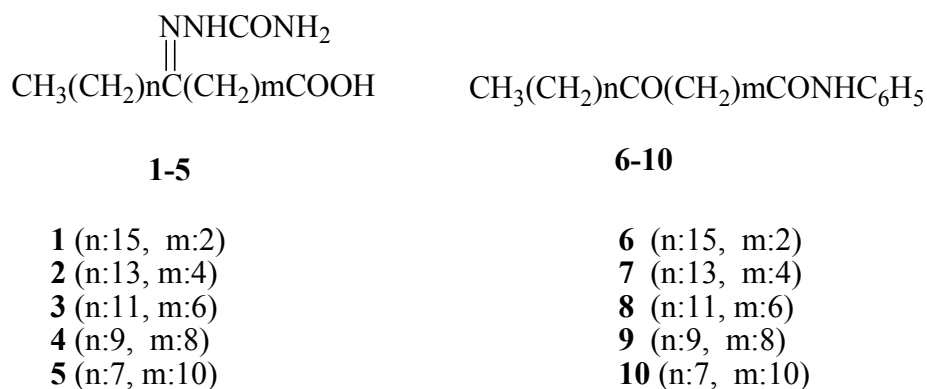
The canine mammary carcinoma cell line CMT-U27 was kindly donated by Dr. Eva Hellmén from Uppsala University, Sweden. Cell line was maintained in Dulbecco's modified Eagles Medium (DMEM-F12) (Invitrogen, CA) supplemented with 1% (v/v) L-glutamine (Gibco, USA), 10% (v/v) heat-inactivated fetal bovine serum (Invitrogen, CA) and 100 U/mL penicillin and 100 µg/mL streptomycin (Gibco, Grand Island, NY, USA) at 37 °C in a humidified atmosphere of 5% CO₂. The cells were cultured at 37 °C in a humidified atmosphere with 5% CO₂. Cells were sub-cultured as they reached 80–90% confluence and adherent cells were detached by incubation with Trypsin/EDTA solution. Cell number was determined using a 0.2% trypan blue dye with the Cedex XS cell counter system (Innovatis, Roche, Germany). Anilide and semicarbazone derivatives of C₂₀ keto fatty acids were dissolved in dimethyl sulfoxide and then further diluted in culture media. Doxorubicin was purchased from Sigma-Aldrich (St Louis, MO, USA) and dissolved in culture media.

MTT assay

Cell viability was assessed using a commercial cell proliferation MTT [3-(4,5-dimethylthiazol-2-yl)-2,5-diphenyltrazolium bromide] kit (Roche Applied Science, Germany) according to the manufacturer's instructions. Briefly, cells were seeded at a density of 1×10⁴ cells/well in 96-well plates (Jet Biofil, Canada) and then allowed to settle and attach overnight in culture media and incubated at 37 °C in a humidified atmosphere of 5% CO₂ for 24h and then treated with varying concentrations of anilide and semicarbazone derivatives of C₂₀ keto fatty acids (3.25 – 100 µM) and doxorubicin (0.2-8 µM) for 72h. At the end of incubation period 10 µL of MTT solution [5 mg/mL in phosphate buffered saline (PBS)] were added to each well. The plates were incubated for 4 h in a humidified atmosphere at 37 °C with 5% CO₂. The purple water-insoluble formazan salt was then dissolved with 10% SDS in 0.01M HCl and the plates were incubated overnight in a cell culture incubator. The optical densities of the wells were measured at 595 nm using a Multi-Mode microplate reader (FilterMax F5, Molecular Devices, USA). The effect of each compound on growth inhibition was assessed as percent cell viability where vehicle (DMSO)-treated cells were taken as 100% viable. The mean of triplicate experiments for each dose was used to calculate the concentration of compounds required for 50% inhibition of cell viability (IC₅₀) as determined using the Biosoft CalcuSyn software (Biosoft, UK).

RESULTS AND DISCUSSION

This work was carried out on the cytotoxic activity of semicarbazone and anilide derivatives of keto eicosanoic acids on canine mammary tumor cell line (CMT-U27). Five semicarbazone compounds (**1-5**) and five anilide compounds (**6-10**) were used in this study (Scheme 1).



Scheme 1. Semicarbazone and anilide derivatives of keto eicosanoic acids.

The cytotoxicity was determined using 3-(4,5-dimethylthiazol-2-yl)-2,5-diphenyltetrazolium

bromide (MTT) assay. The half maximal inhibitory

concentrations (IC₅₀) were calculated by using Calcsyn software.

At the end of the 72 hour treatment, only compounds, 8-semicarbazone eicosanoic acid (**3**) and 10-keto eicosanoic acid anilide (**9**) inhibited cell growth towards CMT-U27 cell line. The other compounds did not show appreciable activity in the experiments performed (Table 1). Among

these compounds, 8-semicarbazone eicosanoic acid (**3**) and 10-keto eicosanoic acid anilide (**9**) displayed effective cytotoxic potential against CMT-U27 and IC₅₀ concentrations were recorded at 1.952 μ M and 54.01 μ M, respectively. The IC₅₀ of doxorubicin as a positive control (chemotherapeutic agent) was founded as 0.8 μ M.

Table 1. Cytotoxic activity of keto eicosanoic acid anilides and semicarbazone eicosanoic acids

Compound	Cytotoxicity (%)						
	100 μ M	75 μ M	50 μ M	25 μ M	12.5 μ M	6.25 μ M	3.125 μ M
1	-	-	-	-	-	-	-
2	-	-	-	-	-	-	-
3	65.77	75.26	70.32	57.95	60.32	60.75	54.27
4	-	-	-	-	-	-	-
5	-	-	-	-	-	-	-
6	-	-	-	-	-	-	-
7	-	-	-	-	-	-	-
8	-	-	-	-	-	-	-
9	61.72	56.45	53.45	31.39	27.43	22.79	26.45
10	-	-	-	-	-	-	-

3: 8-Semicarbazone eicosanoic acid **9:** 10-Keto eicosanoic acid anilide

Cytotoxic activity was not detected in 4-,6-,10-,12-semicarbazone eicosanoic acids and 4-, 6-, 8-, 12-keto eicosanoic acid anilides and, when the keto group is evaluated in terms of its location, it has been found that the keto functional group has a better cytotoxic activity if it is in the middle of the chain. Anilide and semicarbazone containing a keto group at the beginning or at the end of the chain did not show cytotoxic activity against the CMTU 27 tumor.

8-Semicarbazone eicosanoic acid (**3**) was shown to be cytotoxic. In contrast, 10-keto eicosanoic acid anilide (**9**) has been shown to be less cytotoxic towards CMT-U27 cell line.

Our results indicate that 8-semicarbazone eicosanoic acid (**3**) may benefit as a novel chemopreventive compounds for anticancer therapy.

REFERENCES

- Venkatesh P. Synthesis, characterization and antimicrobial activity of various schiff bases complexes of Zn(II) and Cu(II) ions. *Asian J Pharm. Hea. Sci.* 2011; 1: 8-11.
- Hussein MA, Omar RH, Farghaly HS. Design, synthesis, structure elucidation and biochemical evaluation of some schiff's base derivatives bearing pyrazolo [3,4-D] pyrimidine-4-ones. *Int. J. Acad Res.* 2011; 3 (2): 454-462.
- Nair R, Shah A, Baluja S, Chanda S. Synthesis and antibacterial activity of some schiff base complexes. *J. Serb. Chem. Soc.* 2006; 71: 733-44.
- Sathe BS, Jaychandran E, Jagtap VA, Sreenivasa GM. Synthesis characterization and anti-inflammatory evaluation of new fluorobenzothiazole schiff's bases. *Int. J. Pharm. Res. Dev.* 2011; 3: 164-69.
- Pandey A, Dewangan D, Verma S, Mishra A, Dubey RD. Synthesis of schiff bases of 2-amino-5-aryl-1, 3, 4-thiadiazole and its analgesic, antiinflammatory, antibacterial and antitubercular activity. *Int. J. Chem. Tech. Res.* 2011; 3: 178-84.
- Fahmy HH, El-Eraky W. Synthesis and evaluation of analgesic and anti-inflammatory activities of O- substituted salicylamides. *Arch. Pharm. Res.* 2001; 24: 171-179.
- Chinnasamy RP, Sundararagan R, Govindaraj S. Synthesis, characterization and analgesic activity of novel Schiff base isatin derivatives. *J. Adv. Pharm. Technol. Res.* 2010; 1: 342-347.
- Ali MM, Jesmin M, Salam SMA, Khanam JA, Islam MF, Islam MN. Pesticidal activities of some schiff bases derived from benzoin, salicylaldehyde,

- aminophenol and 2, 4-dinitrophenylhydrazine. *J. Sci. Res.* 2009; 1: 641-646.
9. Jesmin M, Ali MM, Islam MN. Pesticidal Activity of some Schiff Base Complexes Derived from some Divalent Metal Acetates, Glycine and Salicylaldehyde. *J. Sci. Found.* 2008; 6: 49-56.
10. Jon JK, Swieczkowski DM, Anthony JC, Truant JP. Fatty Acids and Derivatives as Antimicrobial Agents. *Antimicrob. Agents Chemother.* 1972; 2 (1): 23-28.
11. Maag H. Fatty acid derivatives: Important surfactants for household, cosmetic and industrial purposes. *J. Am. Oil Chem. Soc.* 1984; 61: 259-267.
12. Pasha MA, Nanjundaswamy HM. Reductive fission of azoarenes to aminoarenes by aluminium/hydrazine hydrate. *J. Chem. Res.* 1984; 750-752.
13. Hartley D, Kidd H. *The Agrochemicals Hand Book*, 2nd ed.; Royal Society of Chemistry: Nottingham, 1987; p 215.
14. Maurer EW, Smith FD. Fatty acid amides and anilides, syntheses and antimicrobial properties. *J. Am. Oil Chem. Soc.* 1980; 57: 98-103.
15. Shaikh MMA, Azad MAK, Jesmin M, Ahsan S, Rahman MM, Kraham JA, Islam MN, Shahria SMS. In vivo anticancer activity of vanillin semicarbazone. *Asian Pac. J. Trop. Biomed.* 2012; 438-442.
16. Çelik H, Özeriş S. Synthesis of Even Numbered of (2-12) Monohydroxy Eicosanoic Acid Isomers. *Chim. Acta Turc.* 1996; 24: 23-27.



Bi(NO₃)₃·5H₂O-catalyzed Mannich Reaction: A Potent Catalyst for Synthesis of β-Aminocarbonyl Compounds

Hasniye Yaşa^{1*}  and Kübra Demir² 

¹Istanbul University-Cerrahpaşa, Engineering Faculty, Chemistry Department, 34320 Avcılar, Istanbul, Turkey.

²Istanbul University-Cerrahpaşa, Institute of Science, Chemistry Division, Avcılar-Istanbul, Turkey

Abstract: Biologically active compounds containing nitrogen, natural molecules and drugs are important for organic synthesis. Mannich reaction is one of the most common methods used for the synthesis of these compounds. Bi(NO₃)₃ was used as an efficient catalyst for the one-pot three-component Mannich reactions of ketones with different aromatic amines and aromatic aldehydes at room temperature. It is a good method to prepare β-aminocarbonyl compounds in excellent yield. The high efficiency using simple starting materials and a catalytic amount of a reusable catalyst is especially noteworthy.

Keywords: Mannich reaction, One-pot synthesis, Bismuth(III) nitrate, β-Aminocarbonyls.

Submitted: August 16, 2019. **Accepted:** September 26, 2019.

Cite this: Yaşa H, Demir K. Bi(NO₃)₃·5H₂O-catalyzed Mannich Reaction: A Potent Catalyst for Synthesis of β-Aminocarbonyl Compounds. JOTCSA. 2019;6(3):433–8.

DOI: <https://doi.org/10.18596/jotcsa.605641>.

***Corresponding author.** E-mail: hasniye@istanbul.edu.tr. Tel: 05423831488.

INTRODUCTION

In recent years, β-amino ketones are compounds with significant biological effects such as antibacterial, antifungal, antitumor, antidiabetic effects (1-6). They can be easily converted into their derivatives and are often used in the field of medicine. These compounds are the most important structural units used for the synthesis of 1,3-aminoalcohol and β-amino acid forms (2). Presently, β-aminocarbonyl forms are present in many synthetic drugs available for treatment in various medical conditions (7). β-aminocarbonyl compounds are frequently used in the synthesis of various antibiotics such as neopolyoxin and nikomycin. In the synthesis and modification of β-amino acids have been recorded several methods. Mannich reaction has an important role in organic chemistry for obtaining bioactive compounds and natural products. Several methods have been reported in the literature for the synthesis of β-aminocarbonyl compounds using Brønsted acids (8), Lewis acids (9) and

organocatalysts (10). However, there are also problems such as long reaction time, difficult reaction conditions, toxicity, and difficulties in separating complex molecules. Hence there is an increasing interest in developing environmentally benign reactions for the synthesis of β-aminocarbonyl compounds' syntheses. Nowadays, bismuth(III) salts (11-13) are used as catalysts in organic synthesis because of easy handling, low cost, and eco-friendly behavior. We notify a fast synthesis of β-aminocarbonyl compounds in the presence of Bi(NO₃)₃·5H₂O (BN) for it is non-toxic, stable in air, and cheaper.

The synthesized β-aminocarbonyl compounds (**4a-o**) were purified by crystallization and characterized by elemental analysis, FT-IR, ¹H NMR, ¹³C NMR, and MS methods. Some of these compounds were first synthesized in this study (**4g**, **4j**, and **4o**).

EXPERIMENTAL SECTION

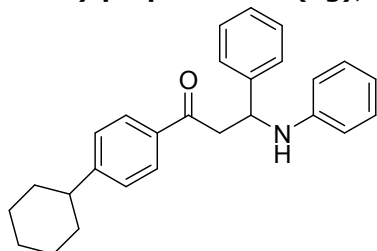
The chemicals used in this study were commercially available from Merck and Aldrich and were used without further purification. The obtained compounds were purified by crystallization. ^1H and ^{13}C NMR (500 and 125 MHz, respectively) spectra were recorded using Me_4Si as the internal standard in CDCl_3 . Mass spectra were obtained on Thermo Finnigan LCQ Advantage MAX MS/MS spectrometer. FT-IR spectra were recorded on Bruker Vertex 70.

General procedure for the synthesis of β -amino carbonyl compounds

Ketone (2.2 mmol), aldehyde (2 mmol) and amine (2 mmol) and 10 mol% $\text{Bi}(\text{NO}_3)_3$ (11-13) were added to a one-necked round bottom flask. The reaction mixture was stirred vigorously with a magnetic stirrer at room temperature (r.t.) for the mentioned time. After reaction completion, EtOH and H_2O at the reaction-mixture were evaporated at ambient temperature. Then 60 mL of hot CH_2Cl_2 was added to dissolve the solid product. The catalyst was removed by filtration and the organic layer was washed twice with saturated NaHCO_3 solution, dried with Na_2SO_4 , and evaporated. The product was purified by recrystallization from an ethanol-acetone mixture (3/2, v/v) to afford the corresponding compounds.

Compounds (**4a-f**, **4h-i**, and **4k-n**) are known in the literature and their results are in accordance with the literature. The analytical and spectral data of the other products (**4g**, **4j**, and **4o**) so obtained were as follows:

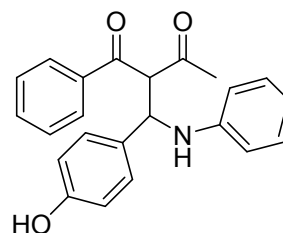
1-(4-Cyclohexylphenyl)-3-phenyl-3-(phenylamino)-propan-1-one (**4g**),



Yield, 91%; white crystals; Mp.: 157,4- 158,5 °C. IR (neat, cm^{-1}): 3384 (-NH), 3045, 3024, 2921, 2847, 1666(-CO), 1178 (C-N), 746, 690. ^1H -NMR (500 MHz, CDCl_3 , δ / ppm): 1.18 (2H, m, alicyclic $-\text{CH}_2-$), 1.33 (4H, m alicyclic $-\text{CH}_2-$), 1.69 (2H, m, alicyclic $-\text{CH}_2-$), 1.78 (2H, m, alicyclic $-\text{CH}_2-$), 2.48 (1H, m, alicyclic $-\text{CH}-$) 3.34 (1H_a, dd, J=16.2 ve 7.8 Hz, $-\text{CH}_{2a}-\text{CH}-\text{NH}$), 3.43 (1H_b, d, J=16.1 ve 5.2 Hz, $-\text{CH}_{2b}-\text{CH}-\text{NH}$), 4.91 (1H, dd, J=7.6 ve 5.2Hz, $\text{CH}_2-\text{CH}-\text{NH}$), 6.51 (2H, d, J=7.8 Hz, arom.- $\text{CH}-$), 6.60 (1H, t, J=7.3 Hz, arom.- $\text{CH}-$), 6.97-7.04 (2H, m, arom.- $\text{CH}-$), 7.15 (1H, t, J=7.3 Hz, arom.- $\text{CH}-$), 7.19 (2H, d, J=8.4 Hz,

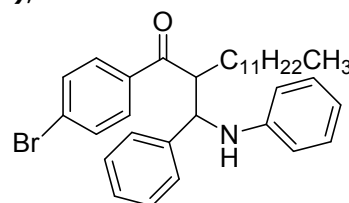
arom.- $\text{CH}-$), 7.24 (2H, t, J=7.6 Hz, arom.- $\text{CH}-$), 7.37 (2H, d, J=7.5 Hz, arom.- $\text{CH}-$), 7.76 (2H, d, J=8.4 Hz, arom.- $\text{CH}-$). ^{13}C -NMR (125 MHz, CDCl_3 , δ / ppm): 26.3 (alicyclic CH_2), 27.1 (alicyclic $2\times\text{CH}_2$), 34.3 (alicyclic $2\times\text{CH}_2$), 34.4 (alicyclic CH_2), 44.9 ($-\text{CHNH}-$), 46.2 ($-\text{COCH}_2\text{CH}-$), 114.5, 126.8, 127.4 ($2\times\text{CH}$), 127.6, 128.7 ($4\times\text{CH}$), 129.0 ($3\times\text{CH}$), 129.3 ($3\times\text{CH}$), 134.7, 154.2, 197.9 ($-\text{C}=\text{O}$). MS (ESI+) m/z (%): 384.0 (100, $[\text{M} + \text{H}]^+$). Anal. calcd for $\text{C}_{27}\text{H}_{29}\text{NO}$ (383.22): C, 84.55; H, 7.62; N, 3.65. Found: C, 84.53; H, 7.63; N, 3.67.

1-Phenyl-2-[(4-hydroxyphenyl)(phenylamino)methyl]-butan-1,3-dione (**4j**),



Yield, 89%; yellow crystals; Mp.: 110,5- 111,5 °C. IR (neat, cm^{-1}): 3404 (-OH), 3291 (-NH), 3024, 3007, 2916, 2856, 1646 (-CO), 1220 (C-N), 752, 698. ^1H -NMR (500 MHz, CDCl_3 , δ / ppm): 1.50 (1H, s, $-\text{NH}-$), 2.08 (3H, s, $-\text{CH}_3-$), 3.70 (1H, brs, -OH), 4.13 (1H, d, J= 5.2 Hz, $-\text{CH}-\text{CH}-\text{NH}$), 5.34 (1H, d, J= 5.2 Hz, $-\text{CH}-\text{CH}-\text{NH}$), 7.11- 7.29 (5H, m, arom. $-\text{CH}-$), 7.30-7.39 (7H, m, arom. $-\text{CH}-$), 7.85 (2H, m, arom. $-\text{CH}$). ^{13}C -NMR (125 MHz, CDCl_3 , δ / ppm): 19.4 ($-\text{CH}_3$), 28.7 ($-\text{CH}_2$), 93.3 ($-\text{CH}_2$), 114.8, 119.8, 123.7 ($2\times-\text{CH}$), 123.8, 124.5, 124.8, 126.0 ($2\times-\text{CH}$), 127.2 ($2\times-\text{CH}$), 128.7 ($2\times-\text{CH}$), 129.7, 129.9 ($-\text{CH}$), 134.6, 139.0, 158.9 ($-\text{C}-\text{OH}$), 161.2 ($-\text{C}=\text{O}$), 187.7 ($-\text{C}=\text{O}$). MS (ESI+) m/z (%): 359.1 (100, $[\text{M}]^+$). Anal. calcd for $\text{C}_{23}\text{H}_{21}\text{NO}_3$ (359.15): C, 76.86; H, 5.89; N, 3.90. Found: C, 76.83; H, 5.83; N, 3.82.

1-(4-Bromophenyl)-2-[phenyl(phenylamino)methyl]-tetradecan-1-one (**4o**),



Yield, 88%; pale yellow crystals; Mp.: 176,8-178,1 °C. IR (neat, cm^{-1}): 3406 (-NH), 3055, 3028, 2915, 2848, 1578 (-CO), 1180 (C-N), 806, 752. ^1H -NMR (500 MHz, CDCl_3 , δ / ppm): 0.81 (3H, t, J= 7.8 Hz, $-\text{CH}_3$), 1.14-1.31 (22 H, m, $-\text{CH}_2$), 2.29 (1H, m, $-\text{CH}-\text{CH}-\text{NH}$), 2.84 (1H, dd, J= 7.5 and 5.2 Hz, $-\text{CH}-\text{CH}-\text{NH}$), 6.85 (1H, s, $-\text{NH}-$), 7.00- 7.03 (5H, m, arom. $-\text{CH}-$), 7.25-7.28

(5H, m, arom.-CH-), 7.51-7.53 (2H, m, arom.-CH), 7.74 (2H, d, J= 5 Hz, arom.-CH). ¹³C-NMR (125 MHz, CDCl₃, δ / ppm): 14.0 (-CH₃), 22.9, 27.9, 28.9 (5x-CH₂), 29.2 (2x-CH₂), 31.0, 31.7, 53.4, 60.0, 116.4 (2x-CH₂), 119.6, 122.3, 127.4, 128.1 (2x-CH₂), 128.2 (2x-CH₂), 129.1 (2x-CH₂), 129.4 (2x-CH₂), 131.8 (2x-CH₂), 136.3, 140.2, 146.2, 207.2 (-C=O). MS (ESI+) m/z (%): 547.1 (100, [M]⁺). Anal. calcd for C₃₃H₄₂BrNO (547.24): C, 72.25; H, 7.72; N, 2.55; Br, 14.57. Found: C, 72.23; H, 7.70; N, 2.52; Br, 14.55.

Mannich reaction of aniline, benzaldehyde, and acetophenone was selected as a model and various catalysts have been tried (Table 1). The highest yield was obtained with Bi(NO₃)₃ (Table 1, entry 3). Several conventional organic solvents such as acetone, ethanol, THF, toluene, and DCM were used to optimize the reaction conditions. Ethanol was found to be a more suitable solvent for the reaction. Different molar ratios of catalyst were investigated to find the best yield. The optimum value was 10 mol% of Bi(NO₃)₃ catalyst (Table 2).

RESULTS AND DISCUSSION

Table 1. Mannich reaction of acetophenone, aniline and benzaldehyde in the presence of several catalysts.

Entry	Catalyst	Time(h)	Yield ^a (%)
1	No catalyst	48	No reaction
2	I ₂	24	80
3	Bi(NO ₃) ₃	24	92
4	Al(NO ₃) ₃ .9H ₂ O	24	68
7	2,4,6-Trichloro-1,3,5-triazine(TCT)	12	75
8	AlCl ₃	20	70

^aIsolated yield. Mannich reaction; 2.0 mmol of aldehyde, 2.0 mmol of amine and 2.2 mmol of acetophenone in 5 mL of ethanol in the presence of catalyst at room temperature.

Table 2. Screening of molar ratios of Bi(NO₃)₃ to synthesize of **4a**.

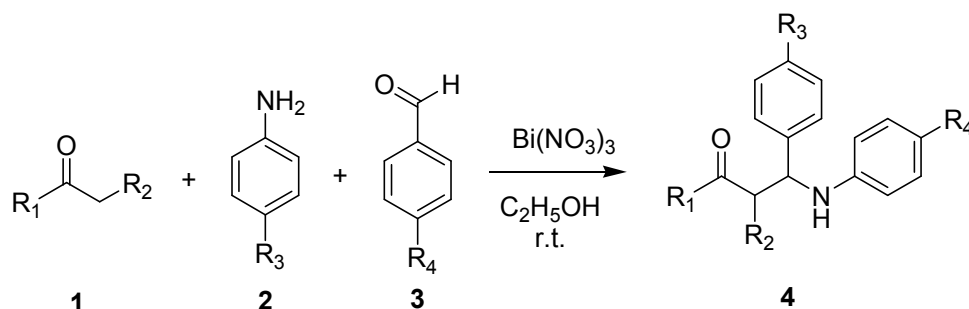
Entry	Bi(NO ₃) ₃ %	Time (h)	Yield ^a (%)
1	2.5	24	42
2	5	24	65
3	7.5	24	70
4	10	24	92
5	15	24	86
6	20	24	84

^aIsolated yield. Mannich reaction; acetophenone (2.2 mmol benzaldehyde (2.0 mmol), aniline (2.0 mmol) in 5 mL of ethanol by Bi(NO₃)₃ catalyst at r.t.

The reactions were also tried with Bi(NO₃)₃ under solvent-free conditions and in ethanol without catalyst, but good yields were not obtained. The optimum molar ratio of aldehyde, amine, and acetophenone was investigated. It was shown that using ethanol as the solvent, aniline/benzaldehyde/acetophenone = 2: 2: 2.2 was optimum to obtain the desired product in good yields.

To investigate the extent and universality of this method, many different ketones, aromatic aldehydes and amines were performed for their Mannich reactions in ethanol at room temperature (see Table 3). Mannich reactions

occurred quite easily by reaction for the time as disclosed in Table 3 in the presence of 10 mol% of bismuth(III) nitrate to give the corresponding β-aminocarbonyl compounds in excellent yields (Table 3, entries 1–18). Numerous ketones and aromatic amines having methoxy and methyl para position and aromatic aldehydes with different substituents, such as para methyl, methoxy, hydroxyl and nitro proved to be suitable for the reactions. The effect of electron-deficient or donating bulky groups were very effective on the reaction yield. Our results are summarized in Table 3. To elucidate the structures of the synthesized compounds we used IR, NMR, MS, and elemental analysis.



Scheme 1. Direct, $\text{Bi}(\text{NO}_3)_3$ -catalyzed, Mannich reaction of various ketones, aldehydes and amines.

Table 3. Results of the obtained β -amino carbonyl compounds.

Entry	Products ^a	R_1, R_2	R_3	R_4	Yield ^b (%)	Mp (°C)	
						Found	Literature
1	4a	$\text{C}_6\text{H}_5, \text{H}$	H	H	92	165-166	166-168 (14)
2	4b	$\text{C}_6\text{H}_5, \text{H}$	CH_3	H	80	158.5-159.5	159 (15)
3	4c	$\text{C}_6\text{H}_5, \text{H}$	OCH_3	H	76	164.5-165.5	166-167 (16)
4	4d	$\text{C}_6\text{H}_5, \text{H}$	H	OH	90	195.2-196.2	181-182 (16)
5	4e	$\text{C}_6\text{H}_5, \text{H}$	H	OCH_3	88	155-156	153-156 (17)
6	4f	$\text{C}_6\text{H}_5, \text{H}$	H	NO_2	94	161.0-161.5	154-156 (18)
7	4g	4-Cyclo- $\text{C}_6\text{H}_{11}\text{C}_6\text{H}_4, \text{H}$	H	H	91	157.4-158.5	
8	4h	$\text{C}_6\text{H}_5, \text{CH}_3\text{C}=\text{O}$ (19)	H	H	87	108-109	
9	4i	$\text{C}_6\text{H}_5, \text{CH}_3\text{C}=\text{O}$ (20)	OCH_3	H	81	109-110	
10	4j	$\text{C}_6\text{H}_5, \text{CH}_3\text{C}=\text{O}$	H	OH	89	110.5-111.5	
11	4k	$\text{C}_6\text{H}_5, \text{CH}_3\text{C}=\text{O}$ (19)	H	OCH_3	85	107.5-108	
12	4l	$\text{CH}_3, \text{C}_2\text{H}_5\text{OC}=\text{O}$	H	H	78	105.5-106	106-107 (21)
13	4m	$\text{CH}_3, \text{C}_2\text{H}_5\text{OC}=\text{O}$	CH_3	H	70	138.5-139.5	137-139 (22)
14	4n	$\text{CH}_3, \text{C}_2\text{H}_5\text{OC}=\text{O}$	H	OH	79	137.2-138.2	137-139 (23)
15	4o	4- $\text{BrC}_6\text{H}_4, \text{CH}_3(\text{CH}_2)_{11}$	H	H	88	176.8- 178.1	

^aMannich reaction; aldehyde and amine (2 mmol) and ketone (2.2mmol) in 5 mL of ethyl alcohol and 10% mol $\text{Bi}(\text{NO}_3)_3$ as catalyst at room temperature. ^bIsolated yield.

In conclusion, we have improved an eco-friendly and high yield reaction for three-component Mannich reactions catalyzed by bismuth(III) nitrate, which is a practical method for the synthesis of β -aminocarbonyls. This method suggests numerous advantages, including good yields of the resulting compounds.

ACKNOWLEDGMENT

This work was supported by Scientific Research Projects Coordination Unit of Istanbul University. Project number: 57459.

REFERENCES

1. Ai T, Han J, Chen ZX, Li G. Chiral N-Phosphonyl Imine Chemistry: Asymmetric Synthesis of α -Alkyl β -Amino Ketones by Reacting Phosphonyl Imines with Ketone-Derived Enolates. *Chem Biol Drug Des.* 2009, 73, 203-208. doi:10.1111/j.1747-0285.2008.00771.x
2. Zhiani R, Nishaburi AT, Abedi F, Moradi M. A rapid and green method for synthesis of β -amino ketones (Mannich reaction) using an acid catalyst nano- SiO_2 . *Indian J. Fund. Appl. Life Sci.* 2014, 4: 779-784. www.cibtech.org/sp.ed/jls/2014/04/jls.htm

3. Srivastava BK, Kapadnis PB, Pandya P, Lohray VB. Novel Mannich ketones of oxazolidinones as antibacterial agents. *Eur. J. Med. Chem.* 2004, 39: 989-992. doi:10.1016/j.ejmech.2004.07.007.
4. Lutz Z, Orban K, Bona A, Mark L, Maasz G, Prokai L, Seress L, Lorand T. Mannich Ketones as Possible Antimycobacterial Agents, *Arch. Pharm. Chem. Life Sci.* 2017, 350: e1700102. doi:10.1002/ardp.201700102.
5. Hollosy F, Lorand T, Orfi L, Eros D, Keri G, Idei M. Relationship between lipophilicity and antitumor activity of molecule library of Mannich ketones determined by high-performance liquid chromatography, clogP calculation and cytotoxicity test. *J. Chromatogr. B.* 2001, 768: 361-368. doi:10.1016/S1570-0232(02)00004-1.
6. Loranda T, Kocsis B, Sohar P, Nagy G, Kispal G, Krane HG, Schmitt H, Weckert E. Synthesis and antibacterial study of unsaturated Mannich ketones. *Eur. J. Med. Chem.* 2001, 36: 705-717. doi:10.1016/S0223-5234(01)01264-8.
7. Filho JFA, Lemos BC, Souza AS, Pinheiro S, Greco SJ. Multicomponent Mannich reactions: General aspects, methodologies and applications, *Tetrahedron.* 2017, 73: 6977-7004. doi:10.1016/j.tet.2017.10.063.
8. Yi WB and Cai C. Mannich-type reactions of aromatic aldehydes, anilines, and methyl ketones in fluorous biphasic systems created by rare earth (III) perfluorooctane sulfonates catalysts in fluorous media. *J. Fluorine Chem.* 2006, 127: 1515-1521. doi:10.1016/j.jfluchem.2006.07.009.
9. Wang R, Li BG, Huang TK, Shi L, Lu XX. NbCl₅-Catalyzed one-pot Mannich-type reaction: three component synthesis of β-amino carbonyl compounds. *Tetrahedron Lett.* 2007, 48: 2071-2073. doi:10.1016/j.tetlet.2007.01.142.
10. Fujisawa H, Takahashi E, Mukaiyama T. Lewis base catalyzed Mannich-type reactions between trimethylsilyl enol ethers and aldimines. *Chemistry.* 2006, 12: 5082-5093. doi:10.1002/chem.200500821.
11. Rajput JK, Kaur G. Bi(NO₃)₃·5H₂O: An Efficient and Green Catalyst for Synthesis of 1,5-Benzodiazepines and β-Amino Carbonyl Compounds. *Asian J. Chem.* 2013, 25: 6545-6549. doi:10.14233/ajchem.2013.14353.
12. Ravikumar Naik TR, Bhojya Naik HS, Raghavendra M, Bindu PJ, Mahadevan KM. Synthesis of novel 1,5-benzothiazepine[7,6-b]-1, 8-naphthyridines under microwave irradiation via Mannich condensation. *J. Sulfur Chem.* 2007, 28: 589-595. doi:10.1080/17415990701625050.
13. Sheik Mansoor S, Aswin K, Logaiya K, Sudhan SPN. An efficient synthesis of β-amino ketone compounds through one-pot three-component Mannich-type reactions using bismuth nitrate as catalyst. *J. Saudi Chem. Soc.* 2015, 19: 379-386. doi:10.1016/j.jscs.2012.04.008.
14. Min W, Yan L, Zhigou S. Aluminium nitrate as an efficient and reusable catalyst for the three components one-pot Mannich reaction: Synthesis of α-amino carbonyl compounds *Indian. J. Chem., Sect. B: Org. Chem. Including Med. Chem.* 2010, 49: 1653-1656. http://hdl.handle.net/123456789/10734.
15. El-Sayed Mansour ME, El-Sadany SK, Kassem AA, Maksoud H. Aminolysis of para-substituted benzalacetophenones., *J. Chem. And Eng. Data.* 1989, 34: 368-370. doi:10.1021/je00057a030.
16. Hua L, Hang-yao Z, Hua-wu. Bismuth(III) chloride-catalyzed one-pot Mannich reaction: three-component synthesis of β-amino carbonyl compounds. *Tetrahedron Lett.* 2009, 50:6858-6860. doi:10.1016/j.tetlet.2009.09.131.
17. Abdghasem D, Afsaneh TN, Niloofar TH. Carbon-based Solid Catalyzed One-pot Mannich Reaction: A Facile Synthesis of β-Amino Carbonyl Compounds. *Bull. Korean Chem. Soc.* 2011, 32: 635-638. doi:10.5012/bkcs.2011.32.2.635.
18. Hai-Tang L, Yu-Ru K, Hong-Yun N, Li-Ming Y. Sulfamic Acid as a Cost-Effective and Recyclable Catalyst for β-Amino Carbonyl Compounds Synthesis. *J. Chin. Chem. Soc.* 2009, 56: 186-195. doi:10.1002/jccs.200900027.
19. Kozlov NS, Kiseleva SA, Buzykin BI. Reaktionen Aromatischer Azomethine Mit Benzoylacetone. *Zh. Org. Khim.* 1974, 10: 1487.
20. Kozlov NS, Kiseleva SA, Buzykin B. Catalytic reaction of azomethines with benzoylactone. *Tr. Perm. Sel.-Khoz. Inst.* 1971, 79: 13.

21. Neelakantan L, Hartung WH. α -Aminoalkanesulfonic Acids. *J. Org. Chem.* 1959, 24: 1943-1948. doi:10.1021/jo01094a029.
22. Wu M, Jing H, Chang T. Synthesis of β -amino carbonyl compounds via a Mannich reaction catalyzed by Salen Zn complex. *Catal. Commun.* 2007, 8: 2217-2221.
- doi:10.1016/j.catcom.2007.05.011.
23. Demirkol O, Akbaşlar D, Giray S, Barış AB. One-Pot Synthesis of Mannich Bases Under Solvent-Free Conditions. *Synth. Commun.* 2014, 44: 1279-1285. doi:10.1080/00397911.2013.853191.

SUPPORTING INFORMATION

Bi(NO₃)₃·5H₂O-catalyzed Mannich Reaction: A Potent Catalyst for Synthesis of β -Aminocarbonyl Compounds

Hasniye Yaşı^{1*}, and Kübra Demir

¹Istanbul University-Cerrahpaşa, Engineering Faculty, Chemistry Department, 34320 Avcılar, Istanbul, Turkey

²Istanbul University-Cerrahpasa, Institute of Science, Chemistry Division, Avcılar-Istanbul, Turkey

*Correspondence: hasniye@istanbul.edu.tr

1) Content	2
2) Experimental section and spectroscopic data of synthesized β -amino carbonyl compounds 4g	4
3) ^1H , ^{13}C NMR, IR and GC-MS spectra of 4j	6
4) ^1H , ^{13}C NMR, IR and GC-MS spectra of 4o	8

2. General procedure

The chemicals used in this study were commercially available from Merck and Aldrich and were used without further purification. The obtained compounds were purified by crystallization. ^1H and ^{13}C NMR (500 and 125 MHz, respectively) spectra were recorded using Me_4Si as the internal standard in CDCl_3 . Mass spectra were obtained on Thermo Finnigan LCQ Advantage MAX MS/MS spectrometer. FT-IR spectra were recorded on Bruker Vertex 70.

General procedure for the synthesis of β -amino carbonyl compounds

Ketone (2.2 mmol), aldehyde (2 mmol) and amine (2 mmol) and 10 mol % $\text{Bi}(\text{NO}_3)_3$ [11-13] were added to a one-necked round bottom flask. The reaction mixture was stirred vigorously with a magnetic stirrer at room temperature (r.t.) for the mentioned time. After reaction completion, EtOH and H_2O at the reaction-mixture was evaporated at ambient temperature. Then 60 ml of hot CH_2Cl_2 was added to dissolve the solid product. The catalyst was removed by filtration and the organic layer was washed twice with saturated NaHCO_3 solution, dried with Na_2SO_4 , and evaporated. The product was purified by recrystallization from an ethanol-acetone mixture (3/2, v/v) to afford the corresponding compounds.

Compounds (**4a-f**, **4h-i**, and **4k-n**) are known in the literature and their results are in accordance with the literature. The analytical and spectral data of the other products (**4g**, **4j**, and **4o**) so obtained were as follows:

Spectral Data

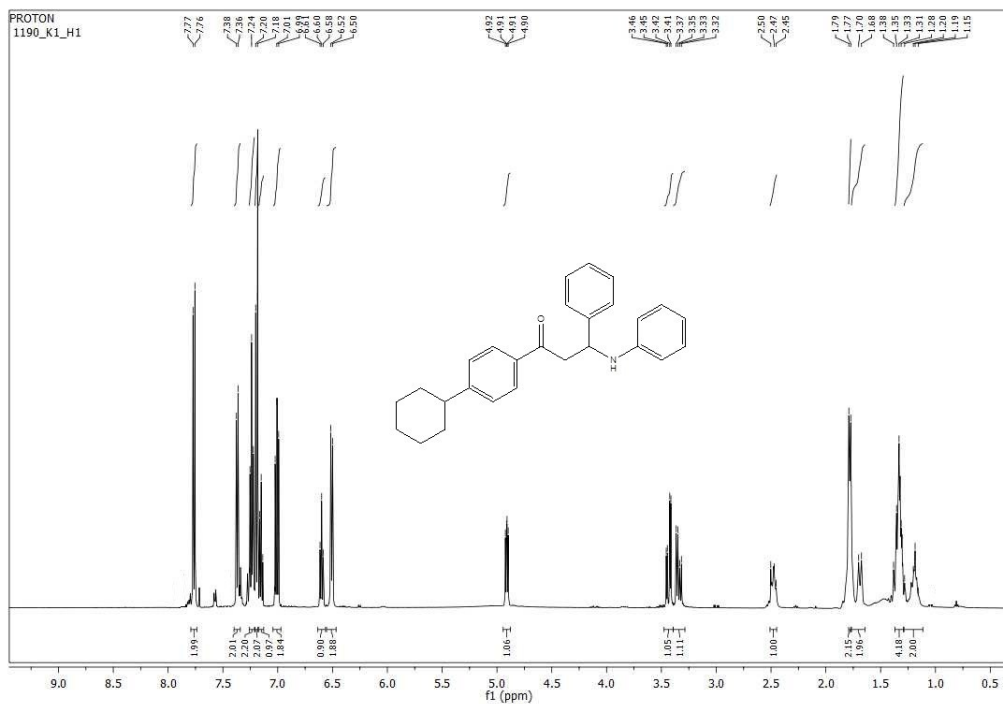


Figure S1. $^1\text{H-NMR}$ spectrum of compound **4g** (500 MHz, CDCl_3)

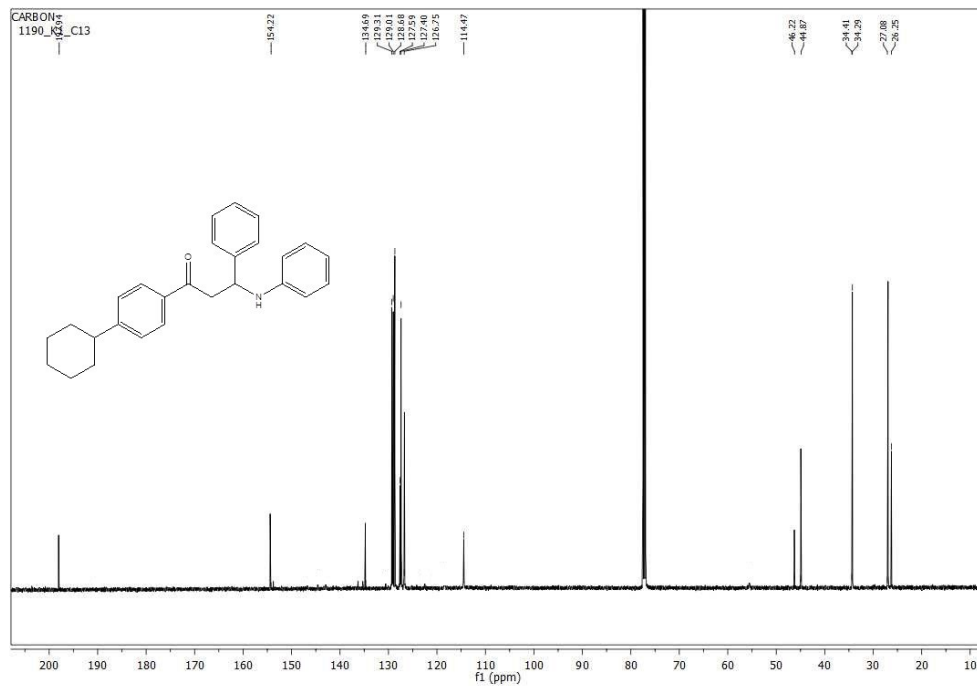


Figure S2. $^{13}\text{C-NMR}$ spectrum of compound **4g** (125 MHz, CDCl_3)

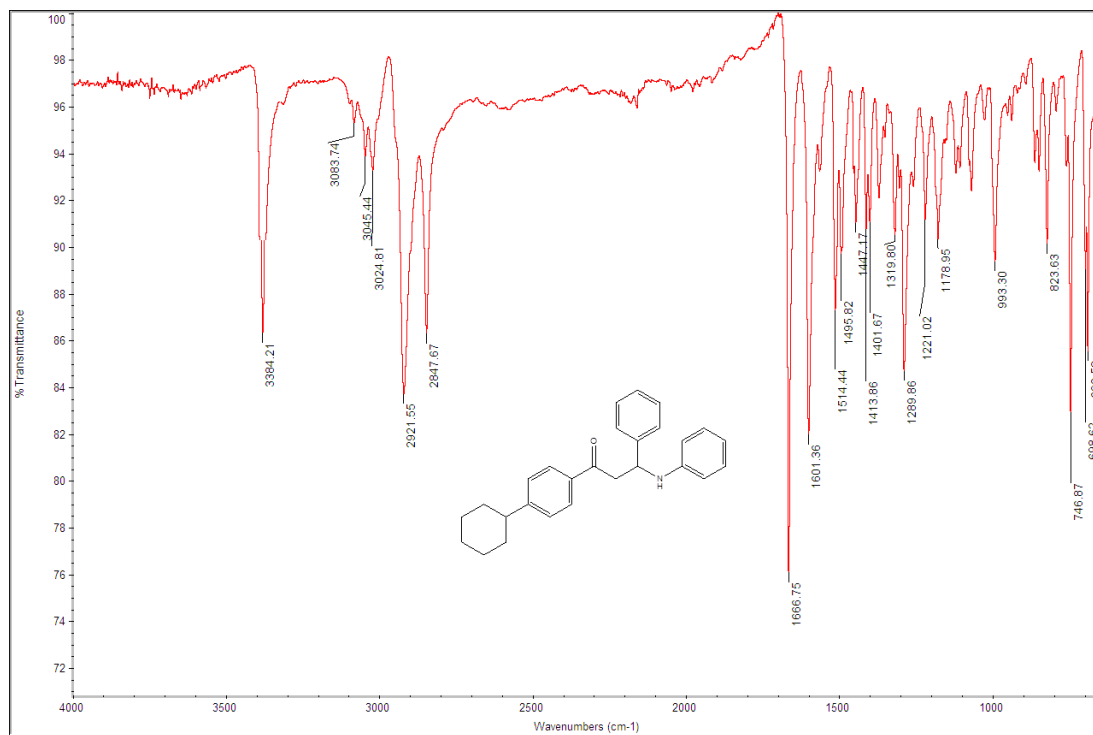


Figure S3. IR spectrum of compound **4g**

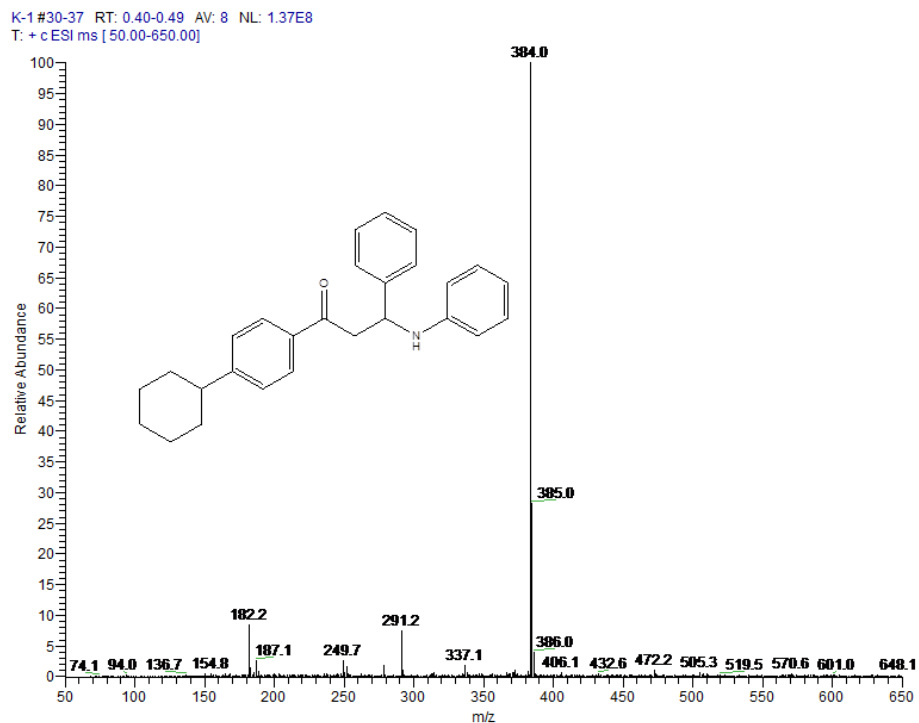


Figure S4. MS spectrum of compound **4g**

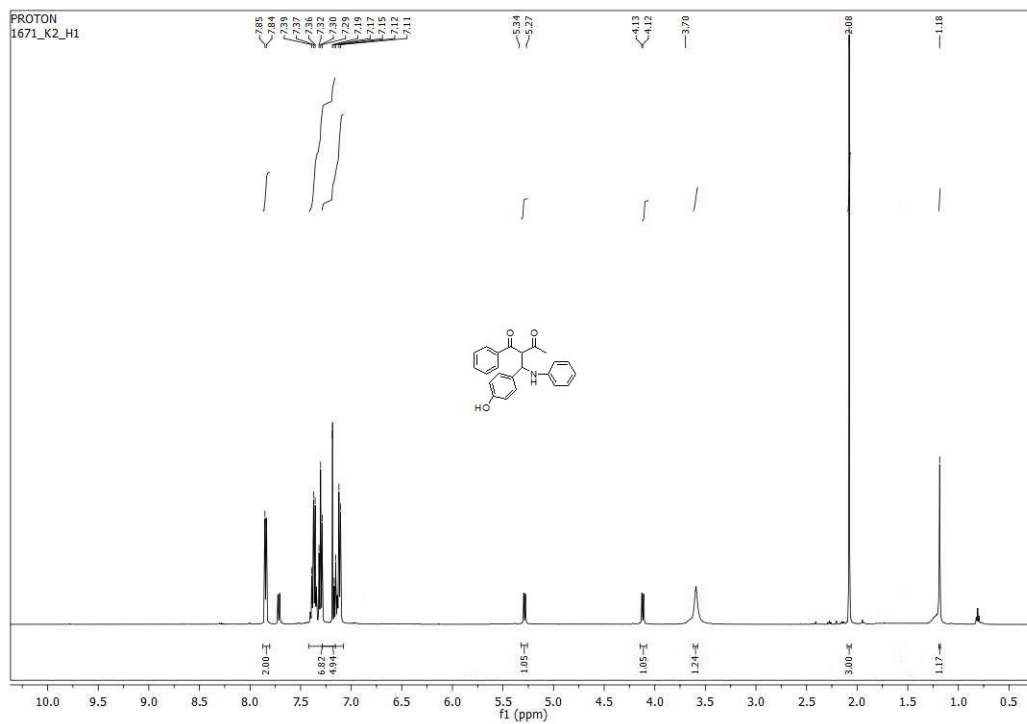


Figure S5. $^1\text{H-NMR}$ spectrum of compound **4j** (500 MHz, CDCl_3)

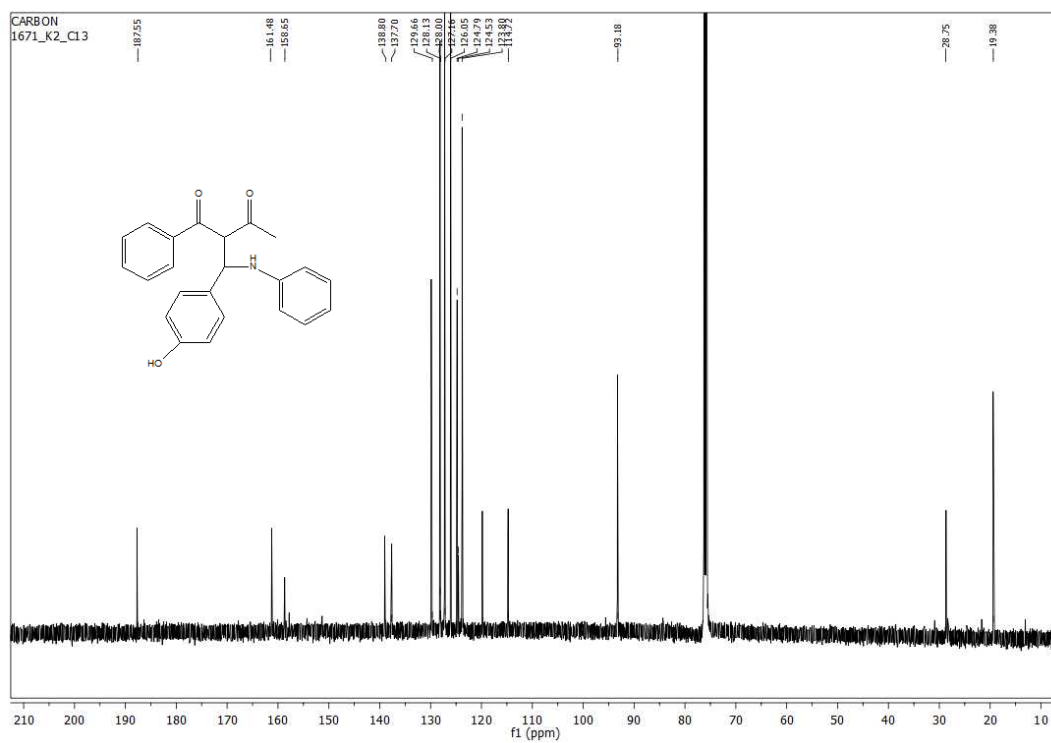


Figure S6. $^{13}\text{C-NMR}$ spectrum of compound **4j** (125 MHz, CDCl_3)

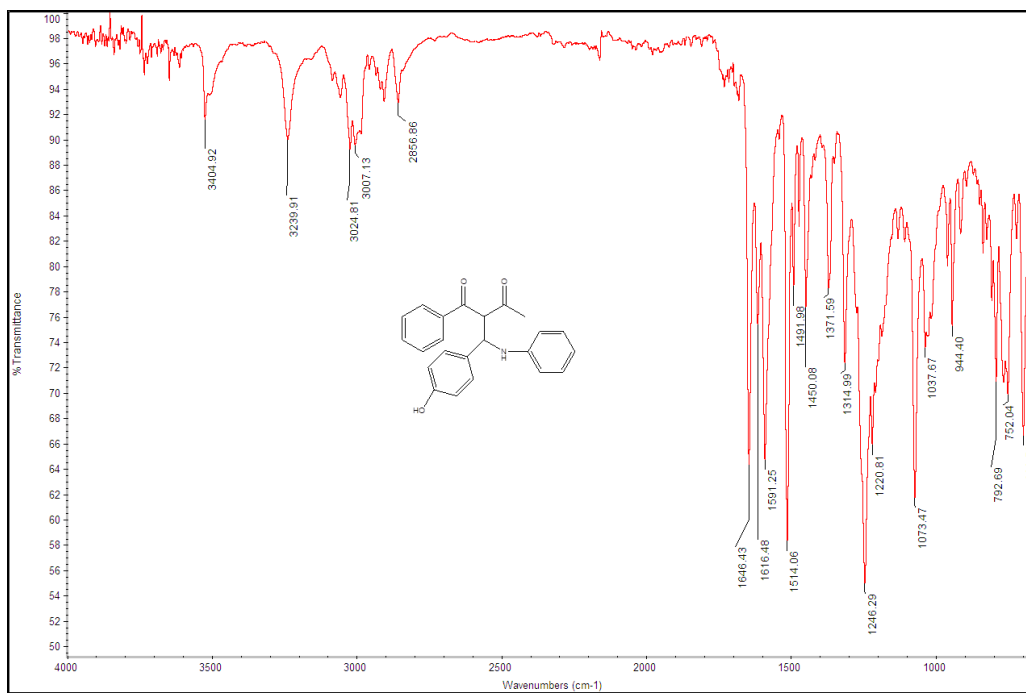


Figure S7. IR spectrum of compound 4j

K2 #146-148 RT: 4.02-4.05 AV: 2 NL: 4.52E6
T: + c ESI Full ms [50.00-2000.00]

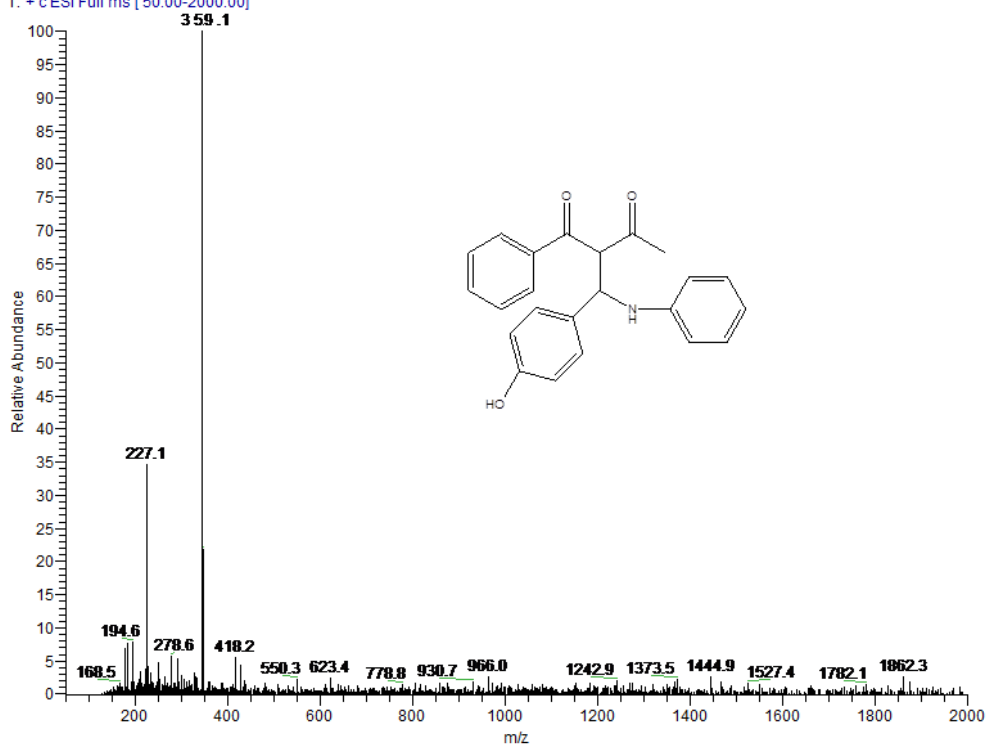


Figure S8. MS spectrum of compound 4j

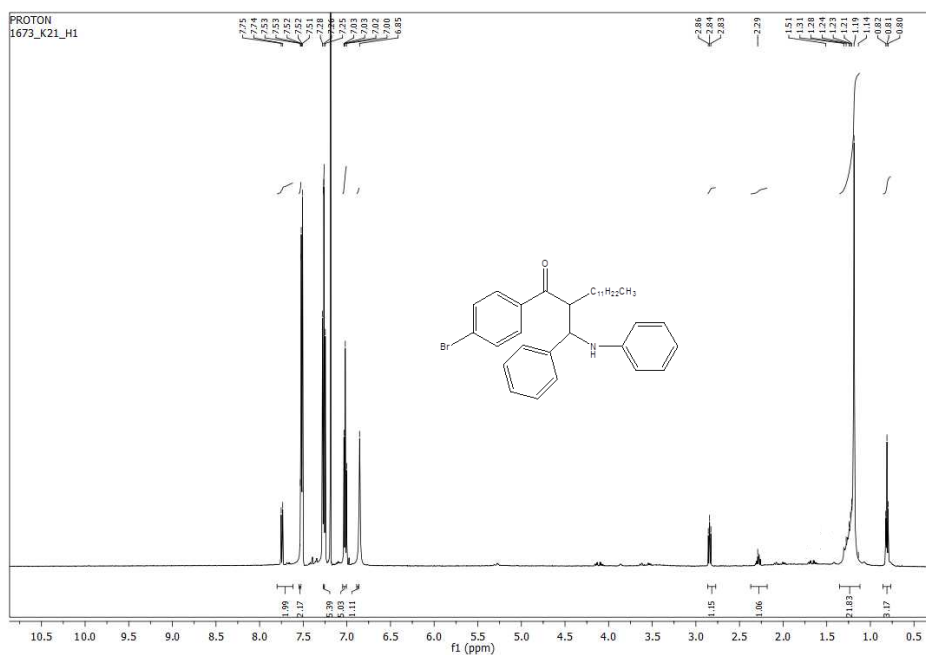


Figure S9. $^1\text{H-NMR}$ spectrum of compound **4o** (500 MHz, CDCl_3)

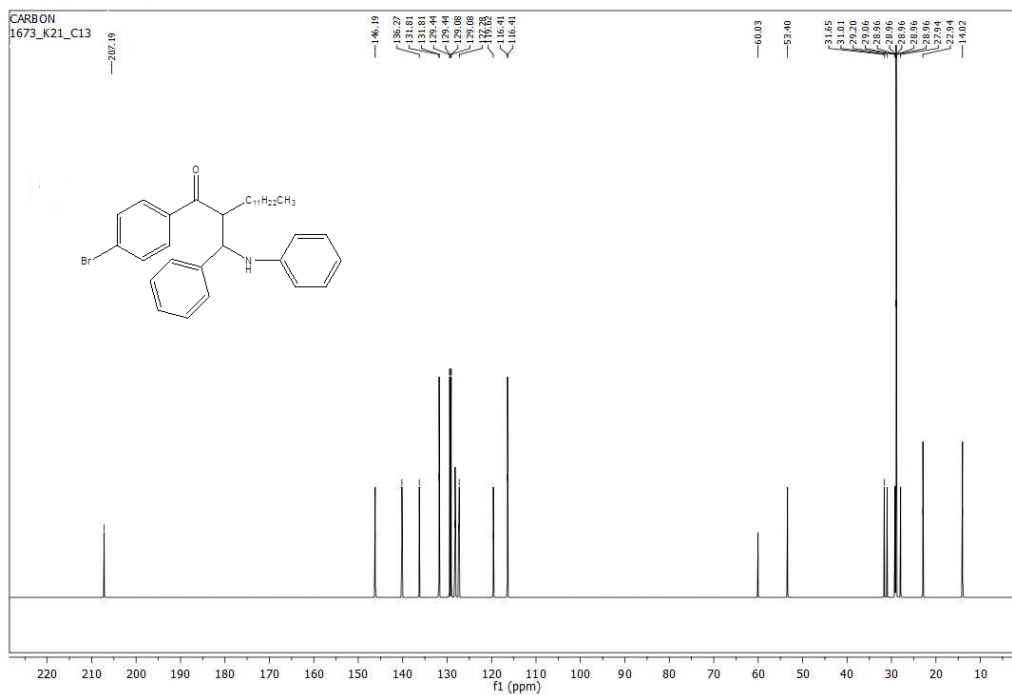


Figure S10. $^{13}\text{C-NMR}$ spectrum of compound **4o** (125 MHz, CDCl_3)

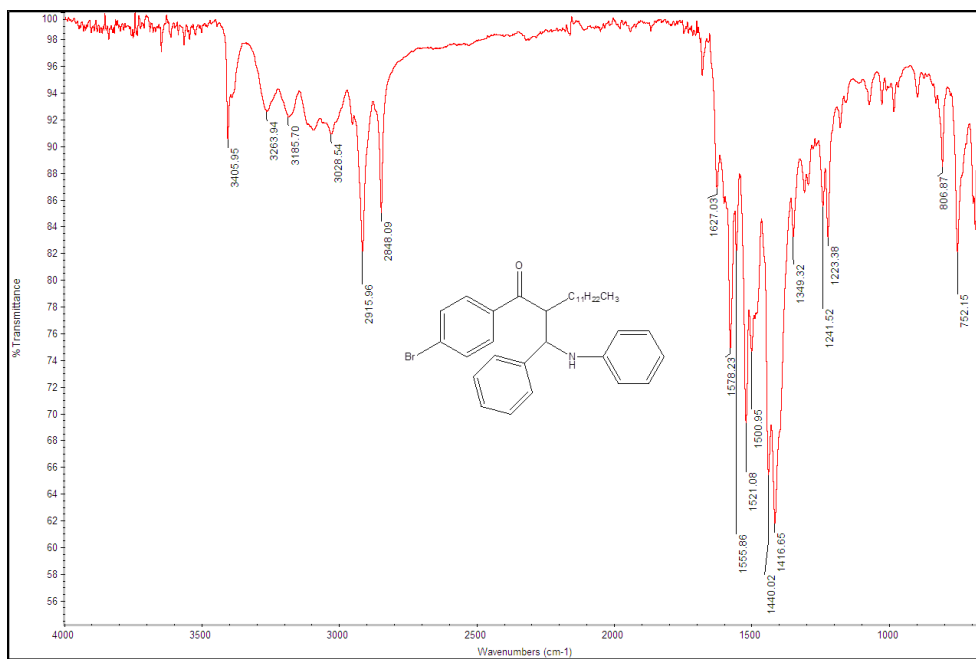


Figure S11. IR spectrum of compound 4o

K21-#248-252 RT: 4.23-4.30 AV: 5 NL: 3.39E6
T: + c ESI Full ms [50.00-1000.00]

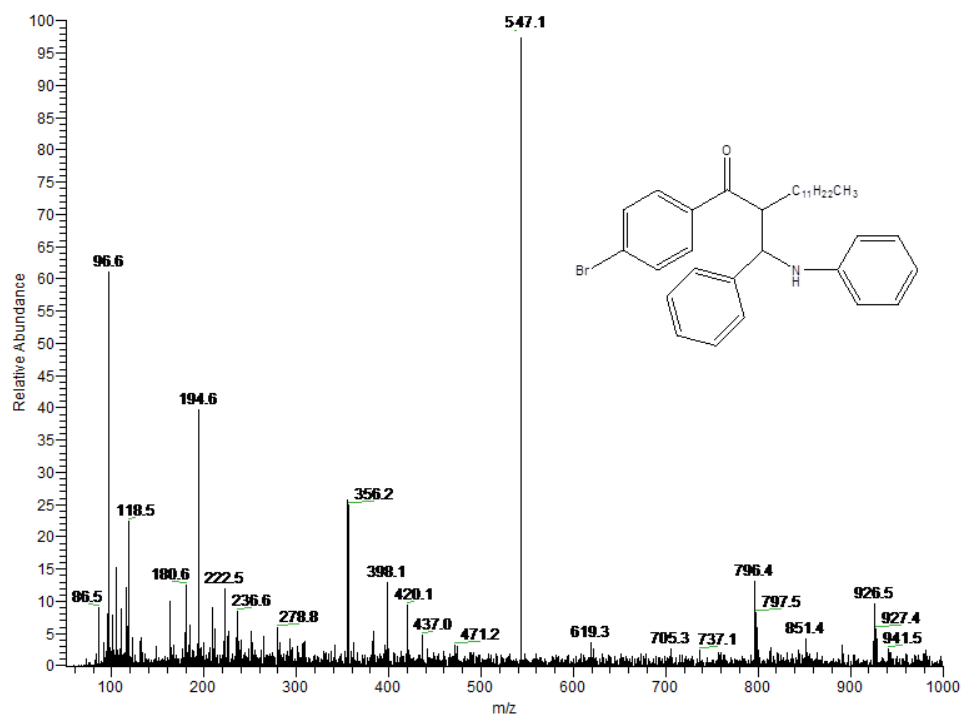


Figure S12. MS spectrum of compound 4o



Effect of Temperature on Stability of Lipid Microbubbles

Sevgi Kılıç*  

Department of Chemical Engineering, Izmir Institute of Technology, Urla, 35430-Izmir, TURKEY

Abstract: The effect of temperature on stability of lipid microbubble shell containing polyethyleneoxide-40-stearate (PEG₄₀St) as emulsifier was investigated. Microbubbles at 4 °C were subjected to different temperatures up to 48 °C (down-to-up) and it was found that both the number and the size of microbubbles remained unchanged in the population up to a certain time, so called "onset time". The onset time was about 6 hours at 10 °C, 2 hours at 20 °C and shorter at elevated temperatures, exhibiting an exponential decrease with increasing temperature. Once the onset time was reached, the number of microbubbles started to decrease and the average size of the population started to increase. Observation of single microbubbles on a constant temperature heating stage exhibited that each microbubble had its own onset time, with the smaller microbubbles vanishing earlier than the larger ones. The Langmuir monolayer studies showed that hydration degree of the emulsifier PEG chains decreased with temperature, causing them go through conformational changes and subsequently destabilization of the shell. By subjecting the freshly produced microbubbles directly to the desired temperatures in up-to-down fashion, more stable microbubbles were able to be produced, with their onset time increased 40% at 10 °C to 500% at 38 °C. Overall, the results suggest that the new strategies need to be developed to control the collapse process in the microbubble shell resulting from the conformational changes in the PEG chains of the emulsifier for the design of more stable microbubbles.

Keywords: Microbubble, ultrasound contrast agent, Langmuir monolayers, temperature, phospholipid, emulsifier, PEG conformations, stability

Submitted: July 19, 2019. **Accepted:** October 01, 2019.

Cite this: Kılıç S. Effect of Temperature on Stability of Lipid Microbubbles. JOTCSA. 2019;6(3):439–54.

DOI: <https://doi.org/10.18596/jotcsa.594219>.

*Corresponding author. E-mail: sevqikilic@iyte.edu.tr. Phone: +90-232-750 6647; Fax: +90-232-750 6645.

INTRODUCTION

Microbubbles, micron-size gas bubbles surrounded by a lipid-based monolayer shell, are contrast agents used in ultrasound to improve the image quality. Microbubbles are also used in targeted gene/drug delivery, metabolic gas transport, and hyperthermia therapy (1). Attachment of therapeutic agents to microbubbles has become one of the popular strategy to achieve more effective targeting, combined with diagnosis and therapy (2). The clinical application of microbubbles with a wide range of applications is however hampered by their restricted lifetime after their administration. Therefore, development of persistent and stable microbubbles has become one of the most promising fields in

medicine in order to enhance the therapeutic and diagnostic capabilities of ultrasound. Microbubble persistency is generally related to the dissolution of the gas core, which is associated with the shell permeation resistance (3-8). It is believed that the Laplace driven dissolution of gas core of lipid microbubbles causes changes in the shell structure through buckling and folding process, followed by the collapse of the shell leading to further dissolution of microbubbles (6, 9-14). However, although temperature can have important effect on the molecular orientation and arrangement of the components in a monolayer (15, 16), its effect on the shell microstructure has not been investigated truly. The studies mostly focused on temperature dependent behavior of microbubbles. For instance,

Mulvana et. al showed that commercial SonoVue® microbubbles exhibit a size dependent dissolution rate, with smaller size microbubbles dissolving at higher rates and increasing with increasing temperature at static and acoustically driven conditions (17). They also showed that SonoVue® microbubbles exhibit an increase in the mean bubble diameter of the population with increasing temperature and a decrease in bubble concentration. Through their investigations on the dynamic behavior of individual SonoVue® microbubbles, they demonstrated that the majority of the microbubbles oscillated approximately spherically at room temperature, while the same size bubbles oscillated more violently at body temperature (18). Swanson et al. monitored the change in average size of the population of oxygen microbubbles of both DSPC and DPPC with PEG₄₀St and observed that both microbubble type have a tendency to grow in size when stored at 4 °C, with the DPPC coated microbubbles exhibiting smaller change in the mean diameter (19). For the microbubbles composed of DPPC and PEG₄₀St, Farook et al reported that while the initial sizes of the microbubbles remained unchanged for almost 2.5 hours at room temperature, the mean size of the microbubbles decreased rapidly from 6.6 µm to 1.3 µm in less than an hour at the body temperature (20). Kwan et al monitored the dissolution behavior of a single microbubble composed of various phosphocholine lipids and PEG₄₀St as the emulsifier, and filled with SF₆ gas, in an air saturated solution and observed that the microbubbles with longer acyl chain length are more persistent at lower temperatures (5, 9). They reported that the use of different emulsifiers, for instance mDSPC-PEG₂₀₀₀ versus PEG₄₀St, did not significantly affect the dissolution behavior of the microbubbles (9). In all these studies, the less stable behavior of the microbubbles with increasing temperature was attributed simply to the changes in the physical properties of the phospholipid shell, which are believed to be determined by the strength of attractive hydrophobic and van der Waals interactions between the hydrocarbon tails of the phospholipid molecules (9, 11, 17, 21, 22). In this respect, considerable amount of research was carried out to investigate the effect of lipid hydrocarbon tail length on microbubble stability at different temperatures (9, 13, 14, 21). Unfortunately, the aforementioned studies still remain insufficient to enlighten the mechanism causing destabilization of the shell under temperature and to provide a roadmap for the design of more stable microbubbles. The study investigating the effect of cooling rate on microbubbles microstructure is very challenging, evoking that some other factors as well as hydrophobic and van der Waals interactions may be effective in the shell gas permeability (14). So far, no attention was paid to the role of temperature on emulsifier, which is the crucial component in microbubble formation and possesses bulky polyethylene glycol (PEG) chain. In

the present study, along with monitoring the microbubbles dissolution behavior at various temperatures, Langmuir monolayer measurements were performed to reveal the changes in the PEG chain of the emulsifier with temperature. The results showed that the conformational changes induced by temperature in the PEG chain of the emulsifier affect the packing density of microbubble shell and thus has important influence on destabilization of microbubbles.

MATERIALS AND METHODS

Materials

1,2-Distearoyl-sn-glycero-3-phosphocholine (DSPC) was purchased from Avanti Polar Lipids Inc (Alabaster, AL). Polyoxyethylene-40 stearate (PEG₄₀St), propylene glycol (PG) and chloroform were all purchased from Sigma-Aldrich (St. Louis, MO). All chemicals were used as received.

Preparation of Microbubbles

A mixture of DSPC and PEG₄₀St at a molar ratio of 9:1 was dissolved in chloroform. The solution was dried under nitrogen gas and kept in a vacuum oven at room temperature overnight to form completely dried lipid/emulsifier film. The resulting film was then hydrated for 2 hours in phosphate buffer saline (PBS)-propylene glycol (PG) solution mixed at volume ratio of 4:1 at 60 °C. The lipid/emulsifier mixture was first sonicated using a probe tip sonicator (Misonix, S4000, Newtown, CT) with the probe tip down in the solution to obtain well dispersed solution. The homogenous mixture was then sonicated continuously for 30 seconds with the tip of the probe at the interface of the air-aqueous solution to form microbubbles. The resulting suspension was diluted with cold PBS at 4 °C. After homogenization, the microbubble solution was aliquoted into 2-mL tubes. Free remaining lipids in the solution were removed via washing of microbubble mixture with cold phosphate buffer solution (PBS) and then centrifugation operated at 2000 rpm for 2 minutes. The infranatant part of the suspension consisting of residual lipids and vesicles were discarded. The resulting cake was re-suspended in the cold PBS and centrifuged again. To the final cake in each tube was added PBS:PG (4:1) mixture up to 1 mL volume. All tubes were combined in a large syringe to get a homogenous mixture and then the microbubble solution was aliquoted into small vials and stored at 4 °C. All analyses were performed on the next day following storage at 4 °C.

Effect of Temperature on Microbubble Stability

Temperature responses of a population of microbubbles were investigated at 4 °C, 10 °C, 20 °C, 30 °C, 38 °C and 48 °C. The microbubble solution was taken from the refrigerator at 4 °C and measured for the concentration and size distribution by optical microscopy. The microbubbles were then diluted to concentration of 3.5×10⁸ microbubble/ml

in a 2 ml tube with temperature equilibrated PBS buffer and then placed back into the same constant temperature water bath. 10 μL of the samples was withdrawn from the tubes at periodic time intervals and distributed on a thoma cell counting chamber to measure the size and concentration of the microbubble population by optical microscopy. Images of the microbubbles were captured using a digital camera attached onto an upright microscope (Olympus CH40) with a 10X objective. Image analysis was performed using ImageJ (NIH free software). In a separate study, 9:1 DSPC/PEG₄₀St microbubbles were produced in the same manner described above. But instead of washing with PBS at 4 °C, they were washed with PBS at the temperature to be tested and submerged in the constant temperature water bath for size and concentration measurements.

The changes in the diameter of individual microbubbles were also investigated over time using a temperature controlled hot stage at 38 °C by observing the same frame of microscope slide without cover slip for approximately 40 minutes (Carl Zeiss Axio Imager.M2 with long working distance 63X objective). Time lapse images were acquired using a high resolution CCD camera (Carl Zeiss AxioCam 506 mono) and analyzed by ImageJ software.

Langmuir Isotherms of Microbubble Shell Components

Langmuir trough (KSV minitrough, Finland) with two movable barriers was used to investigate the phase behavior of DSPC, PEG₄₀St monolayers and their mixture at different temperatures. The trough was thermostated at desired temperature using a circulating bath. The system was enclosed in a box to minimize possible contamination of air-monolayer-water interface and the disturbance of the monolayer by air currents. The trough was filled with ultrapure water with specific resistivity of $1.8 \times 10^7 \Omega \cdot \text{cm}$ produced by a Millipore purification system. Cleanness of the air-water interface was confirmed by closing and opening the barriers and ensuring that the surface pressure readings do not differ by more than $\pm 0.1 \text{ mN/m}$. The solutions of the pure components and the mixture in chloroform were prepared in screw cap septum vials at concentrations less than 1.0 mg/ml to avoid chloroform evaporation

and stored at 4 °C. Prior to spreading the solution, the sealed vial was taken from the refrigerator, homogenized using a bath sonicator and cooled down to room temperature under continuous stirring. The solution was withdrawn via a Hamilton microsyringe from the vial sealed tightly. The surface pressure-area (π -A) isotherms were obtained via symmetric compression of monolayers by the two barriers. A compression speed of 5 mm/min was used in all experiments. Each isotherm was repeated at least 4-5 times to make sure reproducibility of the isotherms. The same procedure was employed to monitor the relaxation behavior of the monolayers. The monolayers were compressed to the specified target pressure (30 mN/m and 40 mN/m) at constant temperature (20 °C and 38 °C) and then the surface pressure was set to zero and the surface pressure evolution was followed with time over a constant area of air-water interface.

RESULTS AND DISCUSSION

Preparation and Characterization of Microbubbles

Air-filled microbubbles were prepared by sonication method from the mixture of DSPC and emulsifier PEG₄₀St mixed at a molar ratio of 9:1, which is the microbubble formulation commonly used in the current literature (9, 13, 14, 23, 24). Sonication method was employed, which is the method used commonly for the production of microbubbles owing to its capability to provide fast production with low cost, but with some polydispersity (25). In this study, polydispersity of the microbubble solution enabled us to observe the microbubbles at different sizes at the same time. Figure 1.a shows optical microscope image of the microbubbles. Figure 1.b shows typical optical image captured under the microscope using a 10X objective and does Figure 1.c the processed micrograph created by the ImageJ program for concentration and size determination of the microbubbles. At least four images from different field of view were taken and analyzed for size and concentration measurements. As can be seen from the figures, the microbubbles have been achieved to be distributed quite homogeneously on the stage, allowing for determination of accurate number and size distribution of the microbubbles.

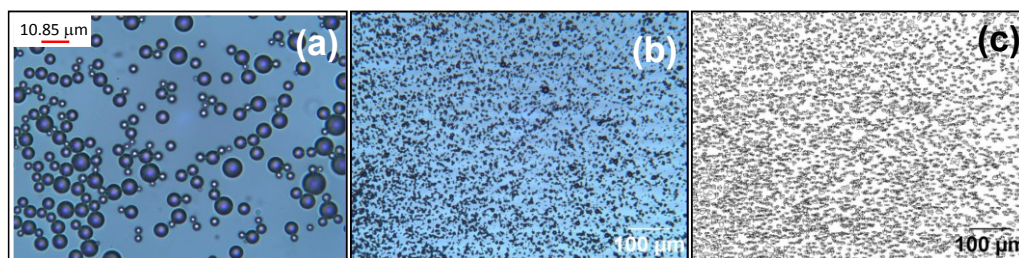


Figure 1. (a) An optical image of the microbubbles captured by 10X objective (b) Microscope image analysis microbubbles (c) image processed by ImageJ for size and concentration measurements.

Effect of Temperature on Microbubble Stability

The change in the concentration of the microbubbles with time at varying temperatures is shown in Figure 2.a. The numbers of the microbubbles counted at each time was determined using optical microscopy and normalized with respect to the initial number. As seen from the figure, while the microbubbles preserved their concentration at 4 °C, at the other temperatures, the microbubbles maintained their concentration only up to a certain time, called 'onset time', exhibiting a plateau. The extent of the plateaus became shorter with increasing temperature. Once the onset time was reached, both the number of the bubbles started to decrease (Figure 2.a) and the mean size of the population started to increase as can be seen from the

cumulative size distribution of the microbubbles at 20 °C as an example (Figure 2.b). As seen from the figure, the initial sizes of the microbubbles were less than 9 μm for the 90 % of the population and exhibited a size distribution up to 14 μm . The size distribution of the microbubbles shifted to the right over time, indicating that the average size of the microbubbles increased in the population while the number of microbubbles decreased. The initial $d_{50\%}$ size, which refers to the value where half of the population resides above this point, and other half resides below this point, was about 4 μm , and it increased to about 10 μm at the end of 8 hours. The microbubbles showed similar behavior at other temperatures as well (data not shown).

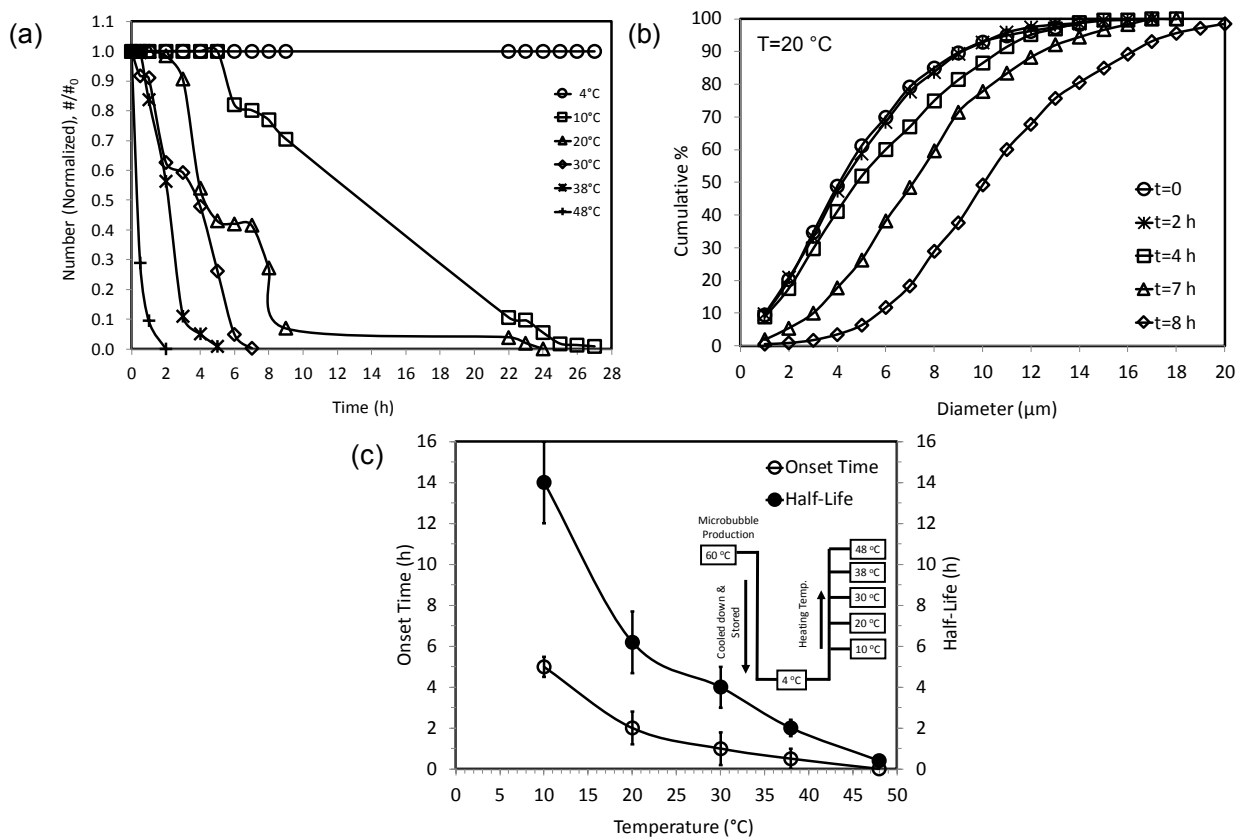


Figure 2. Change of (a) microbubble concentration (normalized with respect to initial concentration) (b) cumulative size distribution at 20 °C, (c) onset time and half-life of the 9:1 DSPC/PEG₄₀St microbubbles over time at different temperatures.

Figure 2.c summarizes the onset time as well as half-life of the microbubbles at different temperatures. Half-life refers to the time at which the number of microbubbles dropped to the half of their initial value. The error bars correspond to the arithmetic mean of at least three independent measurements. The microbubbles kept at 4 °C were observed to remain stable for much longer than the experimental time scale. The onset time was about 6 hours at 10 °C, 2 hours at 20 °C and it was shorter than an hour at elevated temperatures. Half of the population was

lost at 14 hours at 10 °C, 6 hours at 20 °C and in shorter than an hour at elevated temperatures. Both the onset time and half-life exhibited an exponential decrease with increasing temperature, similar to the observations seen with Sonovue[®] microbubbles (17) and SF₆ microbubbles coated with DSPC/PEG₄₀St and DSPC/DSPE-PEG₂₀₀₀ (9).

To understand the fate of the microbubbles in the population under the effect of temperature, the behavior of individual microbubbles was also investigated by observing the microbubble solution

on a temperature controlled hot stage without a coverslip at 38 °C. This allowed to monitor the behavior of individual microbubbles with different sizes at constant saturation and temperature. As seen from Figure 3, each microbubble had a characteristic onset time proportional to its initial size, exhibiting a continuous reduction in size beyond the onset time. The larger microbubbles maintained their initial size relatively for a longer period of time compared to the smaller ones. Evaluation of the

results for population of microbubbles and individual microbubbles together suggest that the smaller microbubbles vanish earlier in the population, leaving the larger ones behind in the suspension. This explains the reason behind the increase in the mean size of the population over time after the onset time. This result is in good agreement with the Epstein-Plesset theory, suggesting that microbubble dissolution accelerates once dissolution begins and ends with a complete disappearance (26).

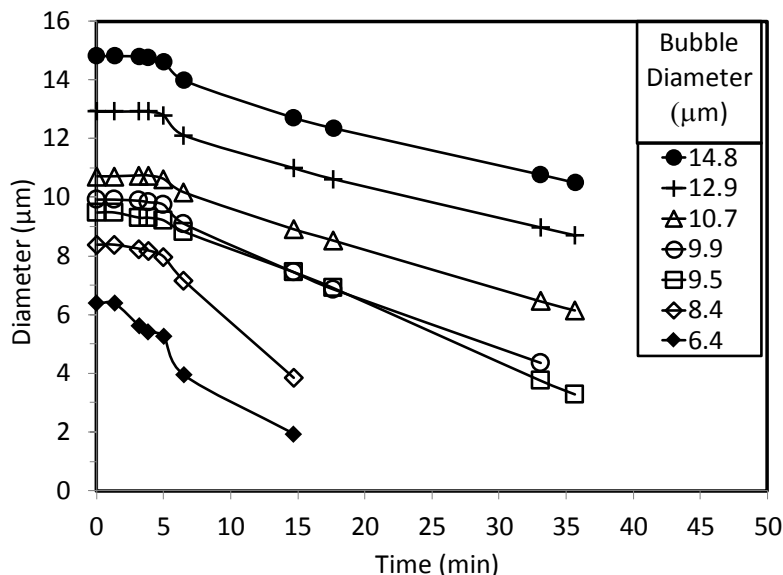


Figure 3. Changes in the diameter of individual 9:1 DSPC/PEG₄₀St microbubbles with different sizes over time at 38 °C. Microbubbles were monitored without a cover slip at constant saturation and temperature.

Langmuir Isotherms of Microbubble Shell Components

Investigations of temperature on microbubble shell is very complex because it is not only the molecules orientations change, but also the gas dissolution can change. Langmuir monolayer technique stands out as the ideal technique to eliminate the gas dissolution effect and investigate the effect of temperature only on molecules orientation at various compression states encountered during gas dissolution. Indeed, Langmuir monolayers composed of microbubble shell components are considered as a two-dimensional "skin" of the microbubble shell (27) and therefore the technique has already been used in several studies as an experimental tool to

investigate microbubble shell characteristics (27-29). The technique has also been used to reveal the morphological changes in the microbubble shell with compression using the Langmuir trough in combination with fluorescence microscopy (9, 13, 14). The Langmuir isotherms of DSPC/PEG₄₀St mixture as well as the pure components were acquired at different temperatures (Figure 4). The Langmuir isotherms of DSPC is illustrated at two different temperatures, being in a good agreement with the previously published literature (30). The isotherm for DSPC at 24 °C showed a steep rise at about 55 Å²/molecule and an extended behavior at 40 °C. However, in the low compressibility region (below ~47 Å²/molecule), the isotherm at 40 °C located to the left of the one at 24 °C.

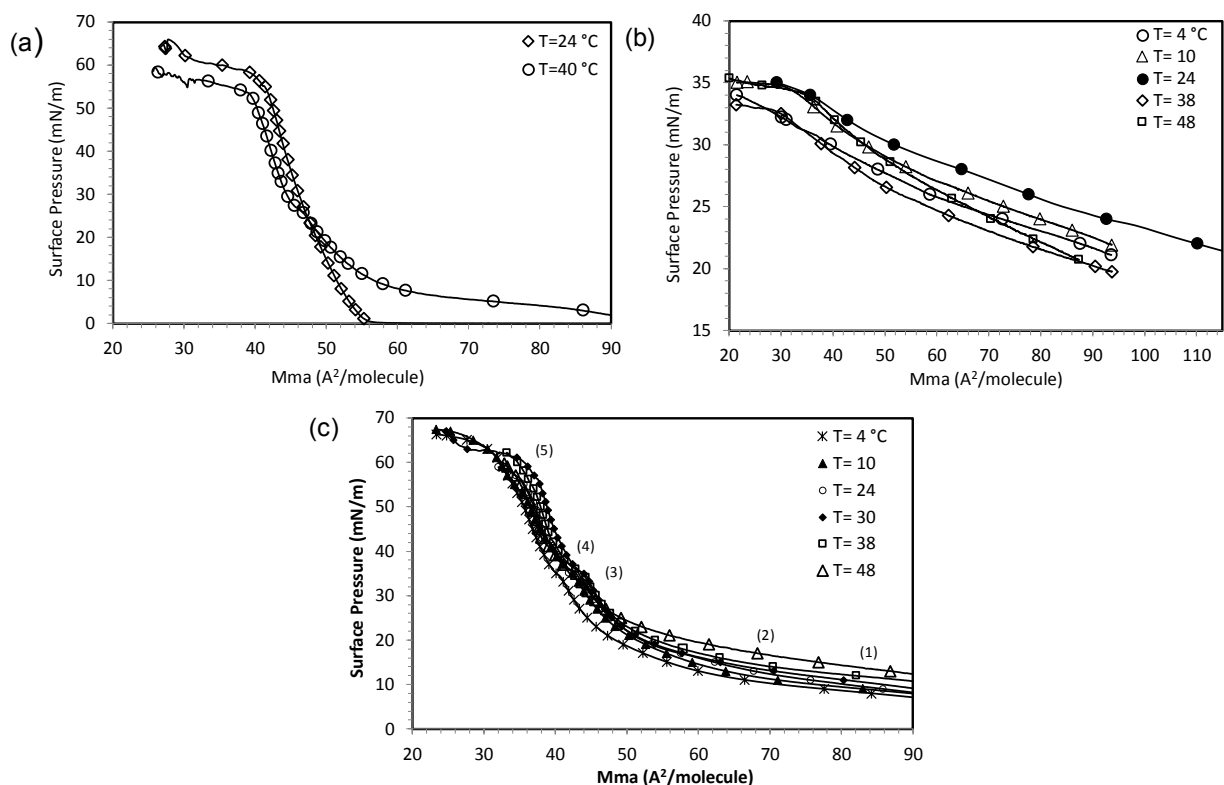


Figure 4. Langmuir isotherms of (a) DSPC, (b) PEG₄₀St (c) 9:1 DSPC/PEG₄₀St mixture at different temperatures. The numbers in figure (c) refers to the stage of the monolayer molecules orientation/organization depicted in Figure 5.

In comparison to DSPC monolayer, PEG₄₀St molecules resulted in much larger surface pressures in mean molecular areas larger than ~ 55 A²/molecule, exhibiting maximum surface pressures of only 33-35 mN/m depending on the temperature, known as collapse pressure (13). The isotherms shifted to the right with increasing temperature from 4 °C to 24 °C. With further increase in temperature to 38 °C, the isotherm moved to the far left of all isotherms. Similar to PEG₄₀St monolayer, in the high compressibility region (above 50 A²/molecule), the mixture isotherm shifted to the right with increasing temperature, exhibiting an extended behavior. All isotherms exhibited a plateau at around 33-35 mN/m, with distinct changes at 38 °C and 48 °C, corresponding to squeeze out of the emulsifier molecules from the monolayer (13). However, in the low compressibility region where intermolecular interactions are more dominant (below about 43 A²/molecule), the isotherms exhibited extended behavior with increasing temperature up to 30 °C and then shifted towards left with further increase in temperature. The numbers in Figure 4.c refers to the molecular organization state of the monolayer depicted in Figure 5.

The mean molecular areas of the isotherms at different temperatures were extracted from the Langmuir isotherms and plotted at different surface pressures to ease the visualization (Figure 6). In

contrast to the insignificant changes in DSPC molecules, the changes in the mean molecular area of the pure emulsifier molecules with temperature were very prominent at all surface pressures. PEG₄₀St monolayer exhibited a capricious behavior with temperature, increasing first and then decreasing followed by an increase again at 48 °C at all surface pressures. Similar behavior was observed also with the mixture. A steady increase in mean molecular area with temperature was observed for the mixture at surface pressures less than about 35 mN/m, most likely because of the PEG₄₀St molecules not being squeezed out yet. However, above this surface pressure, the area per molecule increased with temperature up to 30 °C and then decreased again with further increase in temperature, exhibiting more distinct changes with increasing surface pressures.

In Langmuir monolayers, higher surface pressures are observed if adsorbed molecules pack more densely at the air-water interface, i.e. possessing smaller mean molecular areas. However, in this study, achievement of the same surface pressure at higher mean molecular areas with increasing temperature can be attributed to the adsorption of increasing mass of the molecules at the interface, which can only be explained by 'curling up' of the PEG chain of the emulsifier towards the gas-liquid interface. The observed effect is more pronounced in

pure emulsifier monolayer because the mixture contains only 10% of the emulsifier. Migration of the PEG chains of the emulsifier towards the gas-liquid

interface indicates temperature dependent miscibility of PEG chains with water.

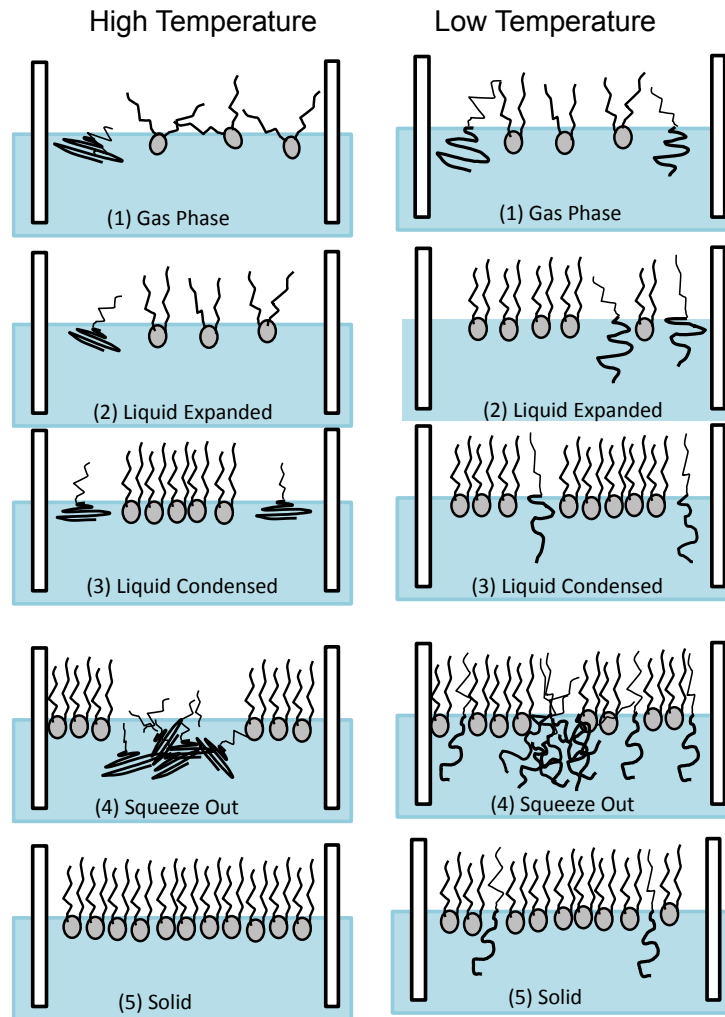


Figure 5. A cartoon depicting conformational changes and molecular organization of the microbubble shell component at various compression stages of the monolayer (as shown in Figure 4.c), mimicking the microbubble shell undergoing gas dissolution at low and high temperatures. Note that, PEG chains are more in extended into aqueous phase at lower temperatures while they curl up more towards the interface at higher temperatures.

Indeed, the interaction of ethylene oxide polymers with water occurs by means of hydrogen bonding, and the strength of the hydrogen bonds diminishes with temperature, reducing the miscibility of the PEG chains with water (31-33). Depending on the degree of miscibility, PEG chains acquire different conformations at the interface (30, 34), as depicted in Figure 6.b. Hence, the steady increase in the mean molecular area of the emulsifier and the mixed monolayer with increasing temperature at all surface pressures is the clear indication of decreased

miscibility of PEG chains with water, indicating migration of the PEG chains towards the interface. The further decrease in the mean molecular areas indicates the local collapse of the monolayer to relieve the stress accumulated at the interface due to excessive accumulation of the PEG chains and thus increased repulsive forces between them (35). The observed effect diminished with increasing surface pressure due to reduced intermolecular spacing and associated squeeze out of the emulsifier from the interface.

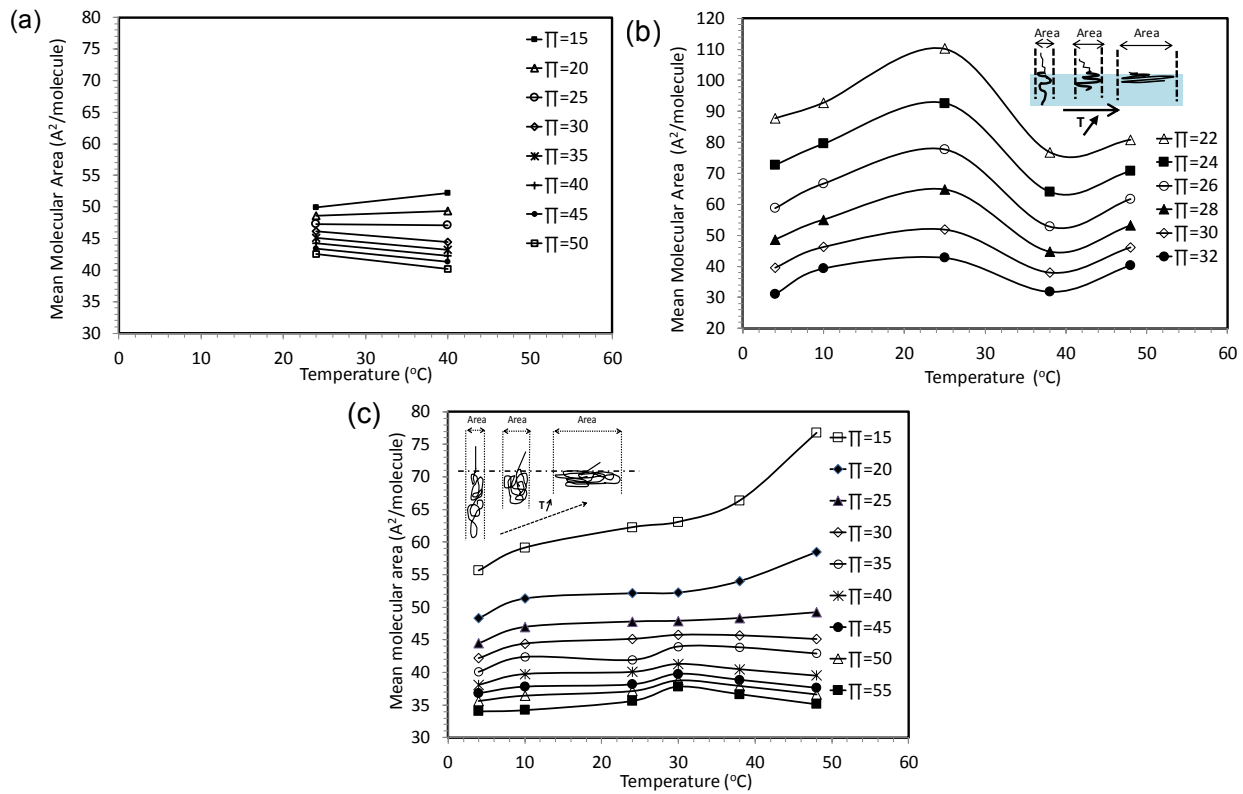


Figure 6. Change in the mean molecular area of (a) DSPC, (b) PEG₄₀St, (c) 9:1 DSPC/PEG₄₀St mixed monolayer at different temperatures and surface pressures. The inset in figure (b) shows the conformational changes in the PEG chain of the emulsifier with temperature due to its reduced miscibility with water.

The response of the Langmuir monolayer to increased lateral interactions at constant temperature can be considered similar to the behavior of microbubble shell undergoing various degrees of compression under gas dissolution at that temperature. In order to further investigate the effects of conformational changes and increasing lateral interactions (i.e. collapse) on the microbubble shell, monolayer relaxation measurements were carried out by monitoring changes in the surface pressure of the monolayer at constant mean molecular area with time. Monolayer relaxation occurs because of the compressed monolayer normally not being in the thermodynamic equilibrium when the surface pressure is higher than the equilibrium surface pressure (35, 36). Monolayer relaxation behavior of the mixed monolayer was monitored at two different surface pressures (below and above the collapse pressure of the emulsifier) and at two different temperatures (20 °C and 38 °C). The mixture isotherms showed that the surface pressure of approximately 33-35 mN/m is the collapse pressure of the emulsifier (Figure 4), in agreement with the published literature (13). As

seen in Figure 7, at 20 °C, the monolayer compressed to 40 mN/m relaxes much more slowly than the monolayer at 30 mN/m (compare curves b and c). Because the PEG chains acquire more extended conformation into the subphase at low temperatures, during the compression of the monolayer to higher surface pressures, some portion of the emulsifier molecules become miscible with DSPC and/or trapped within DSPC domains even if the remaining portion undergoes phase separation and squeeze out, as depicted in Figure 5. Moreover, in contrast to the monolayers compressed to 30 mN/m, the initial fluctuations (see the inset in Figure 7) observed in the surface pressure of the monolayers compressed to 40 mN/m at both temperatures indicates the collapse (exclusion) of excessive emulsifier molecules, remaining temporarily associated to the surface and reinserting, but ultimately collapsing and leaving a more stable DSPC-rich monolayer behind (see Figure 5), as suggested elsewhere (36-38). The molecules in more ordered and rigid domains is known to collapse irreversibly (do not reinsert) (38).

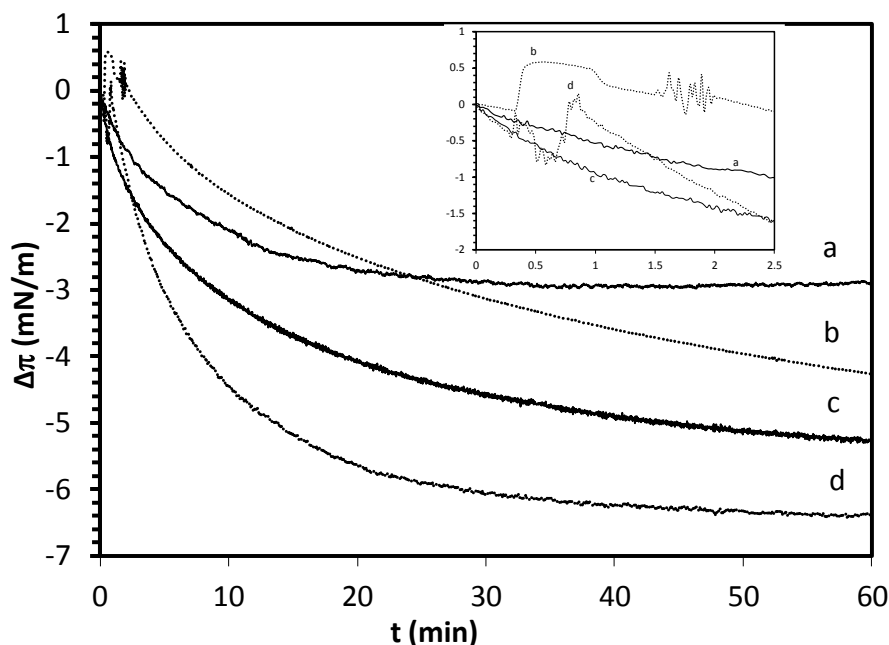


Figure 7. Change in surface pressure (π) of 9:1 DSPC/PEG40 St mixed monolayer with time at different temperatures and target surface pressures (a) $\pi=30$ mN/m and $T=38$ °C, (b) $\pi=40$ mN/m and $T=20$ °C, (c) $\pi=30$ mN/m and $T=20$ °C, (d) $\pi=40$ mN/m and $T=38$ °C. The inset shows the initial fluctuations during 2.5 minutes.

In contrast to the monolayer at low temperature, initial decrease in the surface pressure of the monolayers compressed to 40 mN/m is much higher at 38 °C. This is because PEG chains become more hydrophobic, with higher portion of the PEG chains migrating to the interface and creating larger size fluid-like domains. As a result, the steric hindrance for accommodation of bulky PEG chains at the interface between the hydrocarbon tails of DSPC becomes much greater at higher temperatures (Figure 5). Moreover, the cohesive interactions between the hydrocarbon tails pinning the emulsifier molecules to the interface get weaker at higher temperatures to compensate for the steric repulsions between the bulky PEG chains. As a result, created fluid-like disordered domains with larger size are more prone to collapse, resulting in decrease in surface pressure at higher rates. Equilibration of the monolayer in shorter time (about 35 min) in the case of higher temperature is also another indication for the exclusion of the emulsifier from the monolayer at a faster rate, leaving behind a DSPC rich monolayer.

Translation of these results to microbubbles mean that during low temperature gas core dissolution, emulsifier molecules, if not all, are trapped between DSPC molecules and some remain surface-bound upon collapse. Repetitive reinsertion of the emulsifier followed by collapse alleviates surface deformation, inhibiting gas dissolution and resulting in an onset time during microbubble dissolution. Surface deformation goes with simultaneous collapse and in-plane reorganization of the molecules (6, 9).

Recalling that no microbubble formation is possible without the emulsifier (10, 13, 39), the microbubble shell disintegrates when the emulsifier content decreases below a 'critical' value in the monolayer. During high temperature dissolution however, the lateral distance at the interface decreases at much higher rates under the combined effect of accumulation of more PEG chains at the interface and accelerated gas core dissolution. This results in the shell to undergo collapse with the loss of PEGylated emulsifier from the interface and disintegration at much faster rate.

In a separate study, the freshly prepared microbubbles were washed with the PBS at the target temperatures and tested immediately. The onset time curve for the microbubbles cooled down directly to the target temperature located above the curve for the microbubbles exposed to elevated temperatures from 4 °C (Figure 8). It was observed 40 % increase in the onset time of microbubbles at 10 °C, while 500% at 38 °C. This result suggests that DSPC and emulsifier molecules are initially adsorbed around the gas bubble up to an equilibrium surface value, then upon cooling down to lower temperatures, PEG chains undergo extension into the aqueous phase due to increased hydrophilicity with decreasing temperature while the gas bubbles go to compression at the same time. Apparently, extension of the polymer chains into the aqueous phase created the space needed for the condensation of the molecules around the gas bubble while the surface of the microbubble shell was reaching a new equilibrium surface value. As a result, the emulsifier

molecules were retained in the microbubble shell in extended conformation into the aqueous phase. This argument is also in good agreement with the observed microbubble shell morphology changes with cooling rate reported elsewhere (13, 14). In those studies, formation of larger dark domains surrounded by emulsifier-rich continuous phase (rich-in fluorophore and therefore brighter) during slow cooling process indicates entrapment of more emulsifier molecules between condensed phase

DSPC molecules (deficient in fluorophore and therefore darker) as results of PEG chains enabling to have enough time to extend into the aqueous phase and mix with condensed DSPC molecules, as discussed above. We also showed that conformational changes in the PEG chain of the emulsifier can be controlled by increasing the PEG₄₀St content in the formulation, leading to production of more stable microbubbles (40, 41).

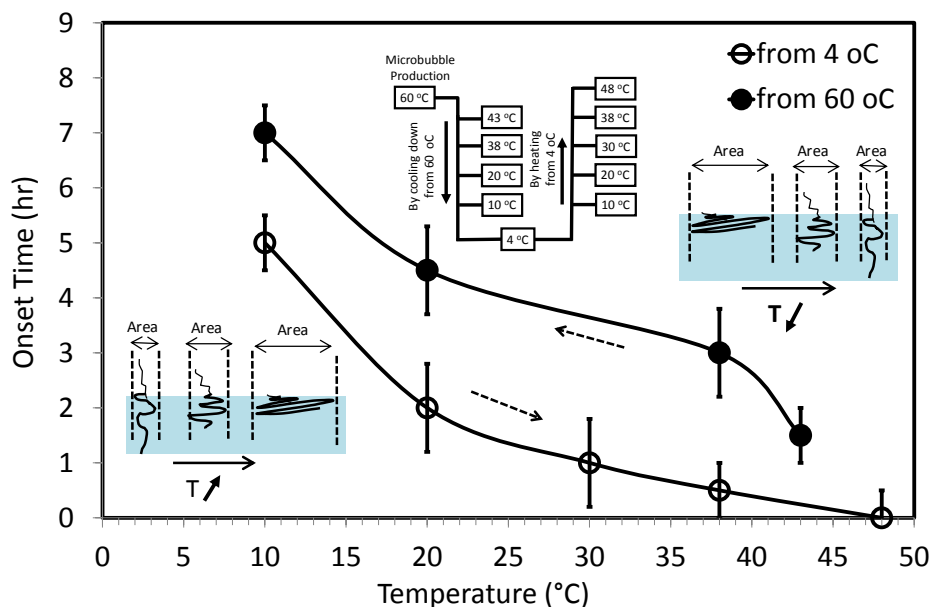


Figure 8. Comparison of the onset time of 9:1 DSPC/PEG₄₀St microbubbles for two cases. In the first case (open circles), the microbubbles were cooled down to 4 °C, and then exposed to elevated temperatures. In the second case (closed circles), the microbubbles were directly cooled down from elevated temperature to target temperature and tested immediately.

CONCLUSIONS

This study demonstrated that the conformational changes induced by temperature in the PEG chain of the emulsifier have important influence on destabilization of microbubbles. Upon their production, microbubbles are usually refrigerated and then exposed to higher temperatures for administration and/or laboratory investigations. Langmuir isotherms and surface pressure relaxation measurements demonstrated that PEG chain of the emulsifier became predominantly hydrophobic with increasing temperature, curling up towards the air-water interface. Accordingly, surface deformations initiates on the microbubble shell. With the initiation of surface deformations and subsequently gas dissolution, microbubble shell undergoes compression, causing lateral distance between the shell components to decrease. At the point where the monolayer exceeds the equilibrium surface pressure value, the shell/monolayer undergoes collapse mostly in the emulsifier rich regions, as evidenced by the reinsertions (i.e. fluctuations) in the monolayer relaxation experiments. Repetitive reinsertion of the emulsifier gives rise to the onset time, which is a

period of time during which the microbubbles preserve their stability and then exhibit a decrease in total number by earlier disappearance of the smaller microbubbles from the population. When combined with the gas dissolution at a faster rate at higher temperatures, the more hydrophobic the PEG chains, the more the surface deformations, resulting in more destructive collapse of the monolayer and lower stability of microbubbles. It was shown that microbubble stability can be improved by controlling the conformational changes in the PEG chain of the emulsifier by cooling down the microbubbles to desired temperature upon their production. As we have shown before, the another way to control conformational changes in the PEG chain of the emulsifier is to increase the PEG₄₀St content in the formulation (40, 41). Overall, the results suggest that the effect of the conformational changes induced by temperature in the PEG chain of the emulsifier should be taken into account for the design of more stable microbubbles.

ACKNOWLEDGEMENTS

The author would like to thank The Scientific and Technological Research Council of Turkey (TUBITAK) for the financial support through the project number of 109M494. The author also would like to thank Elif Seniz Bolukcu and Emine Aysu Sagdic for their help in part of the experiments.

REFERENCES

1. Paefgen V, Doleschel D, Kiessling F. Evolution of contrast agents for ultrasound imaging and ultrasound-mediated drug delivery. *Front Pharmacol.* 2015;6.
2. Lentacker I, Geers B, Demeester J, De Smedt SC, Sanders NN. Design and Evaluation of Doxorubicin-containing Microbubbles for Ultrasound-triggered Doxorubicin Delivery: Cytotoxicity and Mechanisms Involved. *Molecular Therapy.* 2010;18(1):101-8.
3. Borden MA, Longo ML. The dependence of lipid-coated microbubble dissolution behavior on acyl chain length. *Biophys J.* 2002;82(1):35a-a.
4. Garg S, Thomas AA, Borden MA. The effect of lipid monolayer in-plane rigidity on in vivo microbubble circulation persistence. *Biomaterials.* 2013;34(28):6862-70.
5. Kwan JJ, Borden MA. Lipid monolayer dilatational mechanics during microbubble gas exchange. *Soft Matter.* 2012;8(17):4756-66.
6. Pu G, Borden MA, Longo ML. Collapse and shedding transitions in binary lipid monolayers coating microbubbles. *Langmuir.* 2006;22(7):2993-9.
7. Kabalnov A, Klein D, Pelura T, Schutt E, Weers J. Dissolution of multicomponent microbubbles in the bloodstream: 1. Theory. *Ultrasound Med Biol.* 1998;24(5):739-49.
8. Borden MA, Longo ML. Oxygen permeability of fully condensed lipid monolayers. *J Phys Chem B.* 2004;108(19):6009-16.
9. Kwan JJ, Borden MA. Lipid monolayer collapse and microbubble stability. *Advances in Colloid and Interface Science.* 2012;183:82-99.
10. Shen Y, Powell RL, Longo ML. Interfacial and stability study of microbubbles coated with a mono stearin/monopalmitin-rich food emulsifier and PEG40 stearate. *Journal of Colloid and Interface Science.* 2008;321(1):186-94.
11. Shen YY, Powell RL, Longo ML. Influence of the dissolution rate on the collapse and shedding behavior of monostearin/monopalmitin-rich coated microbubbles. *Langmuir.* 2008;24(18):10035-40.
12. Kwan JJ, Borden MA. Microbubble Dissolution in a Multigas Environment. *Langmuir.* 2010;26(9):6542-8.
13. Borden MA, Pu G, Runner GJ, Longo ML. Surface phase behavior and microstructure of lipid/PEG-emulsifier monolayer-coated microbubbles. *Colloid Surface B.* 2004;35(3-4):209-23.
14. Pu G, Longo ML, Borden MA. Effect of microstructure on molecular oxygen permeation through condensed phospholipid monolayers. *Journal of the American Chemical Society.* 2005;127(18):6524-5.
15. Petrache HI, Dodd SW, Brown MF. Area per lipid and acyl length distributions in fluid phosphatidylcholines determined by H-2 NMR spectroscopy. *Biophys J.* 2000;79(6):3172-92.
16. Kucerka N, Nieh MP, Katsaras J. Fluid phase lipid areas and bilayer thicknesses of commonly used phosphatidylcholines as a function of temperature. *Biochimica Et Biophysica Acta-Biomembranes.* 2011;1808(11):2761-71.
17. Mulvana H, Stride E, Hajnal JV, Eckersley RJ. Temperature Dependent Behavior of Ultrasound Contrast Agents. *Ultrasound Med Biol.* 2010;36(6):925-34.
18. Mulvana H, Stride E, Tang MX, Hajnal JV, Eckersley R. Temperature-Dependent Differences in the Nonlinear Acoustic Behavior of Ultrasound Contrast Agents Revealed by High-Speed Imaging and Bulk Acoustics. *Ultrasound Med Biol.* 2011;37(9):1509-17.
19. Swanson EJ, Mohan V, Kheir J, Borden MA. Phospholipid-Stabilized Microbubble Foam for Injectable Oxygen Delivery. *Langmuir.* 2010;26(20):15726-9.
20. Farook U, Stride E, Edirisinghe MJ. Preparation of suspensions of phospholipid-coated microbubbles by coaxial electrohydrodynamic atomization. *Journal of the Royal Society Interface.* 2009;6(32):271-7.
21. Borden MA, Longo ML. Dissolution behavior of lipid monolayer-coated, air-filled microbubbles: Effect of lipid hydrophobic chain length. *Langmuir.* 2002;18(24):9225-33.
22. Grant CA, McKendry JE, Evans SD. Temperature dependent stiffness and visco-elastic behaviour of lipid coated microbubbles using atomic force microscopy. *Soft Matter.* 2012;8(5):1321-6.

23. Borden M. Nanostructural features on stable microbubbles. *Soft Matter*. 2009;5(4):716-20.
24. Upadhyay A, Dalvi SV, Gupta G, Khanna N. Effect of PEGylation on performance of protein microbubbles and its comparison with lipid microbubbles. *Mat Sci Eng C-Mater*. 2017;71:425-30.
25. Stride E, Edirisinghe M. Novel preparation techniques for controlling microbubble uniformity: a comparison. *Medical & Biological Engineering & Computing*. 2009;47(8):883-92.
26. Epstein PS, Plesset MS. On the Stability of Gas Bubbles in Liquid-Gas Solutions. *J Chem Phys* 1950;18(11):1505-9.
27. Wang WH, Moser CC, Wheatley MA. Langmuir trough study of surfactant mixtures used in the production of a new ultrasound contrast agent consisting of stabilized microbubbles. *J Phys Chem-U.S.* 1996;100(32):13815-21.
28. Abou-Saleh RH, Peyman SA, Johnson BRG, Marston G, Ingram N, Bushby R, et al. The influence of intercalating perfluorohexane into lipid shells on nano and microbubble stability. *Soft Matter*. 2016;12(34):7223-30.
29. Xing ZW, Ke HT, Wang JR, Zhao B, Yue XL, Dai ZF, et al. Novel ultrasound contrast agent based on microbubbles generated from surfactant mixtures of Span 60 and polyoxyethylene 40 stearate. *Acta Biomaterialia*. 2010;6(9):3542-9.
30. Chou TH, Chu IM. Thermodynamic characteristics of DSPC/DSPE-PEG(2000) mixed monolayers on the water subphase at different temperatures. *Colloid Surface B*. 2003;27(4):333-44.
31. Bae YC, Lambert SM, Soane DS, Prausnitz JM. Cloud-Point Curves of Polymer-Solutions from Thermo-optic Measurements. *Macromolecules*. 1991;24(15):4403-7.
32. Gao X, Kucerka N, Nieh MP, Katsaras J, Zhu SP, Brash JL, et al. Chain Conformation of a New Class of PEG-Based Thermoresponsive Polymer Brushes Grafted on Silicon as Determined by Neutron Reflectometry. *Langmuir*. 2009;25(17):10271-8.
33. Tyrode E, Johnson CM, Rutland MW, Claesson PM. Structure and hydration of poly(ethylene oxide) surfactants at the air/liquid interface. A vibrational sum frequency spectroscopy study. *Journal of Physical Chemistry C*. 2007;111(31):11642-52.
34. Frey SL, Lee KYC. Temperature dependence of poloxamer insertion into and squeeze-out from lipid monolayers. *Langmuir*. 2007;23(5):2631-7.
35. Jebrail M, Schmidt R, DeWolf CE, Tsoukanova V. Effect of aliphatic chain length on stability of poly(ethylene glycol)-grafted phospholipid monolayers at the air/water interface. *Colloid Surface A*. 2008;321(1-3):168-74.
36. Angelova A, De Coninck J, Ionov R. Equilibrium surface properties of lipid mixtures of retinal, phosphatidylcholine and fatty acid derivatives at the air/water interface. *Supramol Sci*. 1997;4(3-4):207-14.
37. Gopal A, Lee KYC. Morphology and collapse transitions in binary phospholipid monolayers. *J Phys Chem B*. 2001;105(42):10348-54.
38. Lipp MM, Lee KYC, Takamoto DY, Zasadzinski JA, Waring AJ. Coexistence of buckled and flat monolayers. *Physical Review Letters*. 1998;81(8):1650-3.
39. Hristova K, Kenworthy A, McIntosh TJ. Effect of Bilayer Composition on the Phase-Behavior of Liposomal Suspensions Containing Poly(Ethylene Glycol)-Lipids. *Macromolecules*. 1995;28(23):7693-9.
40. Kiliç S, Bolukcu ES. Phase behavior of DSPC/PEG(40)St mixtures at higher emulsifier contents. *Colloid Surface B*. 2018;171:368-76.
41. Kiliç S. Quantification of PEG(40)St squeeze out from DSPC/PEG(40)St monolayers at higher molar ratios. *Colloid Surface A*. 2018;551:58-64.



Understanding Inhibition of Steel Corrosion by Some Potent Triazole Derivatives of Pyrimidine through Density Functional Theory and Molecular Dynamics Simulation Studies

Bello Abdullahi Umar*, Adamu Uzairu and Gideon Adamu Shallangwa
 Department of Chemistry, Ahmadu Bello University, Zaria, Nigeria

Abstract: Density Functional Theory (DFT) calculation at B3LYP level of theory and 6-31G* basis set was applied on some triazole derivatives of pyrimidine which led to the optimization of their structures, generation of electronic and other important Quantum chemical descriptors such as the energy of the highest occupied molecular orbital (E_{HOMO}), the energy of the lowest unoccupied molecular orbital (E_{LUMO}), energy band gap (ΔE), Dipole Moment (μ), chemical hardness (η), chemical softness (σ), global electronegativity (χ) and number of transferred electrons (ΔN) using SPARTAN'14 Software. The obtained results shows a good correlation between the chemical structures of the inhibitors and their experimental inhibition efficiencies (%IEs). The ranking of these efficiencies (%IEs) nicely matched with the order of a good number of the generated descriptors but with a varying degree of correlation as majority of the descriptors indicates that I-4 is the best inhibitor among the data set. Furthermore, molecular dynamic (MD) simulations were carried out to search the best adsorption configuration of the inhibitor on the steel (1 1 0) surface using Material Studio 8.0. The obtained results of MD simulations suggest that the interaction was as a results of the chemical adsorption on the steel surface, since the binding energy $> 100 \text{ Kcalmol}^{-1}$ for all the inhibitors and the best adsorption energy was found to be $-488.07 \text{ Kcalmol}^{-1}$ (I-4). This observation are in good agreement with the DFT results and the experiment findings. Thus; this study provides a valuable approach and new direction to novel steel corrosion inhibitor discovery.

Keywords: Triazole Derivatives of pyrimidine; DFT (B3LYP/6-31G*); MD simulation.

Submitted: July 23, 2018. **Accepted:** October 03, 2019.

Cite this: Umar B, Uzairu A, Shallangwa G. Understanding Inhibition of Steel Corrosion by Some Potent Triazole Derivatives of Pyrimidine through Density Functional Theory and Molecular Dynamics Simulation Studies. JOTCSA. 2019;6(3):455-66.

DOI: <https://doi.org/10.18596/jotcsa.446084>.

***Corresponding author. E-mail:** abdallahbum@yahoo.com.

INTRODUCTION

Corrosion of steel is a serious mechanical problem which affects several areas of industrial processes especially the oil industry which always leads to enormous economic losses (1, 2). The corrosion of steel may cause mechanical damage of equipment and lead to changes in the chemical properties of

processing substances. The cost of corrosion globally reported in 2010 was about \$ 2.2 Trillion, which was around 3 % of \$ 73.33 Trillion (world's entire domestic product) (3, 4). Prevention of corrosion exhibited a vital role for many industries particularly petrochemical industries that often make use of steel (2). Although it is not possible to

completely avoid the corrosion process, there are various methods to prevent it or slow down its rate (5, 6). One of the most economical and simple methods was the use of organic compounds especially those that contain O, N, P, and S heteroatoms and also pi-electron systems as corrosion inhibitors (7, 8).

Experimental techniques like weight-loss method, EIS (electrochemical impedance spectroscopy), potentiodynamic polarization, etc. (9, 10), have been used to understand the corrosion process and its inhibition. Although experiments mostly are time-consuming, costly, and lacking in explaining the mechanism of inhibition of the corrosion (11, 12). Thus, quantum chemical calculation method was endorsed as a potent and easy tool to reduce the cost and time and can help in the interpretation of the experimental findings (13, 14). Additionally, Molecular dynamics (MD) simulation was recently considered as a new tool to study the adsorptive behavior of the corrosion inhibitors on a metallic surface of interest (11, 15).

Furthermore, the corrosion inhibition efficiency of a series of a new set of triazole derivatives of pyrimidine was synthesized lately by Gonzalez-

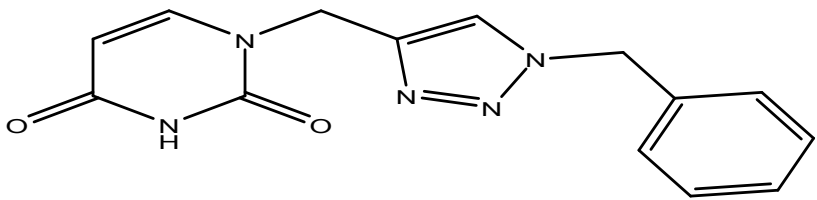
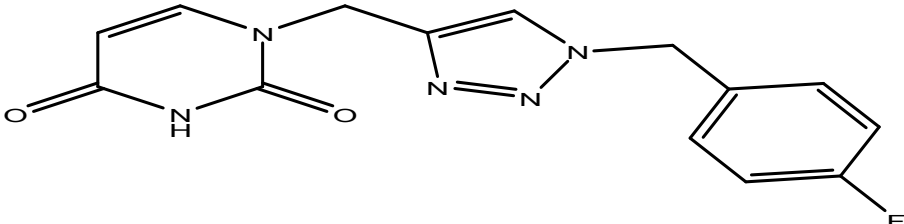
Olvera *et al* (16). The required products were found to have high yields and characterized by mass spectroscopy, IR and NMR. These synthesized compounds were evaluated as inhibitors for steel corrosion in 1 M HCl solution employing EIS method. The findings show the effective behavior of these compounds as inhibitors for steel corrosion in acidic solution. To the best search of the authors, these observations were not studied with any theoretical method. Thus, in the present study, quantum chemical calculations and molecular dynamics simulations were carried out on these compounds in order to give a clear relationship between their electronic structures, geometrical parameters and the binding energies with their experimental inhibition efficiencies (%Es) earlier reported by Gonzalez-Olvera *et al* (16).

COMPUTATIONAL DETAILS

Selection of Inhibitors

A set of ten triazole derivatives as corrosion inhibitors were selected from the literature (16) and used for this present study. The 2D structure of each inhibitor in the data set was drawn using ChemDraw ultra V12.0. The structures of the inhibitors and their experimental inhibition efficiency (%IE) are presented in Table 1.

Table 1. Triazole Derivatives of Pyrimidine Nucleobases and Their Inhibition Efficiency (%IE)

S/N	Structure	%IE
1		93.1
2		95.6

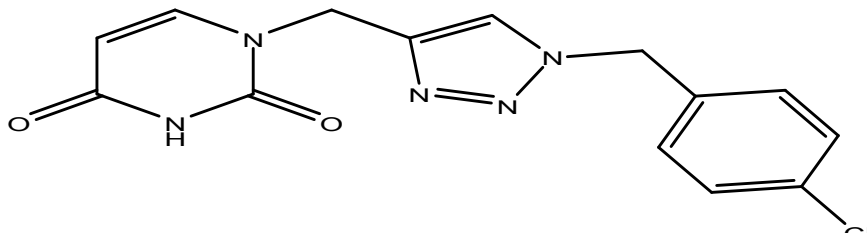
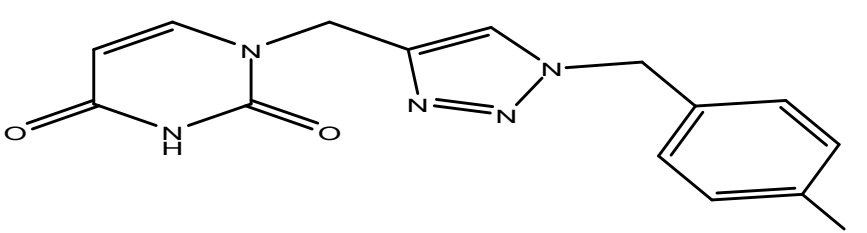
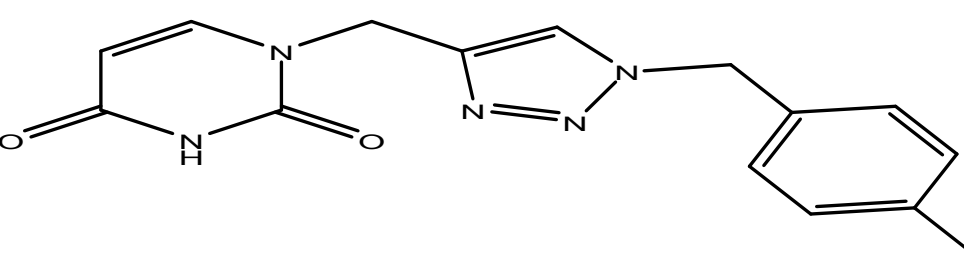
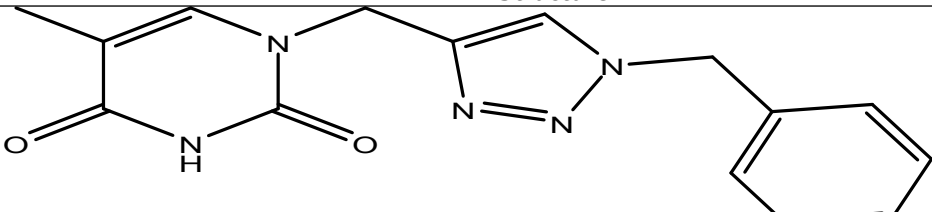
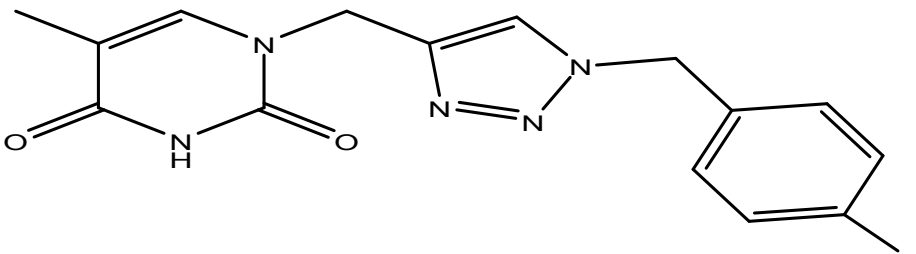
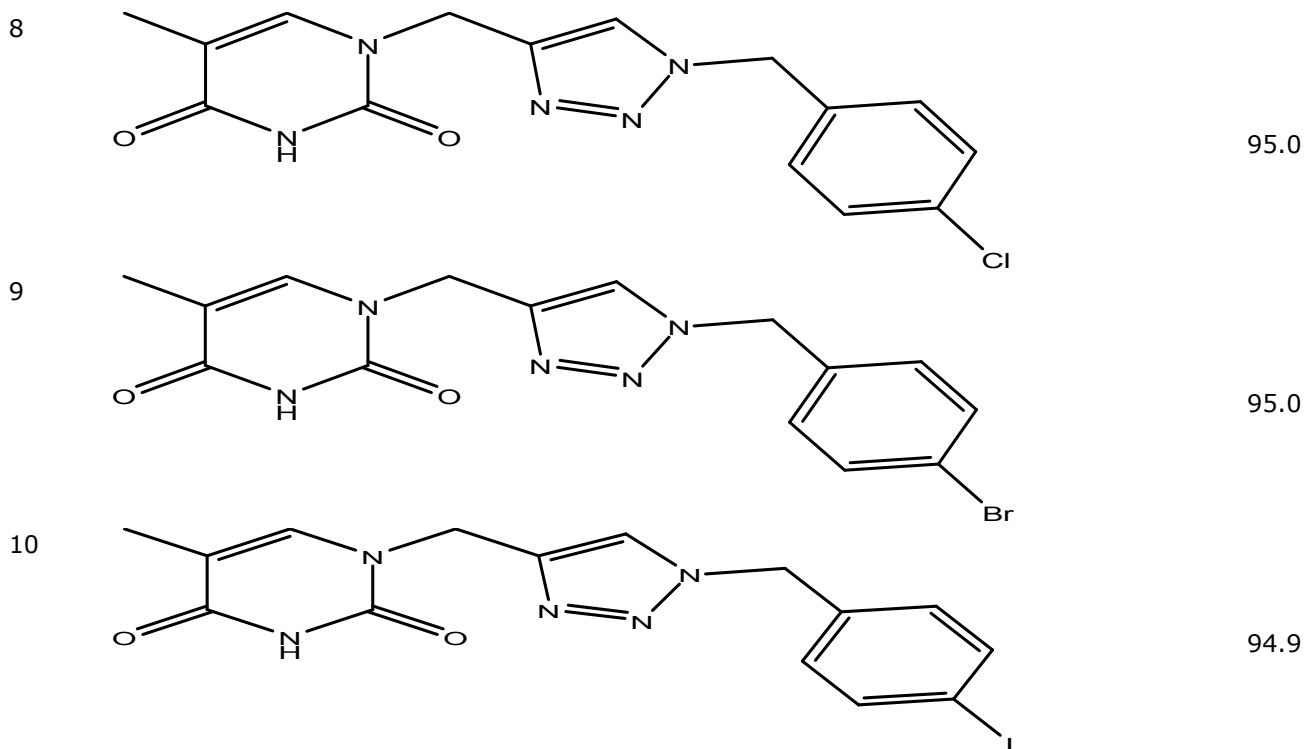
3		95.9
4		96.1
5		92.9

Table 1. (continued)

S/N	Structure	%IE
6		90.2
7		95.0



Optimization and calculation of chemical parameters

The 2D structure of each inhibitor was converted to the 3D structure using Spartan 14.0 software. The molecular mechanic force field (MM+) was used to clean and minimize the structures using of SPARTAN'14 software on Dell Intel(R)Core(TM)i7-5500U CPU), 16.00GB RAM @ 2.400GHz 2.400GHz processor on Windows 8.1 Pro 64-bit Operating system, x64-based processor, so as to remove all the strain on the structures of the inhibitor molecules. Additionally, this guarantee a fully-defined and stable conformation of the studied inhibitor molecules of this study (17, 18). Geometry optimization was set at ground state utilizing the DFT at the B3LYP level of theory and 6-311G (d) basis set. The generated chemical parameters were energy of highest occupied molecular orbital (E-HOMO), energy of lowest unoccupied molecular orbital (E-LUMO), dipole moment (μ) and some others were calculated such as energy band gap (ΔE), chemical hardness (η), chemical softness (σ), global electronegativity (χ), number of transferred electrons (ΔN) using relevant relations (Equations 1–5) as reported before in literature (5, 15).

$$\Delta E = E_{LUMO} - E_{HOMO} \quad (\text{Eq. 1})$$

$$\eta = \frac{-1}{2}(E_{HOMO} - E_{LUMO}) \quad (\text{Eq. 2})$$

$$\sigma = \frac{1}{\eta} = -\left(\frac{2}{(E_{HOMO} - E_{LUMO})}\right) \quad (\text{Eq. 3})$$

$$\chi = \frac{-(E_{HOMO} + E_{LUMO})}{2} \quad (\text{Eq. 4})$$

$$\sigma = \frac{1}{\eta} = -\left(\frac{2}{(E_{HOMO} - E_{LUMO})}\right)$$

$$\Delta N = \frac{(\chi_{Fe} - \chi_{inh})}{2(\eta_{Fe} + \eta_{inh})} \quad (\text{Eq. 5})$$

Where $\chi_{Fe} = 7$ eV and $\eta_{Fe} = 0$ (19)

Molecular Dynamics (MD) simulation

The simulation (MD) was applied to portray the adsorption mechanism between the studied inhibitors and the steel surface using Materials studio version 8.0 material simulation program from Biovia. The inhibitors were optimized and modeled employing COMPASS force field. The system (simulation) was carried out at 298K using Andersen thermostat with NVE microcanonical ensemble at a time step of 1.0 fs and the simulation time was set as 5ps. The simulation was conducted in a box (simulation-box) of (24.82 Å × 24.82 Å × 45.27 Å) under periodic boundaries conditions. The simulation box contains a Fe (110) slab, solvent (acid) molecules (H₂O+H₃O⁺ +Cl⁻) and

an inhibitor. Fe (110) surface was chosen as the studied Fe surface, because Fe (110) was the most density packed Fe surface and stable(20, 21). The Fe crystal has ten (10) layers out of which seven (7) down layers were frozen. The adsorption and binding energies values were calculated using equation 6 and 7 respectively (15).

$$E_{adsorption} = E_{Total} - (E_{Surface} + H_2O + H_3O^+ + Cl^- + E_{inhibitor}) \quad (\text{Eq. 6})$$

$$E_{binding} = -E_{adsorption} \quad (\text{Eq. 7})$$

Where E_{Total} is, $E_{Surface} + H_2O + H_3O^+ + Cl^- + Inhibitor$ (the total energy of the corrosion system) and $E_{Surface} + H_2O + H_3O^+ + Cl^-$ is the energy of the Fe surface together with $H_2O + H_3O^+ + Cl^-$ molecules and $E_{inhibitor}$ is the energy of the inhibitor.

RESULTS AND DISCUSSIONS

Quantum parameters of the studied inhibitors

In order to examine the inhibitive performance of the inhibitors in relation to the molecular structures, some DFT (Quantum) parameters were generated to explain their mode of adsorption. The geometry optimized molecular structure, the distributions of HOMO and LUMO of the first inhibitor are depicted in Figure 1. Table 4 present the results of DFT parameters of the studied inhibitors like the E-HOMO, E-LUMO, Dipole Moment (μ), Energy band gap (ΔE), chemical hardness (η), chemical softness (σ), global electronegativity (χ) and number of transferred electrons (ΔN) computed using Spartan 14 software at B3LYP level of theory, 6-31G (d, p) basis set and some relevant equations.

The HOMOs of the studied inhibitors are mainly dominated on the π -bond and then delocalized

over the whole aromatic pyrimidine ring in each molecule as seen in supplementary Table 1. The halogen substituents in each of the inhibitors from I-2 to I-10 are also involved in the HOMO. Pyrimidine ring of inhibitor 1 in Figure 1 shows a significant contribution of the two nitrogen atoms, π -bond and the two oxygen atoms of the -dione to the distributions of HOMO and LUMO. The HOMO electron density distribution of the studied inhibitors indicate favorable interactions of the inhibitors with an electron lacking metallic orbitals. The distribution of the LUMO electron densities of all the studied inhibitors were also spread all over on the pyrimidine rings. The electronic surfaces of HOMO and LUMO revealed the pyrimidine ring has the potential to donate and accept electrons under favorable conditions. This typical behavior is suitable for donor-acceptor interactions which may be responsible for the adsorption of inhibitors on the steel surface.

Based on the frontier orbital (molecular) approximation, the donor/acceptor relation occur in between HOMOs and LUMOs (frontiers (molecular) orbitals) of reacting molecules (22, 23). The adsorption mechanism of an inhibitor on a metallic surface usually increases with the increase of the HOMO energy and decreases with the decrease of LUMO energy. Therefore, the inhibitor molecule can donate their lone pair of electrons from the HOMO orbital to the d -orbital of the metallic molecule and also the inhibitor molecule will receive the electrons coming from the metallic d -orbital through the LUMO orbital for in-electron-donation and electron-back-donation method. Therefore, E-HOMO has always related with electron donation of an inhibitor; a high value of E-HOMO shows the high tendency of an inhibitor molecule to donate lone pair of electrons to the d -orbital of the acceptor metal.

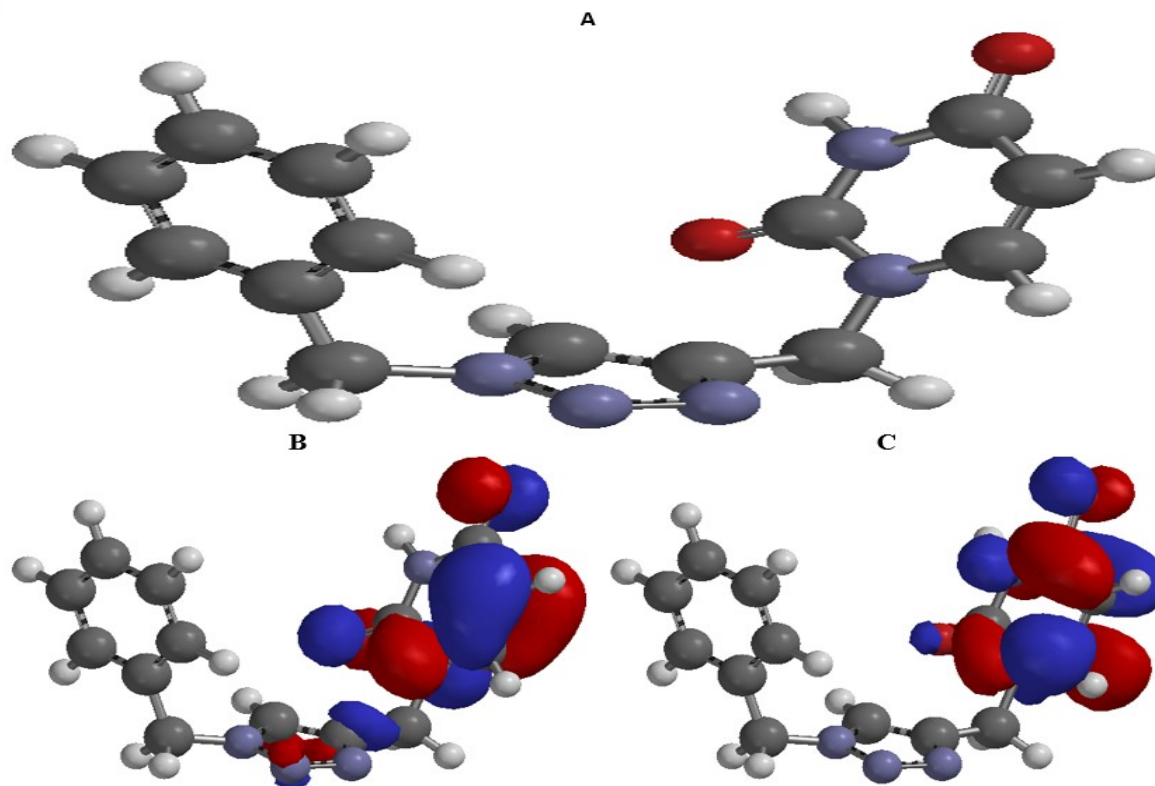


Figure 1. (A) Optimized Structure (B) HOMO distribution and (C) LUMO distribution for I-1(Inh.1).

Table 2. Selected quantum chemical parameters of the studied inhibitors.

S/N	E-HOMO(eV)	E-LUMO(eV)	ΔE	μ (Debye)	η	σ	χ	ΔN
1	-6.59	-1.04	5.55	3.38	2.775	-0.360	3.815	4.419
2	-6.63	-1.07	5.56	3.85	2.780	-0.359	3.850	4.379
3	-6.66	-1.10	5.56	4.04	2.780	-0.359	3.880	4.337
4	-6.66	-1.09	5.57	4.03	2.785	-0.359	3.875	4.352
5	-6.65	-1.08	5.57	3.79	2.785	-0.359	3.865	4.365
6	-6.32	-0.90	5.42	3.99	2.710	-0.369	3.610	4.593
7	-6.38	-0.95	5.43	3.13	2.715	-0.368	3.665	4.527
8	-6.39	-0.96	5.43	2.01	2.715	-0.368	3.675	4.513
9	-6.41	-0.98	5.43	1.92	2.715	-0.368	3.695	4.487
10	-6.40	-1.09	5.31	2.06	2.655	-0.377	3.745	4.321

Energy of highest occupied molecular orbital (E-HOMO), Energy of lowest unoccupied molecular orbital (E-LUMO) Energy band gap (ΔE), dipole moment (μ) chemical hardness (η), chemical softness (σ), global electronegativity (χ), number of transferred electrons (ΔN).

From Table 2, the values of E-HOMO for the studied inhibitors increases in the order I-4 > I-3 > I-5 > I-2 > I-1 > I-9 > I-10 > I-8 > I-7 > I-6 respectively. The trend in the increase of the HOMO energies show some level of consistency with the increase of the efficiencies (inhibition), Thus, I-4 with a high efficiency (96.1%) has a larger HOMO energy and I-6 with the lowest efficiency (90.2%) has a lower HOMO energy as seen in Table 2. Conversely, a low value of E-LUMO of an inhibitor molecule demonstrate the high

tendency of the inhibitor molecule to receive electrons coming from the metallic d-orbital during the back-donation process. From Table 2, the E-LUMO value in the ascending order are: I-6 > I-7 > I-8 > I-9 > I-1 > I-2 > I-5 > I-4 > I-10 > I-3. This indicates that I-3 has a stronger chances of accepting electrons from orbital of the metal as they interact with the Fe surface. Therefore, I-3 may strongly adsorb on the surface of the metallic and achieve better inhibition effectiveness though the second highest in terms of %IE. I-6 strongly

agrees with EIS findings as it has the lowest %IE having the highest LUMO energy.

Energy band gap, ΔE is another crucial property as most efficient inhibitors were characterized by a small value of ΔE (24). In Table 2, the trend at which the energy gap decreases is not consistent with the increase in the experimental %IEs of the studied inhibitors. However, the reverse is the case *i.e.* the ΔE increases when the %IEs decreases. The dipole moment (μ) is another parameter which is commonly used for the prediction of direction of the inhibition process. It shows a distribution of the electrons on the molecule, and also measure the polarity in any given bond (25). The molecules with higher μ values tend to form a strong interactions (dipole-dipole) with the metallic steel surface, resulting to a strong adsorption of the inhibitor on the metallic surface and hence resulting in the better IE% of an inhibitor (26). Nevertheless, there is no established correlation between the μ and IE % reported (21). The results shown in Table 2 indicate that I-3 has the largest μ value and I-9 has the lowest μ value. Among all the ten (10) studied inhibitors, increasing the μ leads to an increment of their IE% due to the increase in the intermolecular forces.

Inhibitor with the large hardness (η) value is expected to be weaker compared to other inhibitors with lower values (7). Thus, as shown in Table 2, the hardness value increases as the %IE increases. I-4 has the highest η value hence the best inhibitor and this agrees with the experimental observation reported in table 1. The larger σ value indicates that the inhibitor have softer nature and will have higher chances of donating electrons to the metallic molecule (27). The arrangement across the inhibitors in the σ values as presented in Table 2 decreases in the order, I-2 > I-3 > I-4 > I-5 > I-1 > I-7 > I-7 > I-8 > I-9 > I-6 > I-10. This suggests that I-2 has the highest and therefore the most reactive inhibitor molecule.

The electronegativity (χ) describes the electron attracting power of an inhibitor molecule. The high value of χ shows the strong attracting capability of an inhibitor molecule to accept the electrons from the metallic (Fe) surface (11). Afterward, the inhibitors that have larger electronegativities would have better interaction with Fe surface and then will have better IE%. From Table 2, it can be observed that the χ values of the ten inhibitors obey the order I-3 > I-4 > I-5 > I-2 > I-1 > I-10 > I-9 > I-8 > I-7 > I-6, hence, it is confirmed that I-3 followed by I-4 has the higher tendency of accepting electrons and I-6 has the least among

the studied inhibitors and these findings are in good agreement with the experimental findings. The values of ΔN demonstrate the fraction of electrons that transfer from the inhibitor to the metallic surface. If $\Delta N > 0$, then electrons was transferred from the inhibitor molecule to the Fe-surface while if $\Delta N < 0$, then electrons were transferred from Fe-surface to inhibitor molecule through electron back donation process (15). From Table 2, it can be observed that the values of ΔN of the studied inhibitors are all greater than 0 ($\Delta N > 0$), this indicates that all the studied inhibitors may donate electrons on to the Fe surface through the formation of a coordinate covalent bond. Examination of the results in Table 2 indicates that the values of ΔN of the inhibitors has a very little difference. This further confirms the electron donating ability of the studied inhibitors as observed from their experimental findings.

Molecular Dynamic Simulation Studies

Electronic parameters alone are not enough to determine the trend of the inhibitive performances of these studied inhibitors despite its success in explaining the mechanism of action of the inhibitors. Thus, it is essential to conduct thorough modelling of the direct interactions of the studied inhibitors with the Fe surface. It is believed that the major mechanism of the inhibition of corrosion is through adsorption. Therefore, adsorption of these inhibitors on the steel (Fe) surface was simulated to predict the nature of interactions between the studied inhibitors and Fe (110) crystal surface in 1M HCl. The first step of this simulation process was the geometry optimization of the studied inhibitors, solvent (acid) molecules (H_2O , H_3O^+ , and Cl^-) and Fe (110) crystal. The geometry optimization of the corrosion system was conducted until the total energy of the system reached a local minimum on the potential energy surface. During the optimization process, the atomic coordinates were adjusted using COMPASS force-field which continues unless the total energies of the individual structures reached to the minimum energy, after which, a box was created for the simulation process by importing the Fe (110) crystal, solvent molecules (H_2O , H_3O^+ and Cl^-) and the inhibitor molecule. Then the MD process were conducted and the system attained equilibrium when both the energy and temperature of the system were balanced. All the other inhibitors were studied similarly. The equilibrium configurations of the simulated system for the first inhibitor are depicted in Figure 4. It could be observed that in Figure 5 and 6 at the middle of the MD simulation process the system moves towards the equilibrium. After the system attained equilibrium, the adsorption and the binding energy values of the inhibitors adsorbed on the Fe surface

was calculated according to equations (6) and (7) respectively and are presented in Table 3.

Table 3. Molecular Dynamic Simulations Results of the studied inhibitors.

S/N	$E_{Fe+soln.}$ (kcalmol ⁻¹)	$E_{Inh.}$ (kcalmol ⁻¹)	E_{Total} (kcalmol ⁻¹)	$E_{Ads.}$ (kcalmol ⁻¹)	$E_{Bind.}$ (kcalmol ⁻¹)	BD(Å)
1	-125832.513	-42.694	-126294.487	-419.28	419.28	2.595
2	-125832.513	-40.231	-126346.164	-473.42	473.42	2.891
3	-125832.513	-40.376	-126353.079	-480.19	480.19	2.390
4	-125832.513	-40.323	-126360.906	-488.07	488.07	2.160
5	-125832.513	-40.284	-126316.487	-443.69	443.69	3.18
6	-125832.513	-78.975	-126350.438	-438.95	438.95	2.920
8	-125832.513	-78.997	-126377.5	-465.99	465.99	2.783
9	-125832.513	-75.505	-126389.708	-481.69	481.69	2.842
9	-125832.513	-72.986	-126383.419	-477.92	477.92	2.780
10	-125832.513	-74.047	-126356.57	-450.01	450.01	3.050

$E_{Fe+soln.}$ (Energy of Fe + H₂O+H₃O⁺ + Cl⁻), $E_{Inh.}$ (Energy of the inhibitor), E_{Total} (total energy of the simulation system), $E_{Ads.}$ (Adsorption Energy), $E_{Bind.}$ (Binding Energy), BD (Bond Distance).

It can be observed from the molecular structures of the examined inhibitors that these molecules contain various electrons (lone pair) on the N and O atoms and also n-bonds of the aromatic systems. Therefore, these electrons (lone pair) on the heteroatoms will be donated to an empty d orbitals of Fe metal. It could be observed in Figure 4, that the inhibitor adsorbs almost flatly in orientation with the Fe surface and the interaction is more through the pyrimidine ring. This flat orientation of the inhibitor molecule on the Fe surface can be as a result of a chemical bond formation between the inhibitor and Fe surface. This observation was supported by the HOMO and LUMO distributions of these inhibitors as the region (pyrimidine ring) was found to be the most active center of adsorption (see Figure 1). Additionally, it could be seen from the results presented in Table 3 that the values of the adsorption energy of the

simulation systems at 298 K were large and negative. These high negative values of adsorption energies may be attributed to the strong interaction which occur between these inhibitors and Fe surfaces. Thus, the calculated adsorption energy values reveal that inhibitor 4 adsorbs on the Fe surface more spontaneously than any other inhibitor among the series. However, the adsorption capability of an inhibitor molecule on the Fe surface may also be determined from the values of the binding energy. The larger the binding energy is, the better will be the adsorption. Therefore, it is further confirmed from the results presented in Table 3, that all the adsorption of the inhibitors on the Fe surfaces occurred through chemical adsorption process since the magnitude of the binding energies is actually within the range of chemisorption (>100 kcal mol⁻¹) (28).

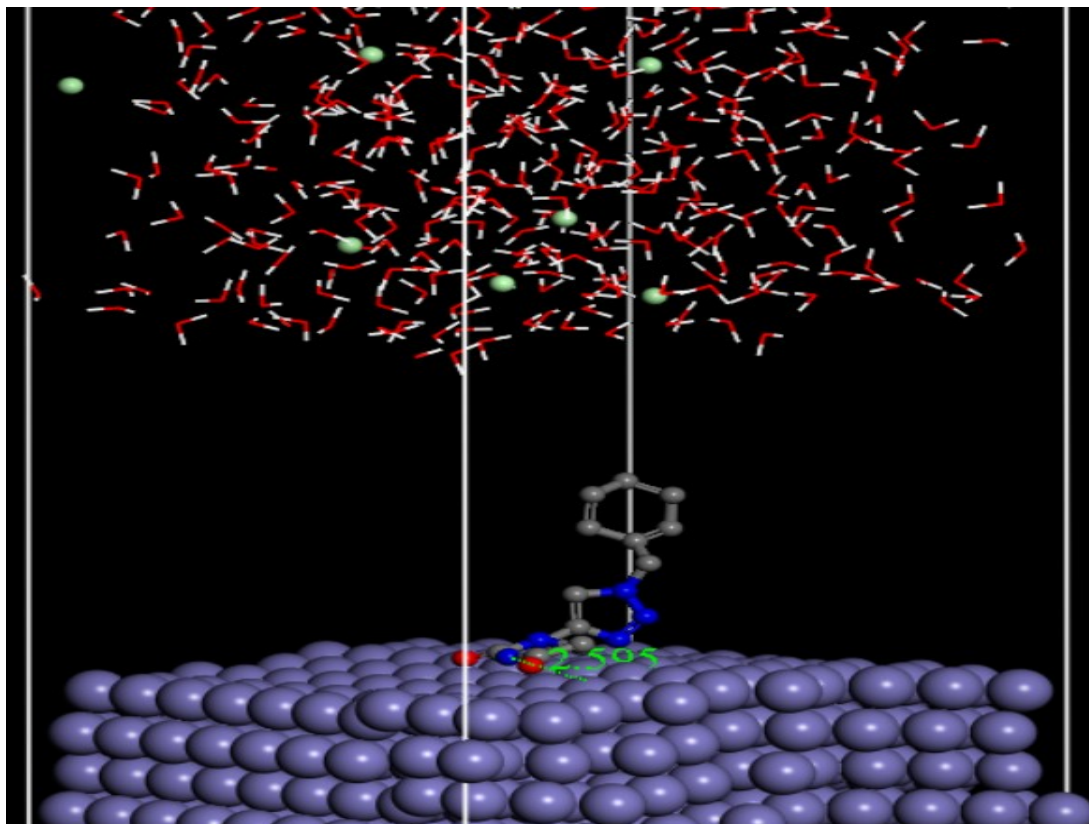


Figure 2. Equilibrium interaction configurations of the first inhibitor on Fe (1 1 0) surface.

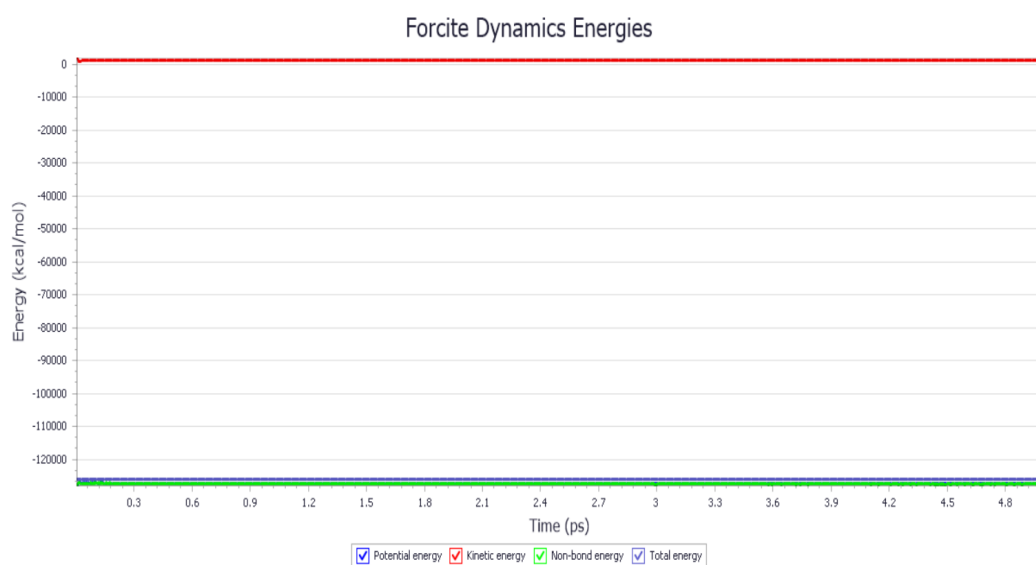


Figure 3. Fluctuation curves of Energies obtained from MD simulation for the first inhibitor.

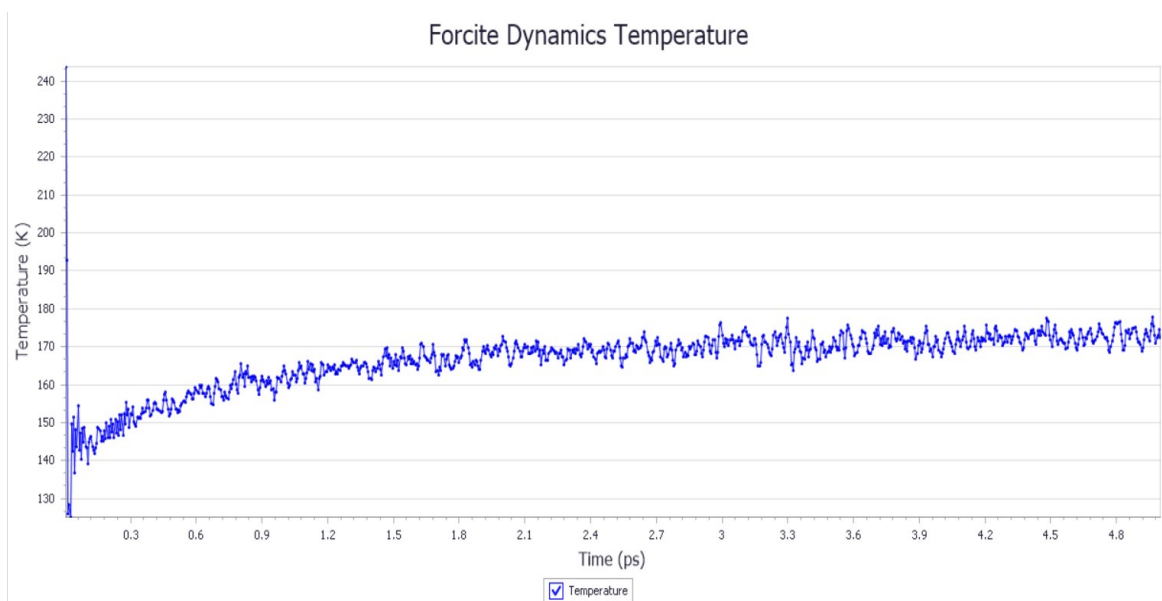


Figure 4. Equilibrium Temperature curve recorded from MD simulation for the first inhibitor.

Generally, bond distance measured within 3.5 \AA describes a strong chemical bond formation between the atoms and the bond distance greater than 3.5 \AA signifies interaction between the atoms are of Van der Waals type (29, 30). Figure 4 indicates the bond distance (shortest) between the N-atom of the pyrimidine ring of the first inhibitor and Fe surface. The measured bond distances for all the studied inhibitors and Fe-surface were shown in table 3. From the mentioned values in Table 3, it can be clearly seen that all the measured bond distances are in the range (3.5 \AA), this indicates that chemical bond was formed between these inhibitors and the Fe surface. Thus, chemical adsorption occurred on Fe surfaces. These findings are consistent with the experimental results obtained from EIS measurement (16) as well as from quantum chemical studies. This could be explained from the molecular structures of the studied inhibitors and the distribution of the HOMOs and LUMOs. Inhibitors having halogen atoms in their molecular structures are more and easily adsorbed on metallic surfaces and shows better efficiency (inhibition). It was clear from the structures given in Table 1 that inhibitor 1-5 has the similar pattern with the introduction of halogen atoms which increases the inhibition efficiency in the order $\text{Br} > \text{Cl} > \text{F}$ while the iodine atom slightly decreased the %IE. For that reason, inhibitor-4 with bromine atom as the substituent was the best corrosion inhibitor among the studied inhibitors. Similarly, inhibitor 6-10 had a similar pattern with F, Cl and Br and methyl group as substituent have the same effect in increasing the inhibition efficiency while the increase with iodine as the

substituent is also slightly lower. In this regard the inhibitors with Br, F or Cl are regarded to be the most potential corrosion inhibitors for steel.

Furthermore, in order to check the affection of the solvent (acidic) solution on the adsorption process of the system, the adsorption behavior of the first inhibitor in vacuum was simulated via MD simulation. The adsorption energy obtained in acidic solution is much less than those obtained in the vacuum. This could be due to the less influential effect in vacuum and the complex nature of the corrosion process in solution, like adsorption of the solvent (acid) molecules, the affection of the acid solution, most especially the anions, that have been proved to have a high influence on adsorption of the inhibitor (8). It was found that the adsorption energy of this inhibitor ($-1811.528 \text{ kcal mol}^{-1}$) changed significantly compared with the one simulated in acidic solution ($-419.28 \text{ kcal mol}^{-1}$). So also, the adsorption behavior is not consistent to those in the acid solution. Therefore, considering a solvent in the molecular dynamic simulation process is very necessary.

CONCLUSION

It has been clearly shown that the approach employed in this study was successful in explaining the inhibition performance of the studied inhibitors. Quantum chemical calculation shows that the reactive sites in the structure of the inhibitors are majorly the N-atom of the pyrimidine ring, π -electron centers, and a halogen substituent. Electron-donation and electron-acceptance

capability of these inhibitors were consistent with the results obtained from the EIS experiment. The interaction energies (E_{ads} and E_{bind}) between the inhibitors and Fe (1 1 0) metal surface via MD-simulation were large indicating chemical bond formation and that the inhibitors can more tightly adsorb on the iron surface. Inhibitor 4 showed high adsorption energy ($-488.07 \text{ kcal mol}^{-1}$) among other co-inhibitors as observed from the experiment. From this molecular dynamics simulations analysis, we realized that the order of values of the adsorption and binding energy were in good agreement to the experimental findings and also the shortest bond distances measured indicates that these inhibitors have a very strong interactions with steel (Fe) surface. Thus, this quantum chemical calculations and molecular dynamic simulation results correlate with each other and suggest the directions for the design of new anti-corrosion molecules with better inhibitive potential toward corrosion of steel.

ACKNOWLEDGMENTS

The authors sincerely acknowledge Ahmadu Bello University, Zaria for providing the softwares used and all the members of the group for their advice and encouragement in the cause of this research.

REFERENCES

1. Szklarska-Smialowska Z, ZS-Smialowska. Pitting and crevice corrosion: NACE International Houston, TX; 2005.
2. Singh P, Ebenso EE, Olasunkanmi LO, Obot I, Quraishi M. Electrochemical, theoretical, and surface morphological studies of corrosion inhibition effect of green naphthyridine derivatives on mild steel in hydrochloric acid. *The Journal of Physical Chemistry C*. 2016;120(6):3408-19.
3. Obot IB. Recent advances in computational design of organic materials for corrosion protection of steel in aqueous media. *Developments in corrosion protection: InTech*; 2014.
4. Al Hashem A. Corrosion in the Gulf Cooperation Council (GCC) states: statistics and figures. proceedings of the Corrosion UAE, Abu Dhabi, UAE. 2011.
5. Nwankwo HU, Ateba CN, Olasunkanmi LO, Adekunle AS, Isabirye DA, Onwudiwe DC, et al. Synthesis, characterization, antimicrobial studies and corrosion inhibition potential of 1, 8-dimethyl-1, 3, 6, 8, 10, 13-hexaazacyclotetradecane: experimental and quantum chemical studies. *Materials*. 2016;9(2):107.
6. Usmana B, MOHAMMED AS, Umarb A. QUANTUM CHEMICAL EVALUATION ON CORROSION INHIBITION PERFORMANCE OF BALANITIN-7 ON MILD STEEL IN 1M HYDROCHLORIC ACID SOLUTION. *Applied Journal of Environmental Engineering Science*.4(3):4-3 (2018) 380-386.
7. Murulana LC, Singh AK, Shukla SK, Kabanda MM, Ebenso EE. Experimental and quantum chemical studies of some bis (trifluoromethyl-sulfonyl) imide imidazolium-based ionic liquids as corrosion inhibitors for mild steel in hydrochloric acid solution. *Industrial & Engineering Chemistry Research*. 2012;51(40):13282-99.
8. Zhao H, Zhang X, Ji L, Hu H, Li Q. Quantitative structure-activity relationship model for amino acids as corrosion inhibitors based on the support vector machine and molecular design. *Corrosion Science*. 2014;83:261-71.
9. Zhang D-Q, Cai Q-R, He X-M, Gao L-X, Zhou G-D. Inhibition effect of some amino acids on copper corrosion in HCl solution. *Materials Chemistry and Physics*. 2008;112(2):353-8.
10. Amin MA, Ibrahim MM. Corrosion and corrosion control of mild steel in concentrated H₂SO₄ solutions by a newly synthesized glycine derivative. *Corrosion Science*. 2011;53(3):873-85.
11. Wazzan NA, Obot I, Kaya S. Theoretical modeling and molecular level insights into the corrosion inhibition activity of 2-amino-1, 3, 4-thiadiazole and its 5-alkyl derivatives. *Journal of Molecular Liquids*. 2016;221:579-602.
12. Usman B, Jimoh I, Umar BA. THEORETICAL STUDY OF 2-(3, 4-DIHYDROXYPHENYL) CHROMAN-3, 5, 7-TRIOL ON CORROSION INHIBITION OF MILD STEEL IN ACIDIC MEDIUM. *Applied Journal of Environmental Engineering Science*.5(1):5-1 (2019) 66-74.
13. Atalay Y, Yakuphanoglu F, Sekerci M, Avci D, Başoğlu A. Theoretical studies of molecular structure and vibrational spectra of 2-amino-5-phenyl-1, 3, 4-thiadiazole. *Spectrochimica Acta Part A: Molecular and Biomolecular Spectroscopy*. 2006;64(1):68-72.
14. Ebenso EE, Arslan T, Kandemirli F, Caner N, Love I. Quantum chemical studies of some rhodanine azosulpha drugs as corrosion inhibitors for mild steel in acidic medium. *International Journal of Quantum Chemistry*. 2010;110(5):1003-18.

15. Saha SK, Banerjee P. A theoretical approach to understand the inhibition mechanism of steel corrosion with two aminobenzonitrile inhibitors. RSC Advances. 2015;5(87):71120-30.
16. González-Olvera R, Espinoza-Vázquez A, Negrón-Silva GE, Palomar-Pardavé ME, Romero-Romo MA, Santillan R. Multicomponent click synthesis of new 1, 2, 3-triazole derivatives of pyrimidine nucleobases: Promising acidic corrosion inhibitors for steel. Molecules. 2013;18(12):15064-79.
17. Viswanadhan VN, Ghose AK, Revankar GR, Robins RK. Atomic physicochemical parameters for three dimensional structure directed quantitative structure-activity relationships. 4. Additional parameters for hydrophobic and dispersive interactions and their application for an automated superposition of certain naturally occurring nucleoside antibiotics. Journal of chemical information and computer sciences. 1989;29(3):163-72.
18. Arthur DE, Uzairu A, Mamza P, Abechi E, Shallangwa G. QSAR MODELLING OF SOME ANTICANCER PGI50 ACTIVITY ON HL-60 CELL LINES. Albanian Journal of Pharmaceutical Sciences. 2016;3(1):4-9.
19. Musa AY, Jalgham RT, Mohamad AB. Molecular dynamic and quantum chemical calculations for phthalazine derivatives as corrosion inhibitors of mild steel in 1 M HCl. Corrosion Science. 2012;56:176-83.
20. Khaled K. Molecular simulation, quantum chemical calculations and electrochemical studies for inhibition of mild steel by triazoles. Electrochimica Acta. 2008;53(9):3484-92.
21. Nwankwo HU, Olasunkanmi LO, Ebenso EE. Experimental, quantum chemical and molecular dynamic simulations studies on the corrosion inhibition of mild steel by some carbazole derivatives. Scientific reports. 2017;7(1):2436.
22. Bereket G, Öğretir C, Özşahin Ç. Quantum chemical studies on the inhibition efficiencies of some piperazine derivatives for the corrosion of steel in acidic medium. Journal of Molecular Structure: THEOCHEM. 2003;663(1-3):39-46.
23. Bello A, Uzairu A, Shallangwa G. MOLECULAR MODELLING AND DYNAMIC SIMULATION OF CORROSION INHIBITORS ON STEEL IN ACIDIC MEDIUM. FUW Trends in Science & Technology Journal. 2018;3 (2A):365-372
24. Ebenso EE, Khaled K, Shukla SK, Singh AK, Eddy N, Saracoglu M, et al. Quantum chemical investigations on quinoline derivatives as effective corrosion inhibitors for mild steel in acidic medium. 2012.
25. Abdallah M, Atwa S, Salem M, Fouda A. Synergistic effect of some halide ions on the inhibition of zinc corrosion in hydrochloric acid by tetrahydro carbazole derivatives compounds. Int J Electrochem Sci. 2013;8:10001-21.
26. Verma C, Olasunkanmi LO, Ebenso EE, Quraishi MA, Obot IB. Adsorption behavior of glucosamine-based, pyrimidine-fused heterocycles as green corrosion inhibitors for mild steel: experimental and theoretical studies. The Journal of Physical Chemistry C. 2016;120(21):11598-611.
27. Wazzan NA. DFT calculations of thiosemicarbazide, arylisothiocyanates, and 1-aryl-2, 5-dithiohydrazodicarbonamides as corrosion inhibitors of copper in an aqueous chloride solution. Journal of Industrial and Engineering Chemistry. 2015;26:291-308.
28. Akalezi CO, Enenebaku CK, Oguzie EE. Application of aqueous extracts of coffee senna for control of mild steel corrosion in acidic environments. International Journal of Industrial Chemistry. 2012;3(1):13.
29. Shi W, Xia M, Lei W, Wang F. Molecular dynamics study of polyether polyamino methylene phosphonates as an inhibitor of anhydrite crystal. Desalination. 2013;322:137-43.
30. Zeng J, Zhang J, Gong X. Molecular dynamics simulation of interaction between benzotriazoles and cuprous oxide crystal. Computational and Theoretical Chemistry. 2011;963(1):110-4.